**NNT : 2017SACLX014**

# THESE DE DOCTORAT
DE
L'UNIVERSITE PARIS-SACLAY
PREPAREE A
L'ECOLE POLYTECHNIQUE

ECOLE DOCTORALE N° 573 Interfaces
Approches interdisciplinaires, fondements, applications et innovation

Spécialité de doctorat : Physique

Par

**M. Jian Tang**

## From Silicon to Germanium Nanowires: growth processes and solar cell structures

**Thèse présentée et soutenue à Palaiseau, le 7 Avril 2017 :**

**Composition du Jury :**

| | | | |
|---|---|---|---|
| Dr. | Patriarche, Gilles | C2N | Président |
| Prof. | Fontcuberta i Morral, Anna | EPFL | Rapporteur |
| Prof. | Dubrovskii, Vladimir | IOFFE | Rapporteur |
| Prof. | Fejfar, Antonin | LNSM | Examinateur |
| Prof. | Topic, Marko | UNILG | Examinatrice |
| Prof. | Yu Linwei | NJU | Examinatrice |
| Prof. | Johnson, Erik | LPICM | Directeur de thèse |
| Dr. | Roca i Cabarrocas, Pere | LPICM | Co-directeur de thèse |
| Dr. | Foldyna, Martin | LPICM | Co-directeur de thèse |

It was your smile,

at the seaside,

longtime ago,

calls me to come to you with all my passion and all my joy.

You are my sense.

To love and science

**Acknowledgements**

To do a thesis in Physics was my dream when I was a bachelor. Now it is finished! It would have been impossible if I had not received an enormous help during the past years! Please allow me to say: thank you!

My first thanks belong to EU-China ICARE institute. People in this master program have built the bridges for me. These brides allow me to step from Mechanical engineering to Physics and from China to France. The study and the life in ICARE were very happy experiences. Thanks to Yang Liu, Lei Liu, Sha Cheng, Didier Mayer, Joaquim Nassar, Michel Farine, Cedric Denis-Remis, and to all the professors, personnel, and students of this program.

A new domain, a new culture, it is a long and not easy way to go. Fortunately I met Pere Roca i Cabarrocas, the director of LPICM, at the beginning of my rode. He accepted me as an internship student and helped me to get a PhD scholarship of Ecole Polytechnique later. I'm a beginner, a normal student or even less good than a normal student, but he didn't mind. I usually give poorly written reports to him and give simply explanations on the experiments. But he is always so patient and spends enormous time to help me to improve little by little, version after version. There is a picture of child Einstein who is calculating 1+2=3 in front of Pere's desk. I guess Pere has the similar look on me. For the research, I don't have professional eyes but I always want big freedom. While for Pere, he just gives me suggestions and permits me to choose the way I like, even the project needs me to work on another topic. However, he is always here to help me even I haven't listened to him at the beginning. For the daily life, I also have the chance to receive plenty of his smiles, plenty of talk heart to heart, plenty of chances to visit his house. What's more, he read my report every day at the last stage of the thesis. A deep thank you to Pere! Pere's enthusiasm to science is also a model for me. He starts work at early morning and finish at late evening, and perhaps 7 days per week. Besides numerous administrative works, he still does experiments by himself and tries to participate into scientific discussions of many groups. It is not easy to see that he stops running and has a cozy rest. I would like to say: Hi Pere, you worked too hard! Go to the beach and have a real rest. But on the beach, he is correcting three 3 PhD theses and replying plenty emails. Pere is the top leader of the lab, but in fact he is the biggest servant of the lab. I would like to compare the activities in our lab with the barbecue in Pere' garden. We are studding samples and have scientific discussion in the lab, as if we are tasting the food, the wine and having conversation is Pere's garden. Pere is always running and trying to serve all the people during the barbecue to make everybody happy. Thank you Pere!

My thanks also belong to Wanghua Chen. He is the person with whom I had the most discussions except Pere. He, as a big brother, explains to me all types of questions. I'm grateful to Jean-Luc Maurice. He has carried out all the TEM experiments measurements presented in this thesis. Apart from his enormous efforts on studding my samples, he is always ready and patient to explain my questions. Even during the experiments, he will stop and explain to me kindly and clearly. Thank you for spending so much of your time on helping me and teaching me! And thank you for your kind encouragement! I have received a big help from Jun Wang. He has worked with me for 4 months on the SiGeNW growth. He works hard and has a lot of ideas. He also gives me a chance to learn how to take the responsibility of a two people research group. It was a happy and fruitful collaboration. Thanks to Martin Foldyna for explaining me the basics of optics, helping me to characterize the

materials and also for serving the NW research group. Thanks to Erik Johnson for his guidance and help to me, and also for serving the PV researching group. A special thanks to the tons of funny jokes of Erik. For this, I would like to do another thesis with you. But this time, you should not just be my supervisor officially. Thanks to Soumyadeep for training me how to grow NWs, fabricate and characterize NW solar cells. He has also generously given me the optimized conditions for fabricating NWs and solar cells. Thanks to Aliénor Togonal, Zuzana Mrazkova, Zahra Asghar, Al-Ghzaiwat Mutaz, Andrii Kulakovskyi, Shiwen Gao, and Letian Dai for being a member of NW group and give me constant support. Thanks to Chiaria Toccafondi for putting enormous time on nanoRaman measurements of my samples. Her attitude to work is touching. Thanks to Ileana Florea for the help on preparing the samples for NanoRaman, and also for her kind concerns on my research progresses. Thanks to Cyril Jadaud, Pavel Bulkin, Jérome Charliac and François Silva. Because of you the reactors run again and again. Thanks to Jacqueline for the training on AFM and SEM. Thanks to Total team on the training and help on the numerous equipments. Thanks to Enric Garcia Caurel for teaching me the theory of ellipsometry with great patience. Thanks to Jean-Eric Bouree, Holger Vach, Didier Pribat, and Marc Chaigneau for the theoretical discussions.

It is the administrative team who makes the life easier. They are Laurence Gérot, Carine Roger-Roulling, Julie Dion, Chantal Geneste, Fabienne Pandolf, and Gabriela Medina. Thank you for the service, big smile and pleasant conversations in the cafeteria. Thans to Jean-Luc Mocel, the master of Kongfu who guarantees the security of the lab. A big thanks to computer man Eric Paillassa and Frédéric Liege. You are the most pleasant people in LPICM. Thanks to your jokes and frank laugh. You make the lab a funny place. A special thanks for providing extra service to my personal computer!

Now it is time to say thanks to my dear PhD student team of LPICM. You have been my partners for a travel, a lunch, a dance, a sport, a stupid talk, a special joke, and everything. You always give me a lot of happy time. Romain Cariou, my first scientific tutor who is loved by the whole LPICM, my intelligent, solemn and funny friend Jean-Christophe Dornstetter, the famous singer Igor Sobkowicz, la crème de la crème who sits in front of me, Bastien Bruneau, our big leader since Master, Paul Narchi. You are so numerous, you are Gwénaelle Hamon, Alice Defresne, Guillaume Fischer, Farah Haddad, Fatme Jardali, Fabien Lebreton, Ronan Léal, Jean-Maxime Orlac'H, Junkang Wang, Xinyang Wang, Yachun Zhang, Rasha Khoury, Sungyeop Jung, Loic loisel, Solomé Forel, Arthur Marronnier, Anna Shirinskaya. Zheng Fan, San Hyuk Yoo, Leandro Sacco, Mengkoing Sreng, Heejae LEE, Zeyu Li and Qijiao Lin. Thank you all!

I also have the chance to receive help from our collaborating labs. They are Isabelle Maurin and Thierry Gacoin from LPMC for the catalyst engineering, Philippe Pareige, Inès Massiot, Sebastien Duguay, Celia Castro, Emmanuel Cadel from GPM for the APT measurements on SiNWs and SiNW solar cells, Jean-paul Kleider, José Alvarez, Raphael Lachaume, Sylvain LeGall and Alexandre Jaffre from Geeps for the discussion on electrical modeling, Olivier Plantevin from IN2P3 for the Photoluminescence measurements, Anna Fontcuberta i Morral and Wongjong Kim from EPFL for the cathodoluminescence measurements. Thank you!

At the end of my thesis, I have stayed in Linwei's group in Nanjing for four months. He has given me a lot of smiles, encouragements and strong support. During the talk with him, I can feel his straight forward personality, rich knowledge and big enthusiasm to science. He gives me a good example. His students also give me a lot of help. We had a lot of happy time during the talking, playing, eating and

studding. Thanks to each member of this group: Ying li, Chengdong Li, Zhongwei Yu, Zhaoguo Xue, Yaolong Zhao, taiga dong, Ying Sun, Zhimin Zhu, Hongxiang Wang, Jiawei Lu, Jimi Wang, Fan Yang, Yakui Lei, and Xiaoxiang Wu.

It is my great honor to have Anna Fontcuberta i Morral, Vladimir Dubrovskii, Antonin Fejfar, Gilles Patriarche, Linwei Yu, and Marko Topic as my jury. Thank you all! Special thanks to Anna and Vladimir for being my referees.

Looking back to the past years in France, it is great. Thanks to French people. Especially to the people in Polytechnique who works in graduate school, housing office, restaurant, material office, library, fireman office, cafeteria, student office, barbershop, sports office, information office, language office, and to every people here. What's more, thank you for your extra smiles and pleasant conversions besides the normal service. I'm grateful to the engineer students of the campus. We know Ecole Polytechnique is in the middle of the fields. Fortunately these smart, friendly and funny students make the campus life colorful. Your numerous activities make me enjoy my spare time. Thanks to the numerous Chinese students who make me not homeless. Thanks to Mâitre Patrice Holiner for the Piano lessons during the past four years. Thanks to the choir directed by him. There are so many happy and beautiful moments during the repetition and performance. Thanks to every member of the choir. One of the most amazing things I have done during the past 3 years is that I opened the door of Christian community of students and stay inside. We come from different background, but you open your arms and hug me. I have found one of the most beautiful sides of humanity here. You have shown me what love is. You made me a better person. My most happy time in France was with you. A special thanks to Père Miguel and Père Nicolas. It is an amazing grace to meet Blaise family. Here I feel the love of a family. They regard me as a member of the family. They love me, educate me, take care of me and help me as if I'm a child of them. They talk with me as if I'm a true brother of them. They give me unbelievable love and joy. The innocent and lovely children also give me a lot of strong and pure happiness. Quentin also helped me to understand that I should be cautious with science. Thanks to Eliette. Thanks you for your beautiful smile at the border of the sea which made me fall in love with you. Your writing accompanies me every morning. You give me the sense, the force, the light and the joy of each day. You made me love the Christianity deeper. You help me to understand what real sense is. The few encounters with you are the most beautiful memories for the past years. Even it was a crazy and naive love, allow me to say: thank you. Even I have just spent quite few weeks with my family during the past years, I still would like to give the biggest thanks to each member of my family, especially to my mother and my father. I feel the love through the meal they prepared, the cloths they washed, a simple look, a simple smile, and the simple words. They let me know that there are two persons in this world who will give me anything they have, who loves me deeper than to themselves.

Together, we go further! Thank you everybody!

# Contents

# Chapter 1 Introduction

## Contents

## 1.1 Let there be light

And God said, “Let there be light”, and there was light.

Why light comes before human? This question can be answered from an energy point of view. Because through almost the whole human history, the energy needed for each movement of human comes indirectly or directly from light.

Since the first human, let’s call him Adam, till the beginning of the industrial revolution, the food and the wood provide almost all the energy we need. These energies eventually come from sunlight, which has been fixed into the organic matter such as plants by photosynthesis processes, as shown in figure 1.1. People may also use other kinds of energy from nature, such as water power and wind power. But these energies also come from sunlight, because the circulation of wind and water is driven by the heating of sunlight.

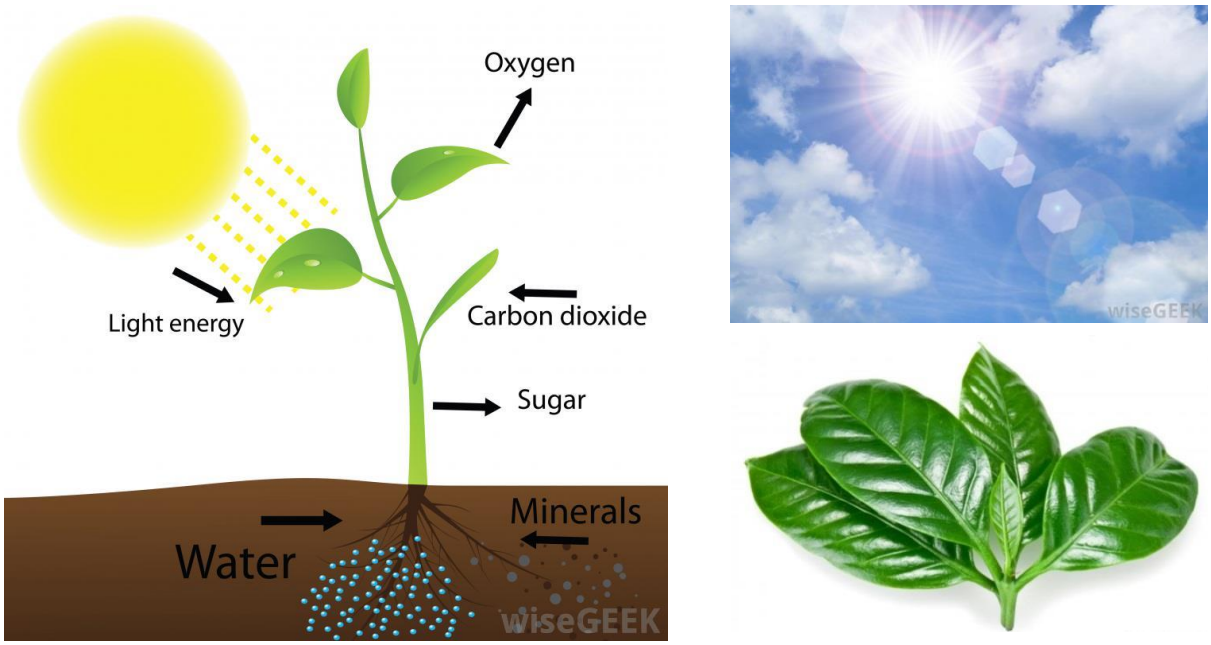


Figure 1.1. Photosynthesis process. The energy from the sunlight is fixed into organic matters, such as the plants, during the photosynthesis process. Photo from website www.wisegeek.com[1].

With the development of society, humans have increasing abilities and activities. We enlarge and multiply our activities by using machines, especially since industrial revolution, as shown in figure 1.2 a. However, these powerful machines require big amounts of fuel for their engines. The amount of energy in these fuels is much bigger than the energy in the food we eat and the wood we burn. Fortunately, the sunlight has already prepared a solution for us. The energy of sunlight stored in the organic matters has been accumulated during billions of years in the form of fossil fuel. We just need to take these fossil fuels out of the earth and release the energy to support the rich and colorful modern life. Figure 1.2 shows the global energy consumption from 1850 to 2013. Now, we are using these fossil fuels at an extremely fast rate. With such a rate, we can finish the fuels formed during billions of years within next 100 years. Such a fast consumption rate also brings numerous problems to our society. Among the most serious ones are global warming and climate change. This is because huge amount of $CO_2$ is released into the atmosphere when we burn the fossil fuel. This gas warms

the earth by making it to absorb more energy from the sunlight. If we continue to emit $CO_2$ at the current rate, the sea level might rise at meter scale[2,3]. The second problem is the pollution. Dust and other pollutants, which have negative effect on human health and environment, are also emitted to the atmosphere when burning fossil fuels. If the fossil energy keeps on dominating the energy production, a blue sky will be a luxury dream soon.

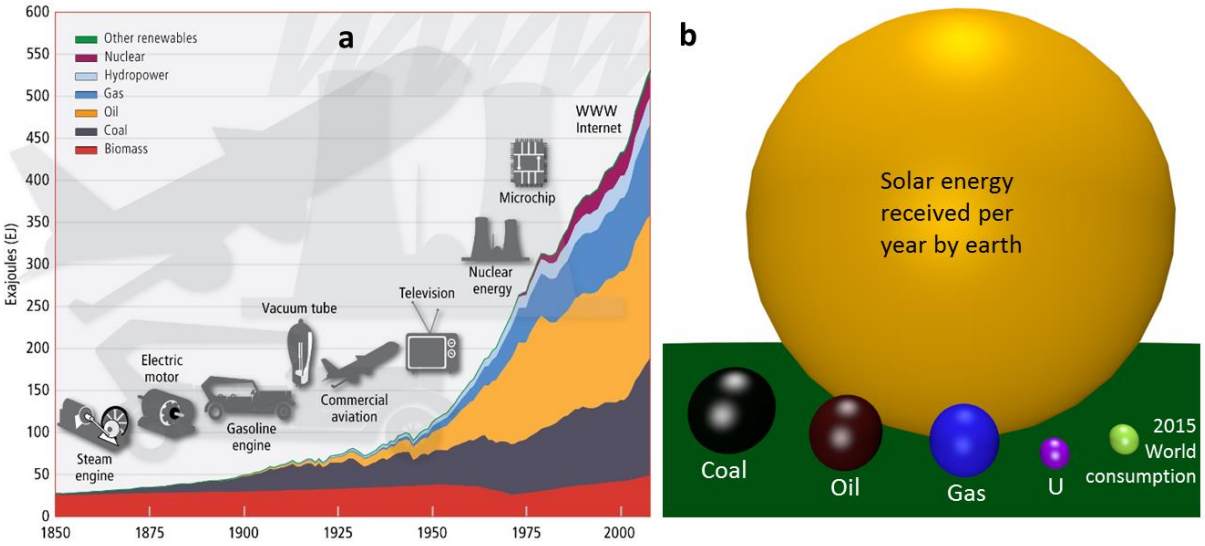


Figure 1.2. a) World energy consumption form 1850 to 2012. Photo from IIASA[4]. b) Illustration of the scale of different forms of energy. The volume of the balls corresponds to the amount of the energy. They are: green ball: 2015 world energy consumption; violet ball: proven uranium reserve; blue ball: proven gas reserves; dark red ball: proven oil reserves; black ball: proven coal reserves; yellow ball: solar energy received per year by earth.

Another fundamental problem is that the fossil fuels are exhausting. World energy consumption in 2013 was around 0.6 zetta joule[5](zetta = $10^{21}$). This is a huge amount of energy which has a similar magnitude with the different forms of proven reserves of energy in the earth. There are 21 zetta joule of coal[6], 9 zetta joule of oil[6], 7 zetta joule of nature gas[7], and 0.6 zetta joule of uranium[8]. The amount of these energies corresponds to the volume of different balls in figure 1.2 b. If we only use the fossil energy and maintain the energy consumption at the rate of year 2013, the proved reserves will last less than 100 years. With yearly increasing energy consumption, the fossil fuel reserves will not able to meet our demand soon. In figure 1.2 b, there is a huge yellow ball which is several thousand times bigger in volume than the ball which corresponds to the yearly energy consumption of mankind. This ball corresponds to the energy we receive from sunlight each year. Its value is around 4000 zettajoule. It can be a nice solution of energy for the near future.

The amount of energy we consume each year is huge. But if we use this amount of energy to lift the total water on the earth which is around 1.3 zetta liters[9], we can lift only 4 centimeters. The development of our society always provides more and more access to more and more people with bigger energy consuming activities. It's hard to imagine the consumption of energy will stop increasing. The solar energy that our planet receives each year is around 4000 zettajoule. This is still a finite number. It is not difficult to imagine the energy consumption by human will exceed this number in the future. Firstly, man-made facilities can already have very big energy consumption rate. For example the European Extreme Light Infrastructure laser will have a 200 Petawatt power[10], that

is bigger than the 174 petawatt total power Earth receives from the Sun. Secondly, individual can have huge energy consumption activity in the future. For example, people may have space-cars for high speed travel. These space-cars might have a higher energy consumption rate than rockets, which is in 100 GW scale[11]. This rate is millions times bigger than the current human average energy consumption rate, which is in the KW scale. Solar energy will not provide the ultimate solution to our energy needs. The solution for the far future needs to be virtually limitless energy. This might be achieved by changing the mass to energy directly. In fact this is how sunlight is generated. In such a way, the mass required to power the world in 2013 is just equal to the mass of an elephant. In fact, mankind already used this technique to transfer mass to energy inside nuclear plants. However, the safety and waste are serious issues for this generation of nuclear technology. We are putting huge effort to look for new ways to do the transfer. The multibillion euro international research project ITER is an example. This project seeks to harness the fusion power which can provides us safe, non-carbon emitting energy. The new technology is expected to be in use in several decades.

From now to the time when we find ultimate solution to our energy needs, it may take several decades or even hundred years. In this period, we need to face the increasing energy demand, serious problems brought by fossil fuel and the exhausting of fossil fuel. We need to find a clean and abundant energy, we need to change the energy structure. Once again, we look at the sun.

## 1.2 A new era of using light

Each year, a huge amount of solar energy is received by the earth. In order to use it, we have to change it to another form which can be used by our devices, for example electricity. To transform light to electricity, one option is to do the transition indirectly through mediums like wind and water. In this way, firstly sunlight heats the air and water, and then the air and water start to circulate. The movements of the wind and water rotate the turbines of the power generators to generate electricity. These are clean ways to generate electricity and have been well developed. In 2014, there are around 6800 GW of installed electricity generation capacity worldwide[7], while hydropower is around 1200 GW[12], and wind power is around 400 GW[13]. Since this is a different topic, we will not talk about it in detail. Here we will talk about another technology which has also reached a level of industrial maturity: photovoltaic solar energy.

A solar cell is a device which converts the sunlight into electricity directly. When the sunlight hits on a solar cell, the solar cell absorbs the energy of the light and gives it to its electrons to generate free electrons. Then the solar cell conducts the free electrons to flow to the power grid to form part of electricity we use. Figure 1.3 illustrates how a roof solar panel generates electricity for home use and power grid. In fact, the electric current generated by solar panels is direct current (DC), while in the power grid it is alternating current (AC), so an inverter is needed to convert the current from solar panel to AC current before home use or injecting to the grid.

Solar cells bring a revolution on using sunlight, because they convert it into electricity in a clean, efficient and direct way. Solar energy has a lot of merits when comparing with other forms of energy. It is clean and no $CO_2$ involved during the energy production. These are the fundamental advantages compared with fossil fuels. Compared with the nuclear energy, it does not have security and waste issues. It doesn't have negative impact on biological and geological systems as hydro power. It does not have moving parts as wind power, thus it does not generate noise and requires less maintenance during operation. The capacity of solar panels depends on its size, which can be easily changed from

milliwatt to kilowatt scale. Therefore its installation can vary from small electrical devices, to house roofs, and to GW scale solar farms. What's more, solar energy has a good public acceptance. It is one of the best candidates to provide the energy for the near future. The main challenge of solar energy is that we do not have sunlight at one place all the time. But there are many solutions. One is to use ultra-high-voltage (UHV) electricity transmission to connect the electricity generated at different places. In China, the single UHV line can be longer than 2000 Km. The UHV transmission lines in operation and under construction by state grid corporation of China are over 190 thousand kilometers[14]. These power lines can surround earth several times. In fact, the state grid corporation of China already planned worldwide power grid which will cost a 50 trillion dollar[15,16]. Once the whole world is connected, there is always electricity generated by sunlight at some place of the earth. Beside power grid, another solution is to store the extra electricity in the storage medium such as battery.

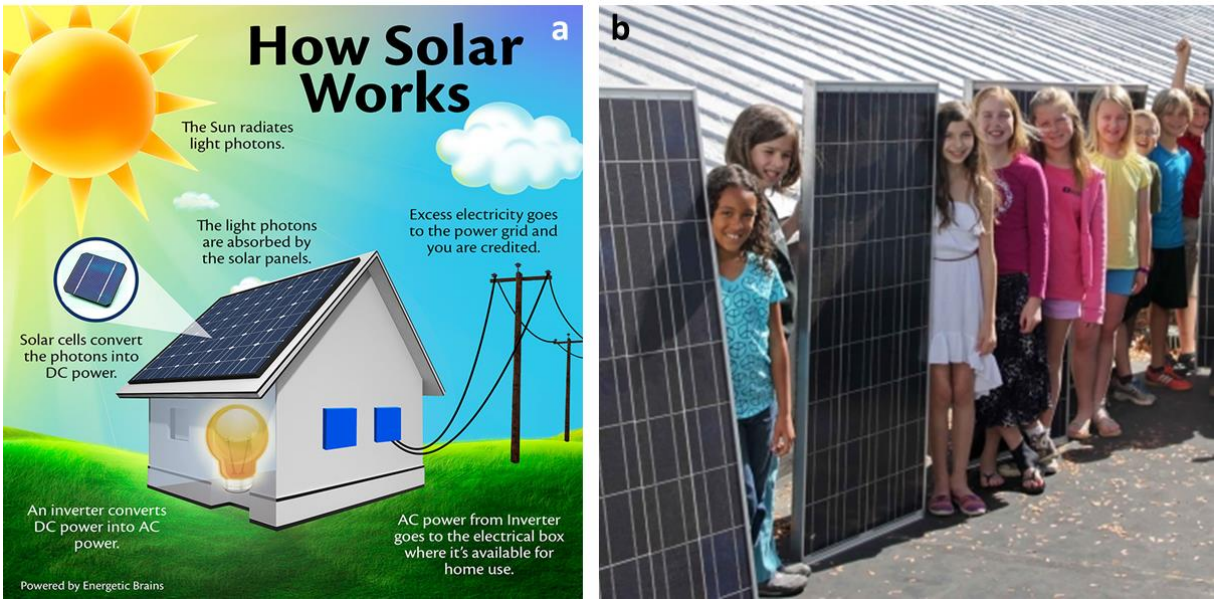


Figure 1.3. a) Working principle of solar cells, photo form website of Whittington Solar energy CO.[17] b) Real solar panel shown by students, photo from website of NREL[18]

The first solar cell can be dated to 1839, when French physicist demonstrated the photovoltaic effect and built the world's first photovoltaic cell[19]. One of the early remarkable demonstrations of solar cells is from 1956, when researchers in Bell Laboratories demonstrated photovoltaic devices with energy conversion efficiency around 6%[20,21]. It means that the device can convert 6% of energy of the coming light into electricity. After several decades of efforts, this number increased to more than 46%. However, these high efficiency solar cells are very expensive. Thus they cannot be used at large scale. The technologies which have reached a level of industrial maturity are crystalline silicon solar cells and a few types of thin film solar cells. The best efficiency solar panels made of these solar cells have an efficiency around 24.4%[22]. The application of the photovoltaic solar energy has already achieved a great success. Till 2015, 226 GW of solar power electricity generation has been installed worldwide[23]. This represents around 3% world electricity generation capacity. China, the world's largest consumer of energy and one of the most important source of growth for global energy demand, has achieved 43 GW of installed capacity, with 15 GW installed in 2015[24]. According to International Energy Agency's forecast, 4600 GW of installed PV capacity will be achieved by 2050, 16% of global electricity will generated by PV,[25] as shown in figure 1.4.

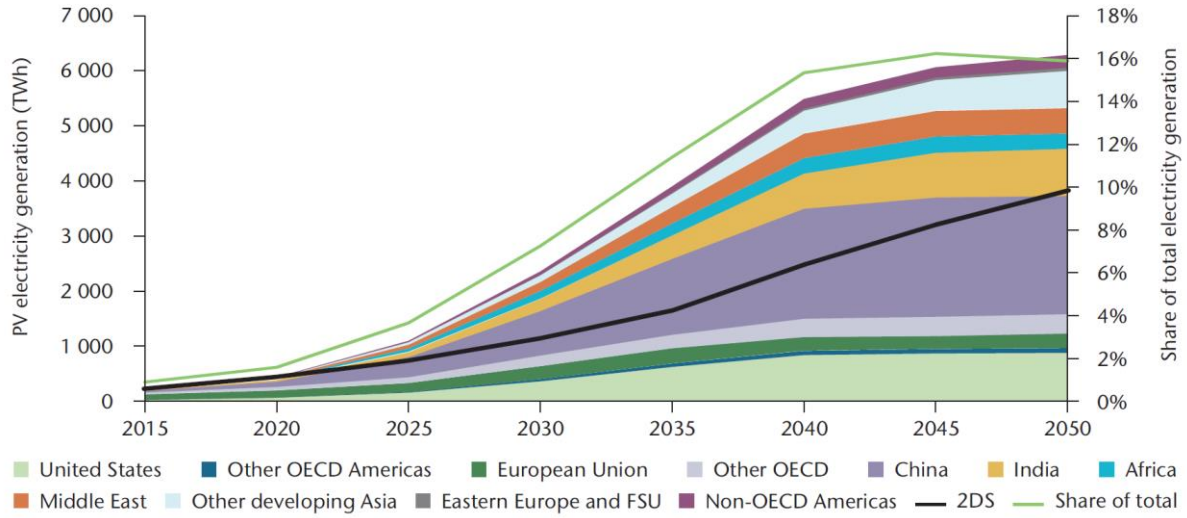


Figure 1.4. Forecast of PV electricity production from 2015 to 2050 under IEA's high-renewables scenario[25]. The different colors correspond to different regions. The green curve on the top shows the share of total electricity. The black curve corresponds to the share of total electricity under IEA's 2°C scenario.

The future of the solar energy is bright and exciting. However, it still costs more to use photovoltaic solar energy than other forms of energy. To install 4600 GW solar energy system, it will cost several trillion dollars. This is several times of France's GDP in 2015. Reduction of the cost of solar energy systems can lead to huge savings. One of the most efficient ways is to increase the solar cells efficiency while maintaining or even decreasing the fabrication costs. This is because for a same PV system, if the solar cells efficiency is increased, the power output will increase significantly without increasing the system cost significantly. Thus the cost of per installed power capacity is decreased.

First let's look at the possibility to increase the efficiency of the current cells in the market. Current PV market is dominated by crystalline silicon solar cells. The theoretical efficiency limit for this kind of solar cells is around 30%[26,27]. Now the best cell efficiency has already achieved 26.3%[22]. This efficiency is very close to the limit. This makes it very difficult to further improve the efficiency. By the way, during the past 20 years, enormous efforts have been made to improve the crystalline silicon solar cell record efficiency, but only 2.3% efficiency improvement has been achieved[22,28]. To increase efficiency, researchers have also tried to use other materials to fabricate solar cells. These materials include inorganic compound GaAs[8], CdTe and CuInGaSe, and organic compounds $CH_3NH_3PbCl_3$[29]. Among these kinds of solar cells, only GaAs solar cells have efficiencies better than c-Si solar cells, which is around 29%. However, this kind solar cells has a higher fabrication cost than silicon solar cells. It is not suitable for large scale applications yet.

The main reason why solar cells have efficiency much lower than 100% is that they do not match the sunlight spectrum very well. We know that sunlight has many colors. Normally, one material can only absorb one color efficiently. If we want to absorb all the sunlight efficiently, theoretically we should use an infinite number of materials. However, technically it gets more difficult when the number of materials increases. For the moment, 34.1 %, 44.4% and 46% record efficiencies have been achieved for solar cells with 2, 3 and 4 absorbing materials, respectively. However, these solar cells are expensive. This is mainly due to the high materials cost and high cost of fabrication processes. Thus

high efficiency solar cells with combined absorbing materials are very attractive. Is it possible to fabricate them at low cost? One answer to this question is to use nanotechnology.

## 1.3 Boost the solar cell performance by nanotechnology

The nano in 'Nanotechnology' refers to nanometer scale. 1 nanometer is $10^9$ times smaller than 1 meter. How small is 1 nanometer? The difference between 1 nanometer and 1 meter is same as the difference between the smallest particle we can see by our naked eye (~100 µm) and the size of the Paris region (~100 Km). Nanometer scale is just one of the plenty length scales of space, as shown in figure 1.5. Modern physics suggest that length can range from Planck length, which is around 1.6 x $10^{-35}$ m, to the size of the observable universe, which is around 8.8 x $10^{26}$ m. Theoretically, the size of the object can be any value between the two size limits. We know that all the objects are composed of elementary particles. If we say the ultimate of the science and technology is to understand, identify and modify each elementary element up to Planck length scale, then we can say that the nanoscience and nanotechnology is to understand and modify the elementary particles or cluster of elementary particles at nanometer scale. This is an attractive ability. However, we human do not have this kind of ability naturally, because the smallest object our naked eye can see is around 100 µm. So naturally we do not manipulate with very small stuff, or we do not pay attention to them. Since thousands of years ago, people have invented lens which can zoom the image of the object. But till now, the best lens can only allow us to see objects with µm scale, not nm scale. In 1895, Wilhelm Röntgen discovered the X-ray, and in 1924 Louis de Broglie discovered the wave property of electron. These two discoveries allow the invention of X-ray tools and electron beam tools. These tools bring our vision from µm scale to nm scale. The concepts of nanotechnology came up soon after the advance of the microscope tools. In 1959, famous physicist Richard Feynnam considered the possibility of manufacture things atom by atom[30]. Generally, people consider that the starting of nanotechnology age is the beginning of 1980s, when scanning tunneling microscope and atomic-force microscopy was invented. These tools allow us to modify material at nanoscale. Nowadays, nanotechnology is familiar to society. It is studied in various domains such as physics, chemistry, and biology. It is also commonly used in semiconductor industry. Since 1989, the semiconductor manufacturing processes enter nanometer scale[31].

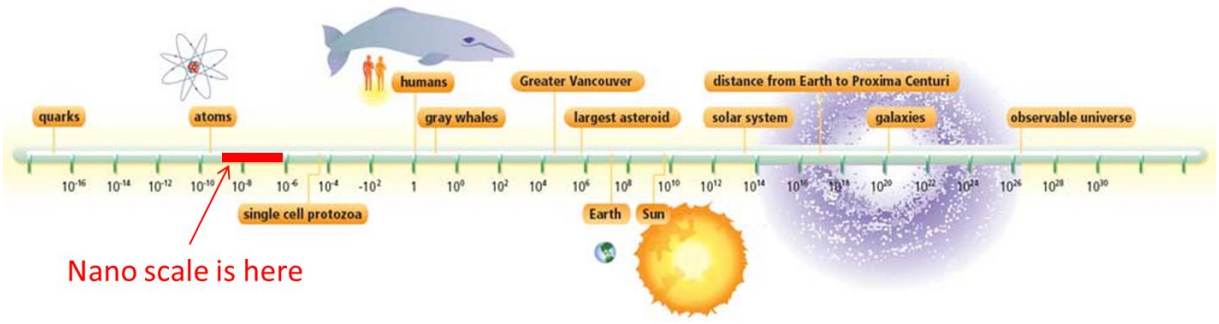


Figure 1.5. Length scale of the Universe. The nanoscale is marked in red. Photo from website[32]

Among the nanotechnology research teams, there is a group of researchers who study nanowires. Nanowire is a wire like object with diameter in the nanometer scale. The research on nanowires was started in 1964 by Ellis and Wagner, they have observed the catalyst induced nanowire growth[33]. Since 1998[34], the nanowire research gets increased interest, and from 2005[35], researchers start to

use nanowires to fabricate solar cells. Figure 1.6 shows the image of a germanium nanowire acquired by scanning electron microscope. This nanowire has a diameter of 60 nm and a length of 1600 nm.

Nanowire structure has many advantages for solar cells application. Firstly, in nanowire solar cells, the light absorption direction is along axial direction, while the electrons and holes generated in the solar cell are collected in the radial direction. Since the distance in the radial direction is nanometer scale, the carriers can be collected efficiently even with low quality materials. This means that high efficiency solar cells can be made with low cost materials and low cost fabrication process. Secondly, the size of the nanowire solar cells is in the similar length scale with the wavelength of the visible light, which contains the majority part of the energy of sunlight. The similar length scale makes the nanowire structure to interact strongly with light. Thus only small amount of material is needed to absorb the incoming light. Lastly, at nanometer scale, the materials can exhibit novel properties such as discrete band structure, ballistic transport, quantum confinement and novel crystalline structures.

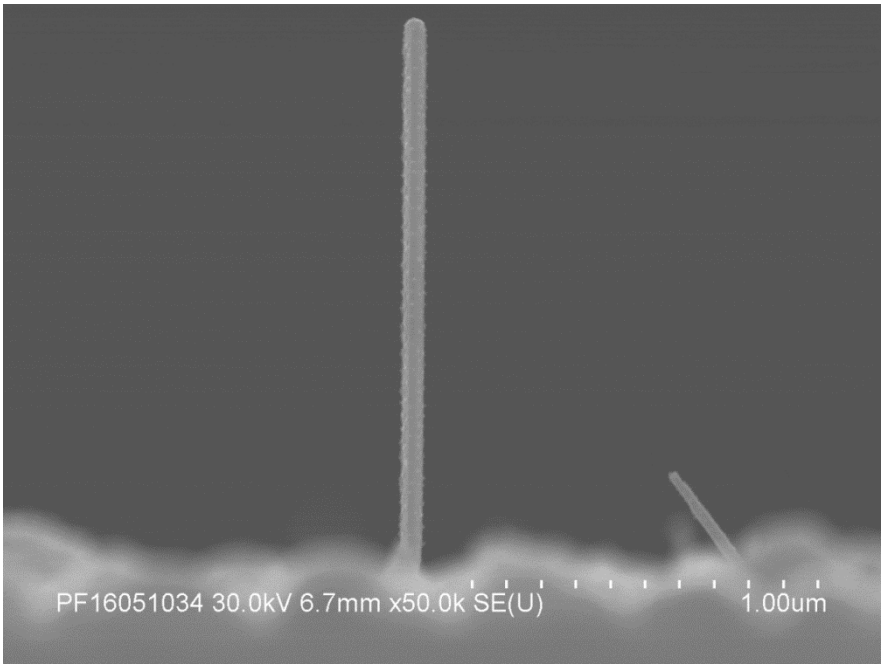


Figure 1.6. SEM image of a germanium nanowire grown by plasma-assisted VLS method. This NW is 60 nm in diameter and 1600 nm in length.

## 1.4 Outline of this thesis

The purpose of this research is to explore the potential of nanowire based radial junction solar cells theoretically and experimentally. Firstly, to find out the maximum light absorption of different solar cell configurations, we have performed optical simulation. Then to get a good understanding of the carrier transport, an electrical model for radial PN junction NW solar cells has been developed from first principles. Then the work has switched to the experimental part. We have carried out a detailed analysis of the plasma-assisted Vapor Liquid Solid Si nanowire growth process. In order to develop low bandgap and high mobility materials for multi-junction solar cells applications, we have grown SiGe and Ge nanowires in the same PECVD reactor used for Si nanowire growth. Finally, single and tandem junction solar cells have fabricated based on the Si and SiGe nanowires. The work will be presented in the following sequence:

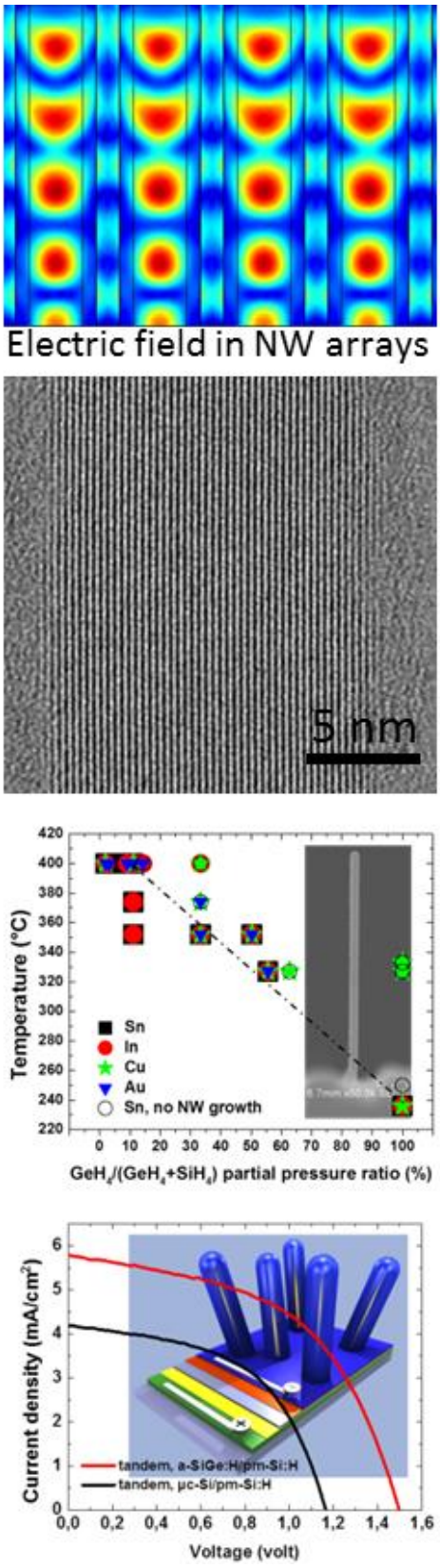


Figure 1.7. Representative pictures for chapter 2 to 5.

**Chapter 2. Optical modeling of nanowire radial junction solar cells**

This chapter starts with the theoretical back ground of the light and material. Then it follows with the general knowledge of simulation with Comsol software. After that, the optical simulation of nanowire radial junction solar cells with different configurations will be presented.

**Chapter 3. Si nanowire growth**

This chapter provides a detailed information of the Si nanowire growth using a plasma-assisted Vapor Liquid Solid process. It starts with the introduction of the experimental setups involved in the study. Then it follows with the results of catalyst droplets engineering. The major part of this chapter is the detailed observation and explanation of the Si nanowire growth process. The rare hexagonal phase of Si has been observed in the as grown Si nanowires will also be presented.

**Chapter 4. SiGe and Ge nanowires growth**

In the first part of this chapter, we will show how to vary the growth from Si nanowires to SiGe nanowires, and finally to Ge nanowires. We will explain the influence of substrate temperature, gas partial pressure ratio and catalyst on nanowire growth. The growth of micrometer long and cylindrical Ge nanowires will be also presented. In the second part of this chapter, we will present the Ge concentration, crystallinity, optical and electrical properties of the SiGe and Ge nanowires.

**Chapter 5. Towards low cost NW based radial junction solar cells**

In this chapter, firstly the synthesis and characterization of nanowire radial junction solar cells will be introduced. Then the performance of single and tandem solar cells with different absorber materials, including the first SiGe nanowire based solar cells, will be presented.

## References


1 What is Photosynthesis, wiseGEEK. Retrieved June 20, 2016, from http://www.wisegeek.com/what-is-photosynthesis.htm.

2 US Global Change Research Program. Climate Change Impacts in the United States: The Third National Climate Assessment(PDF). National Climate Assessment. 3rd Assessment: pg. 45. Retrieved 12 December 2015.

3 Levermann, A. *et al.* The multimillennial sea-level commitment of global warming. *Proceedings of the National Academy of Sciences* **110**, 13745-13750, doi:10.1073/pnas.1219414110 (2013).

4 Nakicenovic, N. The Global Energy Assessment: Toward a Sustainable Energy Future, IIASA, 2012. Retrieved June 23, 2016, from http://www.iiasa.ac.at/web/home/resources/mediacenter/FeatureArticles/Sustainable.en.html.

5 iea 2015 Key world Energy statistics. Retrieved June 23, 2016, from http://www.worldenergyoutlook.org/.

6 Energy Study: Reserves, Resources and Availability of Energy Resources 2015, BGR (Federal Institute for Geosciences and Natural Resources), 2015. Retrieved June 23, 2016, from http://www.bgr.bund.de/EN/Themen/Energie/energie_node_en.html.

7 CIA world fact book. Retrieved June 23, 2016, from www.cia.gov.

8 Colombo, C., Heiβ, M., Grätzel, M. & Morral, A. F. i. Gallium arsenide p-i-n radial structures for photovoltaic applications. *Appl Phys Lett* **94**, 173108, doi:10.1063/1.3125435 (2009).

9 Total water on Earth, the Physics Factbook. Retrieved June 24, 2016, from http://hypertextbook.com/facts/2001/SyedQadri.shtml.

10 The European Strategy Forum on Research Infrastructures 2016 Roadmap, European Commission. Retrieved June 24, 2016, from http://ec.europa.eu/research/infrastructures/index_en.cfm?pg=esfri.

11 Kyle, E. NASA's Space Launch System Data Sheet, Updated July 5, 2016. Retrieved June 24, 2016, from http://www.spacelaunchreport.com/sls0.html.

12 IHA communications team, 33 GW new hydropower capacity commissioned worldwide in 2015. Retrieved June 24, 2016, from http://www.hydropower.org/blog/33-gw-new-hydropower-capacity-commissioned-worldwide-in-2015#sthash.nrIoGGWI.dpuf.

13 Global Wind Report Annual Market Update 2014. GWEC. 22 April 2016. Retrieved May 23, 2016, from http://www.gwec.net/wp-content/uploads/2015/03/GWEC_Global_Wind_2014_Report_LR.pdf.

14 State grid corporation of China, Yuheng-Weifang 1000kV UHV AC Transmission and Transformation Project Starts Construction, Released on 14-05-2015. Retrieved June 24, 2016, from http://www.sgcc.com.cn/ywlm/projects/ultrahighvoltage/05/325791.shtml.

15 SPEGELE, B. China's State Grid Envisions Global Wind-and-Sun Power Network. Retrieved June 24, 2016, from http://www.wsj.com/articles/chinas-state-grid-envisions-global-wind-and-sun-power-network-1459348941. (2016).

16 Minter, A. China Wants to Power the World, Bloomberg. April 3, 2016. Retrieved June 24, 2016, from https://www.bloomberg.com/view/articles/2016-04-03/china-s-state-grid-wants-to-power-the-whole-world.

17 How Solar Energy Systems Work, Whittington Solar energy CO. Retrieved June 24, 2016 from http://www.whittingtonsolar.com/home/start-here/how-solar-energy-works/.

18 National Renewable Energy Laboratory. http://www.nrel.gov/.

19 Timeline of solar cells, Wikipedia. Retrieved June 24, 2016, from https://en.wikipedia.org/wiki/Timeline_of_solar_cells.

20 Chapin, D. M., Fuller, C. S. & Pearson, G. L. A NEW SILICON P-N JUNCTION PHOTOCELL FOR CONVERTING SOLAR RADIATION INTO ELECTRICAL POWER. *Journal of Applied Physics* **25**, 676-677, doi:10.1063/1.1721711 (1954).

21 April 25, 1954: Bell Labs Demonstrates the First Practical Silicon Solar Cell. APS News. American Physical Society. 18 (4). (2009).

22 Green, M. A. *et al.* Solar cell efficiency tables (version 49). *Progress in Photovoltaics: Research and Applications* **25**, 3-13, doi:10.1002/pip.2855 (2017).

23 2015 Snapshot of Global Photovoltaic Markets. report. International Energy Agency. 22 April 2016. Retrieved May 24, 2016, from http://www.iea-pvps.org/fileadmin/dam/public/report/PICS/IEA-PVPS_-__A_Snapshot_of_Global_PV_-_1992-2015_-_Final_2_02.pdf.

24 Statistics of solar energy in 2015, National Energy Admisistration of China. Retrieved June 25, 2016, from http://www.nea.gov.cn/2016-02/05/c_135076636.htm.

25 Technology Roadmap: Solar Photovoltaic Energy - 2014 edition.

26 Richter, A., Hermle, M. & Glunz, S. W. Reassessment of the Limiting Efficiency for Crystalline Silicon Solar Cells. *IEEE Journal of Photovoltaics* **3**, 1184-1191, doi:10.1109/JPHOTOV.2013.2270351 (2013).

27 Shockley, W. & Queisser, H. J. Detailed Balance Limit of Efficiency of p‐n Junction Solar Cells. *Journal of Applied Physics* **32**, 510-519, doi:doi:http://dx.doi.org/10.1063/1.1736034 (1961).

28 Green, M. A., Emery, K., Bücher, K. & King, D. L. Solar cell efficiency tables (version 5). *Progress in Photovoltaics: Research and Applications* **3**, 51-55, doi:10.1002/pip.4670030106 (1995).

29 Kojima, A., Teshima, K., Shirai, Y. & Miyasaka, T. Organometal Halide Perovskites as Visible-Light Sensitizers for Photovoltaic Cells. *Journal of the American Chemical Society* **131**, 6050-6051, doi:10.1021/ja809598r (2009).

30 Feynman, R. There's Plenty of Room at the Bottom, December 29, 1959. Wikipedia. Retrieved February 14, 2017, from https://en.wikipedia.org/wiki/There's_Plenty_of_Room_at_the_Bottom.

31 Semiconductor device fabrication, Wikipedia. Retrieved June 25, 2016, from https://en.wikipedia.org/wiki/Semiconductor_device_fabrication.

32 Size scales of the Universe. Retrieved June 26, 2016, from http://hendrix2.uoregon.edu/~imamura/123/lecture-1/lecture-1.html.

33 Wagner, R. S. & Ellis, W. C. Vapor-Liquid-Solid Mechanism of Single Crystal Growth. *Appl Phys Lett* **4**, 89-90, doi:Doi 10.1063/1.1753975 (1964).

34 Tian, B. *et al.* Coaxial silicon nanowires as solar cells and nanoelectronic power sources. *Nature* **449**, 885-889 (2007).

35 Law, M., Greene, L. E., Johnson, J. C., Saykally, R. & Yang, P. Nanowire dye-sensitized solar cells. *Nat Mater* **4**, 455-459 (2005).

# Charter 2 Optical modeling of nanowire radial junction solar cells

## Contents

## 2.1 Introduction

As explained in the first chapter, nanowires (NWs) have numerous advantages for solar cell applications[1-5]. Among them, a main one is that the NW structure strongly interacts with light[4], which has been demonstrated both experimentally[6-8] and theoretically[9,10]. Optical modeling is an effective way to gain insight into the interaction between light and solar cells. It also provides information for the device optimization. In LPICM, NW solar cells based on randomly oriented Si NWs have been studied since several years.[11-13]. These NW solar cells have core multi shell structure. In the literature, large amount of optical simulation works can be found. However, big majority of them consider the NWs are composed of a single material[14]. These studies can give a good estimation of the maximum absorption of the solar cells, but the detailed absorption in each layer of the solar cells cannot be provided. There are few papers which investigate the detailed absorption in the core multi shell NW solar cells[15,16]. Among these works, single junction a-Si:H solar cell with varied nanowires length and intrinsic layer thickness[17], nc-Si:H/a-Si:H tandem solar cells with balanced photo-current[15], and single junction a-Si:H solar cell with tilted wire axis[18] have been studied. These works give a good starting of the theoretical analysis of core multi shell NW solar cells. However, core multi shell NW solar cell is a complex system with multi variables, such as the thickness and the material of each layer, the pitch and length of the wires, and the simplification method. Such a high order of freedom requires one to build the optical model according to the real structures.

This chapter starts with the fundamental knowledge of light, the interaction between light and the material, and the optical characterization of the material. Then detailed simulation results of different types of solar cells are presented. Finally, it ends with a brief summary.

## 2.2 Theoretical back ground of optical modeling

### 2.2.1 The light

What is light? There has been long debate between particle theory and wave theory before the development of Maxwell's electromagnetic theory. Then people were convinced that visible light is just a certain kind of electromagnetic waves. However, the observations of black body radiation and the photoelectric effect made people realize that light is not just a wave, instead it has a wave-particle duality. It means that light is particles, and it is also wave. This duality is at the core of this optical modeling part because light needs to be considered as a wave to describe its interaction with a material, while the particle nature of light must be used to convert the absorbed energy from the light to the energy of generated free electron-hole pairs.

The wave nature of the light can be described by Maxwell equations:

$$\nabla \cdot \boldsymbol{E} = \frac{\rho}{\varepsilon_0} \tag{2.1}$$

$$\nabla \cdot \boldsymbol{B} = 0 \tag{2.2}$$

$$\nabla \times \boldsymbol{E} = -\frac{\partial \boldsymbol{B}}{\partial t} \tag{2.3}$$

$$\nabla \times \boldsymbol{B} = \mu_0 (\varepsilon_0 \frac{\partial \boldsymbol{E}}{\partial t} + \boldsymbol{J}) \tag{2.4}$$

Where $\nabla$ is the nabla symbol which denotes the three-dimensional gradient operator, $\nabla \cdot$ is the divergence operator, $\boldsymbol{E}$ is the electric field, $\rho$ is the charge density, $\varepsilon_0$ is the permittivity of the vacuum, $\boldsymbol{B}$ is the magnetic field, $\nabla \times$ is the curl operator, $\mu_0$ is the permeability of the vacuum, and $\boldsymbol{J}$ is the electric current density.

In the vacuum, there are no charges, thus equation 2.1 equals 0. The current density in equation 2.4 is also 0, then by combining equation 2.3 and 2.4, we can obtain the wave equation in the vacuum:

$$\nabla^2 \boldsymbol{E} - \mu_0 \varepsilon_0 \frac{\partial^2 \boldsymbol{E}}{\partial t^2} = 0 \tag{2.5}$$

Or,

$$\nabla^2 \boldsymbol{B} - \mu_0 \varepsilon_0 \frac{\partial^2 \boldsymbol{B}}{\partial t^2} = 0 \tag{2.6}$$

Since $\boldsymbol{B}$ is linked with $\boldsymbol{E}$ by equations 2.3 and 2.4, equations 2.5 and 2.6 are equivalent to each other. So one equation among equations 2.5 and 2. 6 is enough to describe the wave. One solution to this equation is,

$$\boldsymbol{E}(\boldsymbol{r}, t) = E_0 e^{j(\boldsymbol{k}\cdot\boldsymbol{r} - wt)} \tag{2.7}$$

Where $E_0$ is the peak amplitude of the electric field, $w$ is the angular frequency, $j$ is imaginary unit, which is defined as $j^2 = -1$ and

$$\boldsymbol{k} = w\sqrt{\mu_0 \varepsilon_0} \tag{2.8}$$

The speed of the wave is

$$c = \frac{1}{\sqrt{\mu_0 \varepsilon_0}} \approx 3 * 10^8 \, m/s \tag{2.9}$$

### 2.2.2 The material

The material is composed of nuclei and electrons. In the electric field, nucleus and electrons can feel the electric force because they are charges. Thus when the electromagnetic wave passes by the material, it induces oscillations to the nucleus and electrons. Since the nucleus are thousands times heavier than the electrons, they do not move much. On the contrary, electrons can gain the energy from the oscillating electric field and reduce the energy of the electromagnetic waves, and this is the absorption of the light by the material.

The interaction between light and material can be calculated by studying the dipole induced to the nucleus and electron system by the electric field. Figure 2.1 a) shows a nucleus and electron system without applied electric field. In this case, the average position of the electron cloud has the same position as the nucleus because the electron cloud is distributed uniformly around the nucleus. Once an electric field with magnitude E is applied to this system, as shown in figure 2.1 b), the initial electron cloud will be deformed, the average position of the electron cloud becomes $\boldsymbol{r}$ refers to the nucleus. This $\boldsymbol{r}$ induced a dipole $\boldsymbol{P}$.

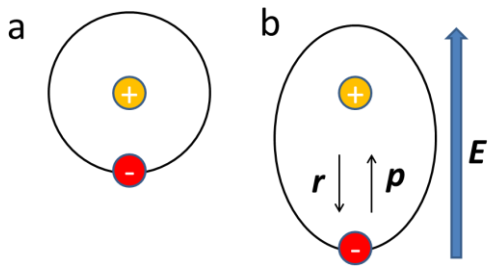


Figure 2.1. Interaction of an electric field with a nucleus-electron system. a) Electron cloud distribute uniformly around nucleus. b) Electron cloud is deformed by the applied electric field $\boldsymbol{E}$. The average position of the electron cloud becomes $\boldsymbol{r}$ with respect to the nucleus, and this induces a dipole $\boldsymbol{P}$.

When a wave described by equation 2.7 passes by the nucleus-electron system, the magnitude of $\boldsymbol{r}$ can be described as:

$$r = \frac{qE_0 e^{-jwt}}{m_e w^2 + jm_e rw - K} \tag{2.10}$$

Where q is electron change, the capital K is the spring constant of the oscillating system, $m_e$ is the electron mass.

The total polarization within a volume of the material induced by the wave can be described as:

$$\boldsymbol{P} = -Nq\boldsymbol{r} = \frac{Nq^2/m_e}{{w_0}^2 - w^2 + j\boldsymbol{r}w} E_0 e^{-jwt} \tag{2.11}$$

Where N is the number of dipoles per unit volume, and

$$w_0 = \sqrt{\frac{K}{m_e} - \frac{Nq^2}{3m_e\varepsilon_0}} \tag{2.12}$$

Then in a material with no free charge and no current, the electric field induced by a dipole should be considered in equation 2.4. This equation becomes:

$$\nabla \times \boldsymbol{B} = \mu_0\varepsilon_0 \frac{\partial \boldsymbol{E}}{\partial t} + \mu_0 \frac{\partial \boldsymbol{P}}{\partial t} \tag{2.13}$$

Then the wave equation becomes:

$$\nabla^2 \boldsymbol{E} - \frac{1}{c^2}\left[1 + \frac{Nq^2/m_e}{\varepsilon_0({w_0}^2 - w^2 + jrw)}\right]\frac{\partial^2 \boldsymbol{E}}{\partial t^2} = 0 \tag{2.14}$$

The solution to this equation still has the same form with equation 2.7,

$$\boldsymbol{E}(\boldsymbol{r}, t) = E_0 e^{j(k_0 \cdot \boldsymbol{r} - wt)} \tag{2.15}$$

But the relation between wave vector $k_0$ and $w$ changes to:

$$w = \frac{c}{\tilde{n}} k_0 \tag{2.16}$$

Where $\tilde{n} = \sqrt{1 + \frac{Ne^2/m_e}{\varepsilon_0({w_0}^2 - w^2 + jrw)}}$ (2.17)

Where $\tilde{n}$ is a complex number with complex form. We can denote it's real part by n and its imaginary part by k. Then

$$\tilde{n} = n + jk \tag{2.18}$$

It can be seen that $w$ and $k_0$ do not have linear relation any more, the wave becomes dispersive in the material.

Combining equation 2.15, 2.16 and 2.18 we can get:

$$\boldsymbol{E}(\boldsymbol{r}, t) = E_0 e^{-k\frac{w}{c}\boldsymbol{r}} e^{j(n\frac{w}{c}\boldsymbol{r} - wt)} \tag{2.19}$$

In this equation $k$ is the imaginary part of $\tilde{n}$.From equation 2.19 it can be seen that $k$ leads to the exponential decay of electric field intensity. This is very important to solar cells application because it determines the absorption of the material. n leads to the reduction of wavelength and wave velocity by n times. $\tilde{n}$ is called the complex refractive index of the material.

### 2.2.3 Characterization of the n and k of the material

Spectroscopic Ellipsometry measurement is a way to obtain $n$ and $k$ of a material. In an ellipsometry experiment, the objective is to measure the complex ratio of Fresnel coefficients, which is given by[19]

$$\rho = \frac{r_p}{r_s} = tan\psi expi\Delta \tag{2.20}$$

Where $r_p$ is the complex Fresnel reflection coefficient for light polarized parallel to the incident plane, $r_s$ is the complex Fresnel reflection coefficient for light polarized perpendicular to the incident plane, and $\psi$ and Δ are ellipsometry angles.

In our experiments, we use a phase-Modulated Ellipsometer UVISEL with a PSMA configuration which is shown in figure 2.2 b). Here P, S, M, and A stand for fixed polarizer, sample, modulator and fixed analyzer, respectively[20]. The signal we measured is:

$$s(t) = s_0\{1 + I_s \sin(\delta[t]) + I_c \cos(\delta[t])\} \tag{2.21}$$

With:

$$I_c = \sin[2(A - M)]\,[sin2M(2M(cos2\psi - cos2P) + sin2Pcos2Msin2\psi cos\Delta] \tag{2.22}$$

$$I_s = \sin[2(A - M)]\, sin2Psin2\psi sin\Delta \tag{2.23}$$

Where $P$, $M$, and $A$ are the azimuth of the polarizer, the photo-elastic modulator and the linear analyzer with respect to the plane of incidence, respectively. $\delta(t) = \sin(wt)$, $w$ is the angular rotation speed of the phase-modulator, $t$ is the acquisition time. For our measurements, the configuration is $M = 0°$, $A = 45°$, and $P = 45°$. This is known as configuration II, and it gives:

$$I_c = sin2\psi cos\Delta \tag{2.24}$$

$$I_s = sin2\psi sin\Delta \tag{2.25}$$

However, when the measured $\psi$ is bigger than 45°, the sample will be also measured with configuration III, with $M = 45°$, $A = 90°$, and $P = 45°$. In this case, $\psi$ will be taken from the

measurement of configuration III, and Δ will be taken from the measurement of configuration II, and it gives:

$$I_c = cos2\psi \tag{2.26}$$

$$I_s = sin2\psi sin\Delta \tag{2.27}$$

With equation 2.24 and 2.25, or 2.26 and 2.27, the ellipsometry angles $\psi$ and $\Delta$, and also $\rho$ in equation 2.20 can be calculated easily. Then the complex pseudo-dielectric function of the material can be calculated as:

$$< \epsilon >=< \epsilon_r > +< \epsilon_i >= sin^2\phi\{1 + [(1-\rho)/(1+\rho)]^2 tan^2\phi\} \tag{2.28}$$

Where $\phi$ is the angle of incidence.

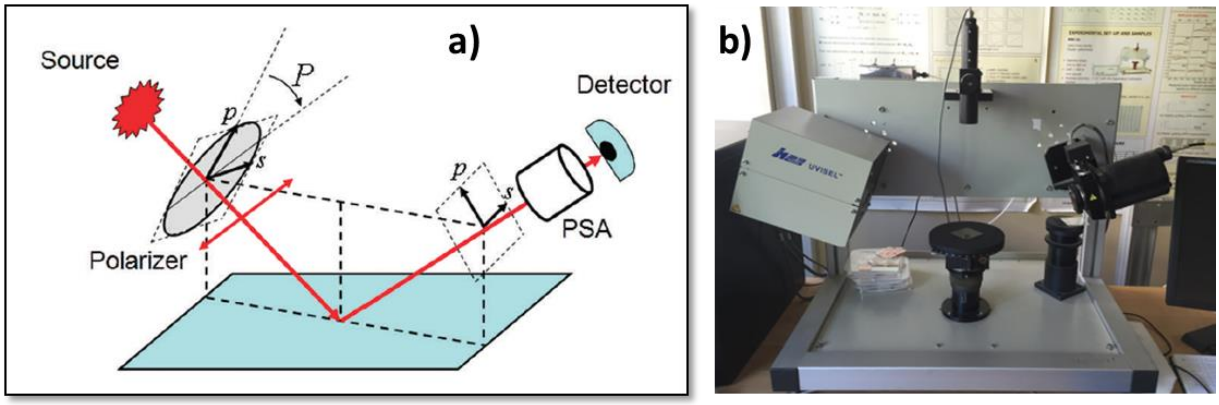


Figure 2.2. a) General scheme of a standard ellipsometer. PAS is the polarization state analyzer[20]. b) A UVISEL ellipsometer with a PSMA configuration used in this study.

Among the materials we have used, the crystalline materials are already well characterized in the literature. On the contrary, the properties of amorphous materials are largely determined by their deposition conditions. Thus in this study we have studied the optical properties of the amorphous materials deposited in our lab.

To extract the material parameters from the ellipsometry measurement data, we use Tauc-Lorentz model for the fitting. In Tauc-Lorentz model, the imaginary part of the complex dielectric function $\epsilon_i$ is the product of Tauc's dielectric function above the band edge[6] and the $\epsilon_i$ obtained from the Lorentz oscillator model[21]. Tauc's dielectric function above the band edge is:

$$\epsilon_{i,T}(E) = \mathrm{A}_T(E - E_g)^2/E^2 \tag{2.29}$$

Where $\mathrm{A}_T$ is the tauc coefficient, and $E_g$ is the optical band gap. The $\epsilon_i$ obtained from the Lorentz oscillator model is:

$$\epsilon_{i,L}(E) = 2nk = \frac{\mathrm{A}_L E_0 C E}{(E^2 - {E_0}^2)^2 + C^2 E^2} \tag{2.30}$$

Where $A_L$ is the strength of the $\epsilon_{i,L}$ peak, $E_0$ is the peak transition energy, and $C$ is a broadening term. The product of equation 2.34 and 2.30 is:

$$\epsilon_{i,TL}(E) = \frac{1}{E}\frac{AE_0C(E-E_g)^2}{(E^2-{E_0}^2)^2+C^2E^2},\ E > E_g \tag{2.31}$$

Where $A = A_T A_L$. The real part of the complex dielectric function $\epsilon_r$ can be obtained by Kramers-Kronig integration, given by:

$$\epsilon_r(E) = \epsilon_r(\infty) + \frac{2}{\pi}P\int_{E_g}^{\infty}\frac{\xi\epsilon_i(\xi)}{\xi^2-E^2}d\xi \tag{2.32}$$

Where $P$ is the Cauchy principle part of the integral, $\epsilon_r(\infty)$ is an additional fitting parameter. The integral gives the following expression[21]:

$$\epsilon_{r,TL}(E) = \epsilon_{r,TL}(\infty) + \frac{ACa_{ln}}{2\pi\zeta^4\alpha E_0}ln\left[\frac{{E_0}^2+{E_g}^2+\alpha E_g}{{E_0}^2+{E_g}^2-\alpha E_g}\right] - \frac{Aa_{arctan}}{\pi\zeta^4E_0}\left[\pi - \arctan\left(\frac{2E_g+\alpha}{C}\right) + \arctan\left(\frac{-2E_g+\alpha}{C}\right)\right] + \frac{4AE_0E_g(E^2-\gamma^2)}{\pi\zeta^4\alpha}\left[\arctan(\frac{2E_g+\alpha}{C}) + \arctan\left(\frac{-2E_g+\alpha}{C}\right)\right] - \frac{AE_0C(E^2+{E_g}^2)}{\pi\zeta^4E}\ln\left(\frac{|E-E_g|}{E+E_g}\right) + \frac{2AE_0CE_g}{\pi\zeta^4}ln\left[\frac{|E-E_g|(E+E_g)}{\sqrt{({E_0}^2-{E_g}^2)^2+{E_g}^2C}}\right] \tag{2.33}$$

where

$$a_{ln} = \left({E_0}^2 - {E_g}^2\right)E^2 + {E_g}^2C^2 - {E_0}^2({E_0}^2 + 3{E_g}^2), \tag{2.34a}$$

$$a_{tan} = \left(E^2 - {E_0}^2\right)\left({E_0}^2 + {E_g}^2\right) + {E_g}^2C^2, \tag{2.34b}$$

$$\zeta^4 = (E^2-\gamma^2)^2 + \frac{\alpha^2C^2}{4}, \tag{2.34c}$$

$$\alpha = \sqrt{4{E_0}^2 - C^2}, \tag{2.34d}$$

$$\gamma = \sqrt{{E_0}^2 - C^2/2}, \tag{2.34e}$$

The figure of merit used to evaluate the fit is[20]:

$$\chi^2 = \frac{1}{N-M-1}\sum\frac{(\psi^{Theory}-\psi^{Experimet})^2}{{\sigma_\psi}^2} + \frac{(\Delta^{Theory}-\Delta^{Experiment})^2}{{\sigma_\Delta}^2} \tag{2.35}$$

Where N refers to the total number of experiment data points, M is the total number of fitted parameters. Each $\sigma$ in the denominators corresponds to the estimated uncertainty.

Once the complex dielectric function is obtained, the $n$ and $k$ can be calculated easily by the following equations:

$$n = \sqrt{\frac{\sqrt{{\epsilon_r}^2+{\epsilon_i}^2}+\epsilon_r}{2}} \tag{2.36}$$

and

$$k = \sqrt{\frac{\sqrt{\epsilon_r{}^2 + \epsilon_i{}^2} - \epsilon_r}{2}} \tag{2.37}$$

An example of the material characterization is shown in figure 2.3. The sample is a thin hydrogenated amorphous SiGe (a-SiGe:H) layer deposited on a corning glass substrate. The optical structure used for fitting is shown in figure 2.3 a). This structure consists of a corning glass substrate, a thin a-SiGe:H layer and a roughness composed of a-SiGe:H and voids. The black dots in figure 2.3 b) show the imaginary part of the measured pseudo-dielectric function. Tauc-Lorentz model is used to model the a-SiGe:H. The fitted imaginary part of the measured complex pseudo-dielectric function is shown in figure 2.3 b) with red curve. Through the fitting, the parameters of the Tauc-Lorentz model of a-SiGe:H are obtained: $E_g = 1.63\,eV$, $\varepsilon^{\infty} = 0.4$, $A = 219$, $E_0 = 3.63\,eV$, $C = 2.36$. With these parameters, the n and k of the a-SiGe:H material are obtained and shown in figure 2.3 c).

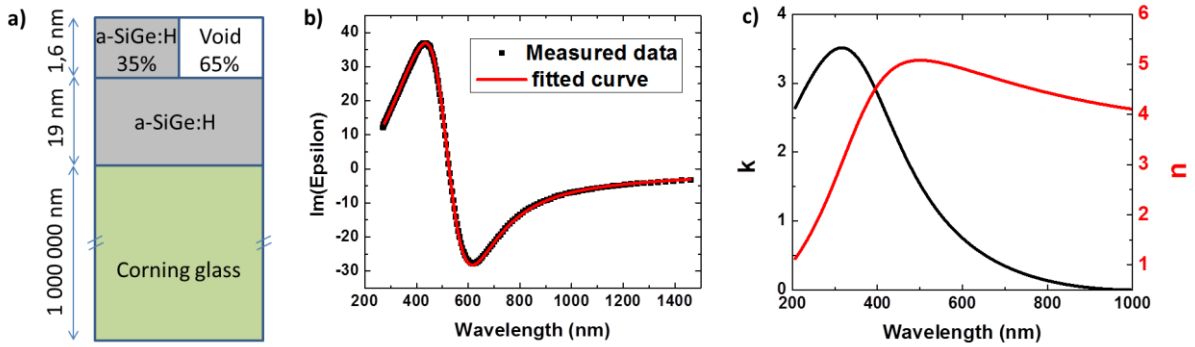


Figure 2.3. a) The optical structure used for fitting. b) Imaginary part of the complex pseudo-dielectric function of the sample. c) The imaginary and real part of the complex refractive index, k and n, obtained from the fitting.

### 2.2.4 The structure of the solar cells for optical simulation

In this study, the main purpose the of the optical modeling is to achieve a good understanding of the interaction of the light and NW solar cells, and also to get information for the solar cell fabrication processes optimization. With such a goal, we have built optical models based on the solar cells structure we have fabricated. A top view SEM image of our solar cell is shown in figure 2.4 a). In this image, each wire is a solar cell which is composed of a p-type NW core, intrinsic absorber shell and a n-type shell. The NWs in this image are randomly oriented, and this brings a big challenge for the modeling. In order to simplify the problem, it is considered that the NWs are perpendicular to the substrate and have a square array arrangement. Figure 2.4 b) shows the top view of the simplified NW array, and figure 2.4 c) shows the detailed structure of each unite in figure 2.4 b). The pitch of NW array is usually around 1 µm. In figure 2.4 c), the axial direction of the NW solar cell is perpendicular to the substrate. The light is incident from the top along the normal direction. The boundary condition for the sidewall is Floquet periodicity. This cell has core multi-shell structure and the shells are layers of different materials and thicknesses. The boundary condition for the bottom surface is a perfect reflector. The space between NW solar cells is filled by air. For all the simulation of NW solar cells, we always use an infinite periodic array configuration, the axial direction of the NW

is perpendicular to the substrate, the light is incident from top plane along normal direction and with a power of 1 w for one cell. Floquet periodicity is used for four sidewalls.

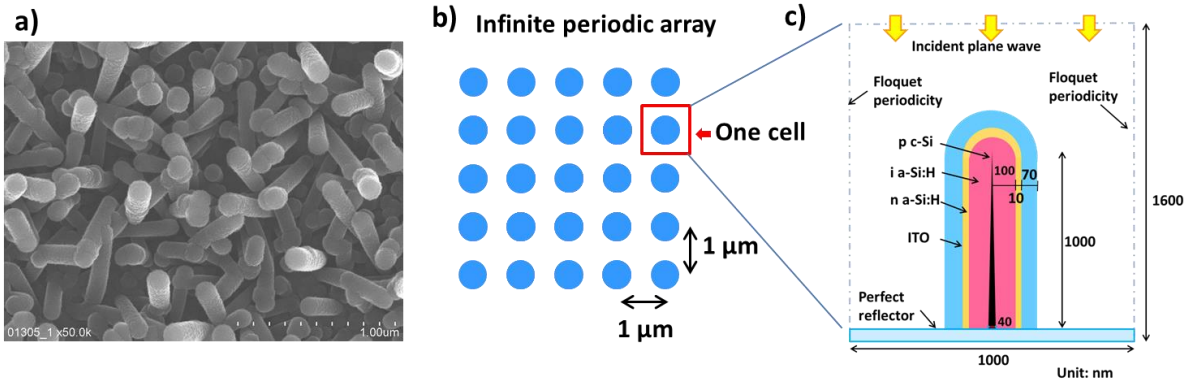


Figure 2.4. a) Top view SEM image of the NW solar cells fabricated in our lab. b) Infinite periodic array of NW solar cells. c) One example of the structure of a NW solar cell unit used for simulation.

### 2.2.5 Optical modeling with Comsol multiphysics

As described before, optical modeling is used to study the interaction between the light and the materials. Since the structure of the material also plays an important role in the light matter interaction, there are three main elements in the optical simulation: light, material and structure. These three elements have been used as inputs of a commercial software (Comsol Multiphysics) to calculate the light absorption.

During the simulation, the main function of Comsol software is to solve the partial differential equations (PDE) which describe the light propagation in the material. In order to use finite element methods to solve PDE, the software firstly generates the mesh of the geometry and the weak form of the PDE. With the weak formulation, it is possible to discretize the mathematical model equations to obtain the numerical model equations. Then the software transfers the weak formulation, the boundary conditions and the meshed structure to matrix equations. After solving the matrix equations, some results can be visualized directly, such as the electric field. While some other results need post-processing. The calculation process is shown in figure 2.5 a). Figure 2.5 b) shows the mesh of a NW solar cell.

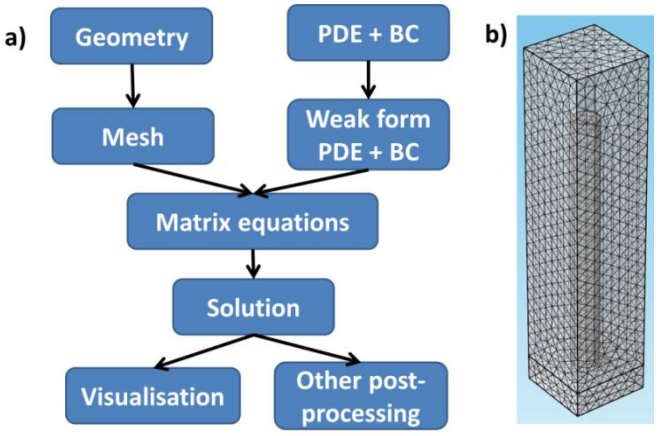


Figure 2.5. a) Calculation processes in Comsol. b) Mesh of a NW solar cell

The energy of the light which has been absorbed by the material can be calculated as:

$$abs = c\frac{\varepsilon E^2}{2}\frac{4\pi k}{\lambda} \tag{2.38}$$

Where $c$ is the speed of the light, $\varepsilon$ is the permittivity of the material, $E$ is the electric field, and $\lambda$ is the wavelength. To calculate the percentage of energy absorbed within a certain volume, one can integrate the absorption in this volume and normalize it by the total incident energy. The equation is shown below:

$$P_{abs} = \iiint abs\frac{4\pi k}{\lambda}dv/P_{incident} \tag{2.39}$$

Where $P_{incident}$ is the total incident power. To convert the absorbed energy to generated free electron, the particle nature of the light has to be used. As the light is composed of photons, the energy of each photon is a function of its wavelength:

$$E_{photon} = \frac{hc}{\lambda} \tag{2.40}$$

Where $h$ is the Planck constant. Equation 2.39 gives the ratio between absorbed energy by the material and the total incident energy as a function of wavelength. To calculate the number of absorbed photon when the material is exposed to the sun light, we can use this ratio to multiply the total photon number in the sun light at each wavelength. By assuming that each absorbed photon generates one free electron, the maximum photo-current can be calculated as :

$$J_{photon} = \int P_{abs}(\lambda)\frac{W_{AM1.5}(\lambda)}{E_{photon}}d\lambda \tag{2.41}$$

Where $W_{AM1.5}(\lambda)$ is the solar power spectrum.

The mesh size is a fundamental parameter for finite element methods calculation. A too big mesh size will lead to incorrect results, while a too fine mesh will lead to heavy computation and large memory requirements. In order to find the optimized mesh size for our problem, a series of simulations with varied mesh size has been done.

In this study, we consider an array of crystalline Si NWs sitting on the top of a silver layer. The SiNWs have a diameter of 200 nm and a length of 2 µm. the pitch of the NWs is 600 nm. The optical parameters for crystalline Si[22] and Ag[23] are from literature and are plotted in figure 2.6 b). We have changed the mesh size threshold to change the mesh number. As shown in figure 2.6 a), the mesh number changes from 5000 to 160000. The maximum theoretical short circuit current density has been calculated for these settings and is shown in Figure 2.6 c). It can be seen that when the mesh number is bigger than 20000, the change in the result is smaller than 5%. This mesh number corresponds to an average mesh volume of 45000 $nm^3$, and an average mesh quality of 0.70. Where the mesh quality is calculated as:

$$q = \frac{72\sqrt{3}V}{({h_1}^2+{h_2}^2+{h_3}^2+{h_4}^2+{h_5}^2+{h_6}^2)^{3/2}} \tag{2.42}$$

Where $V$ is the volume of the mesh, $h_1$ to $h_6$ are the length of the 6 edges of the tetrahedron mesh.

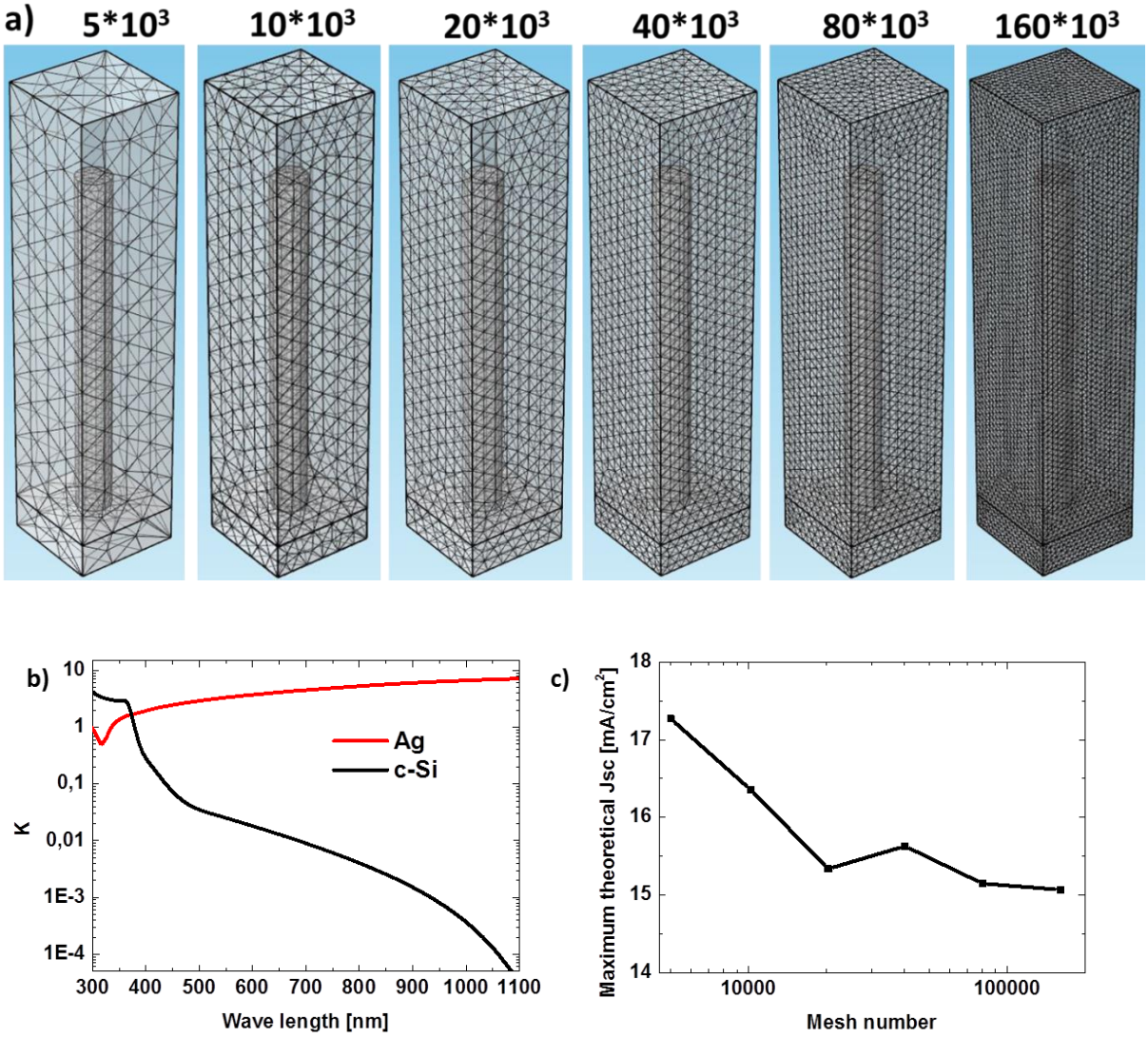


Figure 2.6 a) NW solar cell with different mesh number. b) k value of c-Si and Ag at different wavelength. c) Maximum theoretical short circuit current density calculated with different mesh number.

## 2.3 Modeling of NW solar cells with different configurations

### 2.3.1 cSiNW on a Ag layer

In the literature, there are numerous reports of the synthesis of periodically arranged crystalline SiNWs, using top down methods[7,24-26] and bottom up methods[27]. By inducing doping and a thin coating to form junction, these SiNW can be made to solar cells. Since the structure parameters such as pitch, length and diameter of these NWs can be changed easily, these structures can be optimized once the optimized parameters are known. To obtain the optimized parameters for NW solar cells, optical modeling is needed.

In this simulation, an array of crystalline Si NWs are placed on a 200 nm thick silver layer. The NW length is fixed to 3 μm, the pitch ranges from 500 nm to 700 nm, and the diameter ranges from 100 nm to 400 nm. The boundary condition for the bottom surface of the Ag layer is a perfect reflector.

For crystalline Si solar cells, the photons which can be absorbed usually have a wavelength in the range from 300 nm to 1100 nm. Since the pitch of the NW array, the diameter and the length of NWs have the same order of magnitude of the wavelength, the light will propagate in the form of confined modes. Figure 2.7 shows the electric field in the cut plane which crosses the axis of the NW. The NW part and air part are inside and outside the white frame, respectively. From left to right, the pitch has increased from 500 nm to 700 nm. In figure 2.7 a) it can be seen that the pattern has a similar form when the pitch is increased from 500 nm to 700. However, the intensity decreases. This means that the confinement of energy in the NW decreases with the increase of pitch, and there is more and more leakage to the air. Figure 2.7 c) shows the absorptance of the NW arrays as a function of wavelength. The absorptance at 750 nm decreases with the increase of NW pitch. When the wavelength is increased to 900 nm, the NW array with 600 nm pitch has better light confinement, as shown in figure 2.7 b). In figure 2.7 c), it can be seen that NW array with 600 nm pitch has higher absorptance at 900 nm. This shows that one structure cannot have optimized light confinement for all the wavelength. With the increase of the wavelength, the pitch of the array should also increase to have a better light confinement.

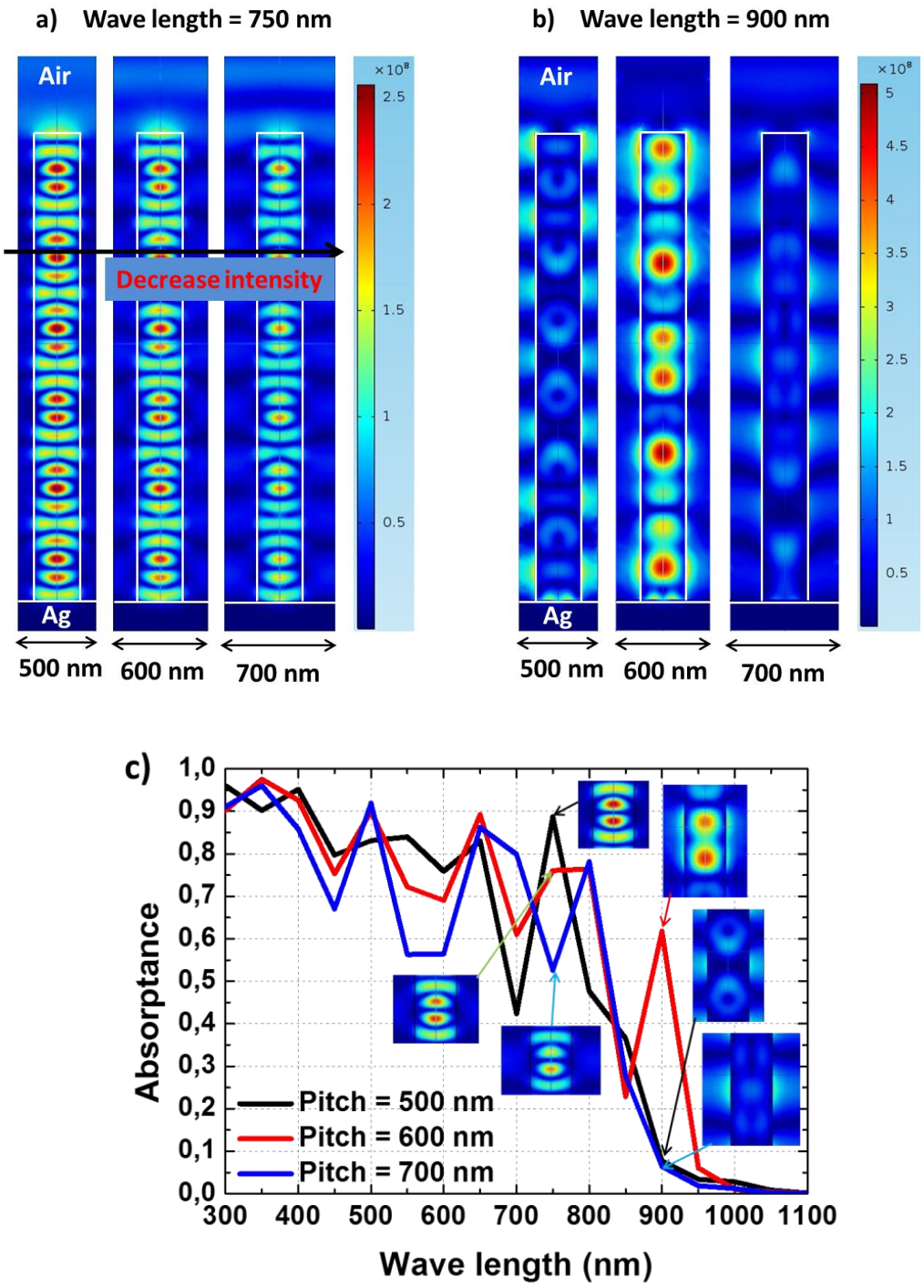


Figure 2.7. a)-b), electric field distribution in SiNWs at different incident wavelengths: a) wavelength is 750 nm; b) wavelength is 900 nm. c) Absorptance of the NW arrays as a function of wavelength. The insets are electric field map of individual NW at wavelength 750 nm and 900 nm. The insets are from a) and b).

With equation 2.41, we have calculated the maximum theoretical Jsc for various configurations. The results are shown in figure 2.8. It can be seen that the values are in the range from 7 to 25 mA/cm$^2$. When the NW diameter is 100 nm, the NW arrays with smaller pitch have a higher current. This is intuitive because the smaller pitch means bigger NW density and bigger material volume. But when the NW diameter is bigger than 300 nm, a 600 nm pitch gives the highest Jsc. Moreover, the increase

of NW diameter from 300 nm to 400 nm decreases the Jsc. This demonstrates that except for the volume of the material, the structural parameters play important roles in the optical performance of the NW arrays. For NWs with 300 nm diameter, the results obtained in this study are in good agreement with the calculation done by Foldyna et al[14].

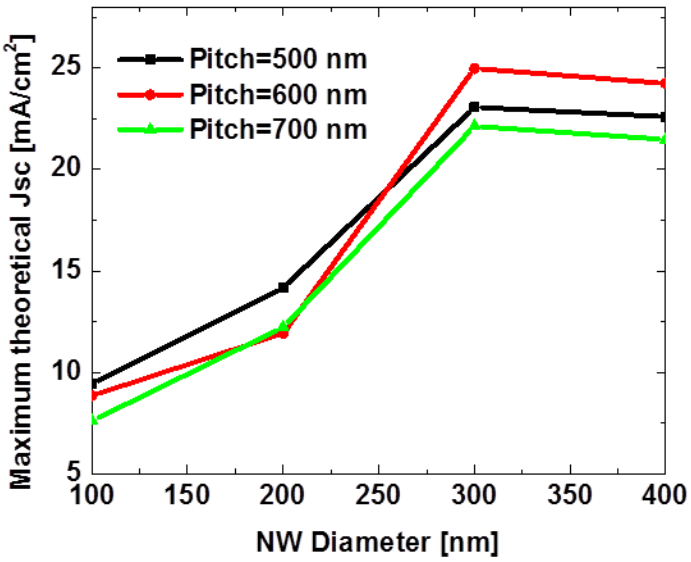


Figure 2.8. Maximum theoretical Jsc as a function NW diameter. Lines with different colors represent different pitch.

### 2.3.2 Comparison of NW solar cells and planar solar cells

As described above, one major attracting character of NW solar cells is that they possesses light trapping effects. It means that the light can be trapped in the NW arrays and lead to a stronger absorption than the planar solar cells. In order to quantify the light trapping, a NW solar cell model and a planar solar cell model have been built for comparison. The two models have the same amount and same kind of material. Figure 2.9 shows the configurations and parameters of these two models. In figure 2.9 a), the NW solar cell has a p-type doped c-Si NW core, an intrinsic a-Si:H shell, a n-type doped a-Si:H shell and an ITO coating. Between the vertical parts of the solar cell, there is a planar part. In figure 2.9 b), the model for the planar solar cell has the same layers, same kind and same amount of materials. Because the c-Si NW core only corresponds to 0.5 nm of planar layer, the absorption in such a thin layer is negligible. So the c-Si planar layer is not included in the planar layer model. The boundary condition at the bottom surface for both solar cells is a perfectly matched layer. In other words, the thickness of the air layer at the bottom is infinite.

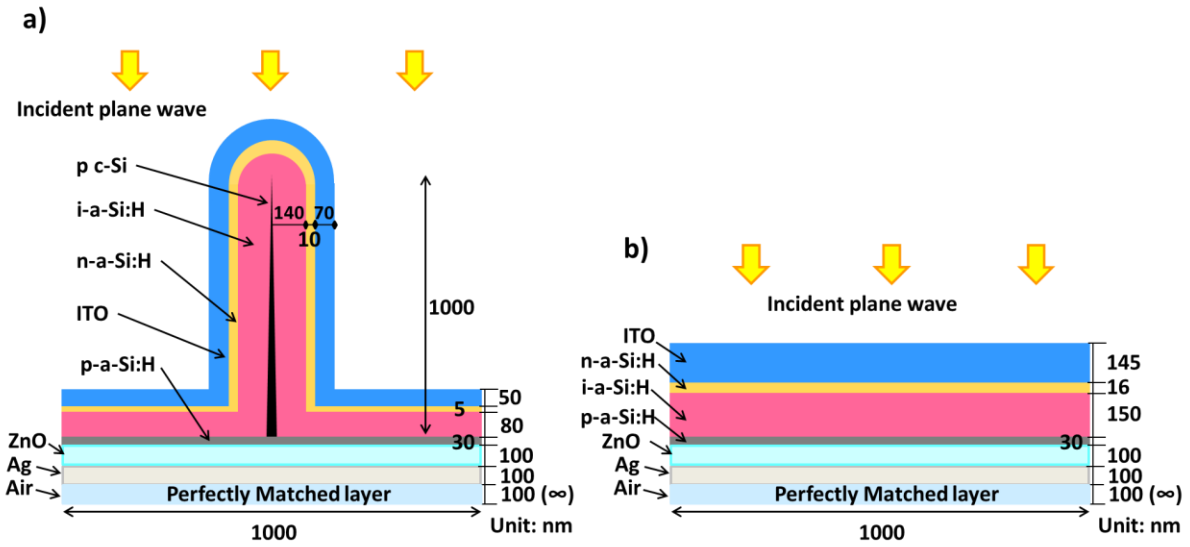


Figure 2.9. Parameters of the solar cell models of different configuration. a) NW solar cell; b) planar solar cells.

During the simulation, n and k of a-Si:H, µc-Si:H and ITO are determined with the method described in section 2.2. The other materials, c-Si, Ag and ZnO[28] are from literature. The plots of n and k of c-Si and Ag are in figure 2.6 a), and the plots of a-Si:H, µc-Si:H, ITO and ZnO are in figure 2.10.

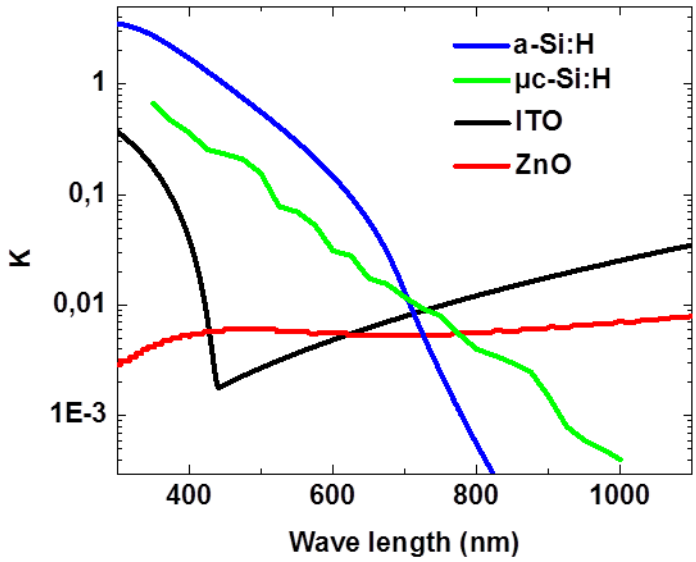


Figure 2.10. Imaginary part of the complex refractive index k of a-Si:H, µc-Si:H, ITO and ZnO materials.

In order to analyze the light response of the two solar cells into detail, we have plotted the electric field and absorption map at wavelength equal to 590 nm in figure 2.11. In the planar solar cell, it can be seen clearly that the E field is a plane wave both in air and in the solar cell. In the air, the distance between the two neighbor E field peaks is 295 nm. This is the half of the wavelength. In the a-Si:H part of the solar cell, the distance between the two neighbor E field peaks is close to 68 nm. This is the half wavelength divided by refractive index of a-Si:H at $\lambda$ = 590 nm, which is 4.329. For the NW

solar cell case, due to the confined mode of propagation, the E field gets largely enhanced inside the solar cell. In the absorption map, it can be seen that the absorption in the NW solar cell is much stronger than in the planar solar cell. At the same time, since the wire guides the propagation of light as a wave guide, the light travels a longer distance in the NW solar cell than in the planar one. This also enhances the absorption.

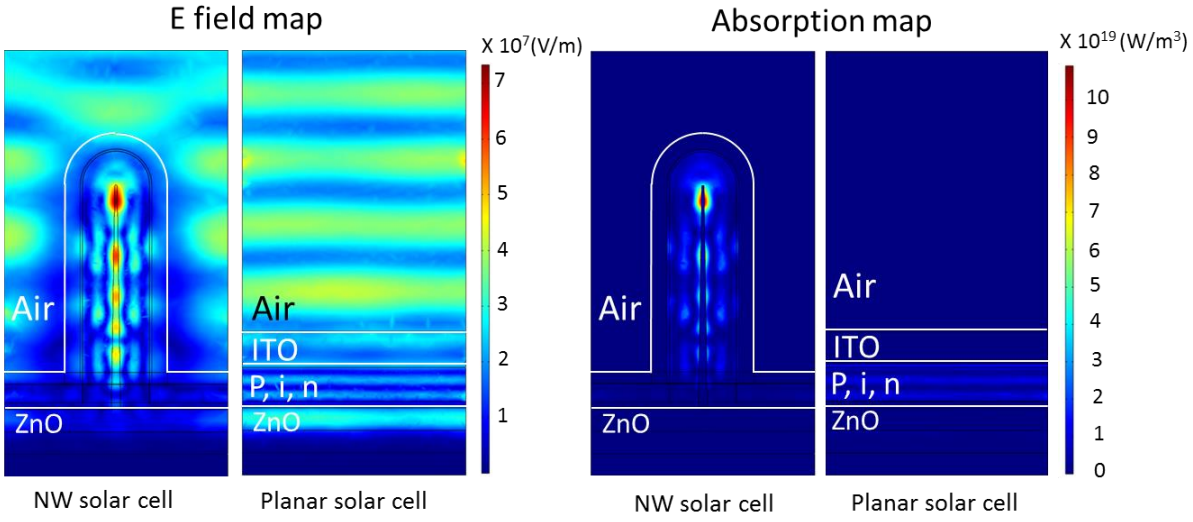


Figure 2.11. Electric field and absorption map in NW solar cells and planar solar cells at λ = 590 nm.

In order to compare the difference of absorptance of the two solar cells quantitatively, the absorptance in each layer of the solar cell is calculated as a function of the wavelength as shown in figure 2.12. Figures 2.12 a) and b) show the results of NW solar cell and of the planar solar cell, respectively. It can be seen that the absorption in the NW solar cell is much stronger than in the planar solar cell for all the wavelengths. The green part shows the absorption in the i-layer. The maximum theoretical Jsc has been calculated for the i-layers, which are 15.6 mA/cm$^2$ for NW solar cell and 7.7 mA/cm$^2$ for planar solar cell. Based on these values, the enhancement of absorption in the i layer is above 100%.

When the wavelength is smaller than 450 nm, the absorptance in figures 2.12 a) and b) is relatively small. This is mainly because ITO has a strong absorption in this wavelength region, as shown by the red curves in figures 2.12 c) and d). When the wavelength is larger than 650 nm, the absortance in p i and n-layers decreases sharply. This is due to the large decrease of k of a-Si:H, as shown in figure 2.10. However, NW solar cell still have a relatively high value of absorption in this wavelength region due to the light trapping effect. The reflectance of the two solar cells is shown by the black curves in figures 2.12 c) and d). Since there is a Ag layer at the bottom of the solar cell, the unabsorbed light will be reflected back and contribute to the reflectance. Compared with planar solar cell, NW solar cell has a much lower reflectance in the whole wavelength range. The reflectance of planar solar cell at 430 nm is almost 0. This is the anti-reflection effect of ITO layer since the n of ITO at such wavelength is 2.22, and the ITO layer thickness is 145 nm. Besides ITO layer, ZnO layer and Ag layer also absorb parts of the light, especially in the long wavelength region.

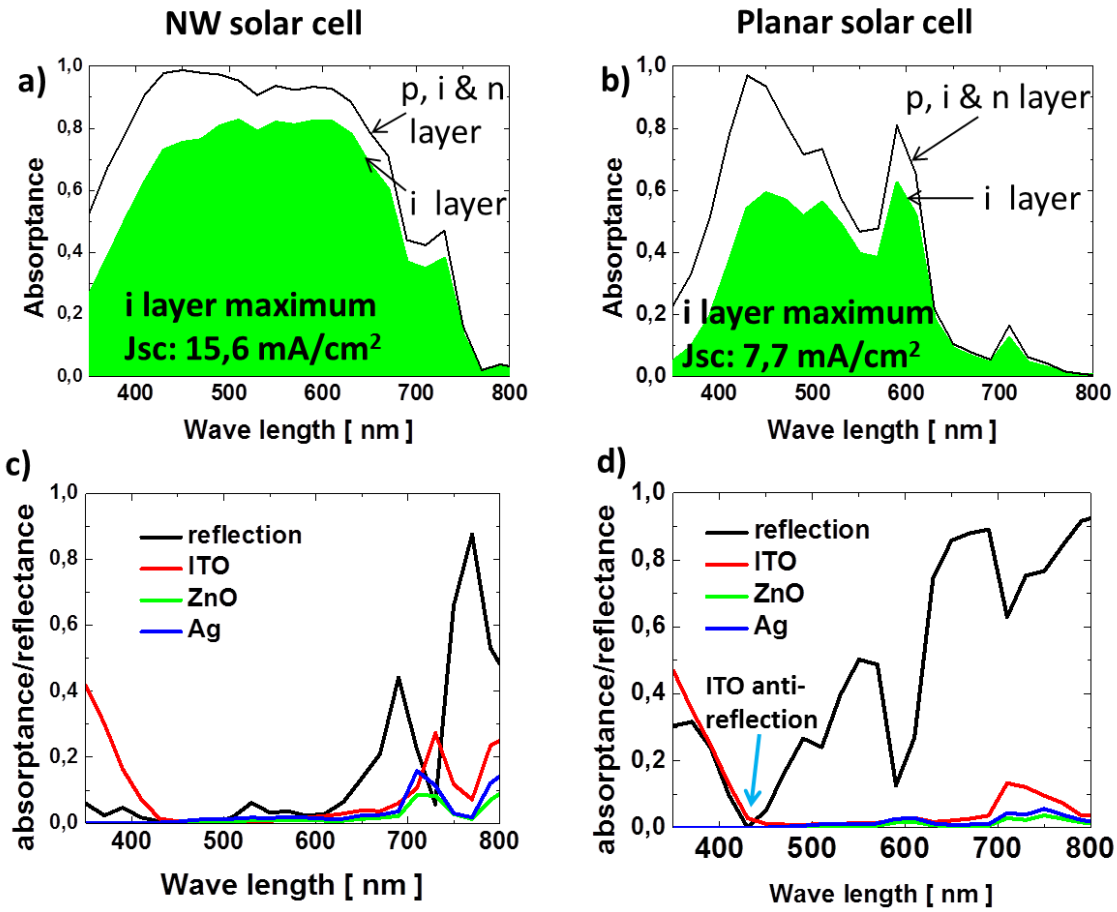


Figure 2.12. Absorptance as a function of wavelength in different layers of a) NW and b) planar solar cells. The black curve shows the sum of p i and n-layers, while the green part shows the absorption in the i-layer. c)-d) Absorptance in ITO, ZnO and Ag layers, together with the reflectance shown in black curve: c) in NW solar cell, d) in planar solar cell.

The absorptance by the NW core of the NW solar cell is shown in figure 2.13. It can be seen that the value is well below 1 percent. This is because firstly, the volume of the c-Si core is only around 0.4% of the i layer volume. Secondly, it is buried in a-Si:H. This makes the electric field difficult to reach the NW core. For example at 450 nm wavelength, the electric field gets absorbed at the n layer and the outer part of the i layer.[13] Thirdly, the absorption coefficient of c-Si is much smaller than that of the a-Si:H at visible wavelength range. This makes c-Si NW core to absorb less. For example at 610 nm, the region of the core is under strong E field, however, the absorption mainly occurs in the a-Si:H.

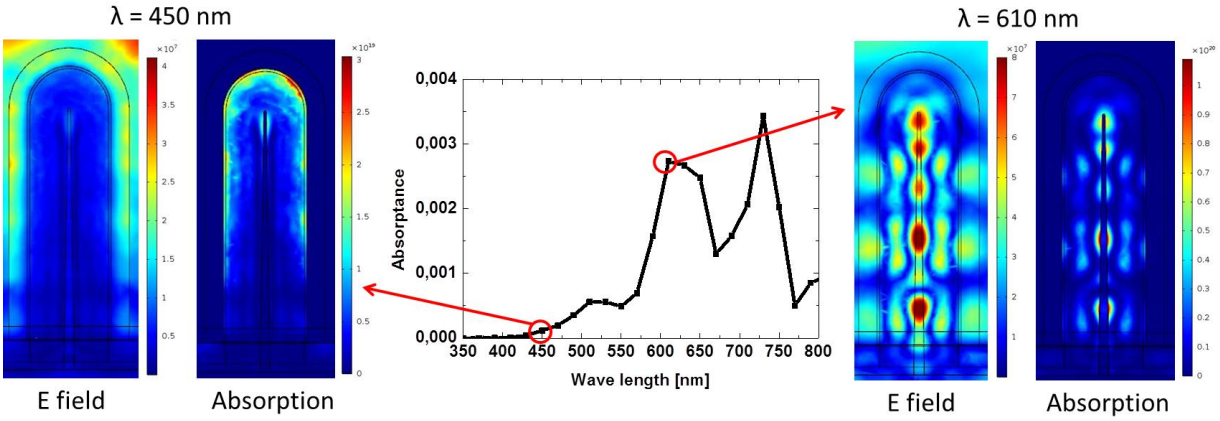


Figure 2.13. Absorptance by the SiNW core inside the NW solar cell. The E field and absorption maps at 450 nm and 610 nm wavelength are shown on the left and right, respectively.

The absorption of light in each layer has been converted into photo-current using equation 2.40. The results are shown in table 2.1 and figure 2.14. It shows that in all the layers (except for n layer), the NW solar cell absorbs more photons than the planar one. For NW solar cell, 12.1% of light for λ up to 800 nm is absorbed in ITO, ZnO and Ag layers, and 16% of light is reflected. For planar solar cell, 8.1% of light is absorbed in ITO, ZnO and Ag layer, and 51.7% of light is reflected.

In our model, the NW solar cell has a vertical part and a planar part. We have calculated the photon current generation in the two parts separately. For same volume of material, the vertical part generates 1.9 times more photo-current than the planar part. This compares quite favorably with the EBIC results measured by L. Yu et al.[16].

Table 2.1. Equivalent photon current generated in each layer

| **Layer name** | **Photon current [mA/cm$^2$]** | | **Percentage [%]** | |
|---|---|---|---|---|
| | **NW solar cell** | **Planar solar cell** | **NW solar cell** | **Planar solar cell** |
| ITO | 1.8 | 1.4 | 6.6 | 5.2 |
| P | 1.1 | 0.5 | 4 | 1.9 |
| i | 15.7 | 7.7 | 58.4 | 28.7 |
| n | 2.2 | 2.6 | 8.1 | 9.6 |
| ZnO | 0.6 | 0.3 | 2.1 | 1.1 |
| Ag | 0.9 | 0.5 | 3.4 | 1.8 |
| Reflection | 4.7 | 13.8 | 16 | 51.7 |

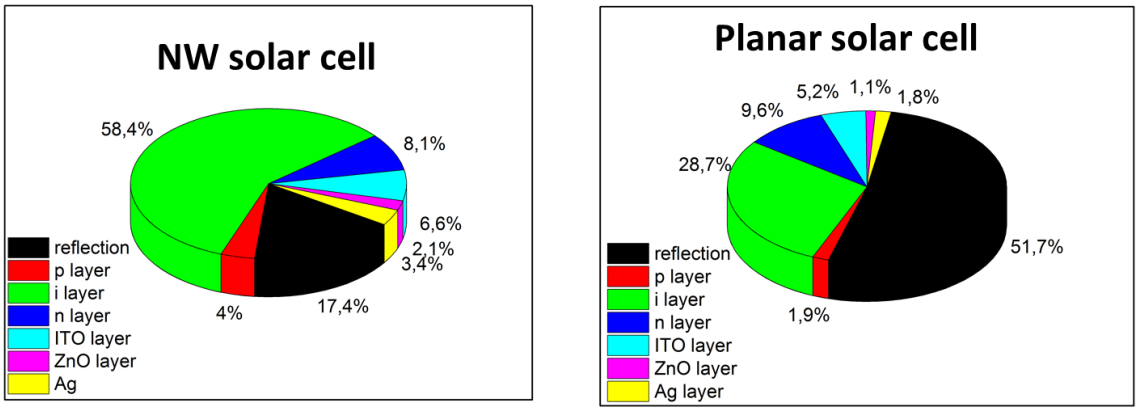


Figure 2.14. Absorption distribution in each layer of NW solar cell, a); and a planar solar cell, b).

This comparison shows that due to the confined and wave-guide propagation mode, the E field in the nanowire solar cell is much stronger and travels a longer distance in NW solar cell than the planar counterpart. This lead to stronger absorption and reduced reflection. With the same amount of material, NW solar cells absorb more. The absorption in the c-Si NW core is negligible because it is buried in a-Si:H, it has a smaller absorption coefficiency compared with a-Si:H, and it has a tiny volume.

### 2.3.3 a-Si:H/μc-Si:H tandem solar cells

We know that light is composed of photons with different energies, or different 'colors'. These photons react differently with materials. Solar cells are usually made of semiconductors which have a certain value of band gap. When the band gap energy of the semiconductor is lower than the absorbed photon energy, the extra energy will be lost quickly in the form of heat. Since a certain semiconductor only has a single band gap, it cannot match the solar spectrum. In order to minimize the energy loss, semiconductors with different band gaps can be combined to match the solar spectrum. As shown in figure 2.15, the top cell with a wide band gap absorbs high energy photons, and the bottom cell with narrow band gap absorbs low energy photons.

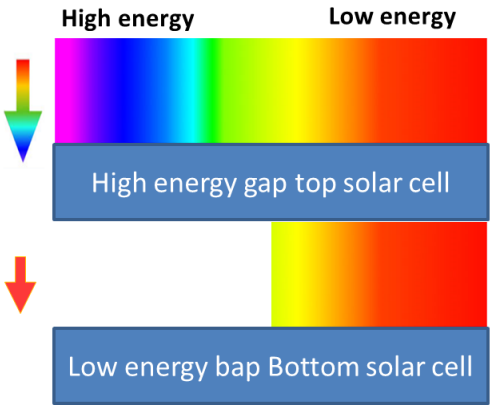


Figure 2.15. Schematic of the principle of a tandem solar cell. The top cell with wide band gap absorbs high energy photons, while the bottom cell with narrow band gap absorbs low energy photons.

Stacking solar cells based on different absorber materials is called a multi-junction solar cell. The theoretical energy convertion efficiency of the multi-junction solar cells increases with the number of junctions[26]. However, the cost and complexity will also increase. The compromise between the efficiency and the cost has to be found. In our lab, low cost single junction a-Si:H NW solar cells have been developed and a conversion efficiency of ~9.2% has been achieved[11,12,29]. However, this is still a relative low value when compared with other kind of thin film solar cells such as CIGS[30] and CdTe[31]. Meanwhile, a-Si:H is a relative high band gap material, multi-junction solar cell can be made by adding relatively low band gap materials. For planar structure, a-Si:H based multi-junction solar cells have been studied over the past four decades[32-34]. A stabilized efficiency of 13.6%[35] and an initial efficiency of 16.3%[36] have been achieved with a-Si:H/a-SiGe:H/nc-Si:H triple-junction and a-Si:H/μc-Si:H/μc-Si:H solar cells, respectively. On the contrary, there is only one study on a-Si:H based multi-junction NW solar cells[15]. The full potential of multi-junction NW radial junction has to be explored both theoretically and experimentally. In our lab, the fabrication process of NW solar cell allows a low band gap material, such as μc-Si:H, to be deposited[37]. Thus radial junction solar cells with a-Si:H top cell and μc-Si:H bottom cell can be fabricated. In order to have insight on the optical design, modeling is needed.

The model used for our optical simulation is shown in figure 2.16 a). This model is composed of a bottom μc-Si:H cell and a top a-Si:H cell. The bottom cell consists of a p-type of c-Si NW core, an intrinsic μc-Si:H shell, and a n-type μc-Si:H shell. The top cell consists of a p, i, and n-type of a-Si:H layers. The outer shell of the tandem solar cell is an ITO layer. The substrate of the solar cell is a ZnO coated Ag layer. The thickness of each layer is marked in figure 2.16. Since all these layers are deposited by PECVD, there is also a deposition between the vertical solar cells. This is the planar part shown in figure 2.16 a).

From the optical point of view, we assume that our doping level does not change the optical properties of the material. Thus the p, I, and n-layers of the a-Si:H cell can be considered as one layer, and the same for the i and n layers of μc-Si:H. As explained before, the absorption of the c-Si:H core is negligible. Thus, the initial 9 layers model can be simplified to a 5 layer model, as shown in figure 2.16 b). This simplification will not change electric field and absorption profile. However, it will simplify the meshing process and improve the mesh quality without increasing the mesh number. The disadvantage here is that the absorption in p and n-layers cannot be quantified. But our main purpose is to optimize the geometry design to get the maximum current. The studied parameters include NW length, layer thickness and pitch. We consider that all the generated carriers are collected to estimate the theoretical photo-current.

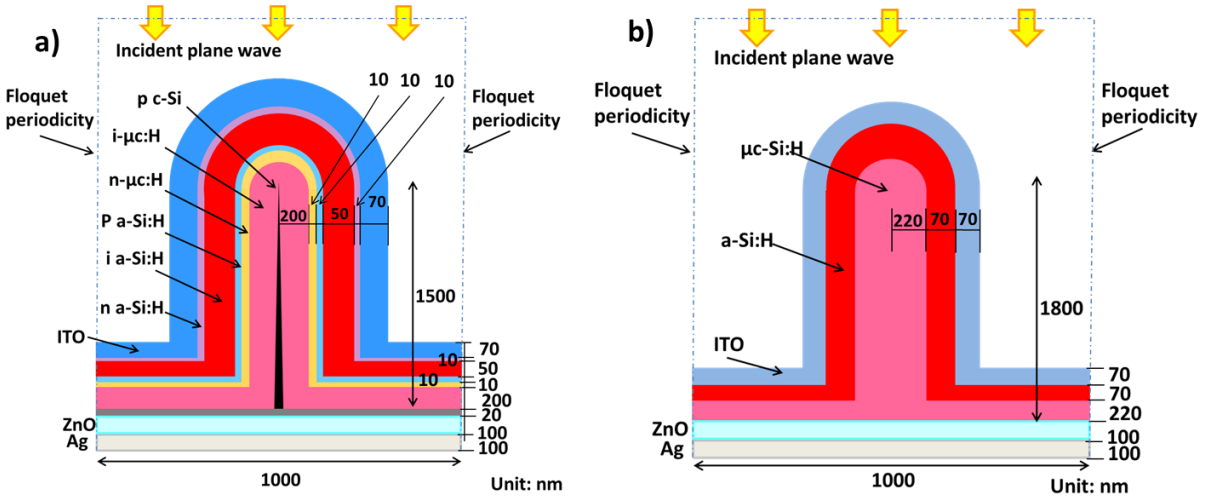


Figure 2.16. a)-b) Scheme of tandem a-Si:H/µc-Si:H solar cell. a) Initial structure of the tandem solar cell, with pin/pin structure. b) Simplified structure of the solar cell, with the p i and n layers combined into a thicker layer.

The optimization has been done by searching the largest matched Jsc in a three dimension parameter space: NW length, solar cell pitch and layers thickness. The layers thickness include the thicknesses of a-Si:H and µc-Si:H layers.We have searched in the NW height range from 1000 nm to 1800 nm, the solar cell pitch ranges from 1000 nm to 1200 nm, the total thickness ranges from 200 nm to 400 nm, and the a-Si:H/(a-Si:H+µc-Si) thickness ratio ranges from 0.15 to 0.35. The imaginary part of the complex refractive index k of µc-Si:H is shown in figure 2.10. c). The µc-Si:H has a high crystalline fraction.

The highest matched current in this parameter space has been found is 14.1 mA/cm$^2$. This is obtained when NW length is 1800 nm, solar cell pitch is 1000 nm, total thickness is 350 nm and a-Si:H/(a-Si:H+µc-Si) thickness ratio is 0.16. In figure 2.17 a), we show the current generated in the a-Si:H layer and in the µc-Si:H layer with a-Si:H/(a-Si:H+µc-Si) thickness ratio varies from 0.15 to 0.35, which corresponds to the thickness variation of µc-Si:H layer thickness from 298 nm to 228 nm. With the increase of µc-Si:H layer thickness and decrease of a-Si:H layer thickness, the photo-current increases in the µc-Si:H layer and decreases in the a-Si:H layer. The highest current is achieved when the µc-Si:H layer is 5.3 times thicker than the a-Si:H layer. This is because a-Si:H has a high absorption coefficient in the visible range (400-650 nm) while µc-Si:H has a weak absorption coefficient in the near infrared range (700-1100 nm). Thus a thicker µc-Si:H layer and a longer NW is needed to achieve a higher matched current. Figure 2.17 b) shows the same curves as the figure 2.17 a). The difference here is that the total thickness of the a-Si:H layer and the µc-Si:H layer is 250 nm. Compared with figure 2.17 a), the current in each layer is reduced. The matched current in this case is reduced to ~ 12.5 mA/cm$^2$. Compared with the literature[15], this matched current is relatively small. The difference might from the absorption coefficient of the µc-Si:H.

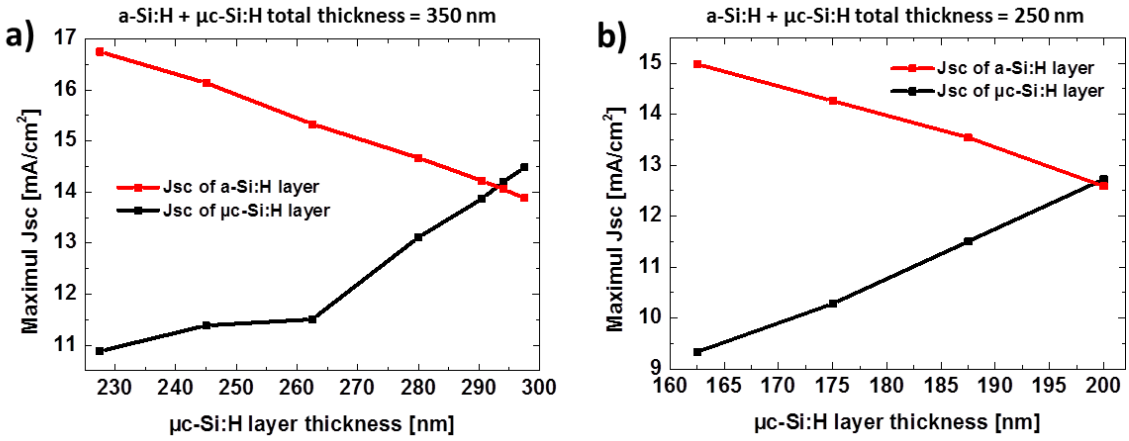


Figure 2.17. Jsc generated in the a-Si:H layer and µc-Si:H layer with different layer thicknesses. a) The total thickness of a-Si:H and µc-Si:H layer is 350 nm. b) The total thickness of a-Si:H layer and µc-Si layer is 250 nm.

The absorptance in each layer of the solar cell which has achieved the highest matched Jsc is shown in figure 2.18. It can be seen that the a-Si:H layer has a relatively high absorptance in the short wavelength range. There is an overlap between the two layers in the wavelength range from 400 nm to 800 nm. The µc-Si:H has a relatively low absorptance in the whole range of the spectrum. This is because the amount of µc-Si:H material is very small. For planar tandem a-Si:H/µc-Si:H solar cell, it usually requires several µm thick µc-Si:H layer. Even if NW structure has a light trapping effect, the thickness of µc-Si:H here is smaller than 300 nm. In figure 2.18 b) it can be seen that there is almost no reflection when the wavelength is smaller than 700 nm, and that there is a significant absorption in the ITO layer when the wavelength is smaller than 400 nm. When the wavelength is larger than 700 nm, the absorption in ITO layer increases. This is because the k of ITO increases with the increase of wavelength, while the k of µc-Si:H layer decreases. There is also absorption in the ZnO and Ag layer in the long wavelength range.

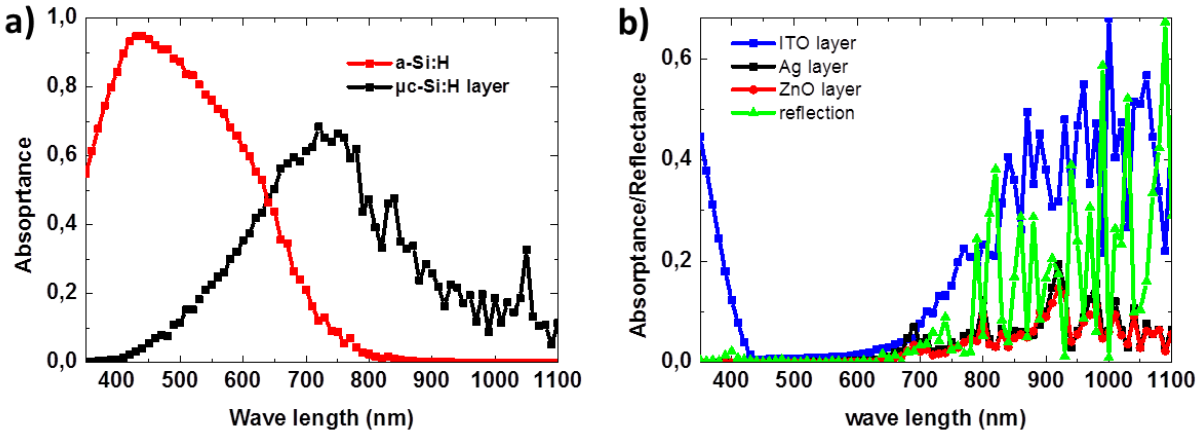


Figure 2.18. Absorptance in each layer of the tandem a-Si:H/µc-Si:H solar cell which has achieved the highest current match. a) Absorptance in a-Si:H layer and µc-Si:H layer. b) Absorptance in ITO layer, Ag layer and ZnO layer. The reflectance is also shown by the green curve.

## 2.4 Summary

In this chapter we have gone through the detailed theoretical back ground of the interaction between light and materials, and the characterization of the material. Then we have explained the process and theoretical background of simulation with Comsol Multiphysics. After that, various NW configurations have been studied. Firstly we have investigated the details of the light absorption in SiNW arrays. Then we have compared the absorption in a NW solar cell to that of a planar solar cell. We show that with same amount of material, NW solar cells can increase the total absorption by 100%. Lastly we have optimized the a-Si:H/μc-Si:H tandem solar cell structure in a 3 dimensional parameter space. For NW length of 1.8 μm, 14.1 mA/cm$^2$ matched Jsc has been achieved with 293 nm thick μc-Si:H layer and 57 nm thick a-Si:H layer. We show that the limiting factor for higher Jsc is the low absorption coefficient of the μc-Si:H.

## 2.5 References


1 Law, M., Greene, L. E., Johnson, J. C., Saykally, R. & Yang, P. D. Nanowire dye-sensitized solar cells. *Nature Materials* **4**, 455-459, doi:10.1038/nmat1387 (2005).

2 Wallentin, J. *et al.* InP Nanowire Array Solar Cells Achieving 13.8% Efficiency by Exceeding the Ray Optics Limit. *Science* **339**, 1057-1060, doi:10.1126/science.1230969 (2013).

3 Tian, B., Kempa, T. J. & Lieber, C. M. Single nanowire photovoltaics. *Chem Soc Rev* **38**, 16-24, doi:10.1039/b718703n (2009).

4 Garnett, E. C., Brongersma, M. L., Cui, Y. & McGehee, M. D. in *Annual Review of Materials Research, Vol 41* Vol. 41 *Annual Review of Materials Research* (eds D. R. Clarke & P. Fratzl) 269-295 (Annual Reviews, 2011).

5 Tsakalakos, L. *et al.* Silicon nanowire solar cells. *Appl Phys Lett* **91**, doi:10.1063/1.2821113 (2007).

6 Tauc, J., Grigorovici, R. & Vancu, A. Optical Properties and Electronic Structure of Amorphous Germanium. *physica status solidi (b)* **15**, 627-637, doi:10.1002/pssb.19660150224 (1966).

7 Foldyna, M., Togonal, A. S., Rusli & Roca i Cabarrocas, P. Optimization and optical characterization of vertical nanowire arrays for core-shell structure solar cells. *Sol Energ Mat Sol C* **159**, 640-648, doi:http://dx.doi.org/10.1016/j.solmat.2016.06.014 (2017).

8 Garnett, E. & Yang, P. D. Light trapping in silicon nanowire solar cells. *Nano Lett* **10**, doi:10.1021/nl100161z (2010).

9 Hu, L. & Chen, G. Analysis of optical absorption in silicon nanowire Arrays for photovoltaic applications. *Nano Lett.* **7**, 3249-3252, doi:10.1021/nl071018b (2007).

10 Yu, Z. F., Raman, A. & Fan, S. H. Fundamental limit of nanophotonic light trapping in solar cells. *P Natl Acad Sci USA* **107**, 17491-17496, doi:10.1073/pnas.1008296107 (2010).

11 Yu, L., O'Donnell, B., Alet, P.-J. & Roca i Cabarrocas, P. All-in-situ fabrication and characterization of silicon nanowires on TCO/glass substrates for photovoltaic application. *Sol Energ Mat Sol C* **94**, 1855-1859, doi:http://dx.doi.org/10.1016/j.solmat.2010.06.021 (2010).

12 Yu, L. *et al.* Bismuth-Catalyzed and Doped Silicon Nanowires for One-Pump-Down Fabrication of Radial Junction Solar Cells. *Nano Lett.* **12**, 4153-4158, doi:10.1021/nl3017187 (2012).

13 Misra, S., Yu, L., Foldyna, M. & Roca i Cabarrocas, P. High efficiency and stable hydrogenated amorphous silicon radial junction solar cells built on VLS-grown silicon nanowires. *Sol Energ Mat Sol C* **118**, 90-95, doi:http://dx.doi.org/10.1016/j.solmat.2013.07.036 (2013).

14 Foldyna, M., Yu, L. & Roca i Cabarrocas, P. Theoretical short-circuit current density for different geometries and organizations of silicon nanowires in solar cells. *Sol Energ Mat Sol C* **117**, 645-651, doi:http://dx.doi.org/10.1016/j.solmat.2012.10.014 (2013).

15 Qian, S. *et al.* Full potential of radial junction Si thin film solar cells with advanced junction materials and design. *Appl Phys Lett* **107**, 043902, doi:http://dx.doi.org/10.1063/1.4926991 (2015).

16 Khan, M. A., Sichanugrist, P., Kato, S. & Ishikawa, Y. Theoretical investigation about the optical characterization of cone-shaped pin-Si nanowire for top cell application. *Energy Sci. Eng.* **4**, 383-393, doi:10.1002/ese3.139 (2016).

17 Yu, L. *et al.* Understanding Light Harvesting in Radial Junction Amorphous Silicon Thin Film Solar Cells. *Sci Rep-Uk* **4**, doi:10.1038/srep04357 (2014).

18 Lu, J. *et al.* How tilting and cavity-mode-resonant absorption contribute to light harvesting in 3D radial junction solar cells. *Opt Express* **23**, A1288-A1296, doi:10.1364/oe.23.0a1288 (2015).

19 Jellison, G. E. Data analysis for spectroscopic ellipsometry. *Thin Solid Films* **234**, 416-422, doi:http://dx.doi.org/10.1016/0040-6090(93)90298-4 (1993).

20 Garcia-Caurel, E., De Martino, A., Gaston, J.-P. & Yan, L. Application of Spectroscopic Ellipsometry and Mueller Ellipsometry to Optical Characterization. *Applied Spectroscopy* **67**, 1-21, doi:10.1366/12-06883 (2013).

21 Jellison, G. E. & Modine, F. A. Parameterization of the optical functions of amorphous materials in the interband region. *Appl Phys Lett* **69**, 371-373, doi:http://dx.doi.org/10.1063/1.118064 (1996).

22 Herzinger, C. M., Johs, B., McGahan, W. A., Woollam, J. A. & Paulson, W. Ellipsometric determination of optical constants for silicon and thermally grown silicon dioxide via a multi-sample, multi-wavelength, multi-angle investigation. *J Appl Phys* **83**, 3323-3336, doi:http://dx.doi.org/10.1063/1.367101 (1998).

23 Lynch, D. W. & Hunter, W. R. in *Handbook of Optical Constants of Solids* 275-367 (Academic Press, 1997).

24 Peng, K. *et al.* Ordered silicon nanowire arrays via nanosphere lithography and metal-induced etching. *Appl Phys Lett* **90**, 163123, doi:http://dx.doi.org/10.1063/1.2724897 (2007).

25 Lefeuvre, E. *et al.* Optimization of organized silicon nanowires growth inside porous anodic alumina template using hot wire chemical vapor deposition process. *Thin Solid Films* **519**, 4603-4608, doi:10.1016/j.tsf.2011.01.333 (2011).

26 Henry, C. H. Limiting efficiencies of ideal single and multiple energy gap terrestrial solar cells. *J Appl Phys* **51**, 4494-4500, doi:10.1063/1.328272 (1980).

27 Spurgeon, J. M. *et al.* Repeated epitaxial growth and transfer of arrays of patterned, vertically aligned, crystalline Si wires from a single Si(111) substrate. *Appl Phys Lett* **93**, 032112, doi:http://dx.doi.org/10.1063/1.2959184 (2008).

28 Major, S., Banerjee, A. & Chopra, K. L. Optical and electronic properties of zinc oxide films prepared by spray pyrolysis. *Thin Solid Films* **125**, 179-185, doi:http://dx.doi.org/10.1016/0040-6090(85)90411-0 (1985).

29 Misra, S., Yu, L., Foldyna, M. & Cabarrocas, P. R. i. New Approaches to Improve the Performance of Thin-Film Radial Junction Solar Cells Built Over Silicon Nanowire Arrays. *Ieee J Photovolt* **5**, 40-45, doi:10.1109/JPHOTOV.2014.2366688 (2015).

30 Jackson, P. *et al.* New world record efficiency for Cu(In,Ga)Se-2 thin-film solar cells beyond 20%. *Prog Photovoltaics* **19**, 894-897, doi:10.1002/pip.1078 (2011).

31 Burst, J. M. *et al.* CdTe solar cells with open-circuit voltage breaking the 1 V barrier. *Nature Energy* **1**, 16015, doi:10.1038/nenergy.2016.15 (2016).

32 Aiga, M., Nakamura, G. & Yukimoto, Y. TANDEM TYPE SOLAR-CELLS CONSISTING OF HYDROGENATED AMORPHOUS-SILICON GERMANIUM ALLOYS. *Proceedings of the Society of Photo-Optical Instrumentation Engineers* **407**, 33-36 (1983).

33 Kida, H., Itoh, M., Fukazawa, S., Ohta, T. & Yamamoto, K. A DEVICE MODELING OF AMORPHOUS-SILICON BASED TANDEM SOLAR-CELLS. *Japanese Journal of Applied Physics Part 2-Letters* **28**, L1499-L1501 (1989).

34 Isabella, O., Smets, A. H. M. & Zeman, M. Thin-film silicon-based quadruple junction solar cells approaching 20% conversion efficiency. *Sol Energ Mat Sol C* **129**, 82-89, doi:http://dx.doi.org/10.1016/j.solmat.2014.03.021 (2014).

35 Sai, H. *et al.* Triple-junction thin-film silicon solar cell fabricated on periodically textured substrate with a stabilized efficiency of 13.6%. *Appl Phys Lett* **106**, 213902, doi:http://dx.doi.org/10.1063/1.4921794 (2015).

36 Yan, B. *et al.* Innovative dual function nc-SiOx:H layer leading to a >16% efficient multi-junction thin-film silicon solar cell. *Appl Phys Lett* **99**, 113512, doi:http://dx.doi.org/10.1063/1.3638068 (2011).

37 Linwei, Y. *et al.* Assessing individual radial junction solar cells over millions on VLS-grown silicon nanowires. *Nanotechnology* **24**, 275401 (2013).

# Chapter 3 Silicon nanowire growth

## Contents

## 3.1 Introduction

A nano-object is an object which has a size in the nanometer scale. With the nano-object, it is possible to make small devices and integrate a large amount of them in a small area. The small size also brings novel material properties to the nano-object. This is because firstly, materials are composed of atoms which have a length scale of 0.1 nm. When the size of the material is in the nm scale, it cannot be considered that there are an infinite number of atoms. The limited number of atoms will give discrete band structure. Secondly, when the electron flows in the material, it usually has a kinetic energy of a few eV. This energy corresponds to an electron wavelength of few nm which is the size of the nano-object, thus the flow of electrons in nano-object will exhibit quantum properties. Lastly, when the material becomes small, the surface states will have a strong influence on the electron behavior. All these make the electrons to behave differently in a nano-object and lead to novel properties of a material. These properties include electrical, optical, thermal, mechanical and chemical properties. As a result, nano-objects find their application in a variety of fields such as electronics[1], photonics[2-4], mechanicals[5], and biologicals[6].

A nanowire (NW) is a kind of nano-object. Its specificity is the wire form, which means it is long in one dimension. The geometry gives another freedom to tune the properties of the NW or the NWs system. Firstly along the axial direction, the wire can have structured form, such as spring or zigzag. The atom arrangement and atom composition can also be changed along the axial direction. Secondly, the NW can have a core-shell or core multi-shell structure in the radial direction. Lastly, the NWs can also be arranged into arrays or more complicate structures. The novel properties makes NWs highly desirable for new generations of applications such as transistors [7], memories [8], biosensors [9], photodetectors [10], solar cells [11-15], and battery electrodes [16-18].

The synthesis of the NWs can be dated to 1960s[19]. Among the pioneers, Wagner and Ellis reported on the solid phase SiNW growth when they exposed the liquid phase Au nanoparticle to vapor phase $SiCl_4$ and $H_2$ gases at 950°C[20]. They named the growth mechanism as Vapor-liquid-solid (VLS). VLS and its variations are still the most used mechanism for NWs synthesis today[21]. This mechanism belongs to a category which is called bottom up approach. In this approach, the NW 'grows up' by adding the composition material little by little. The growth must be anisotropic, otherwise the growth will result in a bulk crystal. There are many ways to realize one dimensional anisotropic growth, such as using a capping catalyst metal or induce confinement by using template[17,22,23]. There is another NW synthesis approach called top down approach. Thanks to the advance of technology, it is possible to remove material at nanoscale with nm precision[24,25]. Then the straight forward top down approach appears. This approach starts with a bulk material and then removes material between NWs to get NWs. High cost equipment, such as electron lithography is usually used in the top down approach[26].

As explained in chapter 2, NW radial junction structure is highly desirable for solar cell applications. However, the competition with different types of solar cells and also from other kind of energy sources requires low solar cell fabrication cost. This means the NW structure in this study should be synthesized at low cost. It requires that the equipment to be low cost, the process to be low cost, and the material to be low cost. As a result, high cost equipment such as electron beam lithography, high cost substrate such as crystalline silicon wafers and complicated synthesis process are not the priority to be chosen. Instead, we use a standard low temperature PEVCD reactor, which is routinely used by the industry to produce low cost material on large areas, and a standard thermal evaporator as main equipment for synthesis, standard Corning glass coated with thin conductive layer of ZnO:Al

as substrate, and use simple process. We use Sn as a catalyst to produce SiNWs by plasma-assisted VLS method. There are several reasons to choose Sn. Firstly, Sn has a low eutectic point with Si. Thus the SiNWs can be grown with low temperature process. Secondly, the defect level in the Si induced by Sn is low. Lastly, according to previous studies on several catalyst candidates, such as Bi[27], In[28], Ga[29], and Sn[30,31], Sn produces NWs with better morphology and gives better solar cell performance. Thus we focus on Sn as a catalyst.

SiNWs or SiNW arrays are nano-structured Si material. It is the structural parameters that give them novel properties with respect to bulk Si. Thus controlling the structural parameters is essential in NW synthesis. A tremendous amount of research effort has been devoted to better understand the NW synthesis process and to achieve better controlled NW synthesis[32-34]. This research is also dedicated to achieve better controlled NW synthesis. With a low cost approach this task is more challenging because the process parameters, such as catalyst layer thickness, substrate temperature, and gas flow rate, do not link with a certain NW structural parameter directly. When one process parameter is changed, it always results in the change of many NW structural parameters. The complexity of the system requires one to have a good understanding of the NW growth process. In the literature, only few papers dedicated to the study the SiNW growth by plasma-assisted-vapor-solid method using tin as a catalyst can be found[35-42]. In these studies, different growth temperature [35], plasma power density [37], catalyst size[35,40] and hydrogen dilution level [35,36] have been used as variables to study their effect on the nanowire geometry and crystallinity. However the growth process was not detailed in these studies. There are few papers which investigate the nanowire diameter and length evolution[36,41] and discuss the growth process. However, the initial growth stage (when catalysts droplets form small NWs) was overlooked, despite the fact that this stage is the most important one for controlling the NW growth. Indeed, the density, the orientation of the NWs as well as the diameter of the crystalline core are mainly determined within this stage. This growth stage is one focus of this chapter. We have developed a positioning method which allows us to return to the same location on the sample after each process step. With this method we studied the behaviors of the catalyst droplets and the initial growth stage precisely. In addition, we have expanded the duration of the NW growth duration until the merging of NWs. Moreover, we also provide detailed statistical analysis and explanations on the evolution of NW density, morphology and crystalline structure.

## 3.2 Experimental setups

### 3.2.1 Thermal evaporator

With a bottom up approach, Si crystal needs to grow anisotopically to form a NW. In our case the Sn nanoparticle is capping on the tip of the SiNW to achieve one dimensional growth. An Edwards FL 400 thermal evaporator is used to deposit Sn thin film catalyst on the substrate. Figure 3.1 a) is a photo of the internal components of the thermal evaporator, and figure 3.1 b) shows the schematic diagram of the evaporator. Its working principle is simple. Firstly the substrate is fixed to the substrate holder and the Sn metal is loaded into the tungsten boat. Then the system will be pumped till the vacuum is under $5 \times 10^{-6}$ mbar. After that an electric current will be applied to the crucible to heat the Sn metal by Joule effect. The thickness of the deposited Sn layer is monitored by a quartz crystal microbalance. The quartz crystal microbalance measures the thickness by measuring the changing resonance frequency. The decrease in frequency can be linked with the increase in mass by using Sauerbrey's equation[43]:

$$\Delta f_s = \frac{-2{f_0}^2 mn}{(\mu_q \rho_q)^{1/2}} \qquad (3.1)$$

Where $\Delta f_s$ is the decrease in frequency, $f_0$ is the fundamental frequency of the crystal, $m$ is the increase in mass, $n$ is the harmonic number, $\mu_q$ is the shear modulus of the crystal, and $\rho_q$ is the density of the evaporated material. During the deposition process, the substrate temperature is room temperature.

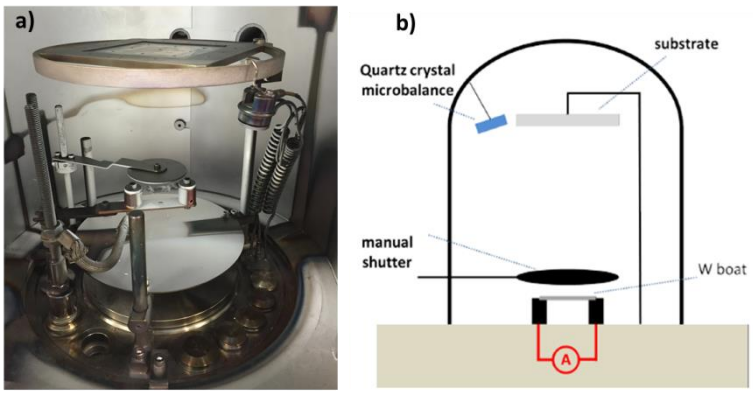


Figure 3.1. a) Internal components of thermal evaporator. b) Schematic diagram of the thermal evaporator.

With thermal evaporator we can deposit films of different thicknesses. We have checked the accuracy of the quartz crystal microbalance by measuring the deposited thickness. Figure 3.2 a) shows a SEM image of Sn catalyst deposited on a flat Si surface with 1 nm nominal thickness as measured by the microbalance. Image treatment software ImageJ[44] has been used to measure the droplets size. Firstly, a binary file is generated, as shown in figure 3.2 b). Then the droplets are identified and their areas are measured, as shown in figure 3.2 c). The volume of the droplets is calculated by considering they are perfect spheres. The total volume of the droplets is equivalent to 1.94 nm of planar Sn layer. Since the droplets have certain level of wetting on the Si surface, the real volume of the Sn droplet will be smaller than the perfect sphere. In the case of semi-spheres the equivalent thickness would be 0.97 nm, very close to the nominal value of 1 nm. This shows that the quartz crystal microbalance gives a relatively good accuracy. Here a Si wafer is also used, this is because that Si wafer has a flat surface and it is easy to cut. During the experiments, the native oxide on the Si wafer was not removed.

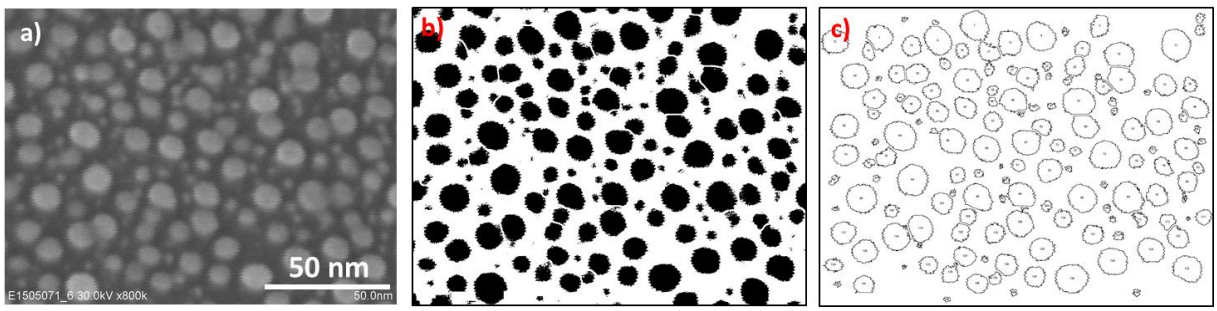


Figure 3.2. a) SEM image of as deposited 1 nm of Sn on Si surface. b) Image a) after binary treatment. c) Droplets which have been identified by the software.

### 3.2.2 PECVD reactor

The NW growth is carried out in a PECVD reactor named Plasfil. Figure 3.3 a) shows the structure of Plasfil, and 3 b) shows a schematic diagram of it. It consists of a chamber which is linked with precursor gas lines and pumping system. When there is no gas injection, the back ground vacuum level is in the 5 x $10^{-4}$ Pa (5 x $10^{-6}$ mbar) range. When the precursor gas is injected, the working pressure is in the ~100 Pa (~1 Torr) range. There are two electrodes in the chamber. The top one is connected to the power injection system, while the bottom one is grounded. Both electrodes can be independently heated. The bottom electrode also works as a substrate holder. During NW growth, the precursor gases flow between the two electrodes. The free electrons are accelerated by the oscillating electric field and collide with the precursor gas molecules. After receiving the energy from electrons, the gas molecules dissociate and become reactive radicals. The radicals diffuse to the NWs to maintain the growth process.

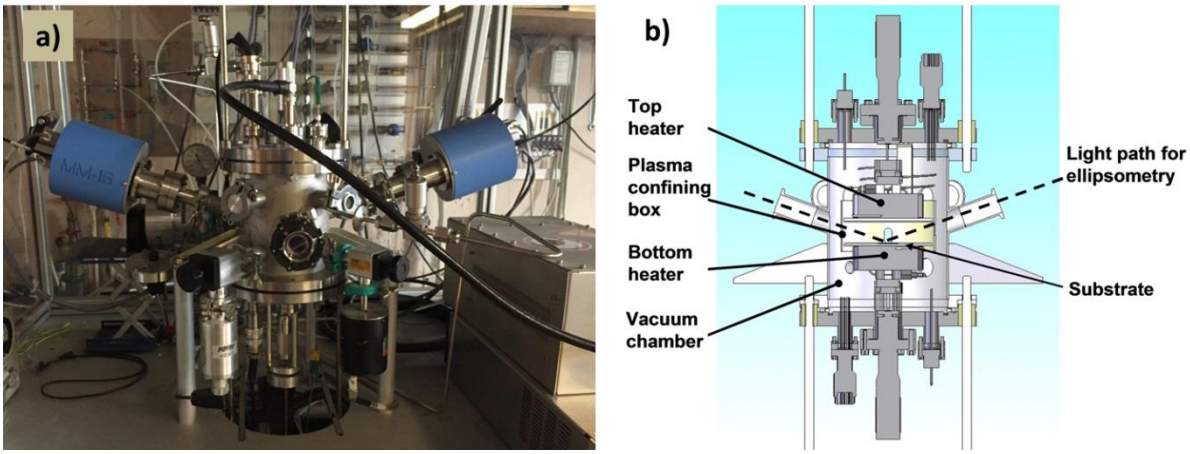


Figure 3.3. a) PECVD reactor Plasfil. b) Schematic diagram of the reactor.

For a PECVD reactor, the most important parameters include gas flow rate, substrate temperature and injection power. We have calibrated these parameters to guarantee the accuracy of the experiments. The substrate temperature was measured by fixing Pt100 platinum resistance thermometers to a 1 mm thick Corning glass on the substrate holder. Figure 3.4 a) shows the real temperature measured by Pt100 as a function of nominal substrate temperature. During the measurement, the $H_2$ flow rate was 100 sccm, pressure was 133 Pa, and the top electrode temperature was set at 200°C. It can be seen that the measured data during heating up and cooling down have a good match which indicates that the temperatures have achieved a steady state value during measurements. The linear fit of the two curves gives a slope around 0.56. This means with the increase of the nominal temperature, the difference between measured temperature and nominal temperature gets bigger. When the nominal temperature is 160°C, the difference is 16°C, while when the nominal temperature is 650°C, the gap increases to 224°C. Figure 3.4 b) shows that when the setting temperature is 600°C, it takes around 15 minutes to reach a steady state value, which is around 393°C. When the setting temperature is 250°C, it takes around 10 minutes to achieve equilibrium at around 202°C.

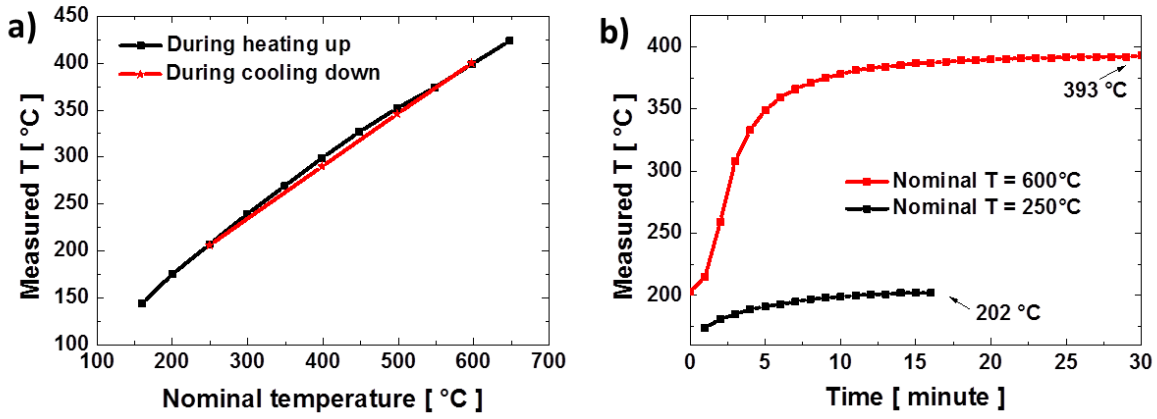


Figure 3.4. Temperature calibration results on Plasfil. a) Real temperature measured with a Pt100 as a function of nominal temperature. b) Temperature increasing profile when the nominal temperature is set at 600°C and 250°C.

The flow rate is calibrated as follows: the volume of the reactor is $V$ in $m^3$, the flow rate is $v$ in sccm, the pumping system is stopped. At time t in seconds, the change of the pressure of the reactor is $\Delta P$ in Pa, T is reactor temperature in K, R is gas constant 8.314 $JK^{-1}mol^{-1}$. Then the real flow rate can be calculated as:

$$v = \frac{1.344*10^6 \Delta PV}{RTt} \qquad (3.2)$$

The volume of the chamber is measured by connecting a tube with known volume $V_t$ to the reactor. There is a valve between the tube and the reactor. At the beginning, keep the valve open and set the pressure at $P_1$, then close the valve and pump the chamber to decrease the pressure to $P_2$, then open the valve, the total pressure will be increased to $P_3$. The volume of the chamber can be calculated as:

$$V = V_t \frac{P_1 - P_3}{P_3 - P_2} \qquad (3.3)$$

The leakage rate of the reactor has also been measured. After closing the pumping system, the increase of pressure of the chamber pressure is shown in figure 3.5 a). The leakage rate of the chamber has been calculated by using equation 3.2, and it has a value around $10^{-4}$ sccm, as shown in figure 3.5 b).

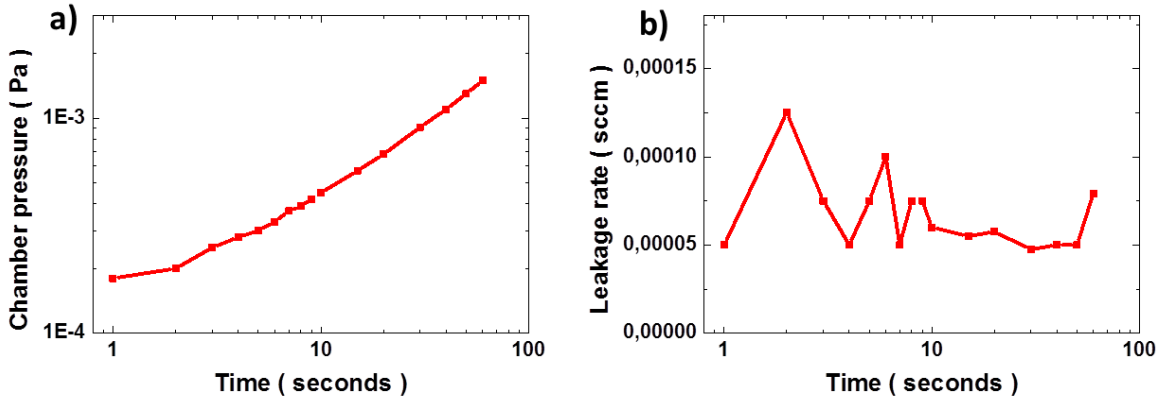


Figure 3.5. a) Chamber pressure after closing the pumping system. b) Chamber leakage rate after closing the pumping system.

### 3.2.3 Other experimental tools and the SiNW growth processes

Besides the thermal evaporator and the PECVD reactor, a sputtering system is used to deposit thin ZnO:Al layers on Corning glass. The characterization tools used in this study include scanning electron microscopy (SEM), Raman spectroscopy and Transmission electron microscopy (TEM). The SEM equipment was a Hitachi S-4800; the TEM instrument was a Jeol 2010F with a point-to-point resolution of 0.23 nm, and a TiTan with a point-to-point resolution of 0.1 nm. The Raman spectrometer was an ARAMIS system from Jobin-Yvon with a lateral resolution around 1 µm and four possible excitation wavelengths: 473 nm, 532 nm, 633 nm and 785 nm.

The typical NW synthesis experiment involves the following steps:

(1) A ~1.4 µm thick ZnO:Al film was sputtered onto Corning glass. During the sputtering process, the substrate temperature was set at 200°C [45].
(2) A Sn layer with a nominal thickness of 1 nm was deposited on ZnO:Al by thermal evaporation. These droplets subsequently oxidize when exposed to atmosphere.
(3) The substrate was loaded into Plasfil, and heated up to 200°C under vacuum.
(4) A hydrogen plasma was applied to reduce the tin oxide and to form Sn droplets. The $H_2$ flow rate, pressure, RF power density, inter-electrode distance and duration of the plasma were 100 sccm, 600 mTorr, 38 mW/cm$^2$, 28 mm and 2 minutes, respectively. This is our standard $H_2$ plasma treatment.
(5) After the hydrogen plasma treatment, the temperature of the substrate was increased to 400°C, and samples were annealed for 2 minutes under a $H_2$ flow. Then 11 sccm of silane were introduced. The total pressure for $SiH_4$ and $H_2$ gas was set to 1000 mTorr, and a RF power of 17 mW/cm$^2$ was applied to trigger the silane plasma. The duration of NW growth was 10 minutes. After growth, the samples were cooled down to 120°C under $H_2$ flow.

## 3.3 Experimental results

### 3.3.1. Droplets engineering

With bottom up NW synthesis, the catalyst droplets play a major role during the NW growth process. Thus engineering the droplets diameter and density distribution is an effective way to control the

NW growth. In this study, various treatments have been carried out to study the evolution of the catalyst droplets.

### *3.3.1.1 The substrate*

The image of the substrate for SiNW growth is shown in figure 3.6 a), and the schematic of it is shown in Fig 6 b). It composed of a 1 inch by 1 inch commercial Corning glass, then a ZnO:Al layer, and finally an evaporated thin Sn layer. The ZnO:Al layer is deposited in the lab using sputtering process. The function of this layer is to provide a transparent conductive contact for solar cells. The most used nominal thickness of Sn layer in this study is 1 nm. Figures 3.6 d) shows a SEM image of the substrate. The diameters of the droplets in figure 3.6 d) have been measured and shown in figure 3.6 c). They are in the range of 2 to 12 nm. The total volume of these droplets calculated from theses diameters data is close to the volume of a 1 nm thick layer. Since 1 nm only corresponds to 3 monolayer of Sn, there should be no Sn layers between the droplets. Figures 3.6 e) and f) show Sn layers deposited on ZnO:Al coated Corning glass with nominal thicknesses of 30 nm and 350 nm, respectively. It can be seen that Sn does not form a uniform layer even when the thickness is as big as 350 nm. This is due to the fact that the interaction between Sn atoms is stronger than the interaction between Sn atoms and ZnO:Al surface, thus the growth of the Sn layer has an island growth mode.

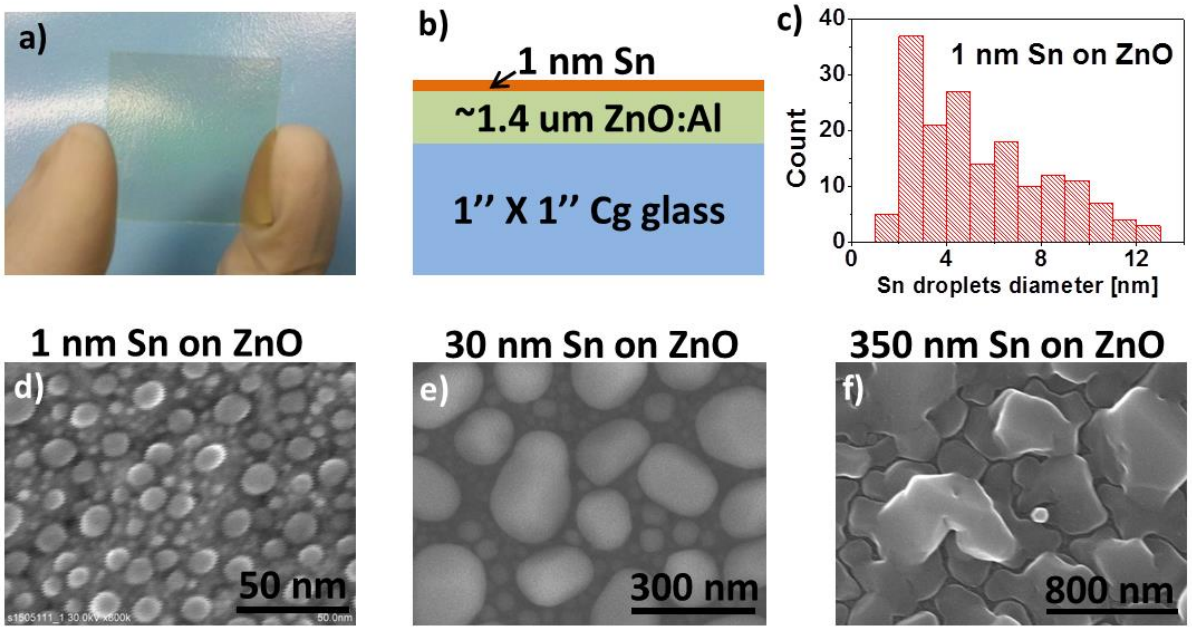


Figure 3.6. a) ZnO:Al coated Coring glass. b) Schematic diagram of substrate with 1 nm of Sn. c) Sn droplets diameter distribution when the Sn layer thickness is 1 nm. d) to f) SEM pictures of Sn layers deposited on ZnO:Al with different thicknesses: d) 1 nm, e) 30 nm; f) 350 nm.

In order to monitor the change of droplets after the treatments, we have developed a positioning method for SEM observation. Firstly, a cross shape scratch is made on Corning glass with a diamond pen. The form of the scratch can be seen in figure 3.7 a). There are two additional scratches in the center to differ the up and down during SEM observation. Then a 1.4 µm thick ZnO:Al layer is coated on the Corning glass. Finally 1 nm of Sn layer is deposited. Figures 3.7 b) to f) show the SEM images at different magnifications. For each picture, the zone indicated by the arrow is magnified in the next

one. On the last image, we can identify single droplets with diameters of few nm. The particles with µm size in the SEM images are glass particles coated with ZnO:Al. The glass particles are generated during the scratching process. The particle with 1 µm size might also be a ZnO:Al particle formed during the sputtering process. The particles are used as a mark for positioning. This positioning method is low cost, fast and gives nm precision, thus suitable for our purposes.

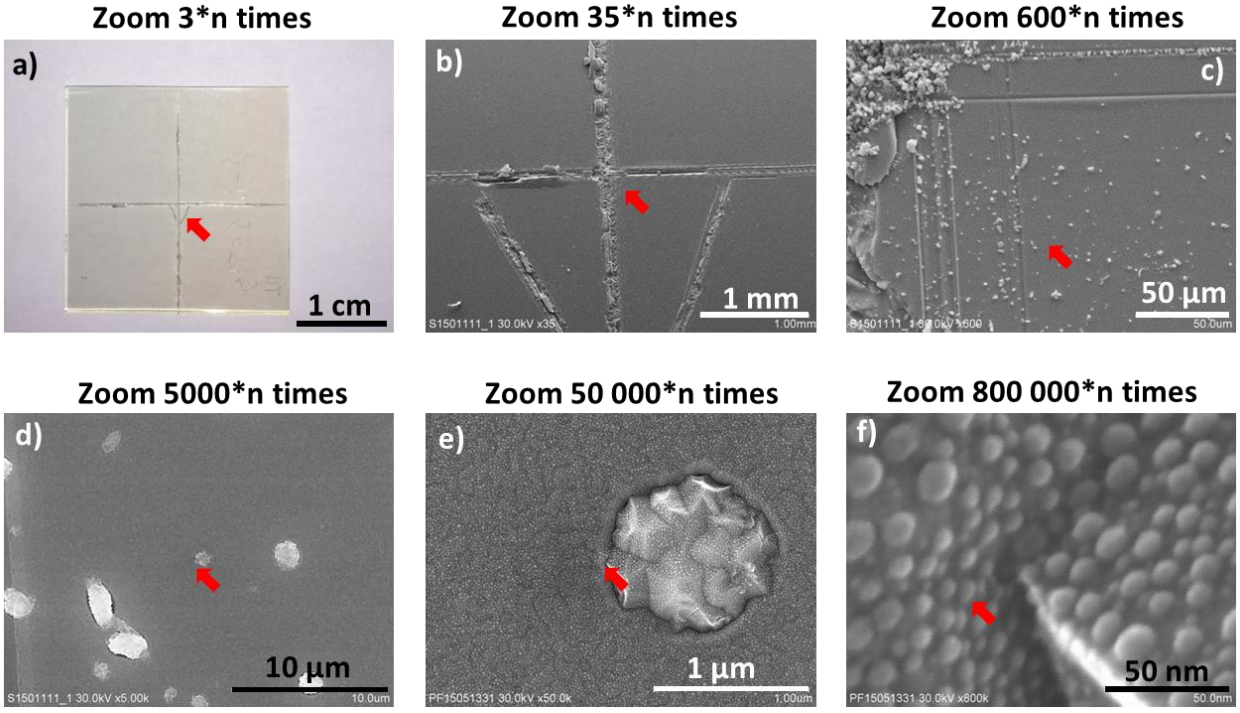


Figure 3.7. Images of the sample at different magnification. The zone indicated by the arrow is zoomed in the next image. a) Normal cameral image zoom at x 3. b) to f), SEM images zoom at x 35*n, x 600*n, x 5000*n, x 50 000*n, and x 800 000*n, respectively. Note that the n which determine the real magnification depends of the final display on the screen or on the paper. When these images are printed on an A4 paper, n ~= 1/3.

### *3.3.1.2 Effect of annealing*

With the positioning method described above, firstly we have carried out annealing treatments on the Sn droplets. Two similar annealing experiments have been done with same parameters except annealing temperature, which are 200°C and 400°C. The substrate used are 1 nm of Sn deposited on ZnO:Al coated Corning glass. Before annealing, a standard $H_2$ plasma has been applied to the Sn droplets to remove the native oxide. In order to prevent the oxidation of the droplets during the annealing, $H_2$ flow has maintained in the PECVD reactor. The annealing times are in the range of 45 minutes to 65 minutes.

The SEM images of the same position of the samples before and after annealing are shown in figure 3.8. For the annealing at 200°C, there is no significant change of the droplets size after the annealing. For the majority of the cases, the position and the size of the droplets remains the same as before the treatment, as indicated by the dashed circle 1. However for some cases, there are droplets disappear accompanied with neighboring droplets size increases, as indicated by the dashed circles 2. The most plausible likely explanation to this is Ostwald ripening, which means the atoms from small

droplets spontaneous transport to large droplets because larger droplets are more energetically favored than smaller droplets[46]. Another possibility is that the droplets move and coalesce. Even the annealing temperature (200°C) is 32°C lower than the melting point of bulk Sn, the real melting point of a Sn droplet of 10 nm diameter can be well below 200°C[47,48]. Thus the liquid phase Sn droplets have the possibility to coalesce during $H_2$ plasma treatment and annealing. Ostwald ripening and coalescence are two phenomena which can lead to same result. The difference between them is that the scale of the change. It is atom by atom for Ostwald ripening, and droplet by droplet for coalescence. For the annealing at 400°C, it is not easy to obtain SEM image with good contrast after the annealing. However, it can still be seen that the majority of the droplets stay at the same position as before the annealing, as indicated by the dashed circles. These two annealing experiments show that the size and the density of the droplets cannot be modified significantly by annealing at a temperature close to the melting point of Sn ( 200°C ) or even at a temperature much higher than the melting point of the Sn (400°C).

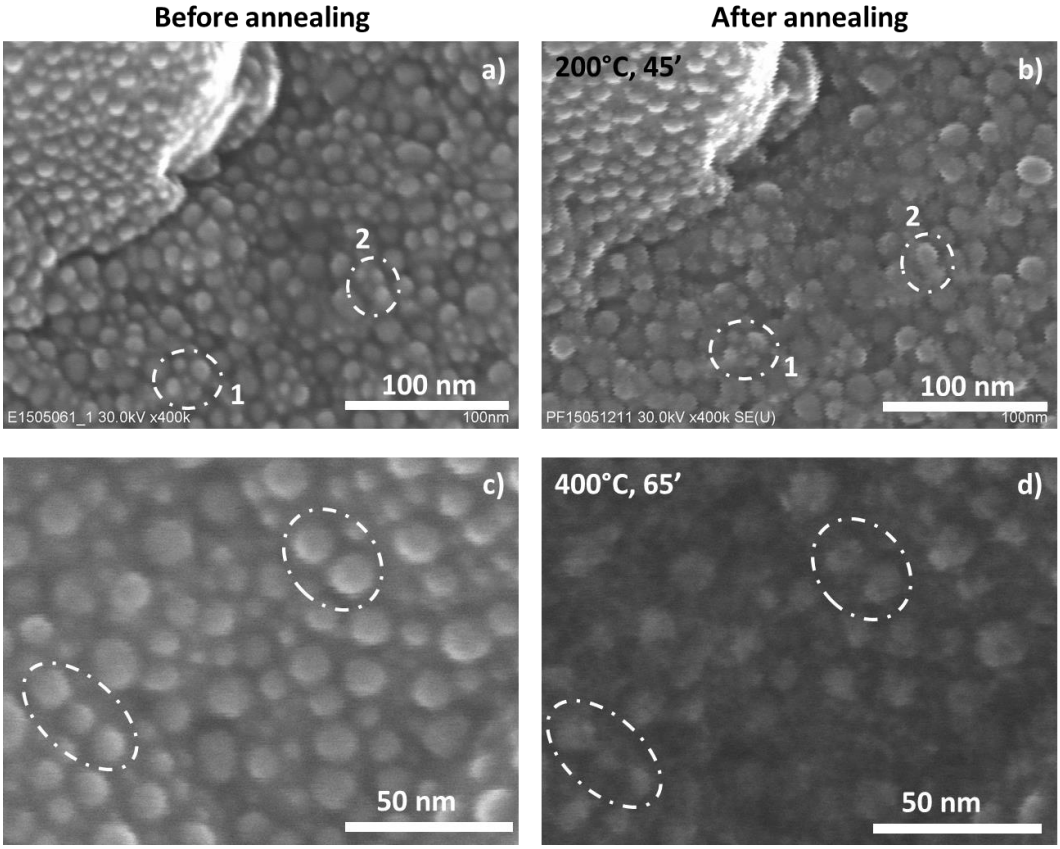


Figure 3.8. SEM images of samples before and after annealing. a) and b) show the same position of a sample annealed at 200°C for 45 minutes; c) and d) shows the same position of same sample annealed at 400°C for 65 minutes.

### *3.3.1.3 Effect of a thin a-Si:H layer*

During the plasma-assisted VLS SiNW growth process, there is a-Si:H deposition on the area between Sn catalyst drops. The a-Si:H layer can change the surface chemistry and the behaviors of the Sn droplets. An experiment has been done to study the influence of a thin a-Si:H layer during annealing.

For this experiment, 1 nm of Sn was deposited both on ZnO:Al coated Corning glass and cSi wafer. Firstly the samples were exposed to a standard $H_2$ plasma treatment to remove the native oxide. Then 30 seconds of a-Si:H deposition was carried out. The $H_2$ flow rate was 100 sccm, the $SiH_4$ flow rate was 10 sccm, and the RF power was 38 mW/cm$^2$. The estimated a-Si:H layer thickness was around 2 nm. In order to avoid SiNW growth during a-Si:H layer deposition, the temperature of a-Si:H deposition was set at 200°C. Indeed, previous studies in our lab show that the a-Si:H layer deposited at lower temperature is more favorable to coalescence for µm scale Sn catalyst droplets.[49,50] Finally 45 minutes annealing was carried out at 400°C under $H_2$ flow.

SEM images of a same position before and after the process are shown in figures 3.9 a) and b), respectively. Figures 3.9 c) and d) shows two different positions of the ZnO:Al coated Corning glass sample before and after annealing, respectively. It can be seen that annealing has a similar effect on the two samples. After annealing, the droplets size increases and their density decreases. By comparing figures 3.9 a) and b), we can see that some droplets stay at the same positon, as indicated by the dashed circles 1 and 2. But in most cases, droplets merge with the neighboring ones and lead to the increase of droplets size and the depletion of the surrounding area, as indicated by dashed circles 3, 4, and 5. This demonstrates that a-Si:H can enhance coalescence or Ostwald ripening of Sn catalyst.

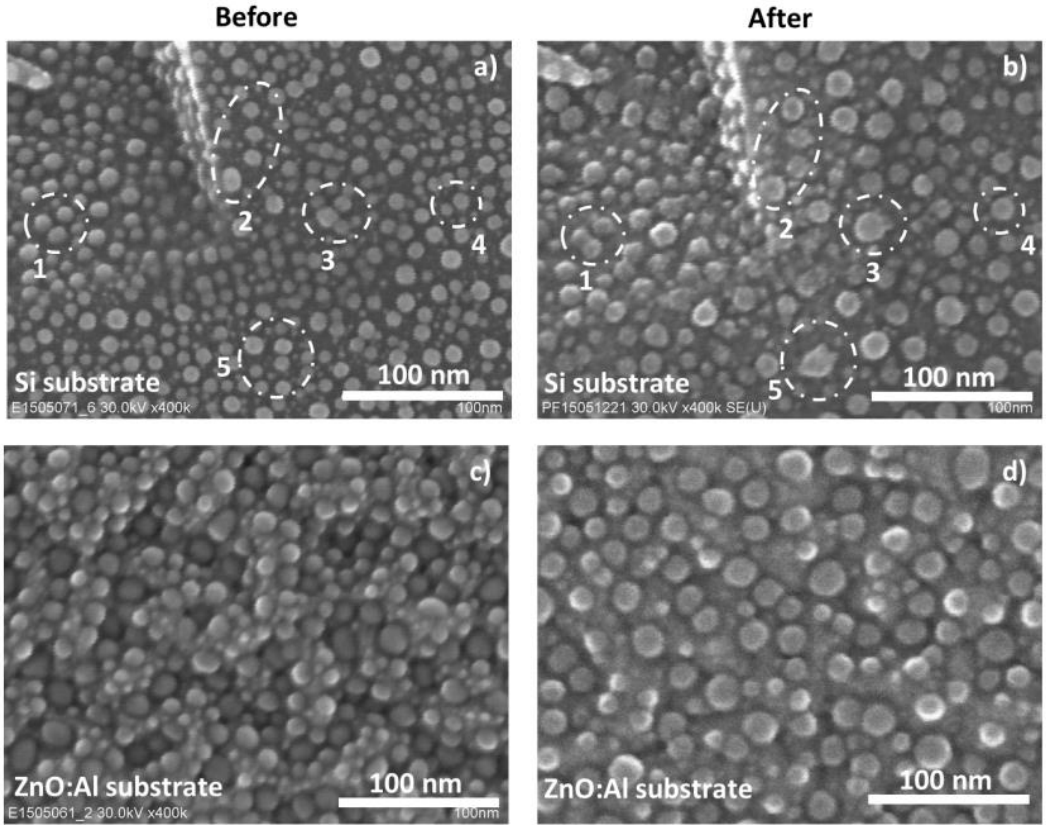


Figure 3.9. SEM images of 1 nm Sn samples before and after annealing at 400°C with a thin a-Si:H layer. a) 1 nm of Sn as deposited on Si wafer. b) Same position as a) but after the annealing. c) 1 nm of Sn as deposited on ZnO:Al. d) Same sample as c), but on a different position after annealing.

### *3.3.1.3 Effect of $H_2$ plasma treatment*

Since $H_2$ plasma produces highly reactive hydrogen radicals, there is a strong possibility that a $H_2$ plasma can modify the Sn droplets distribution. An experiment has been done to study the $H_2$ plasma effects on the Sn droplets. Firstly, 1 nm of Sn has been deposited on ZnO:Al substrate. Then a $H_2$ plasma has applied to the samples. The $H_2$ flow rate, pressure, RF power density, substrate temperature and duration of the plasma were 100 sccm, 326 mTorr, 17 mW/cm$^2$, 310°C and 100 minutes, respectively. As shown in figure 3.10, there is a significant increase of droplets size and decrease of droplets density after the $H_2$ plasma treatment. The distance between two neighboring droplets can exceed 100 nm. The size of the droplets is not uniform. The large ones can reach 40 nm, while the small ones can be smaller than 10 nm.

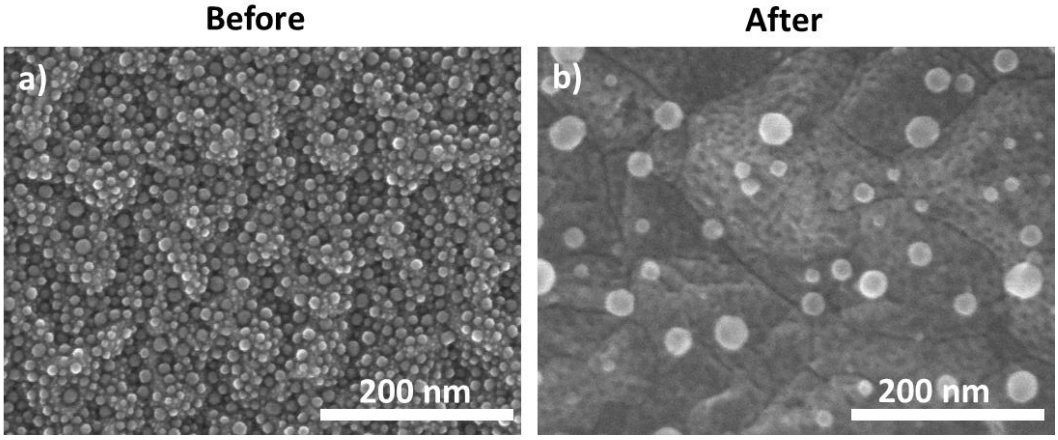


Figure 3.10. SEM image of 1 nm Sn on ZnO:Al sample before and after $H_2$ plasma treatment at 310°C

An experiment has also been done to study the $H_2$ plasma effects on the Sn droplets at 400°C. In this experiment, firstly, 1 nm of Sn has been deposited both on Si wafer and ZnO:Al substrate. Then a $H_2$ plasma has applied to the samples. The $H_2$ flow rate, pressure, RF power density, substrate temperature and duration of the plasma are 100 sccm, 830 mTorr, 17 mW/cm$^2$, 400°C and 90 minutes, respectively. The SEM images of the two samples before and after the treatment are shown in figure 3.11. It can be seen that the morphology of the surfaces has totally changed after the treatment. On the Si wafer substrate, the result is quite similar to that of the $H_2$ plasma treatment at 310°C. As shown in figure 3.11 b), big droplets appear on the Si surface after the treatment. The total volume of these big droplets represents 60% of the initial volume. This indicates that at least the majority of the Sn has not been removed by the $H_2$ plasma. The result for ZnO:Al substrate sample is quite different. In figure 3.11 d), no Sn droplets can be seen on the ZnO:Al substrate after the treatment. Since the same $H_2$ plasma treatment has not removed the Sn on the Si wafer sample, so there should be significant Sn left on the ZnO:Al sample also. The Sn might just have changed its shape after the treatment. Indeed, SiNWs can be grown with the ZnO:Al sample which has experienced the similar treatment.[51]

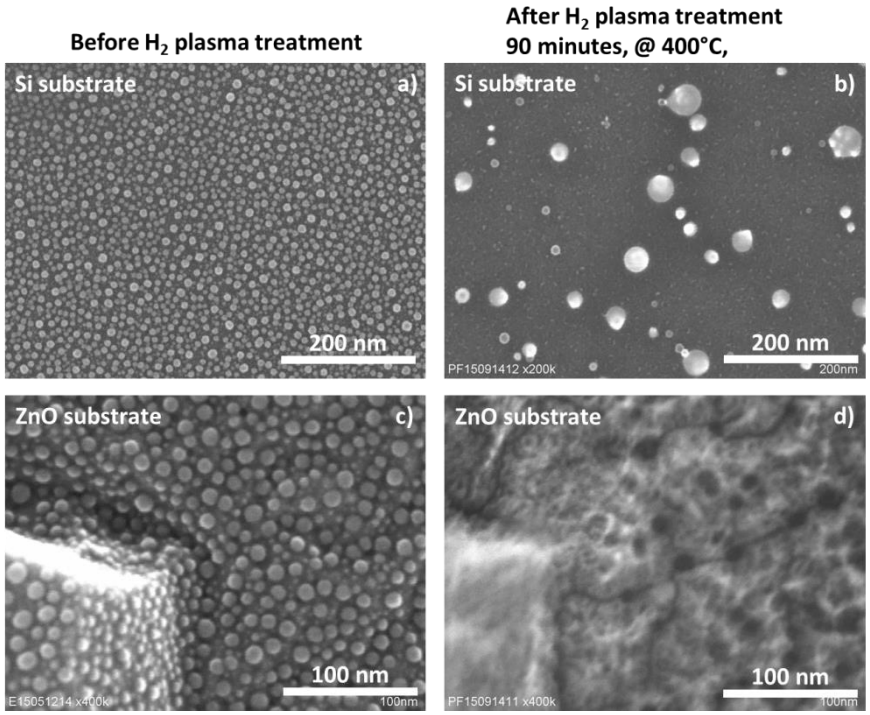


Figure 3.11. SEM images of 1 nm of Sn before and after a $H_2$ plasma treatment. a) 1 nm of Sn as deposited on Si wafer. b) same sample as a), after $H_2$ plasma treatment. c) 1 nm of Sn on ZnO:Al surface, as deposited. d) Same position of the same sample as c), after the $H_2$ plasma treatment.

#### *3.3.1.4 Summary on droplets engineering*

The droplets engineering experiments are summarized in table 3.1. The annealing both at 200°C and 400°C gives quite small changes of the Sn droplets size and density. With the presence of a thin a-Si:H layer, the changement is enhanced but still limited. The $H_2$ plasma treatment both at 310°C and 400°C brings significant changes to the droplets size and density.

Table 3.1. Comparison of different treatment on Sn droplets

| Treatment | Temperature | Detailed description of the changes | Level of changes |
|---|---|---|---|
| annealing | 200°C | Majority of droplets stay at their initial position with similar diameter | **Small** |
| | 400°C | | |
| Annealing with a-Si:H layer | 400°C | Sn droplets increase diameter and decrease density | **Moderate** |
| $H_2$ plasma | 310°C | Sn droplets increase diameter and decrease density significantly | **Strong** |
| | 400°C | On ZnO:Al surface: Sn drops are not visible. On Si wafer substrate: Sn droplets increase diameter and decrease density significantly | |

### 3.3.2 NW growth process

In order to understand the NW growth process, we have carried out a series of experiment to observe the growth process step by step. In this series of experiments, we have fixed all the plasma parameters except the growth duration. The duration of NW growth was varied between 1 second and 8 hours. The detailed experiment parameters and procedures can be found in part 3.2.3.

The NW growth process from catalyst formation to the end of growth (up to 8 hours) has been systematically analyzed by SEM. We roughly divide the whole growth process into four phases: i) the evolution of catalyst droplets and initial formation of NWs, ii) the formation of straight NWs, iii) the NW growth, and iv) the end of NW axial growth followed by a-Si:H coating.

### *3.3.2.1 Evolution of catalyst droplets and initial stages of NW growth*

In order to precisely monitor the evolution of the catalyst droplets at the initial stages of SiNW formation, we have made a mark on the substrates (white stripe on the bottom left corner of the images) allowing us to return to the same location on the sample after each process step in the PECVD reactor. Figures 3.12 a) to d) show the sample with 1 nm of as-evaporated Sn, after 2 minutes of annealing at 400°C, after 10 seconds growth, and after 40 seconds growth, respectively. It can be seen that as-evaporated Sn forms droplets instead of a continuous layer. The droplets have a density around 9000 droplets/$\mu m^2$ and their diameters range between 1 and 13 nm. The average diameter is around 5.5 nm, and only around 20% of the droplets have a diameter larger than 8 nm. After annealing at 400°C, two droplets can merge if they are close enough to each other, as the small droplets inside the white circle figure 3.12 a) which become one single drop in figure 3.12 b). After the annealing, the density of droplets decreases to 6600 droplets/$\mu m^2$ and the average diameter increases to 6.3 nm. For Si NW growth catalyzed by Au or Cu, there is an incubation time which can be several tens of seconds [52]. In contrast, when using Sn as a catalyst, NW growth can start within 10 seconds, presumably due to the low solubility of Si in Sn [53]. Indeed, within 10 seconds of triggering the $SiH_4$ and $H_2$ plasma, NWs start to grow, as shown in figure 3.12 c). The growth of NWs brings dramatic changes to the droplets. Since the initial distance between droplets is only a few nm and the NW length at this growth duration can be 10 to 20 nm, a significant amount of droplets merge, as in the case of the NW indicated by the three dashed white lines in figure 3.12 c). The positions of the three roots of this NW correspond to the positions of three droplets indicated by white dots in figure 3.12 a) and b). It is obvious that these three droplets grow separately and then merge together. In order to illustrate the coalescence due to the NWs growth within the first 10 seconds, this process has been illustrated with 3D software blender, as shown in figure 3.12 e). In this Figure we illustrate how droplets are pushed together and merge during the initial stage of NW growth.

The droplets in figure 3.12 a) can also catalyze a NW without merging with other droplets, as the droplet and NW indicated by the arrow in figure 3.12 a), 3.12 b) and 3.12 c). In figure 3.12 c), it is difficult to find a NW or droplet with a diameter smaller than 5 nm. This can be due to the low solubility of Si in Sn. When a droplet's diameter is 5 nm, the number of atoms inside is less than 2500. The solubility of Si in Sn at 400°C is much less than 0.25% [53], thus the number of Si atoms that can be dissolved inside such a Sn droplet is fewer than 6. In other words, most of the small drops seen in figure 3.12 b) do not catalyze a NW because they do not have a single Si atom dissolved in them. Therefore, the options for small droplets are to merge with other droplets or to get buried. After the coalescence, the NW can continue its growth; this can be seen in figure 3.12 d) which shows the NWs growing upwards after the coalescence (indicated by the white dashed lines). Droplets can continue coalescing between 10 and 40 seconds of growth duration, as in the case of the two NWs indicated by the two dashed lines at the bottom part in figures 3.12 c) and 3.12 d), which get merged due to NW growth.

The above results are summarized in figure 3.12 f) where the black squares show the evolution of the droplet density and the red circles show the evolution of the droplets mean diameter. The process

time from 0 to 240 seconds corresponds to the annealing of Sn droplets, and from 240 to 250 seconds corresponds to the first 10 seconds of NW growth. With the increase of time, the droplet density keeps on decreasing, while the droplet mean diameter keeps on increasing. Since the droplet diameter and density display a much greater change during the 10 seconds of NW growth than during the 2 minutes of annealing, it can be concluded that coalescence plays a much more important role than Ostwald ripening.

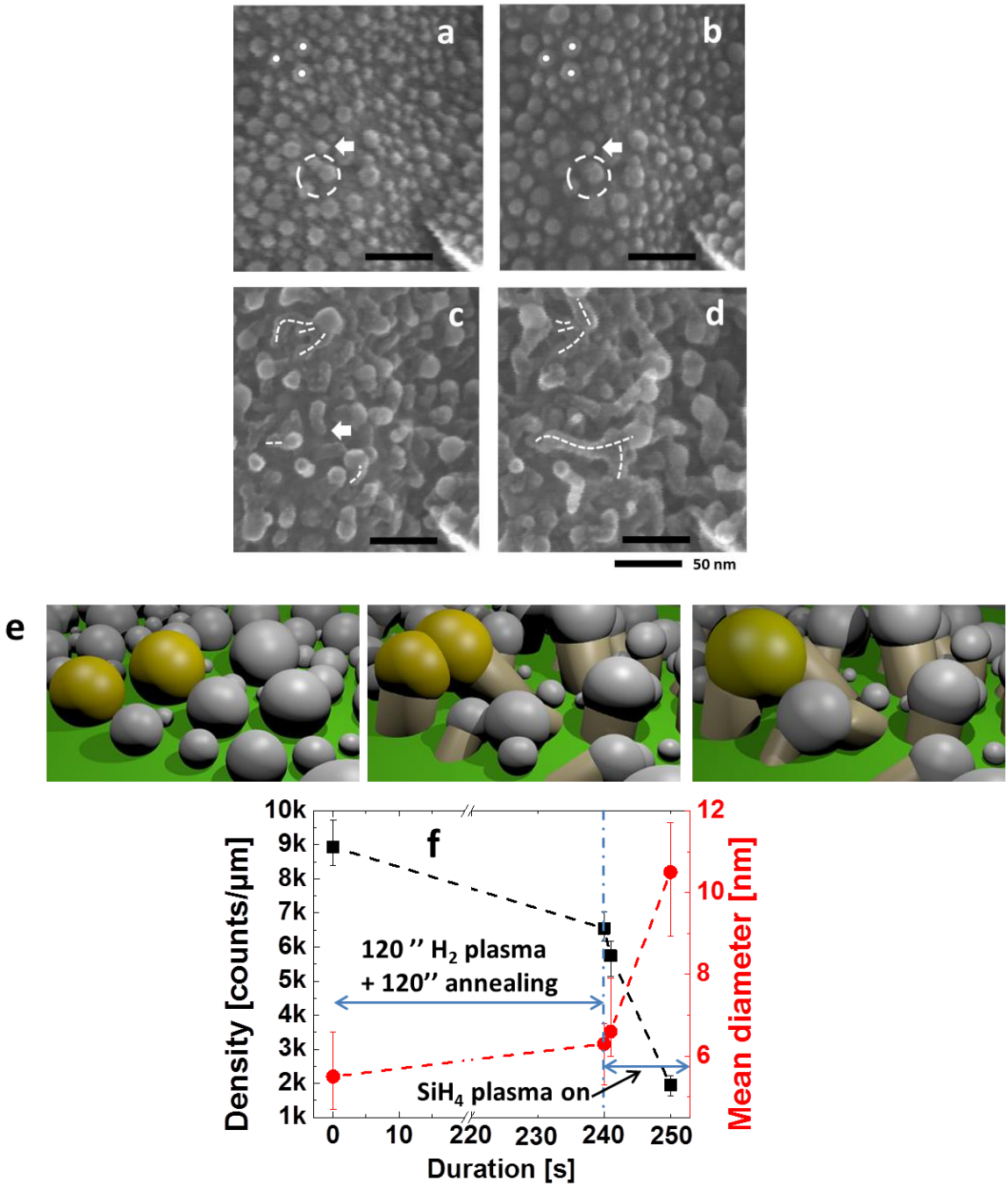


**Figure 3.12.** a)-d): SEM images acquired on the same spot of the sample at different growth durations. a) 1 nm of Sn deposited on ZnO:Al; b) after 2 minutes of $H_2$ plasma treatment at 200°C and 2 minutes of annealing at 400°C; c) after 10 seconds of NW growth at 400°C; d) 40 seconds growth e) 3D illustration of coalescence of droplets during the first 10 seconds NW growth f) evolution of the droplets density and mean diameter as a function of process time.

### *3.3.2.2 Formation of straight NWs*

Let us now look at the NW behavior for longer growth durations. At 2 minutes growth duration, long and straight NWs are clearly observed, as shown in figures 3.13 a) and b). At this stage the NW density is around 170 NWs/μm$^2$, which is far less than the catalyst droplet density previously mentioned. This is mainly because a large proportion of droplets produce irregularly shaped nanostructures instead of a NW, as indicated by the circle in figure 3.13 a). The formation of these irregularly shaped objects might be due to the anisotropic growth (along NW axial direction) breakdown by continuous formation of crystalline defects. The side view SEM image for 2' growth duration is shown in figure 3.13 b). It can be seen that the NWs growth directions are quite random. The NW tip diameter at this growth duration is usually around 10 nm; it is not easy to find a NW with a tip diameter larger than 20 nm, even amongst thousands of NWs. Wetting of the NW sidewalls by catalyst during NW growth has been suggested in the literature [54]. If this phenomenon happens in the present case, the maximum wetting layer length can be estimated by the following equation:

$$L = 2r^2/3cn$$

Where $r$ is the radius of the NW at the base, $c$ is the thickness of a monolayer catalyst ($c^3$ is the atomic volume of catalyst), and n is the number of layers of catalyst on the sidewall. In our case, $c \approx 0.30\ nm, r \approx 8\ nm, n = 1$ (which means 1 monolayer of Sn coverage), then L is around 140 nm. However, in the present case the NWs can grow till several μm long. The existence of such a wetting layer at a growth condition similar to the present condition is a matter of debate in the literature [36,41]. Our results suggest that the wetting layer should follow the tips of NW if it exists during the NW growth.

### *3.3.2.3 NW growth*

As we increase the growth duration, not all the NWs continue their growth along the axial direction. A significant amount of kinking is observed at 5 minutes growth duration, as indicated by the circles in figure 3.13 c). This is mainly caused by crystalline defects such as twinning and change of crystalline phase, as shown in figures 3.13 e) and f). Indeed, in figure 3.13 f) the crystalline phase has changed from diamond cubic Si to hexagonal Si [55,56]. This is an exciting topic and will be explained in the last section of this chapter. NWs can also change growth direction without introducing crystalline defects; as shown in figure 3.13 g), the growth direction has changed from <111> to <211>. The new directions may orient the NWs growth toward the substrate or other directions for which makes it difficult for NWs to continue growth. NWs usually present irregular shapes after kinking, thus they lose their wire-like geometry and cannot be considered as NWs. Thus, kinking decreases NW density sharply. When the growth duration increases to 30 minutes, as shown in figure 3.13 d), the NW "forest" becomes crowded because the NWs become long and their diameters increased. As a result, more and more NWs at the bottom of the NW forest get shaded by the NWs on top of them. The shadowing brings two effects. Firstly, it is difficult for the $SiH_x$ radicals to reach the hidden NWs. Secondly, these NWs are no longer observable. At this growth duration, as indicated by the circles in figure 3.13 d), parts of the NWs start to have a large tip diameter of several tens of nm. This is a contrast to the situation at 2 minutes growth duration, when it was almost impossible to find a single NW with a tip diameter bigger than 20 nm. The increase in the tip diameter can be explained by the deposition of a-Si:H on the NW tip when there is no Sn catalyst on it (or no enough amount of Sn to

continuously catalyze the growth). Therefore, the increase of NW tip diameter can be considered as a sign of the end of the plasma assisted VLS growth.

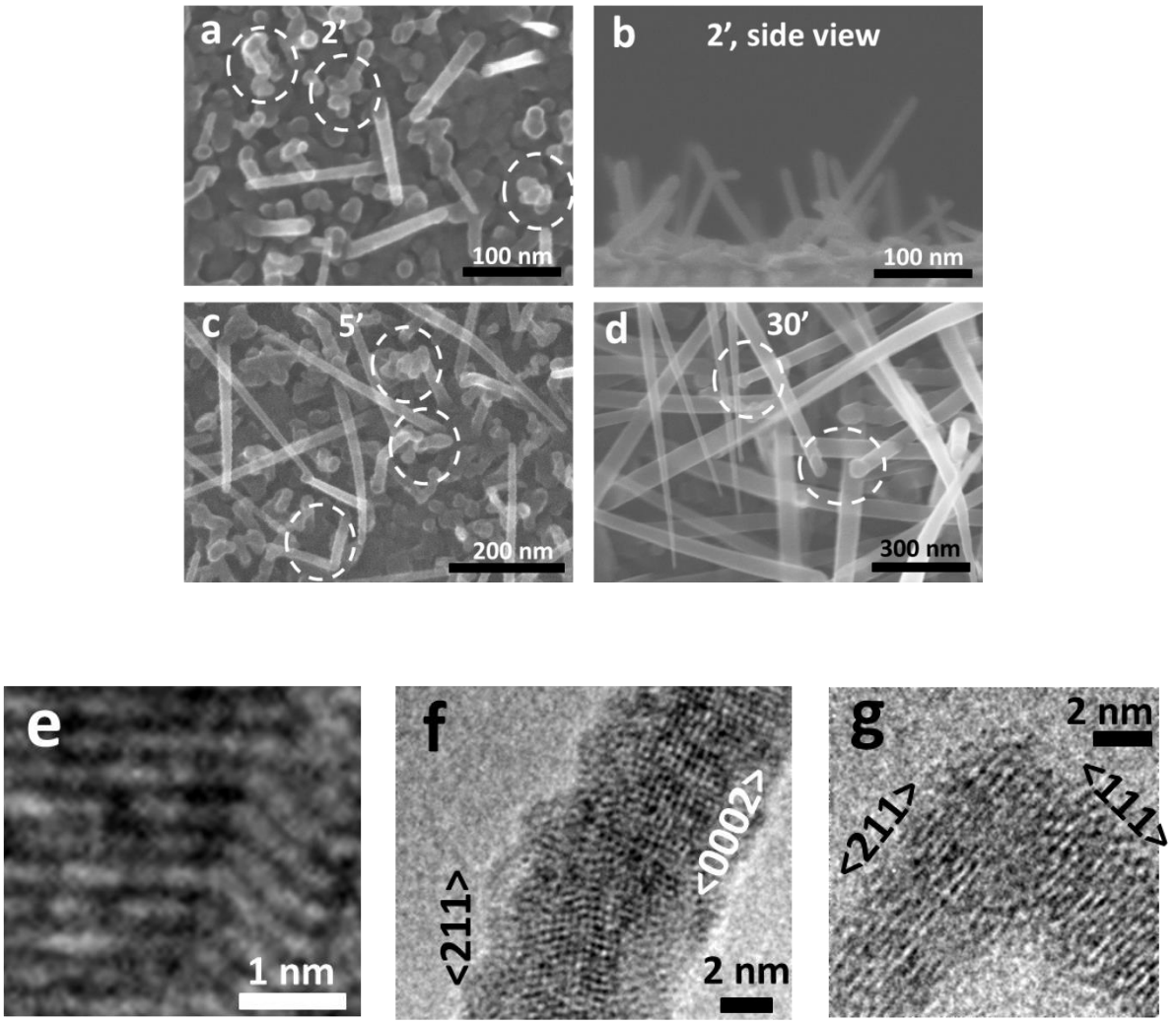


**Figure 3.13.** SEM images of NWs at different growth durations: a) 2 minutes; b) 2 minutes, side view; c) 5 minutes; d) 30 minutes. High resolution TEM images which show e): twinning; f) change of crystalline phase from cubic Si to hexagonal Si; g) change of growth direction from <111> to <211>.

### *3.3.2.4 End of NW axial growth followed by a-Si:H coating*

When the NW growth duration reaches 90 minutes, almost all the NWs have a large tip diameter, as shown in figures 3.14 a) and b). This indicates that all the NWs have eventually run out of catalyst between 30 minutes and 90 minutes growth duration. As a consequence, there is only additional a-Si:H coating if the growth duration is further increased. This is clearly illustrated in figure 3.14 c) for 8 hours growth duration, where the diameters of the NW tips exceed 1 µm. The NW density as determined from a top view SEM image is less than 1 NW/µm$^2$. From the side view SEM image, it can be seen more clearly that NWs touch each other, and most of them merge. This corresponds to standard a-Si:H deposition on a rough surface and the end of NW growth.

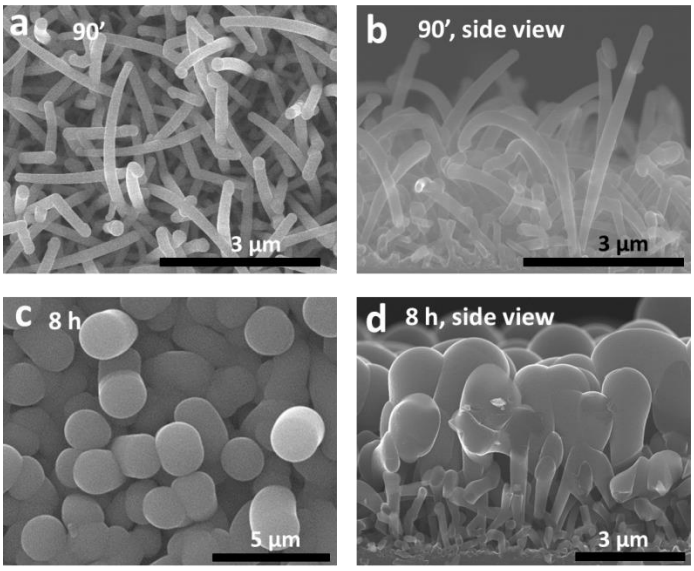


**Figure** 3.**14.** SEM images of NWs at long growth durations: a) 90 minutes; b) 90 minutes, side view; c) 8 hours; d) 8 hours, side view.

### *3.3.2.5 Evolution of the areal density of Si NWs*

The evolution of catalyst droplet and NW density is displayed on a log-log plot in figure 3.15. In this figure, the statistics correspond to observable droplets and NWs. The first data point corresponds to the density of catalyst droplets after evaporation, the second data point corresponds to the droplet density at 10 seconds growth duration, and the rest correspond to the NW density at different growth durations. Overall, there is a decrease of density by 4 orders of magnitude. The decrease can be divided into four stages. The first stage corresponds to the first few tens of seconds of growth, when coalescence of droplets decreases the catalyst density. The second stage corresponds to the first 2 minutes of growth; at this stage we have seen that only a small percentage of initial catalyst droplets produce straight NWs. The third stage corresponds to the NW axial growth process, which roughly takes place between 2 to 90 minutes under our growth conditions. During this stage the decrease is mainly caused by the kinking and shading of NWs. The last stage (between 90 minutes and 8 hours of growth) corresponds to a phase of standard a-Si:H deposition on the top of NWs; the plasma-assisted VLS process is no longer effective due to the exhaustion of Sn. The increase of diameter makes NWs touch and merge with each other.

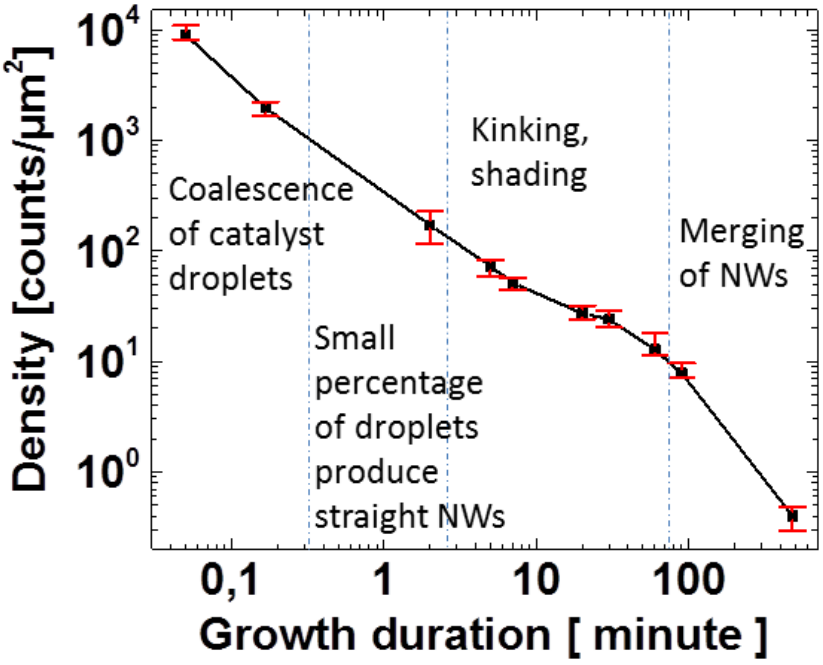


**Figure 3.15.** Evolution of the density of catalyst droplets and Si NWs during the 8 hours growth process.

### *3.3.2.6 Evolution of crystallinity*

We can obtain a clear view on the evolution of the NW crystallinity as a function of growth duration through TEM observations. Samples with 2 minutes, 30 minutes and 90 minutes growth duration have been studied by TEM. The observations show that NWs with short growth duration (~ 2 minutes) are usually monocrystalline with an ultrathin (less than 1 nm) amorphous shell on their surface (figure 3.16 a). The latter has been characterized as native oxide by electron energy loss spectroscopy (EELS). This oxide is due to the fact that the NWs have been exposed to air before TEM characterization. When the growth duration increases to 30 minutes, as shown in figure 3.16 b, the core of the NW is monocrystalline while the shell has broken down to a-Si:H. Interestingly, it can be clearly seen that the transition from the crystalline core to the amorphous phase shell deposition is an epitaxial Si growth. This indicate the NW growth in radial direction does not change from crystalline to amorphous with an atomic layer abruptness[57,58]. When the growth duration increases to 90 minutes, as shown in figure 3.16 c), the NW has a monocrystalline core, defective crystalline shell, and a thick a-Si:H shell. The diffraction pattern in figure 3.16 c) demonstrates that the defects are twins, the mirror plane of which is essentially the <111> plane that lies parallel to the growth axis. In the literature, crystalline core with nanocrystalline shell structure [36,41,59] and crystalline core with amorphous shell structure [37] have been reported. Here we suggest that with the increase of growth duration, the crystalline structure of NWS along radial direction evolves from i) monocrystalline, to ii) monocrystalline core/defective crystalline shell, then iii) to monocrystalline core/defective crystalline shell/amorphous shell. The interface between crystalline part and amorphous part is not atomically sharp.

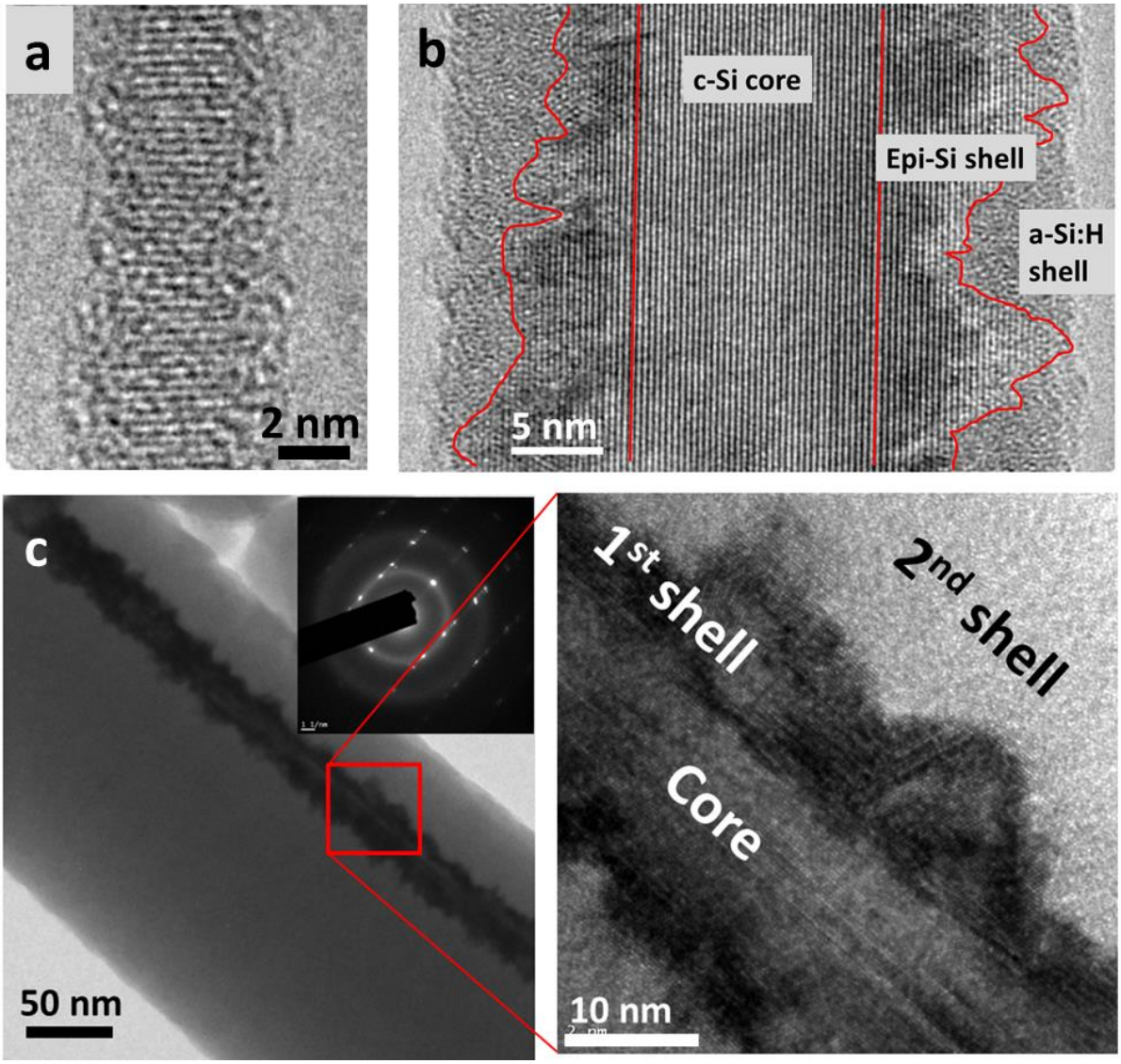


**Figure 3.16.** a) TEM image of a NW with 2 minutes of growth duration. b) TEM image of a NW with 30 minutes of growth duration. c) TEM image of a NW with 90 minutes of growth duration with corresponding diffraction pattern in the inset. On the right of c) we show a zoom of the core double shell structure.

The a-Si:H shell of the SiNW in figure 3.16 c) can be removed by $H_2$ plasma etching. Figure 3.17 shows a sample which has undergone 90 minutes of standard of SiNW growth and 60 minutes of $H_2$ plasma etching. There is no break of vacuum between SiNW growth and $H_2$ plasma etching, otherwise the etching will be difficult due to the formation of a-SiOx on the surface of the a-Si:H. During the $H_2$ plasma etching, the $H_2$ flow rate, pressure, RF power density and substrate temperature are 100 sccm, 500 mTorr, 125 mW/cm$^2$ and 100°C, respectively. Figure 3.17 shows the SEM image of the sample after the $H_2$ plasma etching. It can be seen that the majority of the NWs have changed the morphology compared with the NWs shown in figure 3.14 a). The NWs become long and thin. As highlighted by the red line, the NW is long, thin and has a uniform diameter along a long distance. This indicates that the a-Si:H shell has been successfully removed.

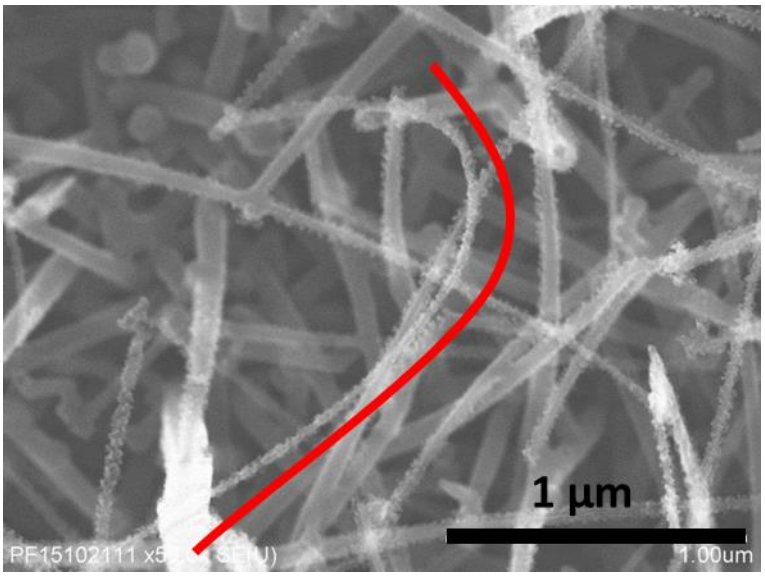


Figure 3.17. SEM image of a sample which has undergone a 90 minutes of SiNW growth and 60 minutes of $H_2$ plasma etching. The red line highlights a NW with a-Si:H shell removed.

The NWs in figure 3.17 have also been studied by TEM. Figure 3.18 a) shows the bright field image of a NW and figure 3.18 b) is a HRTEM image of the region indicated by the red block in a). It can be seen that this NW has a rough surface after etching. The atomic planes can be seen on the major part of the NW except for the surface. The diffraction pattern of the area in figure a) is shown in c). It also shows strong crystalline signal. The particle like stuff on the surface looks like amorphous material. The chemical map acquired by EDX study of the SiNW shown in d) shows the particles at the surface are oxygen rich, as shown in e). Since there is presence of atomic hydrogen during the whole NW growth process and the etching process, the oxide should be formed during the exposure to air after the experiment. The rough surface can be explained by two possible reasons. The first one is that the c-Si core of the NW is rough, as shown in figures 3.16 c) and d). The second one is that $H_2$ plasma etching produces rough surface regardless the initial structure.

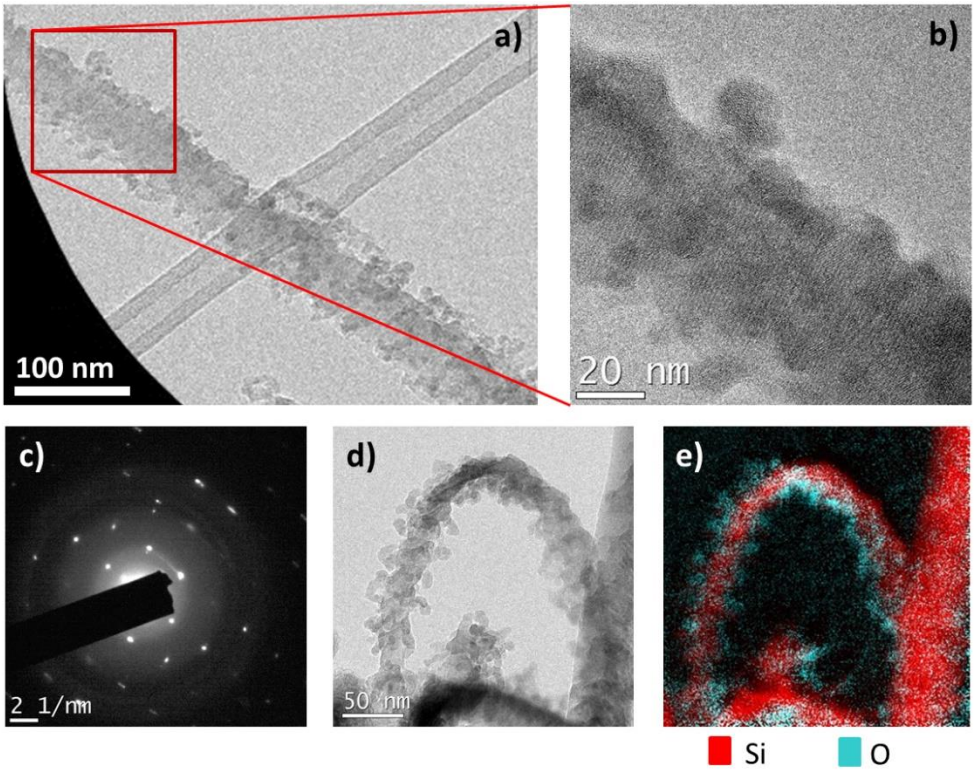


Figure 3.18. TEM characterization of a SiNW after $H_2$ plasma etching. a) Bright field image of the NW. b) HRTEM image of the region indicated by the red box in a). c) Diffraction pattern of the NW shown in a). d) Bright field image of another NW. e) Si and O map of the NW shown in d).

The evolution of the crystallinity has also been studied systematically by Raman spectroscopy for samples with 2 minutes, 30 minutes and 90 minutes of growth duration. The diameter of the laser spot is around 1 µm. Thus, the Raman response is that of several tens or hundreds of NWs, depending on the growth duration. The results are shown in figure 3.19. For the sample with 2 minutes of growth duration, a sharp peak can be observed at around 518 $cm^{-1}$. It indicates that the NWs are almost fully crystalline. There is a 3 $cm^{-1}$ red shift compared with the bulk c-Si Raman peak, which is around 521 $cm^{-1}$. This is mainly because the crystalline NWs have a diameter around 10 nm which produces a red shift of Raman peak [60,61]. For the sample with 30 minutes growth duration, the intensity of the crystalline peak at 518 $cm^{-1}$ decreases and a broad a-Si:H peak centered at ~480 $cm^{-1}$ appears. This indicates an increasing fraction of amorphous material, which is mostly due to the a-Si:H deposition on the sidewall of NWs and also on the substrate between the NWs. At 90 minutes of growth duration, the broad peak at 480 $cm^{-1}$ indicates that the material is mostly amorphous. The very weak shoulder around 520 $cm^{-1}$ shows that the fraction of crystalline material is very small.

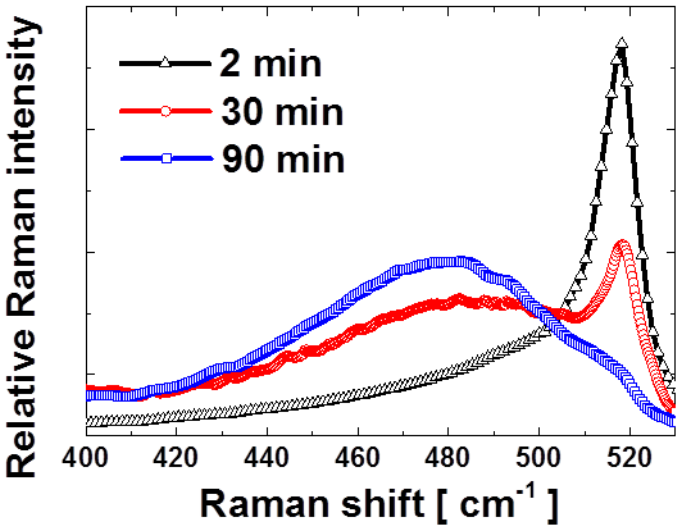


**Figure 3.19.** Raman spectra measured on SiNW samples with durations of 2, 30 and 90 minutes

### *3.3.2.7 Evolution of NW morphology*

During the growth process, NWs undergo a strong evolution of morphology from quasi-cylindrical to conical, then to bent conical, and lastly to bent inverted conical, as shown in figures 3.20 a-d). In figure 3.20 e), the black squares, blue stars and red circles show the evolution of NW length, base diameter and tip diameter as functions of the growth duration. During the first 30 minutes of growth, the NW length increases at a rate around 1.5 nm/s, the base diameter increases at a rate of 0.03-0.05 nm/s, while the tip diameter remains almost constant. The invariance of the tip diameter can be explained by two reasons. Firstly, the decrease of tip diameter is very small, and therefore within the observational error bar. As described in section 3.3.2.3, Sn droplets might not be able to catalyze the growth when their diameter is smaller than 5 nm. So the decrease of the droplets diameter under our growth conditions can only be of a few nm since the starting value is around 10 nm. Secondly, the decrease of tip diameter is hidden by another phenomenon: once the Sn is exhausted on the tip, the tip diameter will start to increase due to the coating by a-Si:H. When the coated tip is less than 20 nm in diameter, it is not possible to tell whether the NW axial growth has stopped. This phenomenon increases the average tip diameter and hides the decrease of the tip diameter during NW axial growth.

The evolution from quasi-cylindrical to conical shapes can be explained by a-Si:H side wall deposition. Since the radial growth rate is 30-40 times smaller than the axial growth rate, it is not easy to recognize differences in diameter when the NWs are short. At 90 seconds growth duration, the length of the NW is ~100 nm, and the diameter difference between tip and base is only ~3 nm. Thus the NWs appear almost cylindrical, as shown in Fig 20 a). As the growth duration is increased to 10 minutes, the NW length ranges from several hundred nm to 1 µm, and the base diameters are usually around 40 nm. The base diameter is around 4 times larger than the tip diameter, and the NWs therefore display a clear conical morphology (Fig 20 b).

The NWs axial growth roughly stops between 30 minutes and 90 minutes due to the exhaustion of Sn. In figure 3.20 e) we can see that above 30 minutes the NWs length does not increase as fast as in the first 30 minutes. At the same time, the tip diameter increases at a rate higher than the base diameter. As a consequence, the tip diameter can exceed the base diameter at 90 minutes growth duration. NWs usually bend during this period, as shown in figure 3.14 b) and 3.20 c). These phenomena can be explained by comparing the mean free path of SiHx radicals with NW size and inter distance of NWs. The mean free path of the SiHx radicals at the pressures in these experiments can be expressed as [62]:

$$\lambda = \frac{kT}{\sqrt{2}\pi d^2 P}$$

Where *k*, Boltzman's constant, $P$, the pressure, $T$, the temperature, $d$ the molecular diameter. In the present case *P*=143 Pa*, T=673 K, d=0.296 nm*. Thus $\lambda$ has a value around 200 micrometers. This value is several orders of magnitude larger than the NW length, diameter and the distance between NWs. When the SiHx radicals arrive at NWs from the top, they can be considered to have a very long and straight trajectory, and arrive with a broad angular distribution. Therefore, due to shadowing effects, the tip of the NW receives more SiHx radicals than the base due to the crowding of NWs, leading to a faster tip diameter growth rate. As the NW diameter increases, the inter NW distance decreases. It gets more and more difficult for the SiHx radicals to arrive the base of the NWs, and the base diameter stays almost unchanged during 90 minutes to 8 hours growth.

The long SiHx radical mean free path also leads to an asymmetric a-Si:H deposition around the NWs. When the NW is tilted, its upper, plasma-facing side receives more radicals than its lower, substrate-facing side. The dark-field TEM image of figure 3.20 f) a shows that the a-Si:H shell deposition is not symmetric; the side which has a smaller curvature has thicker a-Si:H deposition. Numerous SEM observations show that the upper side of the bent NWs has a smaller curvature than the lower side, as shown in figure 3.20 c), indicating that their upper side have a thicker a-Si:H layer. In figure 3.20 f), the high resolution TEM image shows that the core of the NW is crystalline. The pattern of the fast Fourier transforms (FFT) of the HRTEM image rotates clockwise as the zone of the FFT is moved from left to right. This indicates that the crystalline core is bent with the same curvature as this segment of the NW. The curvature of the core is around $2*10^5$ $m^{-1}$, which roughly corresponds to a strain value of 0.5%.

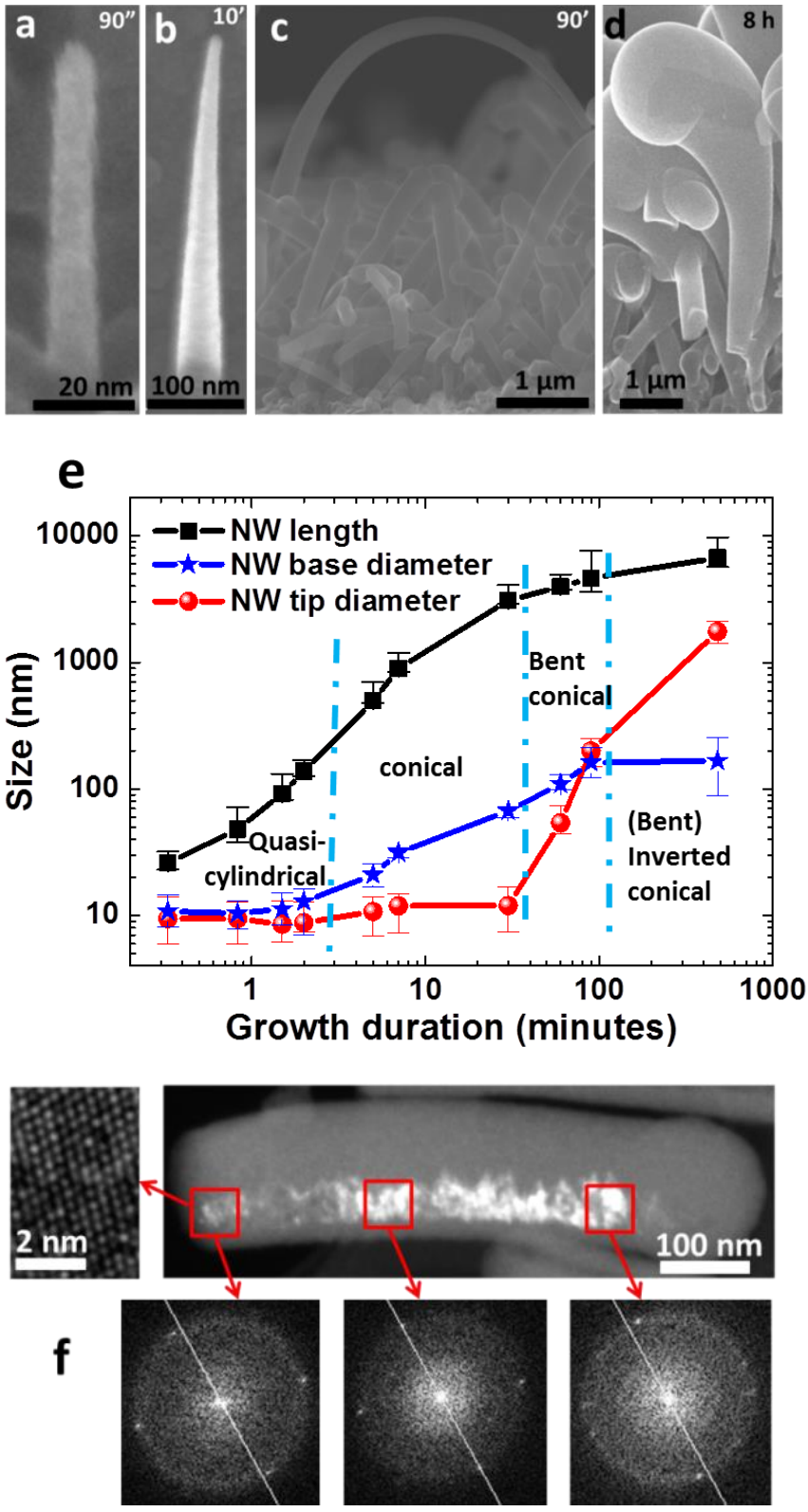


**Figure 3.20.** a)-d) NW morphology at different growth durations: 90 seconds, 10 minutes, 90 minutes and 8 h. e) Statistics of NW length, base diameter and tip diameter at different growth durations. f) TEM dark field image of a segment of a bent NW. The image on the left is a high resolution TEM image of the area indicated by the square. The three images at bottom are FFTs of HRTEM images. The white lines are reference lines which have been set at the same position. Note that the diffraction spots move from left to right of the line as the FFT rotates clockwise.

The bending of the NW can be explained by assuming the a-Si:H shell of the NW is compressively strained. This strain can be built during the deposition process or cooling down process (due to the difference of thermal expansion coefficiency). The compressively strained a-Si:H shell has a tendency to expend, thus it exerts a tensile shear force on the c-Si core at the core-shell interface. As illustrated in figure 3.21, both the a-Si:H layer at the upper and lower part of the c-Si core exert tensile shear force on the c-Si core with values $F_1$ and $F_2$, respectively. Because the thickness of the a-Si:H layer $d_1$ is bigger than that of the lower part $d_2$, thus $F_1$ is bigger than $F_2$. As a result, the generatrix of the c-Si core at upper part $L_1$ will be stretched more than the generatrix at lower part $L_2$. Thus the bending direction of the c-Si core is toward the lower side.

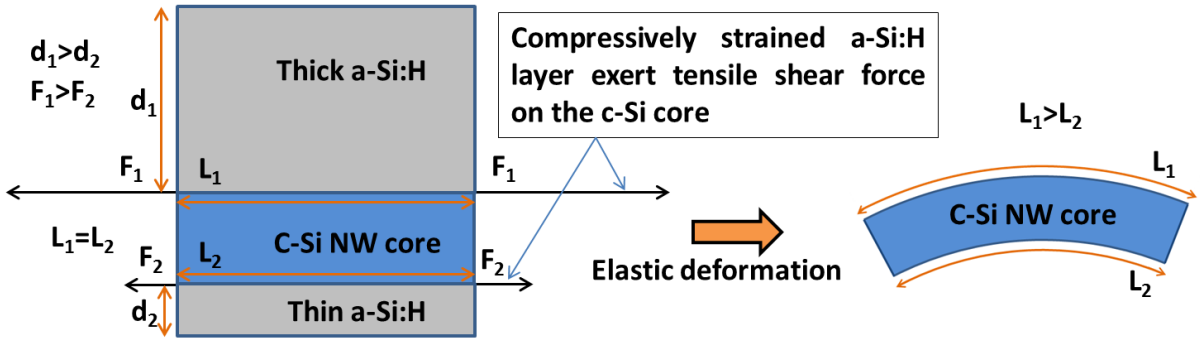


Figure 3.21. Schematic of the strain and the bending of the NW

### *3.3.2.8 Growth scenario*

Based on the experimental observations presented above, we propose a detailed scenario for the NW growth process. At the very beginning, a discontinuous Sn layer with nominal thickness of 1 nm is evaporated on ZnO:Al substrate. However, instead of forming a continuous layer, Sn forms droplets which have a mean diameter around 6 nm (Fig 22 a). The Sn droplets get oxidized due to their exposure to air between the evaporation and loading into the PECVD reactor. A $H_2$ plasma is applied to reduce the Sn oxide into Sn. After that, the Sn droplets are heated to 400°C and a $H_2$ and $SiH_4$ plasma is ignited. $SiH_x$ radicals produced by the dissociation of silane in the plasma reach the Sn droplets and Si atoms get dissolved into the Sn droplets. As more and more Si atoms get dissolved into the Sn droplets, Si atoms start to precipitate at the interface between the ZnO:Al substrate and the Sn droplet. The precipitated Si atoms form an initial nucleus. At the same time, $SiH_x$ radicals continue to arrive at Sn droplet surface, diffuse to the nucleus and form the NW with random growth direction. Since the Sn droplets are only a few nanometres apart, a large proportion of droplets merge during the growth of NWs, as shown in figure 3.22 b). A significant proportion of droplets catalyze Si objects with irregular shapes instead of straight NWs. However, a small percentage of droplets catalyze straight, monocrystalline (or sometimes twinned crystalline) Si NWs, as shown in figure 3.22 c).

These NWs grow rapidly in the axial direction with the help of the Sn catalyst. In the meantime, $SiH_x$ radicals also reach the NW sidewalls. These radicals lead to radial epitaxial growth before breakdown and the development of an amorphous Si coating on the sidewalls. The radial sidewall growth rate is around 30-40 times smaller than the axial growth rate. The diameter of the NWs at their tip remains almost constant during growth. Since the base of the NWs experiences a longer deposition duration, its diameter is larger. This results in a slightly conical tapered geometry for the NWs. During the

growth process, there are always NWs that stop growing due to kinking, as shown in figure 3.22 d). After a certain growth duration, all the NWs stop axial growth because of the exhaustion of the Sn catalyst. Then the top diameters of these NWs start to increase due to the deposition of a-Si:H on the top part. Since the mean free path of $SiH_x$ radicals in the plasma is much longer than the NW length and the distance between the NWs, it is difficult for the $SiH_x$ radicals to arrive at the bottom part of the crowded NW forest. Therefore, the increase of NW diameter at the top part is bigger than that at the bottom part.

When the NW axial direction is not perpendicular to the substrate, there is more a-Si:H deposition on the upper, plasma-facing part of the NW sidewall than on the lower part. Therefore, the asymmetric compressive stress in the a-Si:H bends the NWs toward the substrate (figure 3.22 e). The space between NWs decreases as the diameter of their tops increases, and eventually the NWs merge. At the end, the structure formed includes a dense bottom part with relatively small diameters, a merged middle part, and a low-density top with relatively big diameters, as shown in figure 3.22 f).

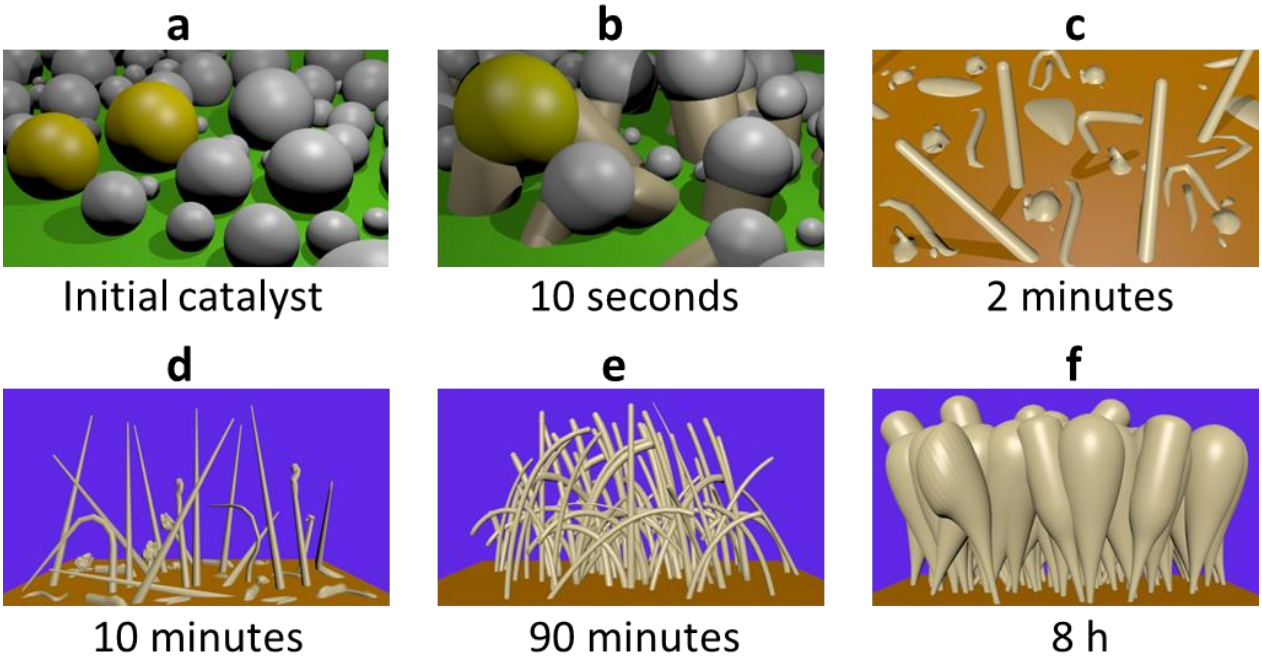


**Figure 3.22.** 3D illustration of samples at different growth durations. a) as-deposited Sn catalyst; b) 10 seconds growth; c) 2 minutes growth; d) 10 minutes growth; e) 8 h growth.

#### *3.3.2.9 Summary on NW growth process*

We have carried out a detailed study of the plasma-assisted VLS silicon nanowire growth process by repeating the same growth experiments many times and stopping at different growth durations. For the initial growth stage, the evolution of the same droplet of a same sample has been traced from catalyst droplets formation to 40 seconds of growth. We have studied the evolution of NW density, morphology and crystallinity during the whole growth process. Our results show that there is a decrease of density by four orders of magnitude. This can be attributed to i) the coalescence of the catalyst droplets, ii) the small percentage of catalysts producing straight NWs, iii) kinking, shading and iv) merging of NWs. We show that NWs undergo a strong evolution in morphology from quasi-cylindrical to conical, then to bent-conical, and finally to bend inverted conical. This is because the

radial growth rate is around 30-40 times smaller than axial growth rate. The NWs tip diameter and base diameter are too small to be distinguished when the growth duration is short. After the Sn catalyst gets exhausted, sidewall growth rate at the tip is higher than at the base, and the tip diameter can catch up to and eventually exceed the base diameter. The asymmetric stress induced by asymmetric a-Si:H deposition on the upper and lower face of the NW bends them. We show that at the beginning of the growth, the NW is single crystalline. The sidewall growth firstly results in a few nm to a few tens of nm of defective epitaxial growth before the development of an amorphous Si coating. These observations allow us to propose a full picture of the plasma assisted VLS growth process, as has never been done to our knowledge.

### 3.3.3 Hexagonal diamond crystalline SiNW

In the periodic table, Si is the element ranks $14^{th}$ with an atomic number of 14. This means the Si atom has 14 protons and 14 electrons, as shown in figure 3.23 a). The 14 electrons have a $1s^2 2s^2 2p^6 3s^2 3p^2$ configuration. In order to form a solid phase with Si atoms, Si atoms need to have a fixed relationship between each other. Here the relationship means the distance between atoms, since the distance determines the force exerted on each other's electrons and nuclei. The distance between all the atoms determines the 3D configuration of the atoms array. Because all the Si atoms are identical and have same way to interact with each other, they tend to form a periodic array which is also called crystalline structure at equilibrium. Si atoms can form many types of crystalline structures[65-70], such as Si II, Si III, Si V, SiIX[63]. However, naturally Si tends to form a diamond cubic crystalline structure. This is determined by the Si atom electron configuration. There are 4 available states in the $3s^2$ and $3p^2$ orbitals of the Si atom. 4 covalent bonds have to be formed for a Si atom to have a stable state. Then $sp^3$ hybridized orbitals will be formed. The $sp^3$ hybridized orbitals have a tetrahedral geometry, thus 5 Si atoms will bonded together to form a tetrahedron, as shown in figure 3.23 b). This tetrahedral structure will be the basic building block of crystalline Si for the $sp^3$ hybridized Si atoms. In order to maximize the distance between the atoms and minimize the system energy, there is a 180° rotation between the two tetrahedrons when they are bonded together. As shown in figure 3.23 c), the three B atoms and two A atoms form one tetrahedron, while the three C atoms and two A atoms form another tetrahedron. It can be seen that the C atoms rotate 180° with respect to B atoms. The diamond cubic crystalline structure can be formed when this rotation occurs between all the tetrahedrons. However, there are other possibilities to form crystalline phase while keeping the tetrahedron basic building block. For example, in figure 3.23 d), the tetrahedron does not rotate along AA direction. This will end up with a 2-hexagonal (2H) crystalline Si structure. Periodically mixing the rotation in AA direction will lead to some other diamond polytypes[64].

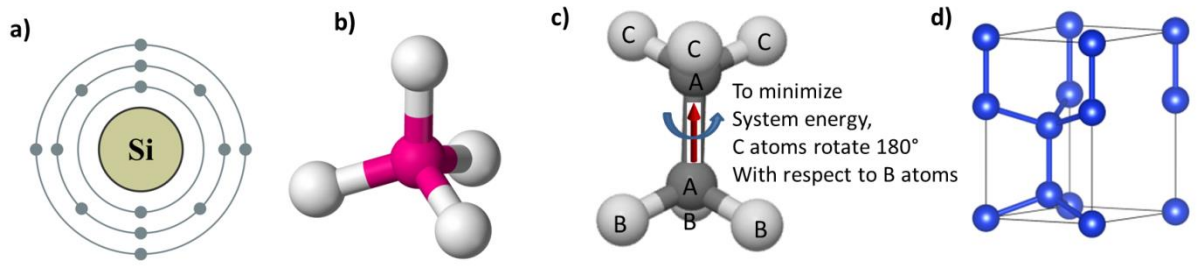


Figure 3.23. a) Si atom with electron orbitals. b) A tetrahedron formed by 5 Si atoms. c) Two tetrahedrons formed by 8 Si atoms, they share the two A atoms. The positions of the C atoms rotate 180° along AA axis with respect to B atoms. d) Similar structure with c), but there is no 180° rotation along AA axis.

The difference of the atom arrangement between 2H Si and diamond cubic Si can be seen directly from $[11\text{-}20]_H/[110]_C$ zone axis. Figures 3.24 a) and b) show the atomic arrangement in this view direction of the diamond cubic Si and 2H Si, respectively. This image is obtained with the crystallography software Vesta[64]. In figure 3.24 a), the two atoms motif which has been highlighted by red boxes has a translational symmetry. While in figure 3.24 b), the two atoms motif has a mirror symmetry. In real material, such a difference between the two crystalline phase can be revealed by TEM observation from $[11\text{-}20]_H/[110]_C$ zone axis.

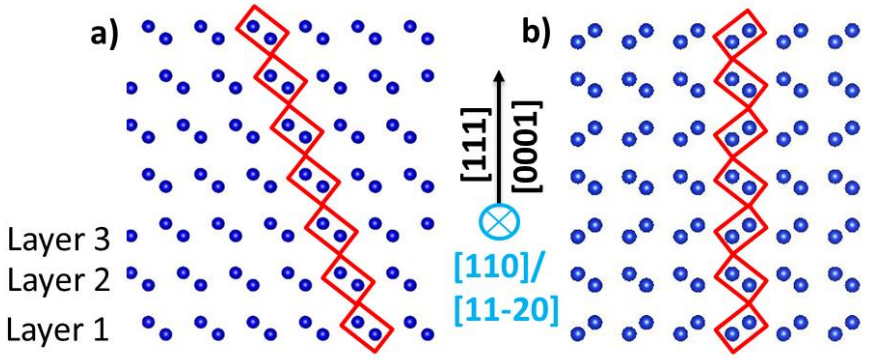


Figure 3.24. a) 110/11-20 direction view of diamond cubic crystalline Si. b) 11-20 direction view of 2-hexagonal crystalline Si.

The existence of a 2H crystalline Si structure in bulk material has been reported since 1963 by Wentorf et al[65]. In their study, the 2H phase is formed by applying a series of high pressure (~15 to 16 GPa) and high temperature (200°C to 1000°C) treatments to diamond cubic crystalline Si. Hexagonal Si possesses novel properties compared with diamond cubic silicon, such as a smaller band gap that would become direct in nanowires[66] or under strain[67]. In the literature, theoretical studies can be found on the hexagonal Si phase[68-71], but only few experimental evidence on it[72]. For silicon nanowires (SiNWs), it is reported that under some specific conditions hexagonal phase can be formed. For example small segments of hexagonal phase can be formed by applying stress treatment after the growth[73], and hexagonal phase Si shell can be achieved by epitaxially growing a c-Si shell on a hexagonal gallium phosphide NW core[74,75]. There are also works reporting showing that hexagonal phase SiNWs can be grown directly[56,76-79]. However, the proofs in these reports are given by

transmission electron microscopy (TEM) analysis carried out in zone axis where it is very difficult to differentiate the hexagonal Si from diamond cubic Si multiple twinning[72,80].

For example, the SiNW shown in figure 3.25 a) has been characterized by TEM both from 111 direction and 110 direction. In figure 3.25 b), the high resolution image shows that the atoms have an inter plane distance of 3.3Å. This is the value of the inter-plane distance of 10-10 planes in 2H structure. The atoms also have a hexagon pattern. One might think that this high resolution TEM image shows a 2H Si structure. However, the diffraction pattern obtained in this direction shows that the 10-10 dots have a much lower intensity than the 222 dots. This will not happen for a real 2H Si. The reason can be revealed from the 110 direction TEM characterization. As can be seen in the figure 3.25 d), the high resolution image obtained from 110 direction shows that the NW has a diamond cubic structure with multi twinning. Figure 3.25 e) shows the diffraction pattern obtained from this direction. The white line corresponds to the 111 reciprocal plane. It can be seen that the 10-10 dots shown in figure 3.25 c) are the 1/3 of 4-22 twin reflection.

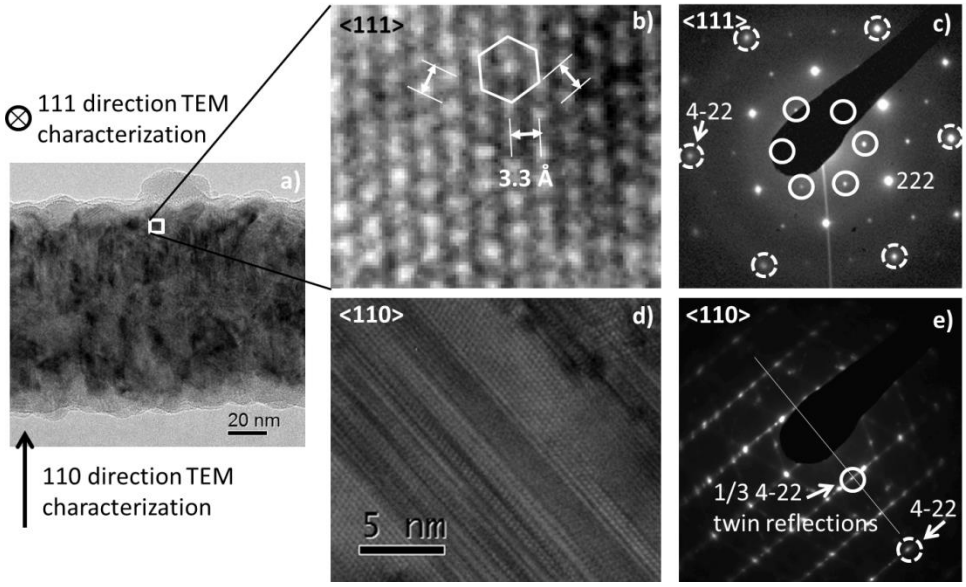


Figure 3.25. TEM characterization of a SiNW both from 111 direction and 110 directions. a) TEM bright field image of the NW. b) 111 direction high resolution image of the region indicated in a). c) Diffraction image obtained from 111 direction; d) 110 direction high resolution image of the same NW. e) Diffraction image obtained from 110 direction. The white line corresponds to the 111 reciprocal plane.

During the TEM observation of the crystallinity of SiNWs with short growth duration, we have observed the hexagonal phase in the as grown SiNWs. These NWs have undergone the same growth experiment as the NWs described before. The specificity here is that the NWs were grown directly on Cu TEM grid and with a short growth duration ( 2 minutes). Such a specific substrate is due to the fact that the NWs with short growth duration have small length, thus it is difficult to transfer them to TEM grid. So we have grown the SiNWs on a TEM grid directly. To prepare this sample, firstly, we have fixed a Cu grid on ZnO:Al coated Corning glass by Silver paste. Then 1 nm of Sn catalyst is deposited on it by thermal evaporation. After that, the substrate is loaded into a standard PECVD reactor to perform the SiNWs growth. During the growth, the gas pressure, substrate temperature, RF plasma power density and growth duration were 133 Pa, 400°C, 17 mW/cm$^2$ and 2 minutes,

respectively. The schematic of the growth experiment is shown in figure 3.26 a). More detailed information on the growth processes can be found in section 3.2.3. After the growth, the sample was firstly analyzed by scanning electron microscopy (SEM). Then the Cu TEM grid was removed from the substrate and loaded into a TEM setup for observations with atomic resolution.

Figure 3.26 b) shows the images of the substrate before the growth. In the center, it is a Cu TEM grid which has been fixed on a ZnO:Al coated Corning glass substrate by silver paste. Figure 3.26 c) to g) shows SEM images of different areas of the sample after the SiNWs growth. The SiNWs have been grown both on the sidewall of the Cu TEM grid and on the ZnO:Al surface, as shown in figures 3.26 e) to g). These SiNWs have a length around 100 to 200 nm, and a diameter around 5 to 15 nm. The NWs grown on the Cu TEM grid have smaller diameter and smaller density than the NWs grown on the ZnO:Al surface. All the observed hexagonal SiNWs were grown on the Cu TEM grid.

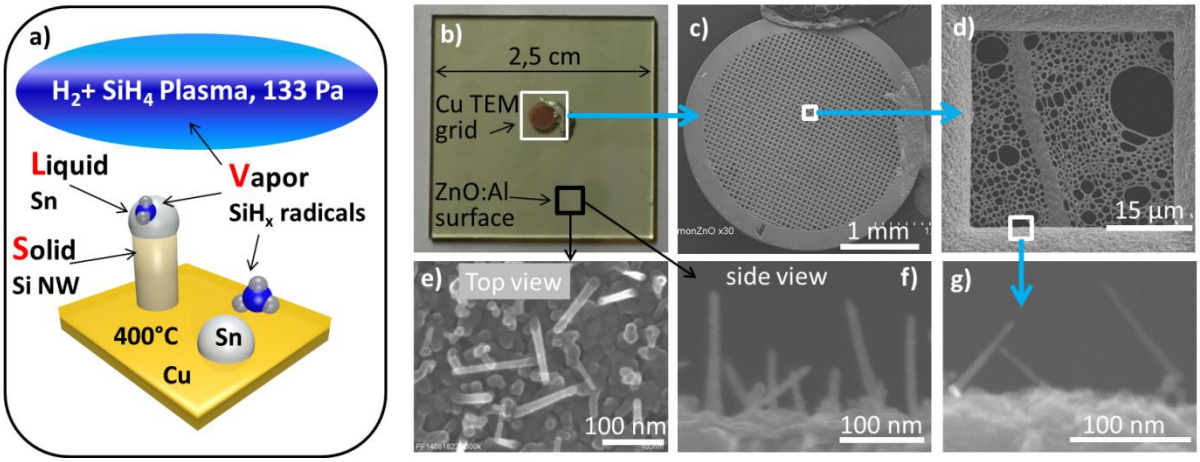


Figure 3.26. SiNWs grown by Plasma-assisted VLS method. a) Schematic of the growth process. b) Image of the substrate before the SiNWs growth experiment. In the center is the Cu TEM grid fixed by Silver paste. c) to g) SEM images of different areas after the growth: c) and d) TEM grid; e) and f) top view and side view of SiNWs grown on ZnO:Al substrate, respectively; g) SiNWs grown on the sidewall of the Cu TEM grid.

Since the NWs have been grown on the Cu TEM grid, there is a possibility that they are catalyzed by Cu. In order to check the chemical nature of the tip of the NW, we have carried out an electron energy loss spectroscopy (EELS) analysis on the NWs grown on TEM grids. Figure 3.27 a) shows a bright field TEM image of a NW grown on TEM grid. The expected darkness contrast of metal tip and SiNW cannot be seen. This might due to the fact that Sn droplets have been oxidized during the exposure to air. In fact, there is still a small dark dot in the tip, as indicated by the arrow. This kind of dots is frequently observed on the tip of these NWs, as shown in the inset the tip of another NW from the same sample. This might be the Sn nanoparticles which have not got oxidized. Figure 3.27 b) and c) are filtered images recorded using electrons before the Sn N4,5 edge and after that edge, respectively. In figure 3.27 b), electrons that participate in image formation have lost energy essentially on silicon plasmon. In figure 3.27 c), they have additionally lost energy on N4,5 (4d) Sn core electrons. From figure 3.27 b) to c), there is a strong increase of signal intensity of Sn at the top of nanowire. This indicates that the top of nanowire is Sn rich.

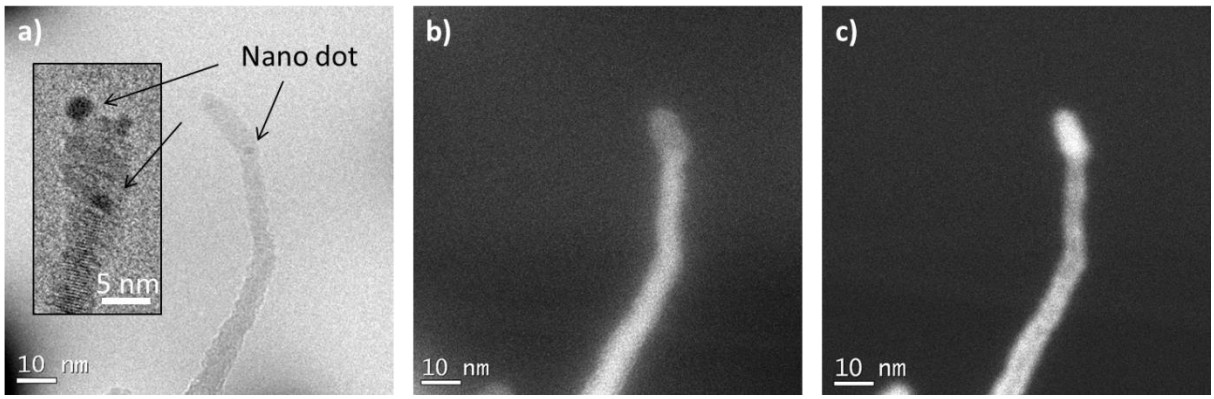


Figure 3.27. TEM images of a nanowire at different acquisition modes: a) bright field image, the inset shows the tip of another NW from the same sample; b) energy-filtered Sn map pre-edge; c) energy-filtered Sn map post-edge.

A high resolution TEM image (HRTEM) of a hexagonal SiNW grown on the Cu TEM grid is shown in figure 3.28 a). In order to strengthen this direct evidence, HRTEM simulations were carried out using the JEMS package[81]. The best fit between the experimental and simulated images was obtained with a defocus of 60 nm (Scherzer defocus was 54 nm); the thickness was taken approximately equal to the crystalline SiNW core diameter: 4.6 nm. In this case, each dark dot corresponds to 2 columns of Si atoms, as shown on the simulated images (figures 3.28 c) and 3.28 e)) where each red dot stands for a column of Si atoms. The enlarged figure 3.28b shows the top part of this NW. It can be seen that the dark dots have a translational symmetry with a periodicity of 6 along the vertical direction. This is a 6H polytype, and it has a good agreement with the simulated 6H Si structure shown in figure 3.28 c). The enlarged figure 3.28 d) shows the bottom part of this NW, it can be seen that the dark dots are almost aligned in the vertical direction. In fact these dots have a translational symmetry with a periodicity of 2 along the vertical direction, that is a 2H polytype (Lonsdaleite)[82], and it has a good agreement with the simulated 2H structure shown in figure 3.28 e). The amorphous contrast at the NW surface indicates the presence of an oxide shell. The Fast Fourier Transform (FFT) of the image in figure 3.28 a) and the micro diffraction pattern of the NW are shown in figures 3.28 f) and 3.28 g), respectively. Both of the patterns have a good match with the summation of the FFT of 6H pattern and 2H pattern, which are shown in figures 3.28 h) and 3.28 i). Meanwhile, in figure 3.28 g) the 0002 spot may also be indexed in terms of diamond cubic silicon pattern. But the fact that no other cubic spot is present indicates that the NW phase is essentially hexagonal.

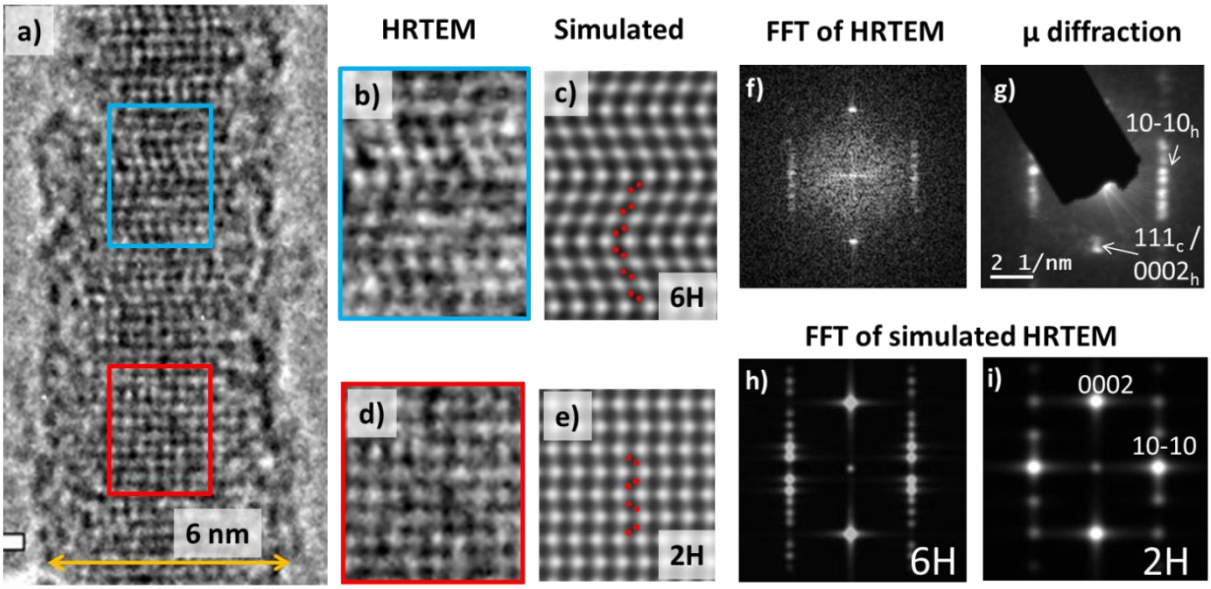


Figure 3.28. TEM characterization results of a hexagonal SiNW. a) High resolution TEM images of the SiNWs in a $[11\text{-}20]_H/[110]_C$ zone axis. b) and d) are the zoom of the indicated area. c) and e) are simulated 6H and 2H Si HRTEM image, respectively. f) FFT of the HRTEM image shown in a). g) Micro diffraction pattern of the NW in a). h) FFT of the simulated 6H Si HRTEM image. i) FFT of the simulated 2H Si HRTEM image.

Pure 2H SiNWs have also been observed in the other SiNWs grown in the same batch. Figure 3.29 shows a NW (~5 nm in diameter) with 90° change in the growth direction. The HRTEM image of the bottom part of this NW is shown in figure 3.29 a), with the corresponding FFT shown in the inset. Both the HRTEM image and the FFT pattern show that NW has a 2H arrangement. The NW growth direction has changed from [0001] to [10-10] without inducing crystalline defects. In figure 3.29 b), the FFT of the middle and top part of the NW are shown in the insets. Even if these FFT patterns are less clear than that of the bottom part of the NW, they all have a similar pattern. This indicates that the whole NW has 2H Si phase.

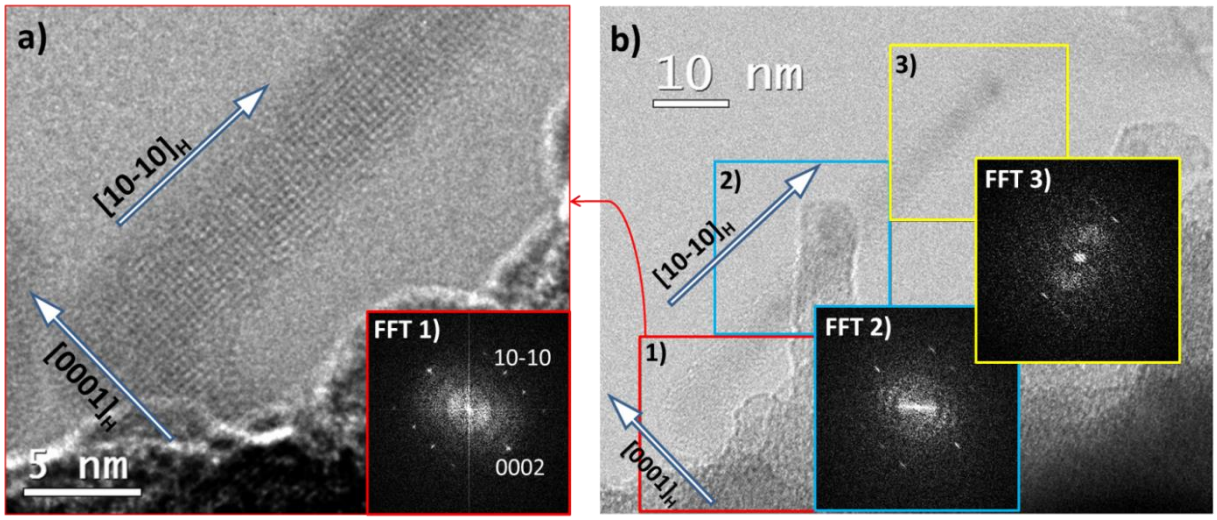


Figure 3.29. HRTEM images of a pure phase 2H SiNW. a) The bottom part of this NW, with the FFT of this image shown in the inset. b) Full view of the NW; the two insets are the FFT of the indicated regions.

The 2H phase can be formed by changing the crystalline phase during the growth. An example is given in figure 3.30 where the NW has a diamond cubic phase at its bottom part and a 2H phase at top part. In the cubic part, there is a twin plane, as shown in the schematic on the right. The first layer of the 2H part also has a twin relation with the cubic part. Probably due to the presence of a dislocation on the left-hand part of the bend, there is a small rotation of the 2H growth axis after the twinning. The rotation is clockwise and has an angle around 3°. The switch from diamond cubic phase to hexagonal phase would indicate that the 2H phase would be energetically favoured in the present growth conditions.

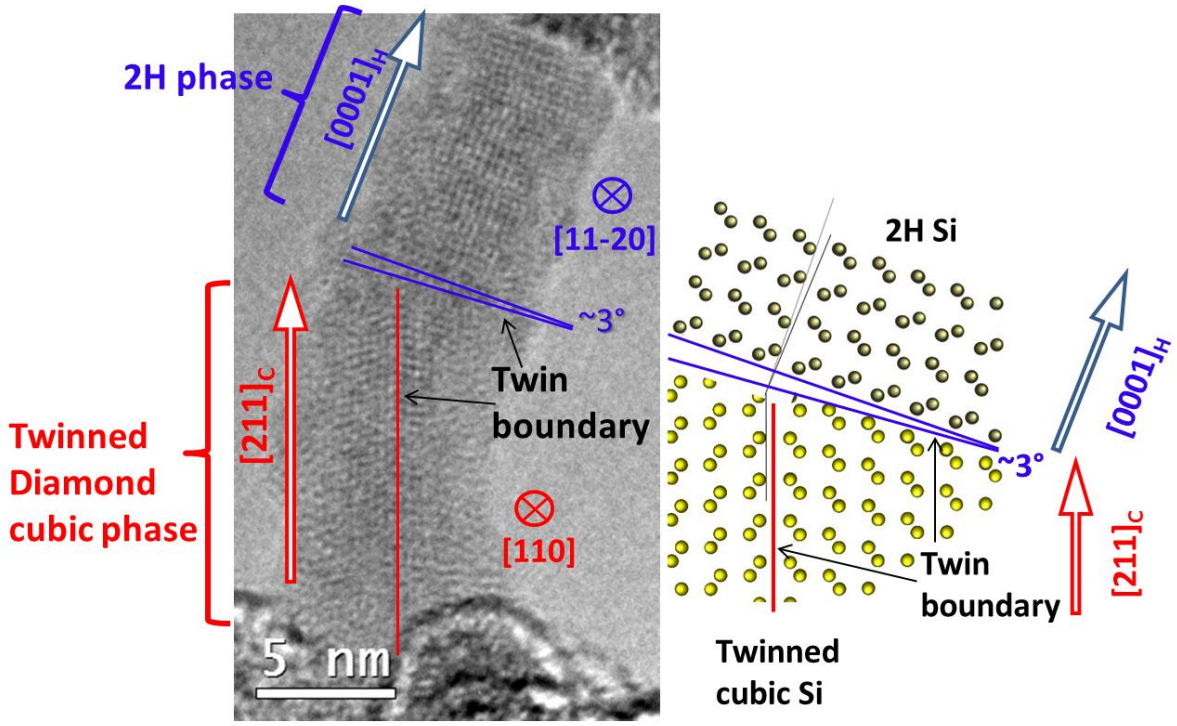


Figure 3.30. Switch from a twinned cubic phase to the 2H phase, associated with a change of growth direction. The schematic shows that the relationship between the two phases is close to epitaxial.

In order to study the stability of the hexagonal SiNWs, we have kept the SiNW sample in standard ambient temperature and pressure for 5 months before further TEM observation. Figure 3.31a shows the TEM image of such a SiNW. This NW has a diameter around 8 nm at base and a length around 90 nm. The enlarged figure 3.31b shows the crystallinity of the NW. It can be seen that there is thick (~2 nm) amorphous SiOx developed at the surface of this NW, and the core part has a 2H crystalline phase. We suggest that the 2H phase in such thin nanowires is stable under standard atmosphere condition.

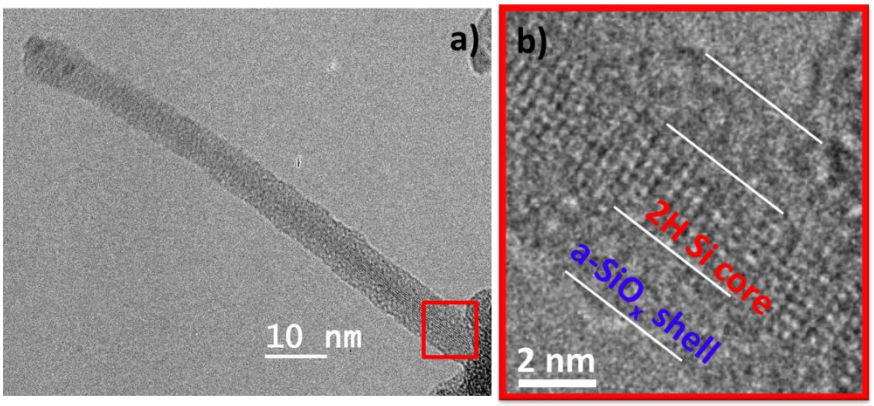


Figure 3.31. Hexagonal SiNW which has been kept in ambient air for 3 months.

After acquiring the HRTEM image of the NW in figure 3.31, the temperature of the TEM grid holder has been increased to anneal the NW and determine the temperature up to which the 2H phase is stable. The temperature increasing profile is shown in figure 3.32 f). Figure 3.32 a) shows the NW after 30 minutes of annealing at 230°C. This is the same NW as the one shown in figure 3.31. The NW has started to bend; however, an FFT of the image shown in figure 3.32 b) still reveals the presence of hexagonal spots, indicating that the phase is stable up to that temperature. Unfortunately, the [1-210] zone axis is lost after further bending due to annealing, which stops further observation of the phase. When the temperature is increased to 700 C, defocus is used so that the core of the NW is darker than the shell (figure 3.32 d). 5 minutes later, as shown in figure 3.32 e), the long and continuous NW core splits into two droplets which have a diameter around 4 nm inside the SiOx shell. This phenomenon is similar to a Plateau-Rayleigh instability[83,84] of water, where a column of water breaks apart into droplets to lower its surface tension. So here we presume that shrinking of the core indicates the melting. It is known that the melting point for bulk crystalline Si is 1414°C. Here the crystalline core would melt at 700°C. As the core diameter is around 3 nm, the present decrease of the melting temperature is consistent with that observed on Si nanoparticles of similar diameter[85]. Another reasons might be the fact that the NW keeps its 2H phase upon annealing and that the latter would have a melting point below that of the cubic phase, or the presence of Sn in the nanowires[86] , and the presence of the electron beam, could further help to decrease the melting temperature. After the melting of the NW core, the amorphous a-SiOx shell around the NW remains in solid phase. It confines the liquid Si inside the tube and leads to the formation of a chain of Si dots inside the tube. Since the a-SiOx has a much higher bandgap than c-Si, this will enhance the confinement effects in the Si quantum dots.

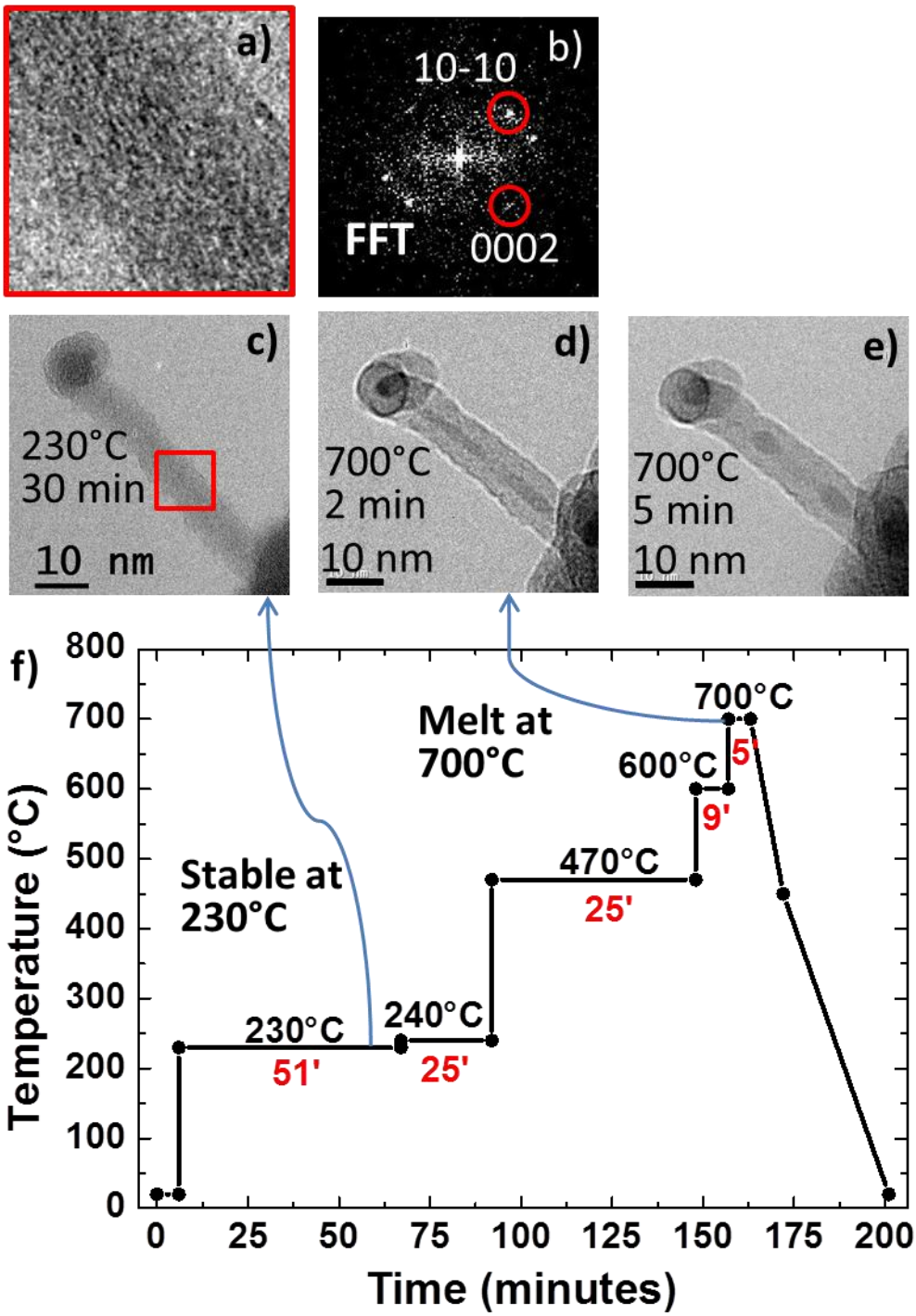


Figure 3.32. a)-c) TEM image of the NW at different temperatures: a) at 470°C; b), after 2 minutes of annealing at 700°C; and c) after 5 minutes of annealing at 700°C. d) The temperature profile during the annealing.

The most possible reason for the formation of 2H Si phase in our case is the size effect. Due to the small diameter, the surface to volume ratio of the NWs has a large value. Thus, the surface tension from the sidewalls becomes significant and will exert a strong anisotropic stress on the NW that could somehow mimic the cases where anisotropic stress is at the origin of the formation of this phase. Another reason might be the kinetic effects during growth. As the 2H polytype was shown to

form kinetically in GaAs NWs[87], it could form in the same way in in SiNWs. However, this mechanism could deliver 2H structure in large III-V NWs but not in SiNWs.

To summarize this section, we have presented TEM recordings in the $[110]_C/[1\text{-}210]_H$ zone axis of VLS grown silicon nanowires that cannot be interpreted in terms of cubic stacking. Those are the first unambiguous TEM observations of the hexagonal Si phase in as grown SiNWs to our knowledge. These nanowires differ from those usually studied essentially by their small diameter (~5 nm). The hexagonal structure appears to be stable: over time in standard ambient temperature and pressure, and upon annealing at 230 °C for at least 30 minutes.

## 3.4 Summary

In this chapter, we have focused on the experimental study of plasma-assisted VLS SiNW growth process. Sn catalyst droplets engineering experiments have been conducted. We found that with annealing, the droplets exhibit small changes in their size and density. However, when annealing is conducted with the presence of a thin a-Si:H layer, there are moderate changes of droplet size and density; with $H_2$ plasma treatment, the size and density of the droplets can be changed significantly.

A comprehensive observation and analysis of the plasma assisted VLS SiNW growth process has been carried out. For the first time, the initial growth stage, which determines the NW density, growth direction and crystalline core size, has been studied step by step. We give a direct evidence of a strong coalescence of catalyst droplets due to the formation of SiNWs within the first 10 seconds of growth. Moreover we have provided a systematic characterization and detailed explanation of the strong evolution of catalyst density and NW density, NW morphology and crystallinity during SiNW growth process.

We found that the small diameter SiNWs grown on Cu substrate have a hexagonal diamond crystalline phase. TEM characterizations in the [11-20] zone axis provide a clear evidence of a hexagonal atomic arrangement. The hexagonal structure appears to be stable: over time in standard ambient temperature and pressure, and upon annealing at 230 °C.

## References


1 Baughman, R. H., Zakhidov, A. A. & de Heer, W. A. Carbon nanotubes - the route toward applications. *Science* **297**, 787-792, doi:10.1126/science.1060928 (2002).

2 Eichenfield, M., Camacho, R., Chan, J., Vahala, K. J. & Painter, O. A picogram- and nanometre-scale photonic-crystal optomechanical cavity. *Nature* **459**, 550-U579, doi:10.1038/nature08061 (2009).

3 Huang, M. H. *et al.* Room-temperature ultraviolet nanowire nanolasers. *Science* **292**, 1897-1899, doi:10.1126/science.1060367 (2001).

4 Heiss, M. *et al.* Self-assembled quantum dots in a nanowire system for quantum photonics. *Nat Mater* **12**, 439-444, doi:10.1038/nmat3557 (2013).

5 Wong, E. W., Sheehan, P. E. & Lieber, C. M. Nanobeam Mechanics: Elasticity, Strength, and Toughness of Nanorods and Nanotubes. *Science* **277**, 1971-1975, doi:10.1126/science.277.5334.1971 (1997).

6 Michalet, X. *et al.* Quantum dots for live cells, in vivo imaging, and diagnostics. *Science* **307**, 538-544, doi:10.1126/science.1104274 (2005).

7 Zhong, Z. H., Fang, Y., Lu, W. & Lieber, C. M. Coherent single charge transport in molecular-scale silicon nanowires. *Nano Lett* **5**, 1143-1146, doi:10.1021/nl050783s (2005).

8 Parkin, S. S. P., Hayashi, M. & Thomas, L. Magnetic domain-wall racetrack memory. *Science* **320**, 190-194, doi:10.1126/science.1145799 (2008).

9 Cui, Y., Wei, Q. Q., Park, H. K. & Lieber, C. M. Nanowire nanosensors for highly sensitive and selective detection of biological and chemical species. *Science* **293**, 1289-1292, doi:10.1126/science.1062711 (2001).

10 Vardi, A. *et al.* Room temperature demonstration of GaN/AlN quantum dot intraband infrared photodetector at fiber-optics communication wavelength. *Appl Phys Lett* **88**, 143101, doi:http://dx.doi.org/10.1063/1.2186108 (2006).

11 Law, M., Greene, L. E., Johnson, J. C., Saykally, R. & Yang, P. D. Nanowire dye-sensitized solar cells. *Nat Mater* **4**, 455-459, doi:10.1038/nmat1387 (2005).

12 Kempa, T. J. & Lieber, C. M. Semiconductor nanowire solar cells: synthetic advances and tunable properties. *Pure Appl Chem* **86**, 13-26, doi:10.1515/pac-2014-5010 (2014).

13 Tanabe, K., Fontcuberta i Morral, A., Aiken, D. J. & Wanlass, M. W. Direct-bonded GaAs/InGaAs tandem solar cell. *Appl Phys Lett* **89**, 102106, doi:http://dx.doi.org/10.1063/1.2347280 (2006).

14 Misra, S., Yu, L., Foldyna, M. & Roca i Cabarrocas, P. High efficiency and stable hydrogenated amorphous silicon radial junction solar cells built on VLS-grown silicon nanowires. *Sol Energ Mat Sol C* **118**, 90-95, doi:10.1016/j.solmat.2013.07.036 (2013).

15 Krogstrup, P. *et al.* Single-nanowire solar cells beyond the Shockley-Queisser limit. *Nat Photon* **7**, 306-310 (2013).

16 Huang, J. Y. *et al.* In Situ Observation of the Electrochemical Lithiation of a Single SnO2 Nanowire Electrode. *Science* **330**, 1515-1520, doi:10.1126/science.1195628 (2010).

17 Laik, B. *et al.* Silicon nanowires as negative electrode for lithium-ion microbatteries. *Electrochim Acta* **53**, 5528-5532, doi:10.1016/j.electacta.2008.02.114 (2008).

18 Song, H. *et al.* Hierarchical nano-branched c-Si/SnO2 nanowires for high areal capacity and stable lithium-ion battery. *Nano Energy* **19**, 511-521, doi:http://dx.doi.org/10.1016/j.nanoen.2015.10.031 (2016).

19 Schmidt, V., Wittemann, J. V., Senz, S. & Gosele, U. Silicon Nanowires: A Review on Aspects of their Growth and their Electrical Properties. *Advanced Materials* **21**, 2681-2702, doi:10.1002/adma.200803754 (2009).

20 Wagner, R. S. & Ellis, W. C. VAPOR‐LIQUID‐SOLID MECHANISM OF SINGLE CRYSTAL GROWTH. *Appl Phys Lett* **4**, 89-90, doi:doi:http://dx.doi.org/10.1063/1.1753975 (1964).

21 Dasgupta, N. P. *et al.* 25th Anniversary Article: Semiconductor Nanowires Synthesis, Characterization, and Applications. *Advanced Materials* **26**, 2137-2184, doi:10.1002/adma.201305929 (2014).

22 Xia, Y. N. *et al.* One-dimensional nanostructures: Synthesis, characterization, and applications. *Advanced Materials* **15**, 353-389, doi:10.1002/adma.200390087 (2003).

23 Lefeuvre, E. *et al.* Optimization of organized silicon nanowires growth inside porous anodic alumina template using hot wire chemical vapor deposition process. *Thin Solid Films* **519**, 4603-4608, doi:10.1016/j.tsf.2011.01.333 (2011).

24 Xia, Y. N. & Whitesides, G. M. Soft lithography. *Annual Review of Materials Science* **28**, 153-184, doi:10.1146/annurev.matsci.28.1.153 (1998).

25 Xia, Y. N., Rogers, J. A., Paul, K. E. & Whitesides, G. M. Unconventional methods for fabricating and patterning nanostructures. *Chemical Reviews* **99**, 1823-1848, doi:10.1021/cr980002q (1999).

26 Barth, S., Hernandez-Ramirez, F., Holmes, J. D. & Romano-Rodriguez, A. Synthesis and applications of one-dimensional semiconductors. *Progress in Materials Science* **55**, 563-627, doi:10.1016/j.pmatsci.2010.02.001 (2010).

27 Yu, L. *et al.* Bismuth-Catalyzed and Doped Silicon Nanowires for One-Pump-Down Fabrication of Radial Junction Solar Cells. *Nano Lett* **12**, 4153-4158, doi:10.1021/nl3017187 (2012).

28 Zardo, I. *et al.* Growth study of indium-catalyzed silicon nanowires by plasma enhanced chemical vapor deposition. *Applied Physics A* **100**, 287-296, doi:10.1007/s00339-010-5802-1 (2010).

29 Zardo, I. *et al.* Gallium assisted plasma enhanced chemical vapor deposition of silicon nanowires. *Nanotechnology* **20**, 155602 (2009).

30 Yu, L., O'Donnell, B., Alet, P.-J. & Roca i Cabarrocas, P. All-in-situ fabrication and characterization of silicon nanowires on TCO/glass substrates for photovoltaic application. *Sol Energ Mat Sol C* **94**, 1855-1859, doi:http://dx.doi.org/10.1016/j.solmat.2010.06.021 (2010).

31 Linwei, Y. *et al.* Assessing individual radial junction solar cells over millions on VLS-grown silicon nanowires. *Nanotechnology* **24**, 275401 (2013).

32 Xia, Y. *et al.* One-Dimensional Nanostructures: Synthesis, Characterization, and Applications. *Advanced Materials* **15**, 353-389, doi:10.1002/adma.200390087 (2003).

33 Wei, L. & Charles, M. L. Semiconductor nanowires. *Journal of Physics D: Applied Physics* **39**, R387 (2006).

34 Wang, N., Cai, Y. & Zhang, R. Q. Growth of nanowires. *Materials Science and Engineering: R: Reports* **60**, 1-51, doi:http://dx.doi.org/10.1016/j.mser.2008.01.001 (2008).

35 Yu, L., Alet, P. J., Picardi, G., Maurin, I. & Roca i Cabarrocas, P. Synthesis, morphology and compositional evolution of silicon nanowires directly grown on SnO(2) substrates. *Nanotechnology* **19**, 485605, doi:10.1088/0957-4484/19/48/485605 (2008).

36 Rathi, S. J. *et al.* Tin-Catalyzed Plasma-Assisted Growth of Silicon Nanowires. *J Phys Chem C* **115**, 3833-3839, doi:10.1021/jp1066428 (2011).

37 Adachi, M. M., Anantram, M. P. & Karim, K. S. Optical Properties of Crystalline−Amorphous Core−Shell Silicon Nanowires. *Nano Lett* **10**, 4093-4098, doi:10.1021/nl102183x (2010).

38 Parlevliet, D. & Cornish, J. C. L. Silicon Nanowires: Growth Studies Using Pulsed PECVD. *MRS Online Proceedings Library Archive* **989**, 0989-A0923-0903, doi:doi:10.1557/PROC-0989-A23-03 (2007).

39 Misra, S., Yu, L., Chen, W., Foldyna, M. & Roca i Cabarrocas, P. A review on plasma-assisted VLS synthesis of silicon nanowires and radial junction solar cells. *J Phys D: Appl Phys* **47**, 393001, doi:10.1088/0022-3727/47/39/393001 (2014).

40 Al-Taay, H. F., Mahdi, M. A., Parlevliet, D. & Jennings, P. Controlling the diameter of silicon nanowires grown using a tin catalyst. *Mat Sci Semicon Proc* **16**, 15-22, doi:10.1016/j.mssp.2012.07.006 (2013).

41 Misra, S., Yu, L., Chen, W. & Roca i Cabarrocas, P. Wetting Layer: The Key Player in Plasma-Assisted Silicon Nanowire Growth Mediated by Tin. *J Phys Chem C* **117**, 17786-17790, doi:10.1021/jp403063d (2013).

42 Yu, L. *et al.* Plasma-enhanced low temperature growth of silicon nanowires and hierarchical structures by using tin and indium catalysts. *Nanotechnology* **20**, doi:10.1088/0957-4484/20/22/225604 (2009).

43 Sauerbrey, G. Verwendung von Schwingquarzen zur Wägung dünner Schichten und zur Mikrowägung. *Zeitschrift für Physik* **155**, 206-222, doi:10.1007/bf01337937 (1959).

44 Rasband, W. ImageJ.

45 Charpentier, C., Prod'homme, P., Maurin, I., Chaigneau, M. & Roca i Cabarrocas, P. X-Ray diffraction and Raman spectroscopy for a better understanding of ZnO:Al growth process. *EPJ Photovolt* **2**, 25002 (2011).

46 Ng, J. D. *et al.* The crystallization of biological macromolecules from precipitates: evidence for Ostwald ripening. *J Cryst Growth* **168**, 50-62, doi:http://dx.doi.org/10.1016/0022-0248(96)00362-4 (1996).

47 Wronski, C. R. M. The size dependence of the melting point of small particles of tin. *British Journal of Applied Physics* **18**, 1731 (1967).

48 Lai, S. L., Guo, J. Y., Petrova, V., Ramanath, G. & Allen, L. H. Size-Dependent Melting Properties of Small Tin Particles: Nanocalorimetric Measurements. *Physical Review Letters* **77**, 99-102 (1996).

49 Yu, L., Alet, P.-J., Picardi, G. & Roca i Cabarrocas, P. An In-Plane Solid-Liquid-Solid Growth Mode for Self-Avoiding Lateral Silicon Nanowires. *Physical Review Letters* **102**, doi:10.1103/PhysRevLett.102.125501 (2009).

50 Yu, L. & Roca i Cabarrocas, P. Growth mechanism and dynamics of in-plane solid-liquid-solid silicon nanowires. *Phys Rev B* **81**, doi:10.1103/PhysRevB.81.085323 (2010).

51 O'Donnell, B. Plasma grown Silicon Nanowires catalyzed by post-transition metals. (2012).

52 Kalache, B., Roca i Cabarrocas, P. & Fontcuberta i Morral, A. Observation of incubation times in the nucleation of silicon nanowires obtained by the vapor-liquid-solid method. *Jpn J Appl Phys 2* **45**, L190-L193, doi:10.1143/Jjap.45.L190 (2006).

53 Olesinski, R. W. & Abbaschian, G. J. The Si–Sn (Silicon–Tin) system. *BULL APD* **5**, 273-276, doi:10.1007/bf02868552 (1984).

54 Hannon, J. B., Kodambaka, S., Ross, F. M. & Tromp, R. M. The influence of the surface migration of gold on the growth of silicon nanowires. *Nature* **440**, 69-71, doi:10.1038/nature04574 (2006).

55 Tan, T. Y., Foll, H. & Hu, S. M. On the Diamond-Cubic to Hexagonal Phase-Transformation in Silicon. *Philos Mag A* **44**, 127-140 (1981).

56 Fontcuberta i Morral, A., Arbiol, J., Prades, J. D., Cirera, A. & Morante, J. R. Synthesis of Silicon Nanowires with Wurtzite Crystalline Structure by Using Standard Chemical Vapor Deposition. *Advanced Materials* **19**, 1347-1351, doi:10.1002/adma.200602318 (2007).

57 Xiang, Y. *et al.* Single crystalline and core-shell indium-catalyzed germanium nanowires-a systematic thermal CVD growth study. *Nanotechnology* **20**, doi:10.1088/0957-4484/20/24/245608 (2009).

58 Roca i Cabarrocas, P., Cariou, R. & Labrune, M. Low temperature plasma deposition of silicon thin films: From amorphous to crystalline. *J Non-Cryst Solids* **358**, 2000-2003, doi:10.1016/j.jnoncrysol.2011.12.113 (2012).

59 Yu, L., O'Donnell, B., Maurice, J. L. & Roca i Cabarrocas, P. Core-shell structure and unique faceting of Sn-catalyzed silicon nanowires. *Appl Phys Lett* **97**, 023107, doi:http://dx.doi.org/10.1063/1.3464557 (2010).

60 Campbell, I. H. & Fauchet, P. M. The Effects of Microcrystal Size and Shape on the One Phonon Raman-Spectra of Crystalline Semiconductors. *Solid State Commun* **58**, 739-741, doi:Doi 10.1016/0038-1098(86)90513-2 (1986).

61 Wang, R. P. *et al.* Raman spectral study of silicon nanowires: High-order scattering and phonon confinement effects. *Phys Rev B* **61**, 16827-16832, doi:DOI 10.1103/PhysRevB.61.16827 (2000).

62 Paik, S. T. Is the mean free path the mean of a distribution? *Am J Phys* **82**, 602-608, doi:10.1119/1.4869185 (2014).

63 McMahon, M. I. & Nelmes, R. J. New high-pressure phase of Si. *Phys Rev B* **47**, 8337-8340 (1993).

64 Wen, B., Zhao, J., Bucknum, M. J., Yao, P. & Li, T. First-principles studies of diamond polytypes. *Diamond and Related Materials* **17**, 356-364, doi:http://dx.doi.org/10.1016/j.diamond.2008.01.020 (2008).

65 Wentorf, R. H. & Kasper, J. S. Two New Forms of Silicon. *Science* **139**, 338-339, doi:10.1126/science.139.3552.338-a (1963).

66 Amato, M., Kaewmaraya, T., Zobelli, A., Palummo, M. & Rurali, R. Crystal Phase Effects in Si Nanowire Polytypes and Their Homojunctions. *Nano Letters* **16**, 5694-5700, doi:10.1021/acs.nanolett.6b02362 (2016).

67 Rödl, C. *et al.* Wurtzite silicon as a potential absorber in photovoltaics: Tailoring the optical absorption by applying strain. *Phys Rev B* **92**, 045207 (2015).

68 Mullner, P. & Pirouz, P. A disclination model for the twin-twin intersection and the formation of diamond-hexagonal silicon and germanium. *Materials Science and Engineering a-Structural Materials Properties Microstructure and Processing* **233**, 139-144, doi:10.1016/s0921-5093(97)00058-0 (1997).

69 Garcia-Castello, N., Prades, J. D., Orlando, R. & Cirera, A. Stability Model of Silicon Nanowire Polymorphs and First-Principle Conductivity of Bulk Silicon. *J Phys Chem C* **116**, 22078-22085, doi:10.1021/jp307449y (2012).

70 Wang, S. Q. & Ye, H. Q. Ab initio elastic constants for the lonsdaleite phases of C, Si and Ge. *Journal of Physics-Condensed Matter* **15**, 5307-5314, doi:10.1088/0953-8984/15/30/312 (2003).

71 Zhang, D. B., Hua, M. & Dumitrica, T. Stability of polycrystalline and wurtzite Si nanowires via symmetry-adapted tight-binding objective molecular dynamics. *Journal of Chemical Physics* **128**, doi:10.1063/1.2837826 (2008).

72 Cayron, C. *et al.* Odd electron diffraction patterns in silicon nanowires and silicon thin films explained by microtwins and nanotwins. *Journal of Applied Crystallography* **42**, 242-252, doi:10.1107/s0021889808042131 (2009).

73 Qiu, Y. *et al.* Epitaxial diamond-hexagonal silicon nano-ribbon growth on (001) silicon. *Scientific Reports* **5**, 12692, doi:10.1038/srep12692 (2015).

74 Hauge, H. I. T. *et al.* Hexagonal Silicon Realized. *Nano Letters* **15**, 5855-5860, doi:10.1021/acs.nanolett.5b01939 (2015).

75 Hauge, H. I. T., Conesa-Boj, S., Verheijen, M. A., Koelling, S. & Bakkers, E. P. A. M. Single-Crystalline Hexagonal Silicon–Germanium. *Nano Letters*, doi:10.1021/acs.nanolett.6b03488 (2016).

76 Miyamoto, Y. & Hirata, M. Polytypism and Amorphousness in Silicon Whiskers. *Journal of the Physical Society of Japan* **44**, 181-190, doi:10.1143/JPSJ.44.181 (1978).

77 Prades, J. D., Arbiol, J., Cirera, A., Morante, J. R. & Morral, A. F. i. Concerning the 506 cm(-1) band in the Raman spectrum of silicon nanowires. *Appl Phys Lett* **91**, doi:10.1063/1.2786606 (2007).

78 Fabbri, F., Rotunno, E., Lazzarini, L., Fukata, N. & Salviati, G. Visible and Infra-red Light Emission in Boron-Doped Wurtzite Silicon Nanowires. *Scientific Reports* **4**, 3603, doi:10.1038/srep03603 (2014).

79 Arbiol, J., Kalache, B., Cabarrocas, P. R. I., Morante, J. R. & Morral, A. F. I. Influence of Cu as a catalyst on the properties of silicon nanowires synthesized by the vapour-solid-solid mechanism. *Nanotechnology* **18**, 8, doi:10.1088/0957-4484/18/30/305606 (2007).

80 Pashley, D. W., Stowell, M. J. & Law, T. J. The Crystal Structure of Evaporated Gold Films. *physica status solidi (b)* **10**, 153-163, doi:10.1002/pssb.19650100115 (1965).

81 Stadelmann, P. Stadelmann, P. JEMS-Saas. (2014).

82 Weill, G., Mansot, J. L., Sagon, G., Carlone, C. & Besson, J. M. CHARACTERIZATION OF SI-III AND SI-IV, METASTABLE FORMS OF SILICON AT AMBIENT PRESSURE. *Semiconductor Science and Technology* **4**, 280-282, doi:10.1088/0268-1242/4/4/029 (1989).

83 Day, R. W. *et al.* Plateau–Rayleigh crystal growth of periodic shells on one-dimensional substrates. *Nat Nano* **10**, 345-352, doi:10.1038/nnano.2015.23 (2015).

84 Xue, Z. *et al.* Engineering island-chain silicon nanowires via a droplet mediated Plateau-Rayleigh transformation. *Nature Communications* **7**, doi:10.1038/ncomms12836 (2016).

85 Goldstein, A. N. The melting of silicon nanocrystals: Submicron thin-film structures derived from nanocrystal precursors. *Appl. Phys. A-Mater. Sci. Process.* **62**, 33-37, doi:10.1007/bf01568084 (1996).

86 Chen, W. *et al.* Incorporation and redistribution of impurities into silicon nanowires during metal-particle-assisted growth. *Nature Communications* **5**, doi:10.1038/ncomms5134 (2014).

87 Glas, F., Harmand, J.-C. & Patriarche, G. Why Does Wurtzite Form in Nanowires of III-V Zinc Blende Semiconductors? *Physical Review Letters* **99**, 146101 (2007).

# Chapter 4 SiGeNW and GeNW growth

## Contents

# 4.1 Introduction

## 4.1.1 Why we study SiGeNWs

In the periodic table, Germanium (Ge) is an element in the same column as Silicon (Si). This means the Ge atom has the same outer shell electron number and configuration as Si. This makes Si and Ge to have similar chemical and physical properties including that both of them are semiconductors, and they have same crystalline structure at equilibrium state. The lattice constant of crystalline Si and crystalline Ge differ by 4%, this makes it is easy to alloy Ge into Si while maintaining a pure crystalline phase. Since Si is the fundamental material for the microelectronic industry, the possibility of alloying Ge into Si brings great significance. By alloying with Ge, the properties of Si enjoy several significant improvements such as higher carrier mobility[1], higher absorption coefficient[2] and better lattice match with III-V materials. What's more, SiGe is a material with good tunability. Its properties can be easily tuned by changing the Ge concentration in the material. It also offers a big play ground for solar cell applications. Multi-junction solar cells are the most successful way to achieve high energy conversion efficiency. One of the biggest challenges for multi-junction solar cells is to optimize the sub-cell band gap and to match the photo current generated by each sub-cell. SiGe has a tunable bang gap between 0.67 eV to 1.1 eV. These values are suitable for the bottom cell of the multi-junction solar cells with a sub-cell number ranging roughly from 2 to 6.[3] Due to all these merits, the SiGe material system attracts intense research attention during the past 4 decades.[4,5]

Making SiGe into nanowire structures brings additional advantages. Firstly, the heterojunction structure such as core-shell and axial multi-quantum well structures[6,7] can be realized with Si and Ge system. Secondly, with the increase of Ge concentration from 0 to 100%, the Bohr exciton radius increases from 4.9 nm to 24.3 nm. This makes the prominent quantum confinement effects easier to be observed with SiGeNWs. Thirdly, with bottom up nanowire synthesis techniques, the crystalline SiGe material can be synthesized without requiring expensive crystalline wafer substrates. Lastly, in low dimension nanowire geometry, the strain induced by lattice mismatch can be easily released by elastic deformation.[8]

In our lab, Si NWs have been successfully used to fabricate low cost high efficiency NW solar cells.[9,10] Because the absorption coefficiency of Si is low, the light absorption in the SiNW is negligible. So far, SiNWs have been only used as the electrode and to make the nano-structure in the solar cells. Due to the numerous advantages explained above, SiGe NW and Ge NW have high potential to enhance solar cells performance. However, SiGeNWs have not been used in nanowire radial junction solar cells in the literature yet, as explained in the review article.[11] The purpose of this study is to prepare SiGeNWs with a low cost approach for solar cells applications.

## 4.1.2 The state of the art of the SiGeNW and GeNW synthesis

The synthesis of the single material SiNW, GeNW can be dated to the very beginning of the NW research in 1964.[12] On the contrary, the synthesis of the SiGeNWs is quite recent. They have been firstly synthesized by CVD VLS method in 2000.[13] Since SiGe is a compound material, it is not common to find crystalline SiGe wafers with desired composition, so the SiGeNWs are usually synthesized using a bottom up method.[11,14] Due to the similar chemical properties, Si and Ge usually use similar precursor for bottom up synthesis, such as $SiH_4$ and $GeH_4$. Thus the synthesis method for SiNWs or GeNWs can be also used to synthesis SiGeNWs. These include the chemical vapor deposition (CVD)[15], supercritical fluid-liquid-solid (SFLS)[16], laser ablation[17], molecular beam epitaxy (MBE)[18], and thermal

evaporation[19]. CVD is the dominant synthesis method, and Au is usually used as catalyst. SiGeNWs and GeNWs have been heavily studied, there is a large amount of papers related to SiGeNWs and GeNWs. These papers are dedicated to study the growth[20], characterization[21] and applications[22] of SiGeNWs. However, to the best of our knowledge, very few papers report on the growth with Sn[23] or In catalyst[24]. The merits of Sn and In is that they do not induce deep level electrical defects to the SiGe[25]. This is essential for high performance electronics.[26] Additionally, a sharp Si/Ge heterojunction interface can be achieved due to the low solubility of Si in Sn and In. The disadvantage of Sn and In is that they do not promote or only have a narrow parameter space with the normal synthesis method such as CVD. Plasma-enhanced CVD is an effective way to broaden the parameter space of these two catalysts. However, only one paper which uses plasma enhanced CVD method to grow SiGeNW or GeNW can be found in the literature.[27] In this paper, highly kinked Ge nanorods are obtained with In catalyst. Besides the crystalline defects, the morphology of these nanorods is not suited for solar cells applications. Due to the very limited research been done on plasma-assisted VLS growth of SiGeNWs and GeNWs, there is a vast field to be explored. In this chapter we explore the parameter space for NW growth, to obtain SiGeNWs with Ge concentration varying from 0 to 100%, and optimize the growth conditions to get SiGeNWs with good morphology and density for solar cells applications. Finally we present preliminary studies on the properties of the NWs such as crystallinity and absorption. Since Au and Cu are commonly used as catalyst to synthesize SiGeNWs and GeNWs in the literature, we also use Au and Cu[28] besides In and Sn as catalysts for the purposes of comparison.

## 4.2 SiGeNW and GeNW growth

### 4.2.1 Growth of SiGeNWs at 400°C

Bottom up NW synthesis methods offer the opportunity to change the NW composition by easily tuning the precursor composition. In our plasma-assisted VLS growth reactor, in principle we just need to add the $GeH_4$ gas precursor to $SiH_4$ gas precursor to change the SiNWs into SiGeNWs.

The NW growth procedures have been kept the same as these described at the beginning of chapter 3. The only change is that for the NW growth step, $GeH_4$ gas has been added to the $SiH_4$-$H_2$ gas mixture used for SiNW growth. The $GeH_4$ is 1% diluted in $H_2$. We have fixed the substrate temperature at 400°C and the $H_2$ flow rate to 100 sccm. We have varied the $SiH_4$ and $GeH_4$ flow rates to change the gas flow rate ratio and the total pressure. Besides Sn, In, Cu and Au have also been used as catalysts.

Figure 4.1 shows top view and the side view SEM images of SiGeNWs catalyzed by Au, Cu, Sn and In. All the experimental parameters for these 4 sample are same, including the thickness of the catalyst and the material of the Si wafer substrate. The partial pressure ratio of $GeH_4/(GeH_4+SiH_4)$ in this experiment is 1.96%. It can be seen that the SiGeNWs catalyzed by different catalysts at low $GeH_4/(GeH_4+SiH_4)$ ratio exhibit similar morphology. All the NWs are tapered and have a random growth direction. A detailed statistics of the NW length, NW bottom diameter, NW growth angle and NW tip diameter are shown in figure 4.2. The lines are normal fit of the distribution, and the values of the expectation of the normal distributions are marked with corresponding color. It can be seen that the Au catalyzed NWs have the smallest tip diameter, bottom diameter and length, which are 7 nm, 20 nm and 165 nm, respectively. The Cu and Sn catalyzed NWs have similar tip diameter, bottom diameter and NW length. This indicates that the axial and radial growth rate of the NWs catalyzed by the two metals are similar. Cu and Sn have very different surface energy[29], but in this growth

condition it seems that the surface energy of the catalyst does not influence the morphology of the NWs. Since the sidewall incorporation and diffusion are the mean mechanism which influences the radial growth, the sidewall incorporation and diffusion should be similar for the Cu and Sn. This shows in this particular case (Cu and Sn) the surface energy of the catalyst does not influence the morphology of the NWs in this experiment. In catalyzed NW have much bigger tip diameter, bottom diameter and length than the rest of the NWs. More interestingly, In catalyst droplets usually have a large diameter which can exceed 100 nm; this is much larger than the NW tip diameter. In the inset of figure 4.1 d), the NW has a catalyst droplet with diameter of 128 nm, while the NW tip diameter is only 30 nm. During the growth, the large droplet should have a large contact angle with the small NW tip.

The length differences between these 4 samples are tightly linked with the NW tip diameter. Au catalyzed NWs have smallest tip diameter, and also have the shortest NWs. Indeed, it is commonly observed that larger Au droplets produce longer NWs. As shown in the inset of figure 4.1 e), the big Au droplet catalyzed a much longer NW than the small droplets did. This NW has a tip diameter of 13 nm and length of 460 nm, which is very similar to that of the Cu and Sn catalyzed NWs. Sn and Cu catalyzed NWs have similar tip diameters, and the length of these NWs turns out to be similar also. This indicates that the catalyst droplets diameter plays a more important role on the growth velocity than the chemical nature of the catalyst. This also suggests that the gas precursors are incorporated through the effects of plasma, not the effects of the metal catalysts. At the same time the growth is less likely due to the surface diffusion, otherwise the NWs with smaller diameter will grow longer. For the case of In, the large droplets collect sufficient SiHx and GeHx radicals to feed the small NW tip. This helps NWs to have a higher growth rate.

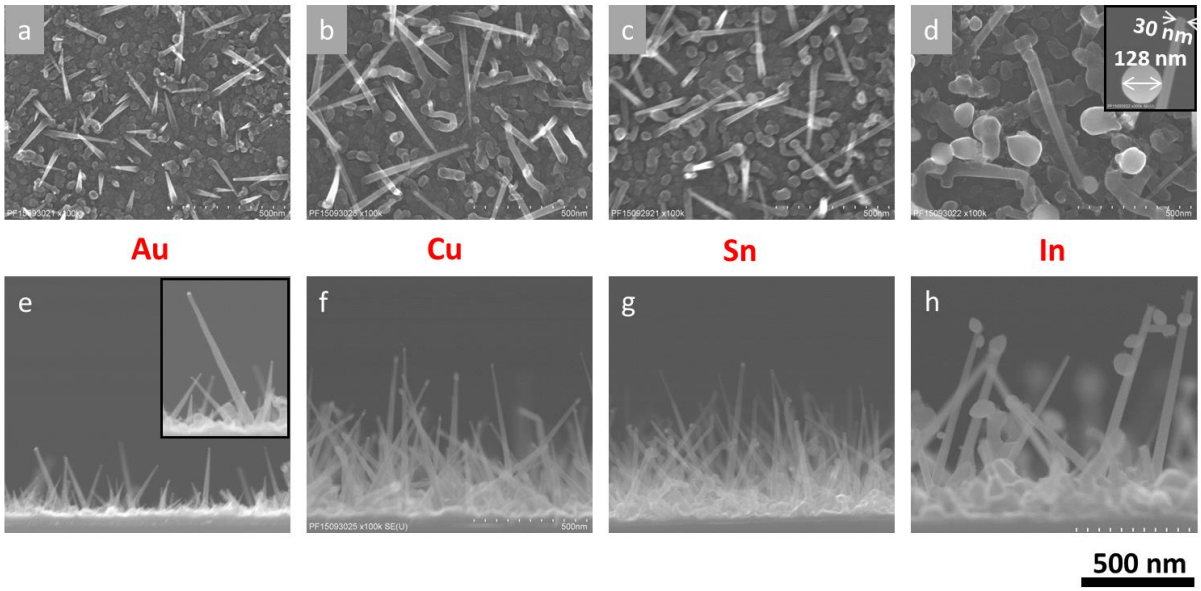


Figure 4.1. Top view and side view of SiGeNWs catalyzed by Au, Cu, Sn and In. The $GeH_4/(GeH_4+SiH_4)$ partial pressure ratio is 1.96%. All the figures, including the two insets in figure d) and figure e), share the common scale bar which is shown in the bottom of the figures.

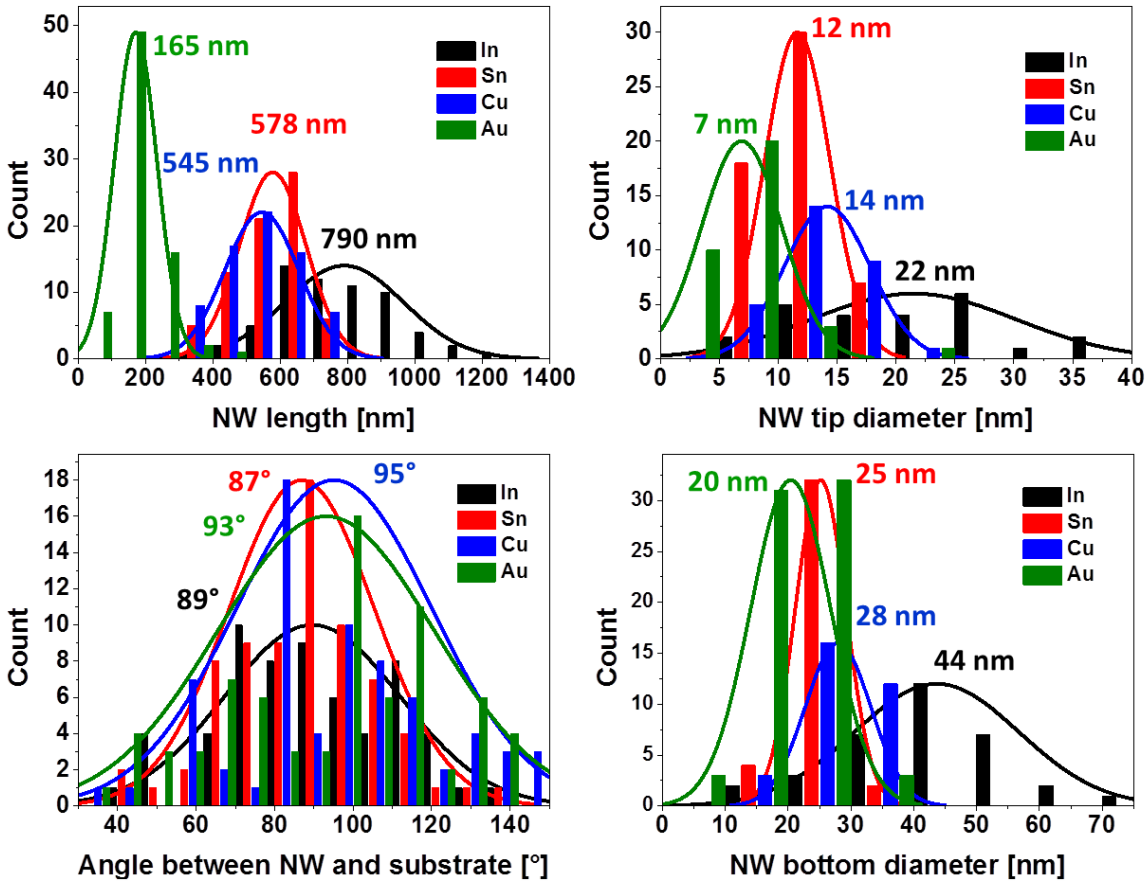


Figure 4.2. Statistics of the NW length, NW bottom diameter, NW growth angle and NW tip diameter. The lines are the normal fit of the data. The value of the expectation of each normal distribution is marked with the corresponding color.

The growth parameters which lead to SiGeNWs growth are plotted in figure 4.3. In this figure, the partial pressures of $SiH_4$ and $GeH_4$ of each experiment are plotted. For each catalyst, a line connecting 0 and the data point which has the maximum $GeH_4/(GeH_4+SiH_4)$ partial pressure ratio is plotted. The parameters between this line and the horizontal axis usually result in NW growth, while above this area will end up with crystal or thin film growth. Thus this area is considered as the parameter space of the catalyst. It can be seen that the parameter space increases from Sn, to Au, and then to In and Cu. For Sn, NW can grow when the $GeH_4$ partial pressure is low. For the majority of these experiments, the $GeH_4/(GeH_4+SiH_4)$ ratio is smaller than 14%.

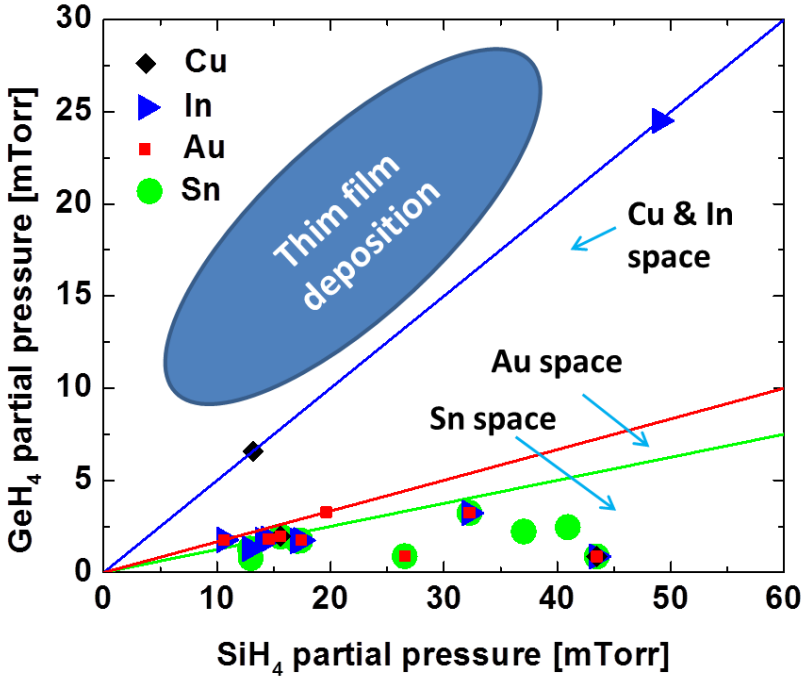


Figure 4.3. Parameter space of Sn, Au In and Cu. The substrate temperature is fixed at 400°C. The $H_2$ flow rate is fixed at 100 sccm. The flow rates of $SiH_4$ and $GeH_4$ and the total gas pressure have been changed. $GeH_4$ is 1% diluted in $H_2$.

### 4.2.2 Increasing the Ge content of the SiGeNWs

For the metal catalyzed crystal growth, the super saturation level of the source atoms in the catalyst is crucial to the growth. Depending on the super saturation level, there are island growth, NW growth, and film growth modes.[30] The $GeH_4$ gas used in our experiments is 1% diluted in $H_2$. This is a much lower concentration than the $GeH_4$ used in the literature, which is usually 5% or 10%. The low $GeH_4$ concentration might lead to a low supersaturation level of Ge atom in the catalyst. In order to study the effect of precursor gas partial pressure on the growth, we have carried a SiGeNWs growth experiment with a $SiH_4$ partial pressure of 9 mTorr and the $GeH_4$ partial pressure of 0.9 mTorr. As a contrast, SiGeNWs can be grown when the $GeH_4$ plus $SiH_4$ total partial pressure is around 90 mTorr.

In order to observe the initial growth process. A special treatment to the substrate has been done. In this experiment, as shown in figure 4.4, a small piece of p-type doped Si wafer is positioned on a standard substrate. The resistivity of this wafer is < 0.005 Ω cm and its thickness is around 500 µm. Standard NW growth processes using Sn as catalyst have been carried out. Due to the effect of the mask, there is a distribution of $SiH_x$ and $GeH_x$ flux at the sample surface. Under the mask, there is no radical flux. As the distance to the edge of the mask increases, the radical flux increases from 0 to normal value. As a consequence, the growth rate increases continuously when the distance to the edge of the mask increases. SEM top view images of the sample after growth are shown in figure 4.5. In this figure, a) shows the area under the mask, while images form b) to f) are taken at increasing distance with respect to the edge of the mask. The image in f) is far enough from the mask that there is no change in the growth rate with further increase of distance.

In figure 4.5, it can be seen that under the mask, there are only Sn droplets which have a diameter between 10 to 20 nm. With increasing distance to the mask in b), small NWs with a diameter around

10 nm and length around 10 nm appear. More interestingly, the smaller NWs push the Sn droplets together and merge. In c), it can be seen that more and more merging events occur. In chapter 3, we have also observed that at the initial growth stage of SiNWs, there the merge of Sn droplets are also due to the SiNW growth. In that case, the NWs did grow vertically. However, in the present case the Sn droplets are not pushed upwards. In d) and e), it can be seen that the material behind the Sn droplets keep on growing bigger and merging. In f) it can be seen that a continuous film is formed. This observation shows when the $SiH_4$ and $GeH_4$ gas partial pressure is too low, the islands are formed firstly, then the growth and coarsening of these islands cause the continuous film formation. The formation of the initial island starts with Sn droplets, and they are high probably catalyzed by Sn. This experiment suggests that SiGeNWs might grow at high supersaturation level.

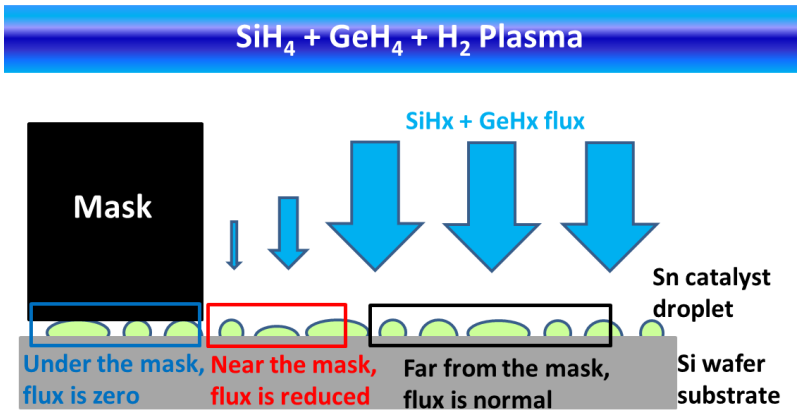


Figure 4.4. Configuration of the experiment dedicated to observe the initial stage of the film formation. A 500 µm thick p-type doped Si wafer mask is positioned on a normal substrate. Due to the effects of the mask, the SiHx and GeHx flux increase as the distance to the mask increases.

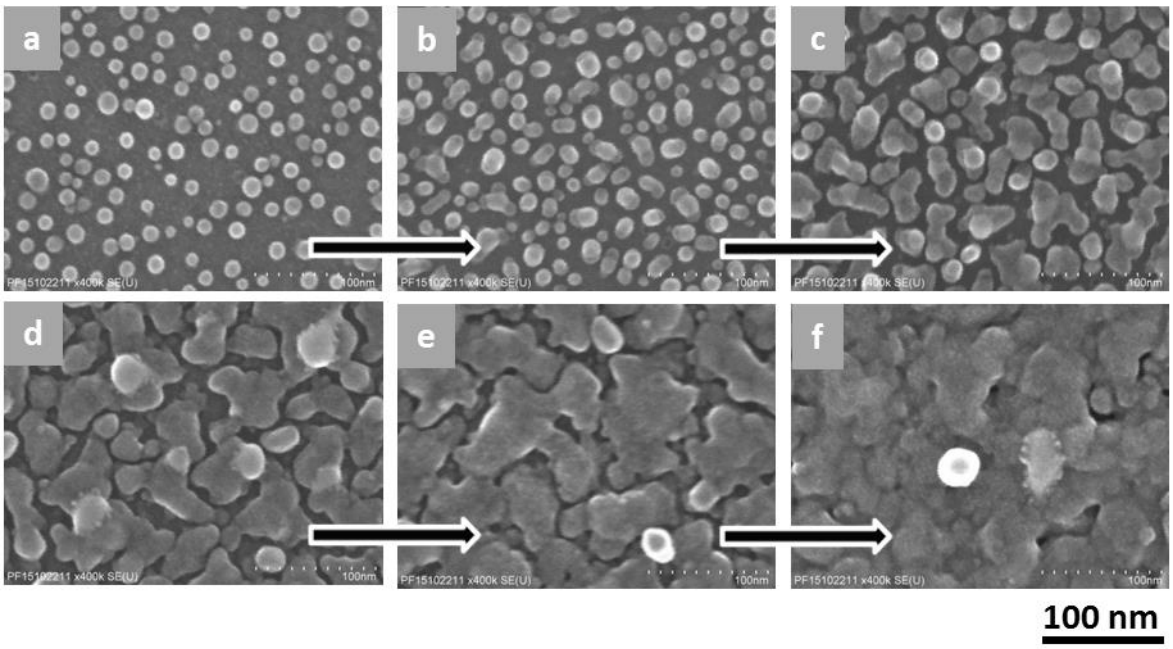


Figure 4.5. SEM images taken on different areas of the sample described in figure 4.4 after deposition. a) area under the mask; b) to f), areas at increasing distances from the mask.

To achieve a higher super saturation level, there are two options: to increase the partial pressure and to decrease the substrate temperature. Experiments with both high precursor gas partial pressure and low substrate temperature have been carried out. We found that compared with the substrate temperature, the precursor gas partial pressure plays a much less important role. Once the $SiH_4$+$GeH_4$ partial pressure is above 13 mTorr or the $GeH_4$ partial pressure is above 6 mTorr, the NWs growth or not is determined by substrate temperature. With partial pressure higher than these critical value and reduced substrate temperature, we have achieved SiGeNWs with different $GeH_4$/($GeH_4$+$SiH_4$) partial pressure ratio and different catalysts.

Top view SEM images of SiGeNWs grown with different values of the $GeH_4$/($GeH_4$+$SiH_4$) partial pressure ratio (R), different temperatures (T) and different catalysts are shown in figure 4.6. For these experiments, the value of R has been increased from 11% to 100%. We found that the experiments with a higher R usually lead to NWs growth at lower temperature. With the decrease of substrate temperature and increase of R, there is no degradation of the NW morphology. Straight SiGeNWs have been obtained over a wide parameter space. For Cu, the NWs grow over a wide range and a wide $GeH_4$/($GeH_4$+$SiH_4$) ratio. More importantly, the substrate temperature here is well below the eutectic point of Si-Cu and Ge-Cu, both of them are 644°C. In the literature, Cu has been used as a catalyst to growth GeNWs by VLS method at a temperature down to 200°C, and the growth process has been proved to be VSS.[28,31] In a plasma-assisted VLS growth process, the main function of the plasma is to enhance the gas precursor decomposition. It is not likely that the plasma will change the phase of the catalyst. So we suggest that Cu catalyzed growth here is also VSS. When the temperature is lower than 325°C, no NW growth has been observed with Au. This might be due to fact that both of the eutectic temperature of Au-Si and Au-Ge are 361°C.[32] Due to the nano-size effect, the eutectic temperature of Au-Si-Ge might decrease to a value around 325°C. When the substrate temperature decreases even lower, the VSS growth process with Au catalyst does not occur. Pure GeNWs have been obtained with Cu, Sn and In. These NWs have a conical morphology. With Sn catalyst, the GeNWs have a quite small size and density. Since Sn can be incorporated in Ge with a ratio higher than the solubility limit, these NWs catalyzed by Sn might be GeSn alloy which is a direct bandgap material[33,34].

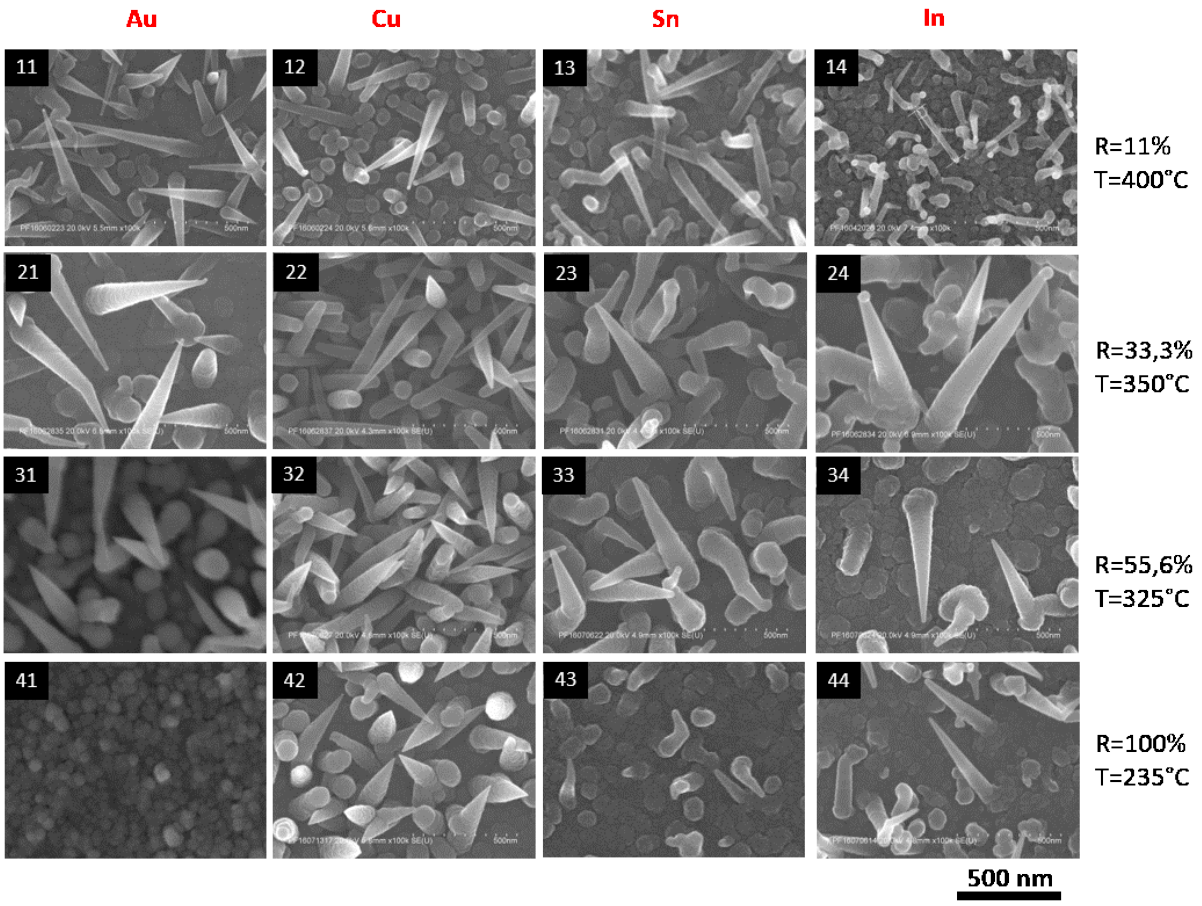


Figure 4.6. Top view of SiGeNWs catalyzed by Au, Cu, Sn and In. From 11 to 14, the $GeH_4/(GeH_4+SiH_4)$ partial pressure ratio is 11%, and the substrate temperature is 400°C. From 21 to 24, the $GeH_4/(GeH_4+SiH_4)$ partial pressure ratio is 33.3%, and the substrate temperature is 350°C. From 31 to 34, the $GeH_4/(GeH_4+SiH_4)$ partial pressure ratio is 55.6%, and the substrate temperature is 325°C. From 41 to 44, the $GeH_4/(GeH_4+SiH_4)$ partial pressure ratio is 100%, and the substrate temperature is 235°C.

As mentioned before, the $SiH_4$ and $GeH_4$ partial pressure plays a less important role when the $SiH_4+GeH_4$ partial pressure is above 13 mTorr or the $GeH_4$ partial pressure is above 6 mTorr. So we have summarized all the experiments which lead to SiGeNWs growth in figure 4.7 by taking the substrate temperature and parameter R as variables. In this figure, the black squares, red circles, green stars and blue tringles represent the Sn, In, Cu and Au, respectively. The experiments which do not lead to NW growth with Sn have also been plotted with black circles. It can be seen that In, Au and Cu have a larger parameter space than Sn. With the increase of R, the substrate temperature has to be decreased for Sn catalyst to produce SiGeNWs. The black line is a guide to the eyes. Above this line, the growth experiments usually lead to thin film deposition with Sn catalyst. This might be because compared to Si, Ge has a much high solubility in Sn[32]. The Ge/Si atomic percentage ratio in the metal droplets might increase with the increase of $GeH_4/SiH_4$ partial pressure ratio, and this might decrease the supersaturation level. In order to maintain the supersaturation level, the substrate temperature needs to be decreased.

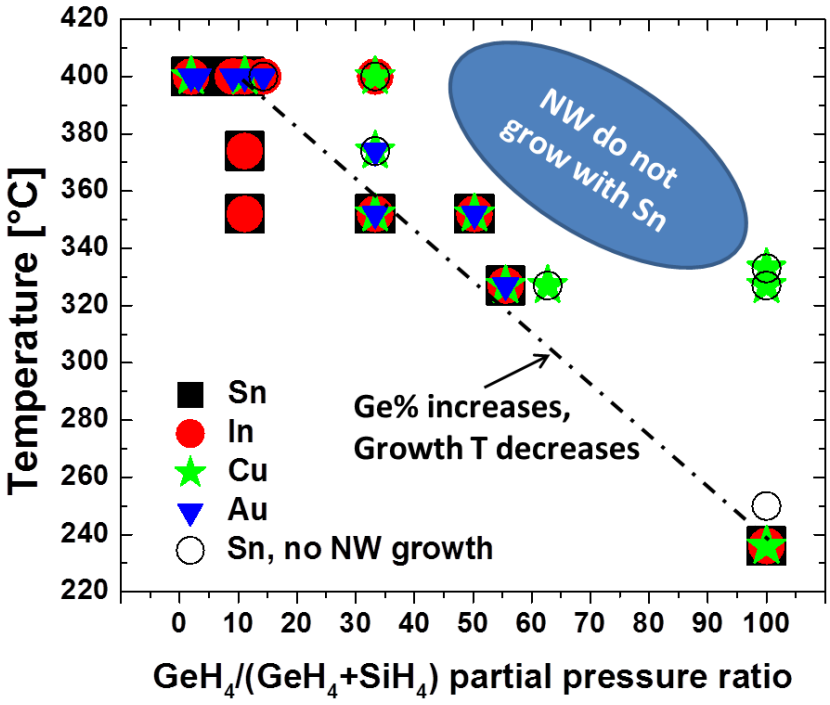


Figure 4.7. Substrate temperature as a function of $GeH_4/(GeH_4+SiH_4)$ partial pressure ratio of the SiGeNWs growth experiments. The dashed line is a guide to the eyes.

Figure 4.7 shows that GeNWs can be grown at both 235°C and 325°C with Cu. A detailed comparison of the morphology of these GeNWs has been carried out. Figure 4.8 a) and b) show SEM images of GeNWs catalyzed by Cu at 235°C and 325°C, respectively. These two GeNWs growth experiments have the same parameters except the substrate temperature. It can be seen that the NWs of the two samples have similar conical morphology, and the main difference of the two samples is the NW density. The sample grown at 325°C has a higher NW density than the sample grown at 235°C. The statistics of the NW length and NW bottom diameter have been done with the top view SEM images and the results are shown in figures 4.8 c and d. The lines show the normal fit of the statistical data. It can be seen that there is no significant difference of the NW length. The 90°C of temperature difference does not influence the growth rate. This could be due to the fact that with plasma-assisted VLS NW growth, the precursor gases are dissociated by plasma, and the temperature plays less important role on the incorporation rate. However, there is big difference of the NW bottom diameter. This is firstly because that the GeNWs grown at 325°C have a higher density; therefore there is a bigger chance for the bottom of these NWs to be hidden (Thus the NW length and NW bottom diameter measured through top view SEM image might be slightly under estimated). The second reason is that the second sample has a larger amount of NWs per area, so the radical flux reaching in each NW is reduced and there is less side wall deposition.

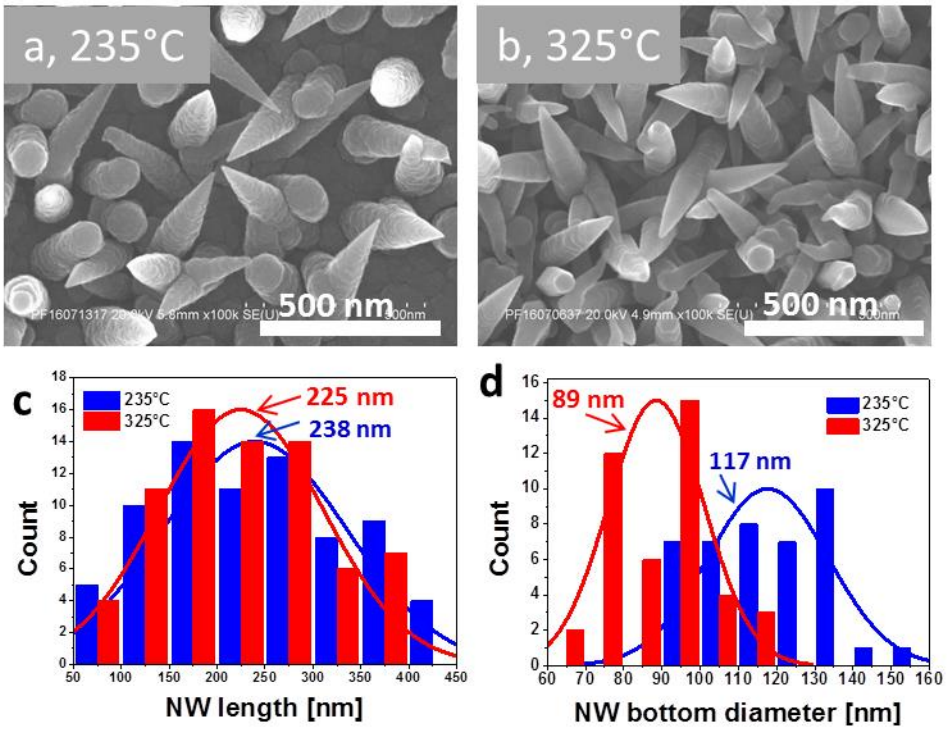


Figure 4.8 GeNWs catalyzed by Cu at different temperatures. a) 235°C; b) 325°C. c) Statistics of the NW length of the two samples; d) Statistics of the NW bottom diameter of the two samples. The statistics are done with the top view SEM images. The lines are the normal fit of the statistical data. The value of the expectation of the normal distribution has been marked with the corresponding colors.

### 4.2.3 GeNW growth at high temperature

The GeNW growth experiments described in the previous part shows high supersaturation level of Ge in the catalyst is essential for the GeNW growth. Increasing the $GeH_4$ precursor gas partial pressure is another way to increase the Ge supersaturation level. With such an approach, it might allow GeNW growth at high temperature. Thus, we have carried out GeNW growth experiments at 400°C with increased $GeH_4$ partial pressure. In these experiments, the $GeH_4$ flow rate is fixed at 50 sccm, the precursor gas pressure varies in the range of 2.6 Torr to 9 Torr, the RF power density varies in the range of 110mW/cm$^2$ to 165mW/cm$^2$, and the growth duration is 10 minutes.

Figure 4.9 shows the GeNW growth experiments which have been carried out at 400°C with different catalysts. It shows that the NW growth is different with In, Sn, Au and Cu catalysts. In figures 4.9 a) and b), long, thin and cylindrical GeNWs are grown with In and Sn catalysts. In figures 4.9 c), thick NWs with a rough surface are obtained With Au catalyst. In figures 4.9 d), no NW can be grown with Cu catalyst.

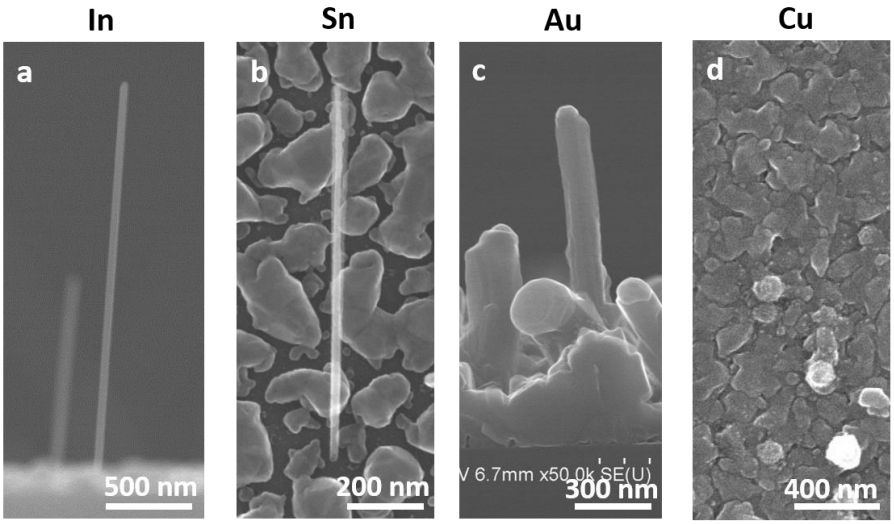


Figure 4.9 SEM images of GeNWs grown with catalysts In, Sn, Au and Cu at 400°C.

Due to the high reactivity of the plasma, there is always sidewall deposition for plasma-assisted VLS NW growth. Thus the standard NW morphology is a conical shape. There are no reports which show long cylindrical NWs grown by plasma-assisted VLS. In order to find out which growth parameter determines the morphology of the GeNWs, we have grown GeNWs at different temperatures and $GeH_4$ partial pressures with In catalyst. In these experiments, the catalyst are 3 to 5 nm of In deposited on ZnO:Al surface or $SiO_2$ surface. The SEM images of the GeNWs grown in these experiments are shown in figure 4.10. It can be seen that when the substrate temperature is lower than 350°C, the GeNWs have a standard conical shape. However, when the substrate temperature is above 350°C, they change to a cylindrical shape. The $GeH_4$ partial pressure and substrate temperature of these experiments have been plotted in a two dimensional map, as shown in figure 4.11. Sample b and d have a similar $GeH_4$ pressure, the only difference is the substrate temperature. This suggests that the main factor determining the NW shape is the substrate temperature. Similar experiments have also been done with Sn, and the parameters are also show in figure 4.11 with red dots. The GeNWs catalyzed by Sn have similar transition as the GeNWs catalyzed by In. The SEM images are shown in figures 4.6 and 4.9.

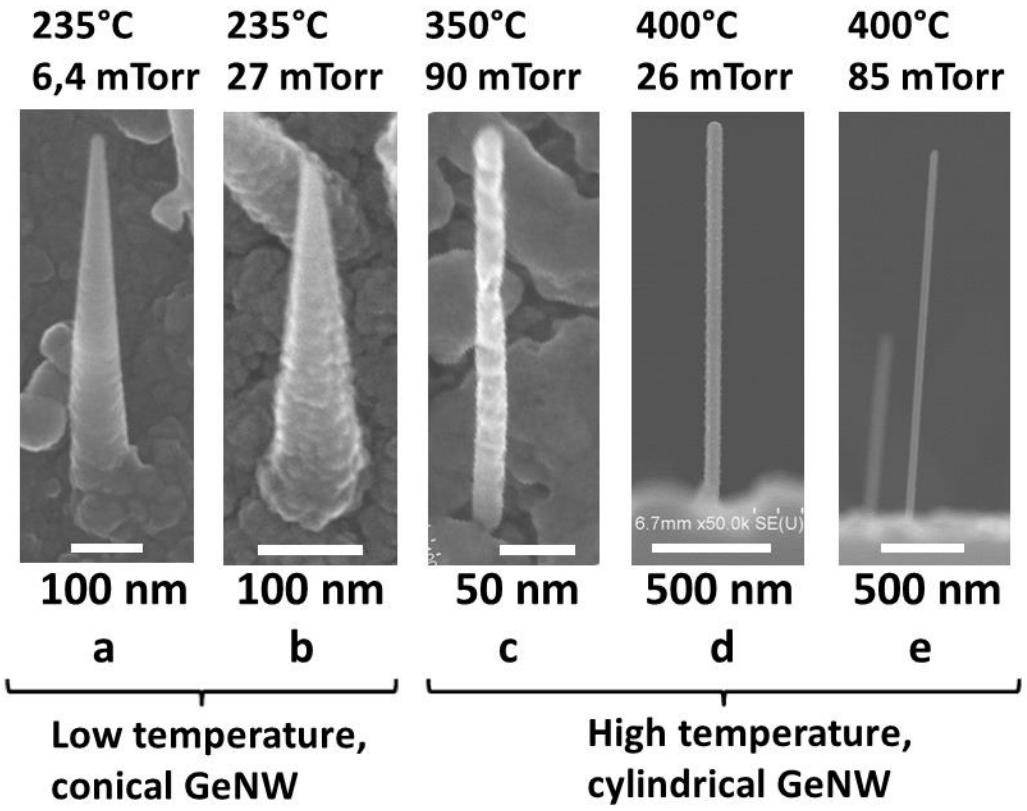


Figure 4.10. GeNWs grown by plasma-assisted VLS method at different temperatures and $GeH_4$ partial pressures. a) 235°C, 6.4 mTorr; b) 235°C, 27 mTorr; c) 350°C, 90 mTorr; d) 400°C, 26mTorr; and e) 400°C, 85 mTorr. The catalyst is In.

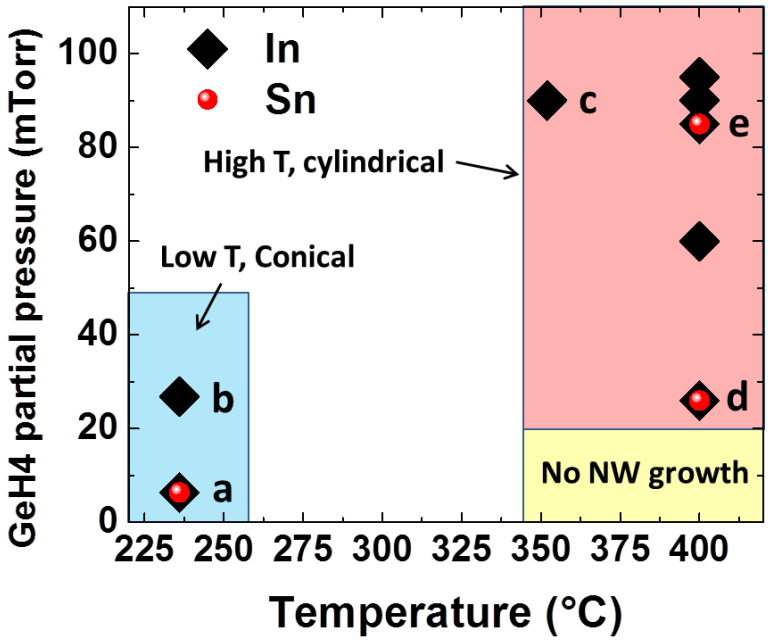


Figure 4.11. $GeH_4$ partial pressure and the substrate temperature of the GeNW growth experiments. Note the changing in shape from conical to cylindrical with the increase of substrate temperature.

With CVD VLS NW growth, cylindrical GeNWs can be obtained at certain condition[35,36]. In order to check the CVD contribution to the growth, we have carried out the same experiment without plasma assistance. Figure 4.12 a) shows the SEM image of the sample after the growth. It can be seen that there are only In droplets on the surface of the Si wafer. In the literature, GeNW growth with CVD method using In as catalyst has been reported at a temperature below 400°C[24]. But in our case, it is clear that there is neither GeNW growth, nor Ge material deposition. The reason could be that the gas precursor used here is 1% of $GeH_4$ diluted in $H_2$. During the experiments, we have also put a Corning glass substrate in the chamber to check the deposition rate. The imaginary part of the pseudo-dielectric function of the Corning glass substrate measured by spectroscopic ellipsometry is shown in figure 4.12 b). In this figure, black dots are the data before the CVD deposition experiments, while the red dots are the data after the experiments. It can be seen that the values of the two sample have difference below 0.05 when the photon energy varies from 1 eV to 4.5 eV. This suggests that there is no deposition on the Corning glass substrate. The inset in figure 4.13 b) shows the optical image of the Corning glass substrate. It can be seen that it has a good transparency.

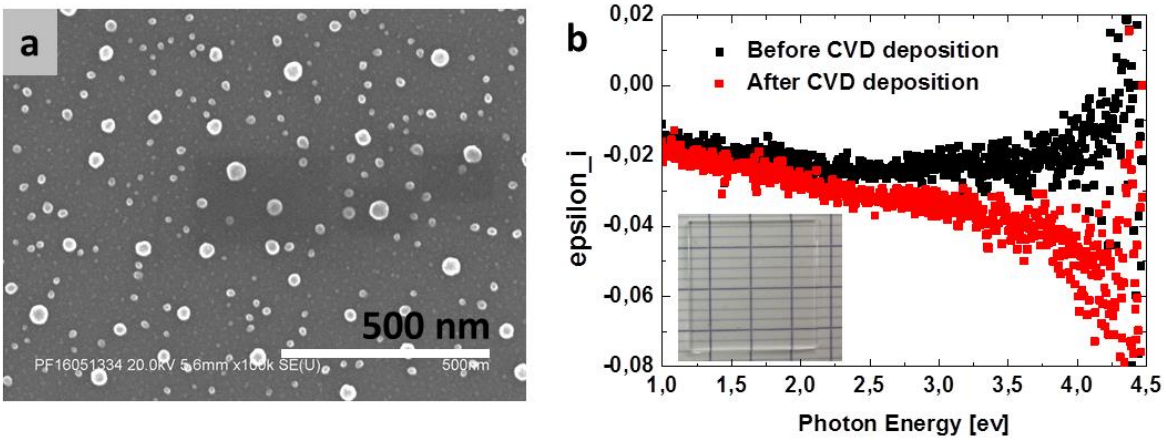


Figure 4.12. a) GeNW growth experiments without plasma-assistance, the substrate is a c-Si wafer. b) Imaginary part of the pseudo-dielectric function of the Corning glass substrate. The black dots are measured before the experiment and the red dots are measured after the experiment. The inset shows the optical image of the Corning glass simple after deposition.

In the literature, it is reported that catalyst-free nanowires can be synthesized[37,38]. For example, there are few reports showing that nucleation of nano-crystalline seeds can be obtained on a reactive oxide surface without metal catalyst, and subsequently achieve anisotropic growth using low-pressure chemical vapor deposition (LPCVD) process.[38] In order to check if GeNWs are In catalyzed or not, we have carried out the GeNWs growth experiment without catalysts. In this experiment, the $GeH_4$ flow rate is 50 sccm, the pressure is 8 Torr, the temperature is 400°C, the RF power density is 165mW/cm$^2$, and the growth duration is 10 minutes. Three substrates loaded are a Si wafer, a ZnO:Al coated Corning glass and a bare Corning glass. The SEM images of the three substrates after growth are shown in figure 4.13; it can be seen that there is no GeNW growth on any of the substrates. However, there is Ge deposition on all of them. In figure 4.13 a) it can be seen clearly that the Ge film deposition has a Volmer-Weber growth mode. It means that the island is formed firstly, then the growth of these islands along with coarsening cause the continuous film formation. Raman measurements have been done with the Corning glass substrate, and the result is

shown in figure 4.13 d). There is a strong crystalline peak at 300 $cm^{-1}$. This shows that with PECVD deposition, Ge can be crystalized on Corning substrate at 400°C.

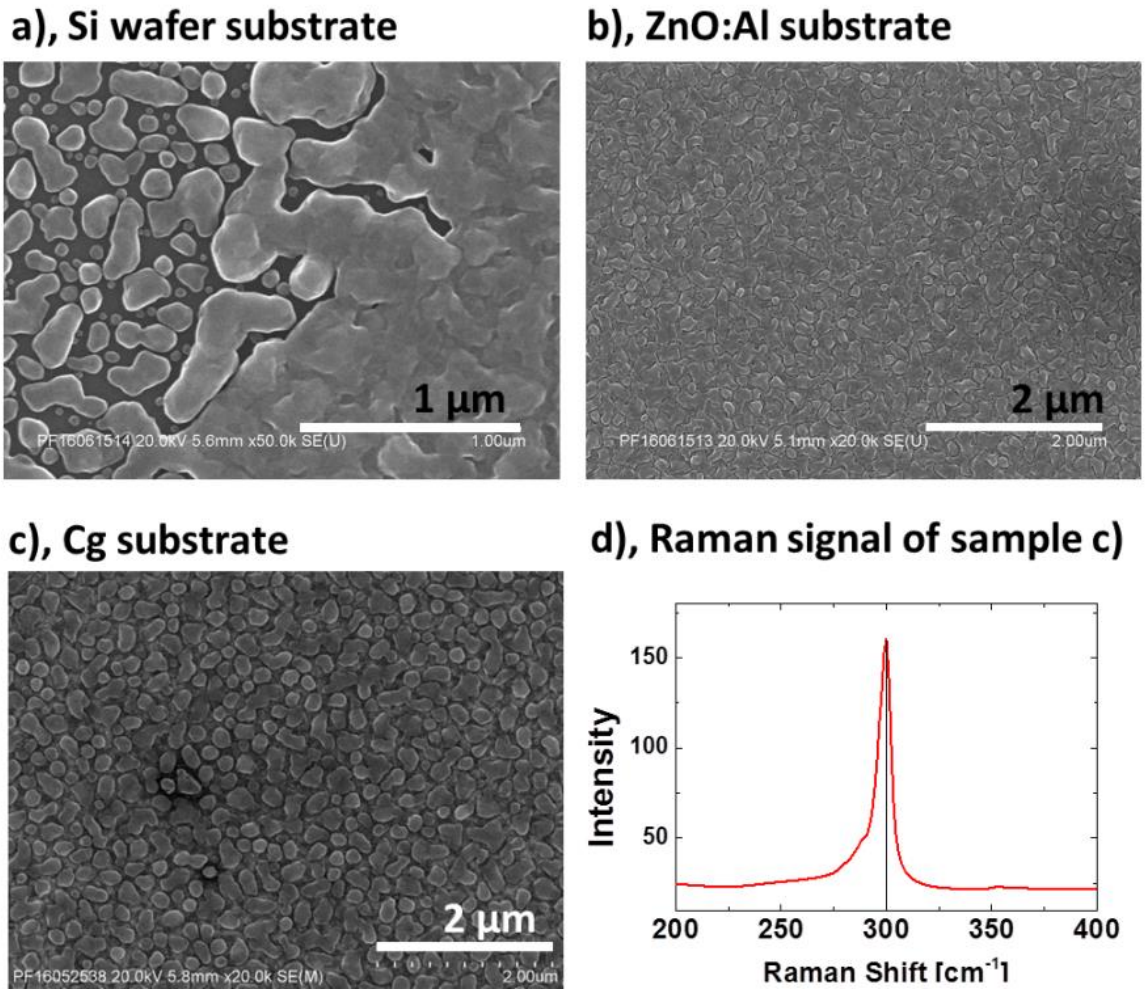


Figure 4.13. a)-c) GeNW growth experiments without catalysts done on different substrates: a) Si wafer; b) ZnO:Al coated Corning glass; c) Corning glass. d) Raman spectrum of sample c).

In order to understand the formation of the long cylindrical GeNWs shown in figure 4.9 a), we have carried out an experiment to observe the initial formation processes. As the experiment illustrated in figure 4.4, we have put a piece of Si wafer on the substrate. The substrate is Si wafer with 1 nm thick evaporated In layer. Due to the presence of the mask, there is a distribution of GeHx flux near the border of the mask. Thus the growth of GeNWs will have a continuous variation in this region. The optical image of this sample is shown in figure 4.14 a). In this image the mask has been removed. The square region with light color in the center corresponds to the region that was covered by the mask during growth. Figure 4.14 b) illustrates the configuration of this experiment. The red arrows in a) and b) show the direction in which the variation of the GeHx flux occurs. As illustrated in b), when the region is under the mask, there is no GeHx radical flux due to the coverage. At the region near the mask, the GeHx flux is reduced due to the presence of the mask. It continuously varies from 0 to the normal value, far away from the mask where the influence of the mask is negligible. The SEM scan has been done along the red arrow indicated in figure 4.14 a). The scan started from the region under the mask till the region far from the mask. The SEM observation results are also shown in figure 4.14. These images have been arranged according to the distance to the mask. From c) to k)

are side view SEM images, and from l) to v) are top view SEM images. In figure 4.14 c), it can be seen that at the region under the mask no NW growth occurs. As going on leftward, short and sparse NWs appear. Both the length and the density of the NWs increases with the distance to the mask. In the enlarged side view image d) and top view images l) and m), it can be seen that there are spherical In droplets with similar diameters (around 200 nm) under the mask. The distance between them is several hundred nm. The initial In catalyst has been prepared with standard procedure and standard parameters, and they usually have a diameter below 20 nm. This suggest that the big droplets here are formed by Ostwald ripening of small In droplets. Between the big droplets, there are small particles with diameters smaller than 10 nm, as seen in figure 4.14 n). These small particles are usually accompanied with material which has a lower brightness. From the image contrast, we presume the part with high brightness is In metal, and the part with low brightness is Ge. Since the Si wafer mask is naturally positioned on the substrate, no special seal process at the edge has been made. So there can be a small amount of GeHx entering the space between the mask and the substrate. This results in the tiny Ge crystal growth induced by In. As the distance to the mask increases, as shown in figure 4.14 p), it can be seen that there are three kind of growth. The first one is the big In droplets catalyzed Ge crystal growth. These Ge crystals have a size above 100 nm but smaller than the size of the droplets. The second one is the small crystal growth. These small crystals do not have a regular shape. They have a length of few tens of nm. As described before, Ge crystals can be grown on Corning substrate without catalyst at a similar condition, so here it is not clear that these small Ge crystals are catalyzed by In or not. The third one is the NW growth, as show in the enlarged figure 4.14 o). The wire form can be seen more clearly in the side view image in figure 4.14 e) and f). These wires have a very narrow diameter distribution, which is between 10 to 20 nm.

With even larger distance to the mask, the GeNWs grow longer, as shown in figure f), g), q) and r). It can be seen the GeNWs start the wire form from the very beginning of the growth. The NWs stand directly on the substrate, instead of on a crystal. More interestingly, the bottom diameter of these NWs does not increase during the NW growth, and it has the same diameter as the tip. In figure 4.14 s) and t), it can be seen that the small crystals increasing size. Their size is comparable with that of the big droplets. Comparing the side view image 4.14 g) and j), it can be seen that the small crystals in figure g) grow as big as the big In droplets in figure 4.14 j). The continuous increase of the size of these droplets might eventually lead to continuous film formation. In figure 4.14 u), the bottom of the NW is buried by a big crystal. This big crystal might be formed by the merging of the small crystals. Figure 4.14 k), u) and v) are taken at a distance of more than 1000 µm from the border of the mask. In these images, both the NW density and the NW length become much bigger than near the mask.

The cylindrical GeNW morphology might be related to the high $H_2$ dilution level of the $GeH_4$ gas. In our experiments, $H_2$ represents 99% mol volume of the precursor gas. Such a high $H_2$ ratio can lead to a high concentration of atomic hydrogen. These hydrogen atoms can form bonds with the surface Ge atoms. Hydrogen termination on curved surfaces is energetically more stable than on flat surface.[39] Since the NW diameters are usually below 20 nm, the large curvature of the sidewall might have a stable hydrogen atom passivation. The hydrogen atoms passivation could prevent the sidewall deposition. A similar phenomenon has been reported with CVD VLS NW growth.[40,41] Another possibility is that Ge atoms have a high diffusion length on the sidewall at 400°C, thus the Ge atoms diffuse to the In catalyst at the tip of the NWs. In such a way, there is growth only at the interface of the In catalyst and the NW.

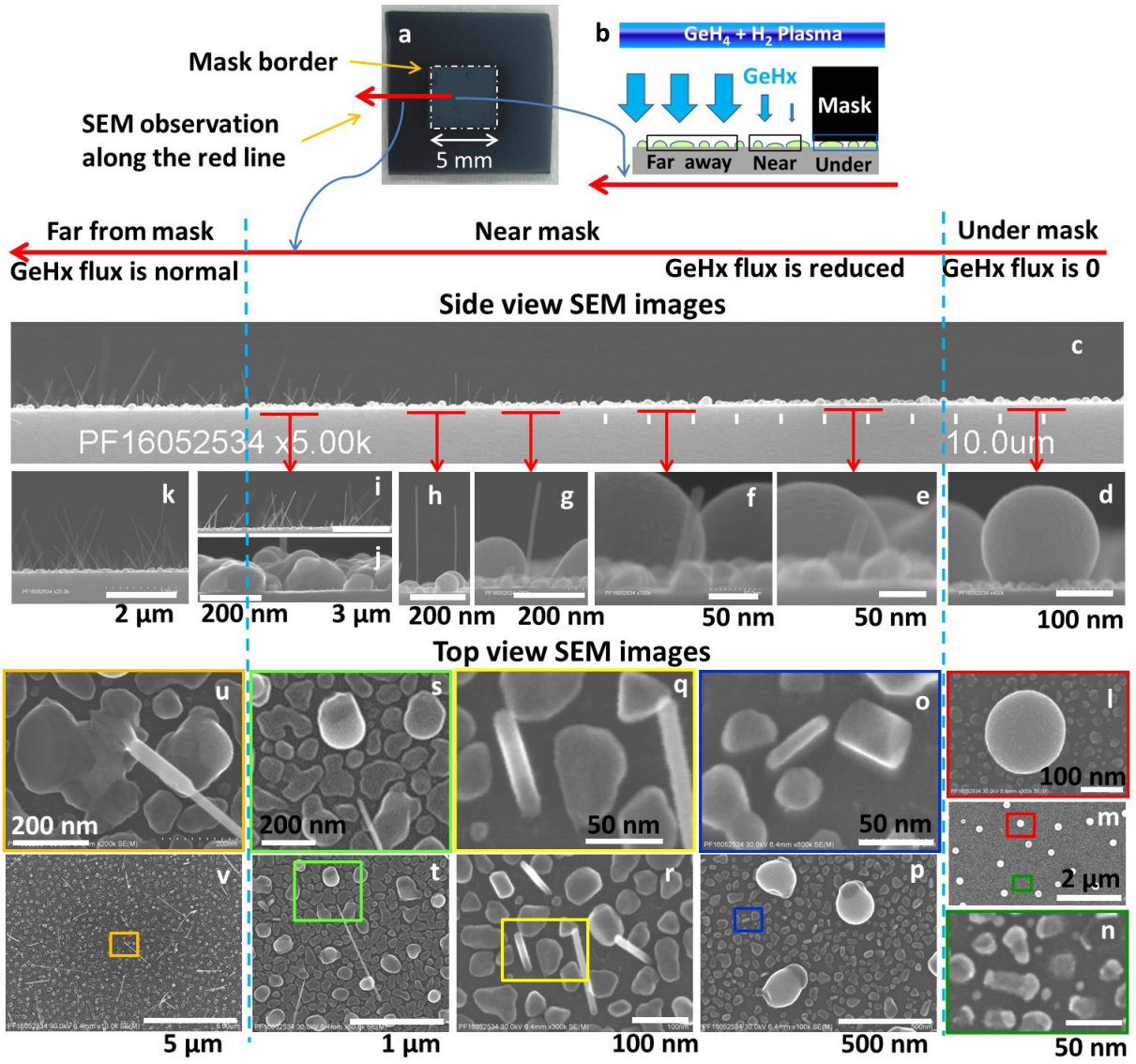


Figure 4.14. Experiment dedicated to observe the growth process of cylindrical GeNWs. a) Optical image of the sample after the growth (The c-Si mask has been removed). The square region with light color in the center is the region under the mask during the growth. b) Schematic of the experiment. c) to k) Side view SEM images of the sample along the red arrow indicated in a). l) to v) Top view SEM images of the sample along the red arrow indicated in a). The catalyst is In.

It is widely reported that CVD VLS GeNW growth can occur with Au catalyst at temperatures lower than 400°C[31,42-45]. In order to check the CVD VLS growth contribution of our GeNWs, we have carried two GeNW growth experiments with and without plasma-assistance. For these two experiments, 1 to 5 nm thick Au is evaporated on Si wafer substrate and 10 minutes of CVD growth have been carried out. During growth, the $GeH_4$ flow rate is 50 sccm, the pressure is around 4 Torr, and the substrate temperature is 400°C. An additional 10 minutes of plasma-assisted CVD growth have been followed for the second sample without changing the $GeH_4$ flow rate, pressure and substrate temperature, and the RF power density is 165 mw/cm$^2$. The SEM images of the two samples after the growth are shown in figure 4.15 a) and b); c) shows a side view SEM image of the second sample.

In figure 4.15 a), it can be seen that there is only bulk crystal growth. With In catalyst, there is no deposition under similar experiment condition, as shown in figure 4.11. This suggests that Au is a catalyst which can dissociate the $GeH_4$ gas. Compared with the GeNWs growth with similar growth conditions in the literature[24], the main difference of the present experiment is the low $GeH_4$ concentration in the precursor gas. In figure 4.15 b) and c), it can be seen that the bottom of the sample has similar bulk crystal as shown in figure 4.15 a). This corresponds to the bulk Ge crystal growth during the CVD step. However at the top of the sample, there is NWs growth due to the plasma-assisted step. The plasma has changed the growth mode from bulk crystal growth to NW growth. The main function of the plasma is to enhance the dissociation of the $GeH_4$ gas. This might lead to more GeHx flow to Au catalyst and thus a higher supersaturation level. This suggests that the GeNW growth might require a high supersaturation level.

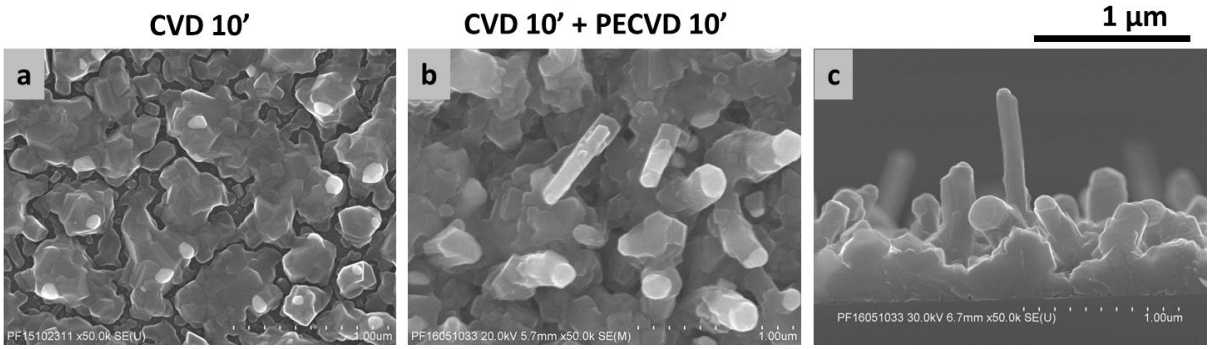


Figure 4.15. GeNW catalyzed by Au at 400°C with different processes. a) 10 minutes of CVD growth; b) 10 minutes of CVD growth followed with 10 minutes of plasma-assisted CVD growth. c) Side view SEM image of the sample shown in b).

A major advantage of using Sn and In catalysts for SiGeNW growth is that sharp Si/Ge axial heterojunction can be obtained. In this study, we have also tried to achieve a sharp axial Si/Ge interface in the NWs. For that purpose, we have first grown a segment of SiNWs with the standard condition described at the beginning of chapter 3. Then we have stopped the $SiH_4$ gas and introduced the $GeH_4$ gas. For the GeNW growth step, the substrate temperature is 400°C, the $GeH_4$ flow rate is 50 sccm, the pressure is 7 Torr and the RF power density is 165 mw/cm$^2$. However, the NW growth stopped after changing the precursor gas. There is only non-continuous Ge crystal growth on the sidewall of the SiNWs, as shown in figure 4.16. This is known as plateau-Rayleigh crystal growth in the literature.[46-48] The surface reduction drives the Ge to form non-continuous crystals on the SiNWs sidewall instead of conformal shell.

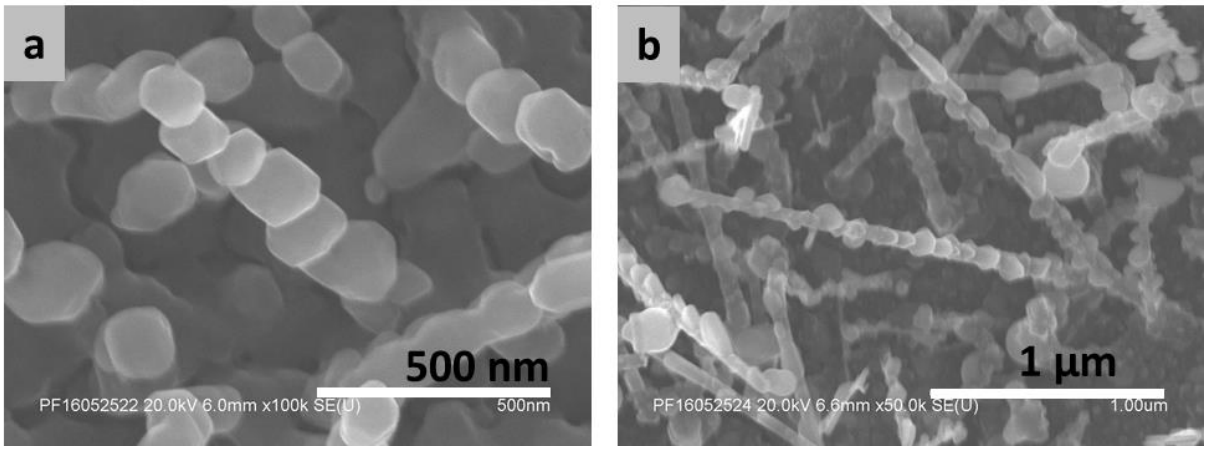


Figure 4.16. Plateau-Rayleigh Ge crystal growth on SiNW substrate. a) SiNWs are catalyzed by Sn; b) SiNWs are catalyzed by In.

## 4.3 Properties of SiGeNWs and GeNWs

### 4.3.1 Ge content studied by Raman and EDX

The concentration of Ge in the SiGe alloy is a key parameter for the properties of this material. It determines its fundamental properties such as the lattice constant and energy band diagram. It is essential to characterize the Ge concentration in the synthesized SiGeNWs.

Raman spectroscopy is a fast way to study the concentration of Ge in the SiGe alloys. In the Raman spectra of the SiGe alloy, there are three peaks correspond to the optical phonons caused by the motions of adjacent Si-Si, Si-Ge, and Ge-Ge pairs, respectively.[49,50] The position of the three Raman peaks is a function as the Ge content and strain. In the literature, Raman spectra have been widely used to study the Ge atomic concentration in SiGeNWs.[50-54] Figure 4.18 shows the Raman spectra of SiGeNWs with different Ge concentration. It can be seen that with the increase of Ge concentration, the intensity of the Si-Si peak decreases, while that of the Ge-Ge peak increases. At the same time, the position of the Si-Si peak shifts to a lower wavenumber. In the low dimension NW geometry, the strain can be released easily through elastic deformation. The relation between the Raman peak positions and the Ge concentration (under the strain-free conditions) can be written as:[49,50]

$$w^{Si-Si}(x) = 520.2 - 68x$$
$$w^{Si-Ge}(x) = 400.5 + 14.2x$$
$$w^{Ge-Ge}(x) = 282.5 + 16x \quad (4.1)$$

In these 3 equations, there is only one unknown, the Ge concentration. Thus only one equation is enough to determine the Ge concentration. In our experiments, the majority of samples have an intense and clear Si-Si peak, so we use the first equation to determine the Ge concentration in the SiGeNWs.

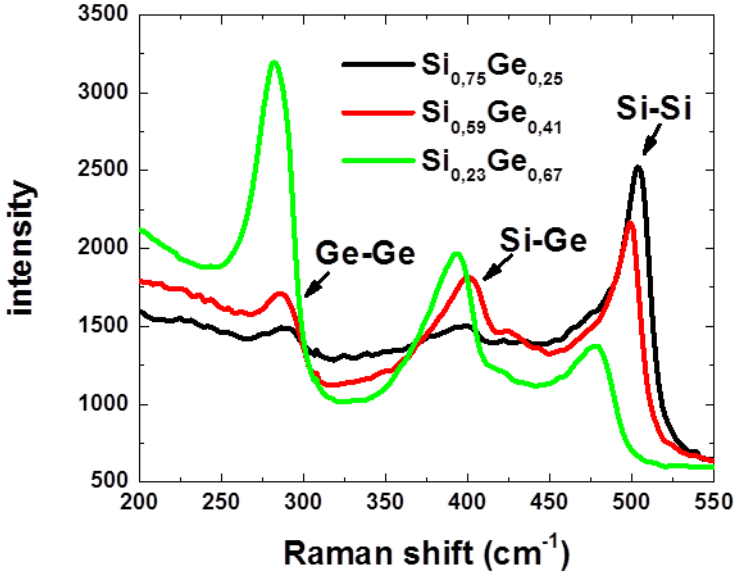


Figure 4.17, Raman spectra of SiGeNWs with different Ge concentration.

In our measurements, the Raman spectrometer was an ARAMIS system from Horiba Jobin-Yvon. A 473 nm excitation wavelength laser was used for the measurements. The objective lens has a magnification of 100 times, thus the lateral resolution is around 1 µm. We found that the SiGeNWs are very sensitive to the laser power. As shown in figure 4.18, when the laser power is bigger than 2.5 µw, the Si-Si peak position shifts to the left.

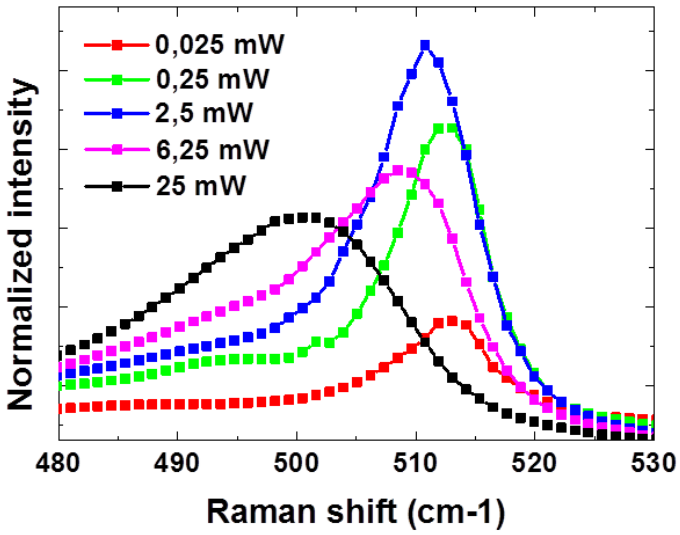


Figure 4.18. Raman spectra measured on SiGeNWs at different values of the laser power in a µRaman system with a blue laser and an objective lens of X100.

The statistics of the peak position are shown in table 4.2. It can be seen that the shift of the peak position is small when the laser power is 0.025 µw and 0.25 µw. It is possible to use a power smaller

than 0.025 μw, however, it is difficult to get a high signal/noise ratio. So in our experiments, we have mainly used 0.025 μw and 0.25 μw laser power.

Table 4.2. Raman Si-Si peak position measured with different laser powers and positions on the same sample.

| Power mW | spot1 | Spot 2 | Spot 3 | Spot 4 | Spot 5 | average |
|---|---|---|---|---|---|---|
| 0,025 | 511,9 | 513 | 511,9 | 513 | 511,9 | 512,34 |
| 0,25 | 513 | 513 | 513 | 513 | 511,9 | 512,78 |
| 2,5 | 510,8 | 510,8 | 510,8 | 511,9 | 510,8 | 511,02 |
| 6,25 | 508,5 | 508,5 | 509,6 | 508,5 | 509,6 | 508,94 |
| 25 | 495,9 | 498,1 | 502,7 | 500,5 | 501,6 | 499,76 |

Energy-dispersive X-ray spectroscopy (EDX or EDS) is another way to carry out the elemental analysis of the SiGeNWs. With this technique, a high-energy beam of particles such as electrons or photons is focused on the sample being studied. The incident beam may knock out electrons from the inner shell and generate holes where the electrons are. Then electrons from outer shell fill these holes. The energy difference between the higher-energy and the lower energy shell may be released in the form of X-rays. The number and the energy of the X-rays can be detected by an energy-dispersive spectrometer.[55] Due to the unique atomic structure and the electromagnetic emission spectrum of each element, the energy of the emitted X-ray can be used to determine the type of the element, and the amount of the X-rays can be used to determine its concentration.

We have used the EDX setup in both TEM and SEM electron microscopes to determine the Ge concentration in the SiGeNWs. For the EDX measurements in TEM, we scratched the SiGeNWs by a diamond pen and deposited them on a TEM carbon membrane. A 300KeV electron beam is focused on a single SiGeNW, Si K lines around 1.8 Kev and Ge K lines around 9.8 Kev are used to determine the Ge concentration. For the EDX measurements in the SEM setup, as grown SiGeNWs samples are loaded into SEM setup. The measured areas have a surface in the range of 1 $\mu m^2$ to 100 $\mu m^2$. The incident electron beam has an energy in the range of 5 Kev to 30 Kev. The substrate of the SiGeNWs are ZnO:Al/ITO double layers coated Corning glass. We have carefully chosen the incident electron beam energy to make sure there is no Si signal contribution from the Corning glass.

The atomic concentration of Ge in SiGeNW samples measured by Raman spectroscopy and EDX set up in both SEM and TEM steups are shown in figure 4.19 a). They are plotted as a function of the $GeH_4/(GeH_4+SiH_4)$ gas flow rate ratio (R). The solid symbols are the results of Raman measurements, while different symbols represent SiGeNWs catalyzed by different catalysts. The red circles represent the results of the EDX study with SEM setup, while the blue square frames represent the results of the EDX study in the TEM setup. The results deduced from Raman measurements and EDX measurements are in good agreement, this indicates that Raman spectroscopy is an accurate way to

estimate the Ge concentration of the SiGeNWs. The Ge atomic concentration increases with the increase of the R. This suggests that as the standard thin SiGe films deposition, the Ge concentration can be controlled by the R. This indicates that nucleation process of Si and Ge from the supersaturated alloy is not under equilibrium, thus the Ge concentration in the SiGeNWs is not pined at the value of eutectic point of the Si-Ge and catalyst metal. All the data points are above the y=x line. This means that the Ge atomic concentration is always bigger than R. It indicates that Ge is easier to be incorporated into SiGeNWs than Si. The most possible reason is that $GeH_4$ decompose easier than $SiH_4$. Based on pyrolysis studies of $SiH_4$[56] and $GeH_4$,[57] the reaction rate for unimolecular decomposition of $GeH_4$ ($GeH_4 \rightarrow GeH_2 + H_2$) at 800 K is 8.5 x $10^{-2}s^{-1}$, this is 56 times faster than that of $SiH_4$ (1.5x$10^{-3}s^{-1}$) under similar conditions. This big difference of decomposition rate might not change a lot under plasma-assisted condition at 400°C. The data points at R=11% and R=33% have significant difference in the Ge concentration. This is mainly due to the difference of the substrate temperature. The Ge concentration as a function of substrate temperature is plotted in figure 4.19 b). It can be seen that the substrate temperature plays an important role on the Ge concentration. With the increase of the substrate temperature, the Ge concentration decreases.

At the same $GeH_4/(GeH_4+SiH_4)$ gas flow rate ratio and same substrate temperature, there is no significant difference on the Ge concentration in the NWs produced by different catalysts. This suggest that the difference of reactivity between the metal and the GeHx radical and SiHx radicals, the difference of alloy binary diagram are not the key factors to determine the Ge concentration, instead, it is mainly determined by the GeHx and SiHx fluxes.

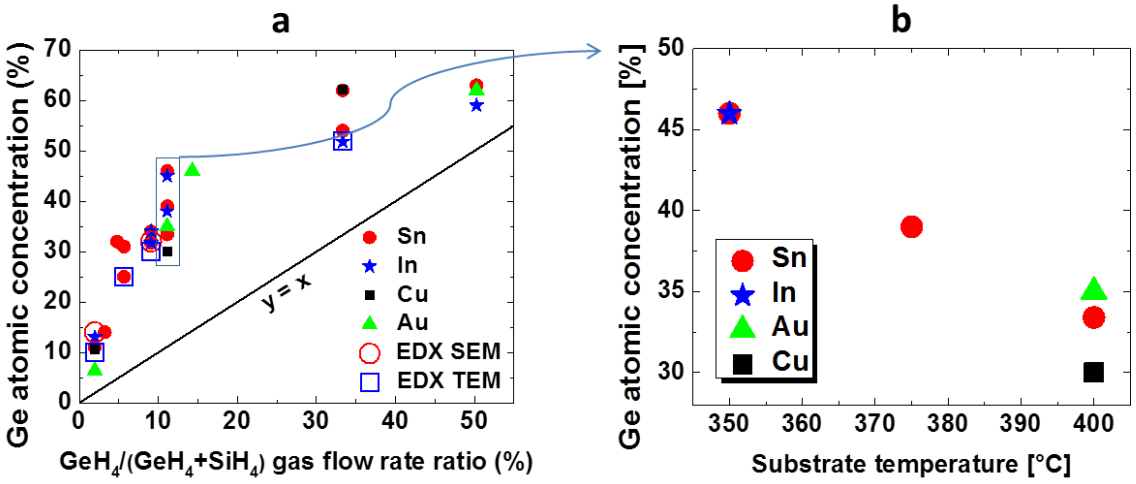


Figure 4.19. a) Ge atomic concentration in SiGeNWs as a function of $GeH_4/(GeH_4+SiH_4)$ gas flow rate ratio measured by Raman spectroscopy and EDX in SEM and TEM steups. The solid symbols are the results of Raman measurements, while different symbols represent SiGeNWs catalyzed by different catalysts. The red circles represent the results of the EDX study with SEM, while blue square frames represent the results of the EDX study in the TEM. The black line is y=x. b) Ge atomic concentration in SiGeNWs as a function of substrate temperature, the $GeH_4/(GeH_4+SiH_4)$ gas flow rate ratio is 11%

### 4.3.2 Crystallinity and chemical composition studied by TEM

The crystallinity of the SiGeNWs and GeNWs has been studied by TEM. Figure 4.20 shows the results of SiGeNWs catalyzed by different catalysts. These NWs are grown in same experiments and have a Ge concentration of 6%. The detailed growth condition and SEM images can be found in part 4.2.1

and figure 4.1, respectively. In figure 4.20 a), the Au catalyzed NW has a mono-crystalline structure, the crystalline part extends almost till the surface of the NW. The crystallinity of the Sn catalyzed NWs has been observed mainly have two types. The first type is shown in figures 4.20 b) and 4.20 f). This NW is almost fully crystalized but has multiple twin planes in the radial direction. The twinning also occurs in the axial direction and leads to the change of the growth direction, as shown in figure 4.20 b). The second type is near mono-crystalline, as the NW shown in figure 4.20 c). The FFT of this figure is shown in figure 4.20 e). It gives a set of <111> dot. This indicates that the NW is crystalline and has a growth direction of <211>. Figure 4.20 d) shows the enlarged HRTEM image at the surface of this NW. It can be seen that the crystalline part almost extends to the surface of the NW, and there in only 1 to 2 nm of amorphous material at the surface. Figure 4.20 g) and h) show a NW catalyzed by In. The HRTEM image is taken in <110> direction. In the enlarged image in h), it can be seen clearly that the NW has multiple twins in the radial direction.

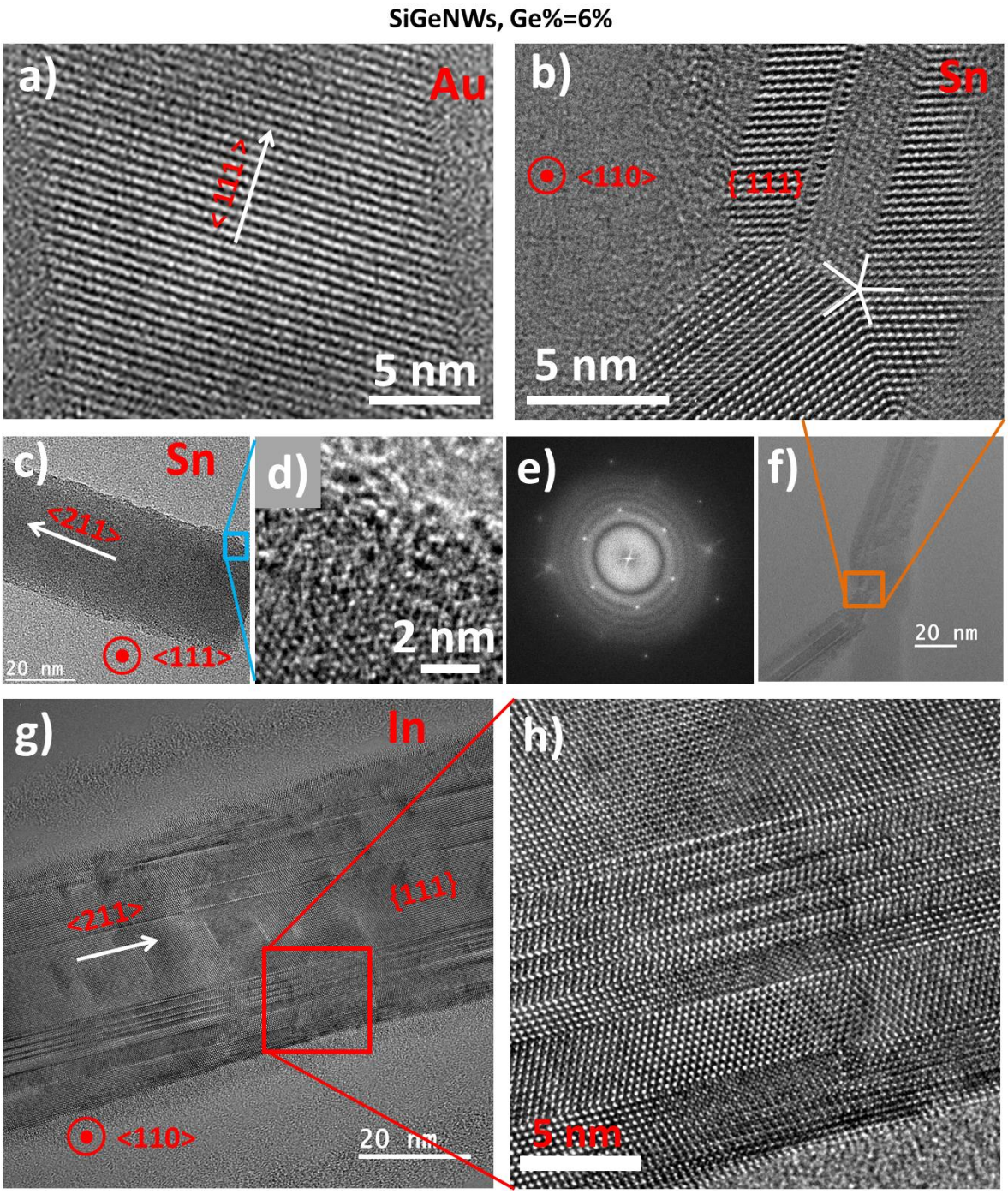


Figure 4.20. TEM characterization of SiGeNWs catalyzed by different metals: a) Au; b) Sn; c) Sn; d) In. b) is a zoom of the area indicated in f). d) is enlarged area indicated in c). e) is FFT of c). h) is the enlarged area of g).

With increased Ge concentration, the crystallinity of the SiGeNWs still shows a large variation. Figure 4.21 shows the HRTEM images of two SiGeNWs catalyzed by Sn. These two NWs are from same growth experiment and have a Ge concentration around 25%. The NW in figure 4.21 a) has a monocrystalline structures. The atomic arrangement shows a Si <111> plane, and the growth direction is <211>. The second NW in figure 4.21 b) has a core-shell structure. The core part has a defective crystalline structure and the shell has an amorphous structure. The FFT of the figure 4.21 c) is shown in the inset. The pattern shows Si <111> atomic planes with multiple twins. This structure is

very similar with the one which has been observed in the SiNWs, which has been explained in chapter 3.

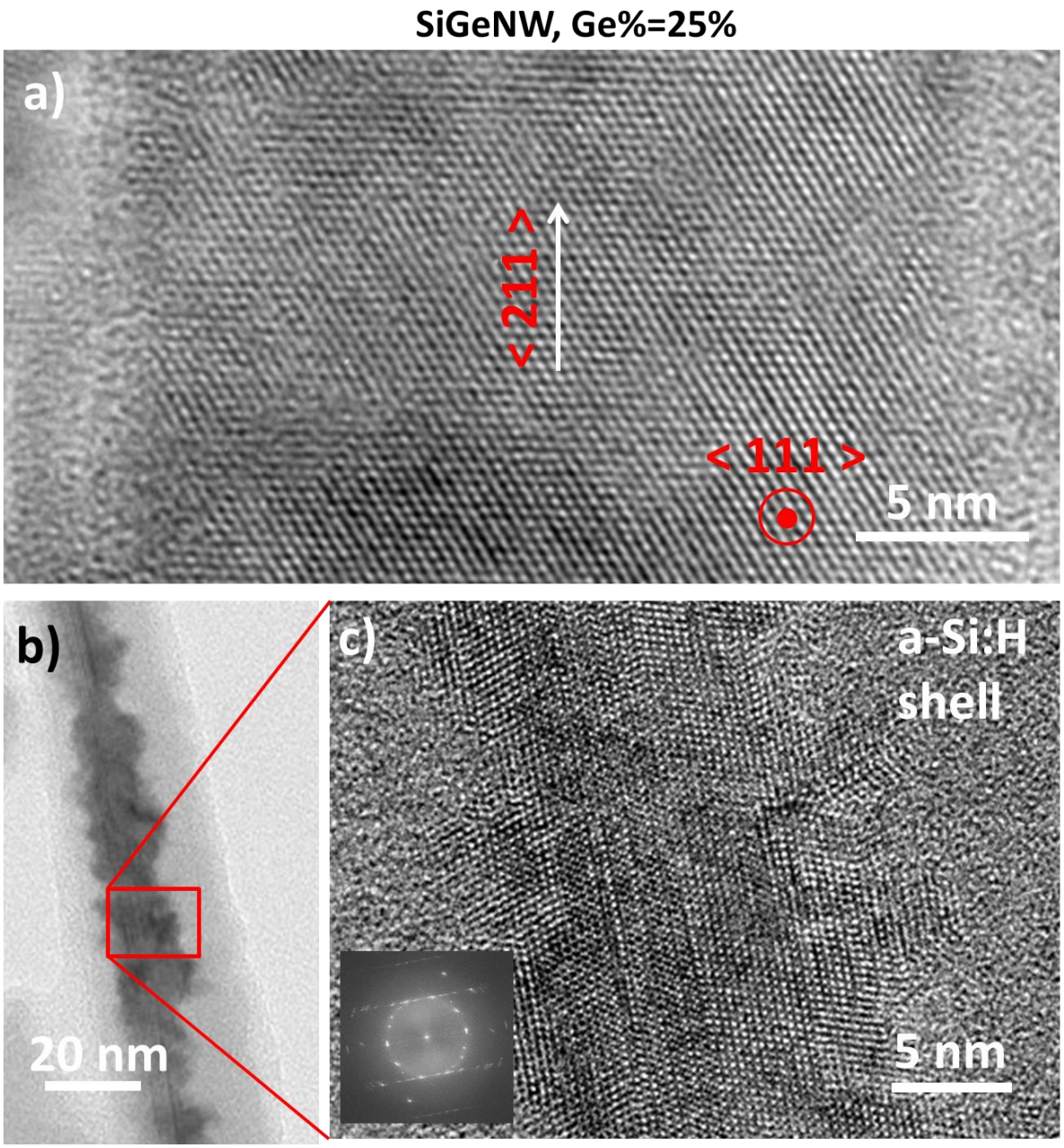


Figure 4.21. High resolution TEM image of SiGeNWs catalyzed by Sn. a) HRTEM image of a SiGeNW. b) HRTEM image of another SiGeNW. c) Zoom of the area indicated in b), with the FFT shown in the inset.

Figure 4.22 shows a high resolution TEM image of GeNWs grown at 400°C. The catalyst is In. The SEM characterization of the same sample can be found in figure 4.10 d). It can be seen that the GeNWs are fully crystallized. The NW has a <111> growth direction. Almost no amorphous layer can be observed at the surface of the NW. Interestingly, nanodots can be seen on the surface of the NWs shown in figure 4.21 a). From the contrast of the image, it can be infered that the nanodots are not metal. In figure 4.21 c), it can be seen that same crystalline structure is observed at the area where the dot stays. There are two possible ways to explain the HRTEM image. The first one is that the dots

are amorphous Ge, it is transparent to the e-beam during the formation of HRTEM image. The second is that due to the high energy e-beam, the nanodots recrystallized on the GeNW surface.

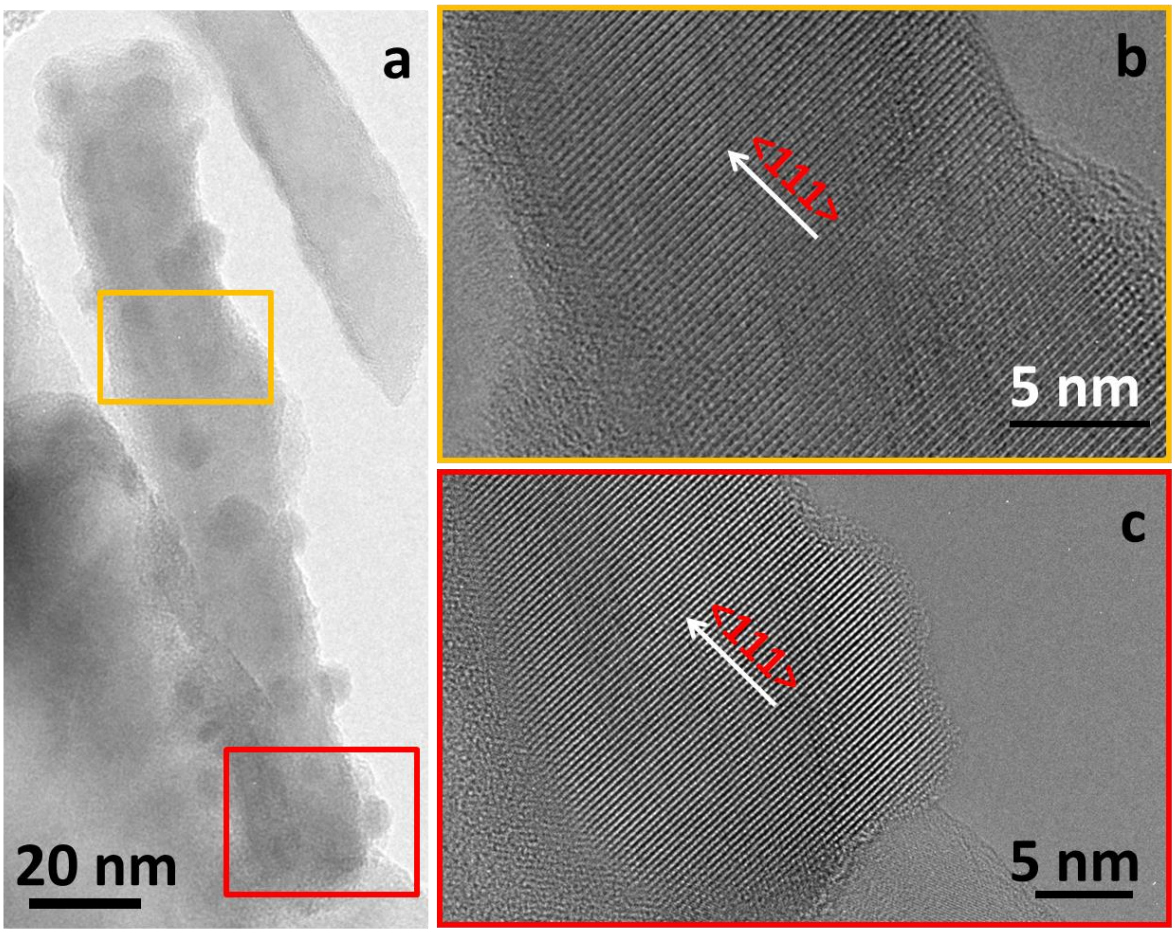


Figure 4.22. High resolution TEM images of In catalyzed GeNW grown at 400°C. a) Bright filed TEM image of the GeNW; b) zoom of the area indicated by the orange frame in a); c) zoom the area indicated by the red frame in the bottom of a).

The STEM-EDX measurements have been done for the cylindrical GeNWs which are grown at 400°C and catalyzed by In. Figure 4.23 a) shows the High Angle Annular Dark Field (HAADF) image of such GeNW. The NW has a uniform diameter along the axial direction which is in the range of 10 to 20 nm. The atomic mapping in figure 4.23 b) shows that this NW is composed of Ge. At the same time, In signal is also detected along the whole NW length with a low intensity, as shown in figure 4.23 c). Figures 4.23 d) to g) show the Ge, Si, In and O map of the area indicated by the red frame in a). It shows that the main component of the NW is Ge. Si, In, and O distribute uniformly in the NW. Since there is Si material on the sidewall of the PECVD which has been used to synthesis the GeNWs, it is no surprising that some Si is incorporated in the GeNWs. The presence of In proves that this GeNW is catalyzed by In. There is In incorporation into the GeNW during the growth[58]. The distribution of the In signal is quite uniform along the radial and axial direction.

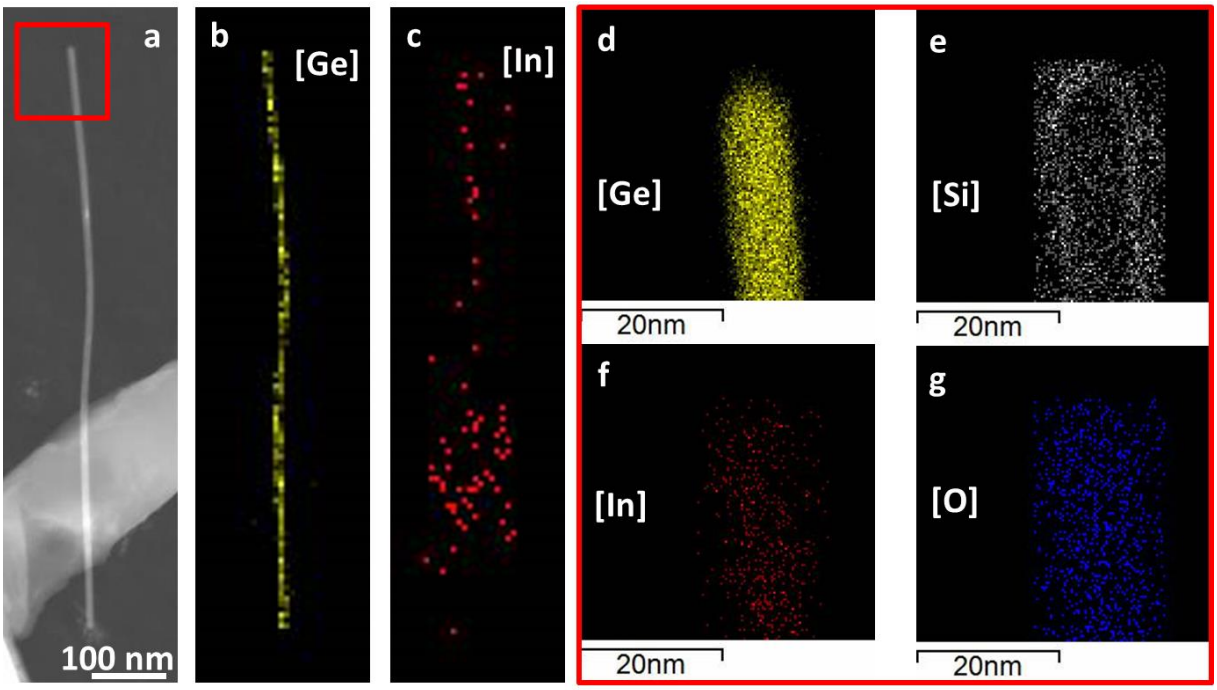


Figure 4.23. STEM-EDX study of a In catalyzed GeNW grown at 400°C. a) High Angle Annular Dark Field (HAADF) image of a GeNW. b) Ge map of the GeNW shown in a). c) In map of the GeNW shown in a). d)-e) Ge, Si, In and O maps of the area indicated by the red frame in a).

### 4.3.3 Electrical and Optical properties studied by photoluminescence and absorptance measurements

The bandgap is an important parameter for semiconductor materials. In order to check the effect of the alloying of Ge on the bandgap, we have conducted photoluminescence (PL) measurements on a SiGeNW sample. The NW growth is carried out on Si wafer substrate with Sn catalyst. Raman characterization of this sample gives a Ge concentration around 14%. Figure 4.24 shows the photon emission spectrum of this sample at different temperatures. The measurements started at room temperature 300K, and then the temperature was decreased to 9 K directly. After the PL measurement at 9 K, the temperature was increased step by step till room temperature and measurements have been done at each step. The signals obtained at the beginning and at the end of the experiment are quite similar, indicating that cooling down to 9 K did not modify the sample and that the system has a good stability. At 9 K, the main peak is around 1183 nm. This corresponds to an electron energy of 1.05 eV. At same temperature, the crystalline Si peak is at 1127 nm. The 56 nm shift is a clear proof of the bandgap narrowing. The small value of the shift is Due to the low Ge concentration in the SiGeNWs. With the increase of temperature, the PL signal decrease rapidly. This indicates that the NW has a high defect density and that a surface passivation should be applied.

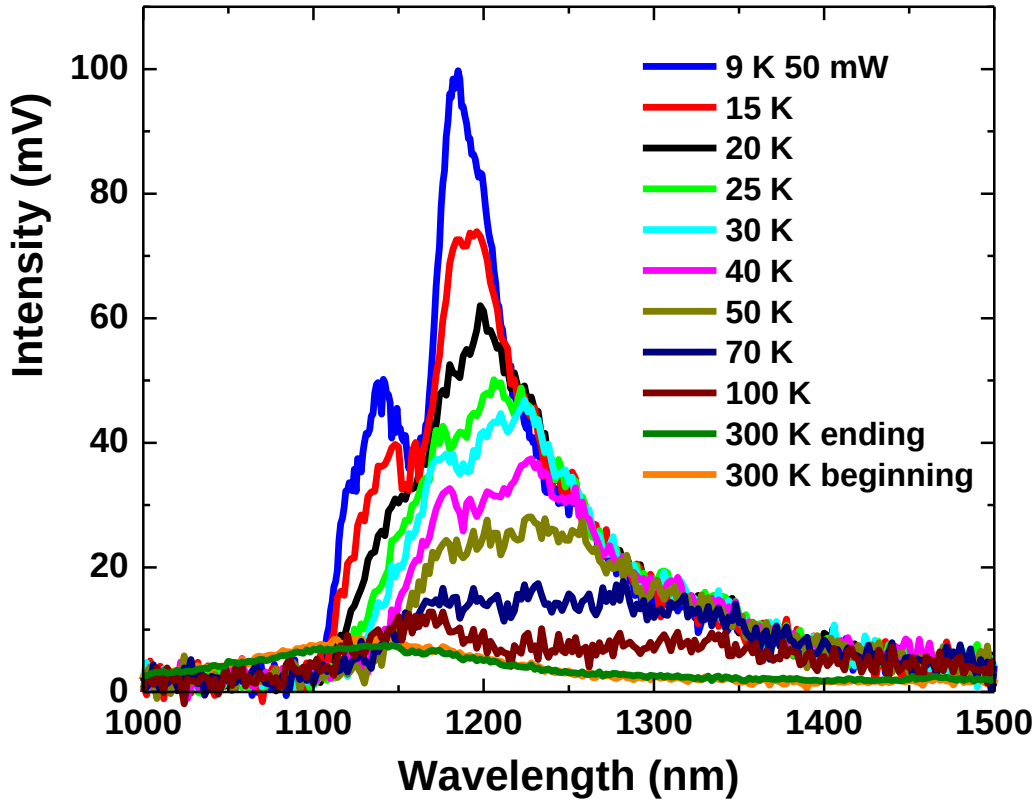


Figure 4.24. Photoluminescence signal of a SiGeNW (Ge content ~ 14%) sample measured at different temperatures.

With the increase of Ge concentration, the absorption of the SiGe material can be increased significantly. In order to check the enhancement of the absorptance of SiGeNWs with increased Ge concentration, we have carried out reflectance and transmittance measurements on SiGeNWs with different Ge concentrations. All the measured SiGeNW samples are grown on Al doped ZnO deposited on Corning glass substrates. They are Cu catalyzed and have Ge concentration of 35%, 75% and 100%. The absorptance and the reflectance of the three SiGe samples as well as that of the substrate are shown in figure 4.25. The absorptance is calculated as:

$$absorptance = 1 - reflectance - transmittance$$

In figure 4.25 a), the absorptance of the four samples has been plotted as a function of wavelength. Between 300 and 600 nm, all the SiGeNW samples have an absorptance above 90%. This is due to the fact that high energy can be absorbed by the SiGe material easily, even with low Ge concentration. When the wavelength is above 600 nm, it is apparent that the increase the Ge concentration can enhance the absorptance significantly. Such an enhancement demonstrates that the SiGeNWs and GeNWs are suited to be used as bottom cell absorber in multi-junction solar cells. The reflectance of the samples is shown in figure 4.25 b). There is a sharp decrease when the wavelength is in the range of 1100 to 1400 nm. This is due to the presence of the ZnO:Al layer, since

the thickness of this layer is in the range of 300 to 400 nm (around one fourth of the wavelength). When the wavelength is above 1500 nm, the reflectance of the SiGeNW samples is higher than that of the planar substrate. This can be explained by two main reasons. Firstly, SiGe material has low absorption to photons with such a big wavelength. Secondly, as shown in figure 4.6, the SiGeNWs have a small diameter and small inter distance compared with the wavelength. Thus the anti-reflection effect of the NW array doesn't occur.

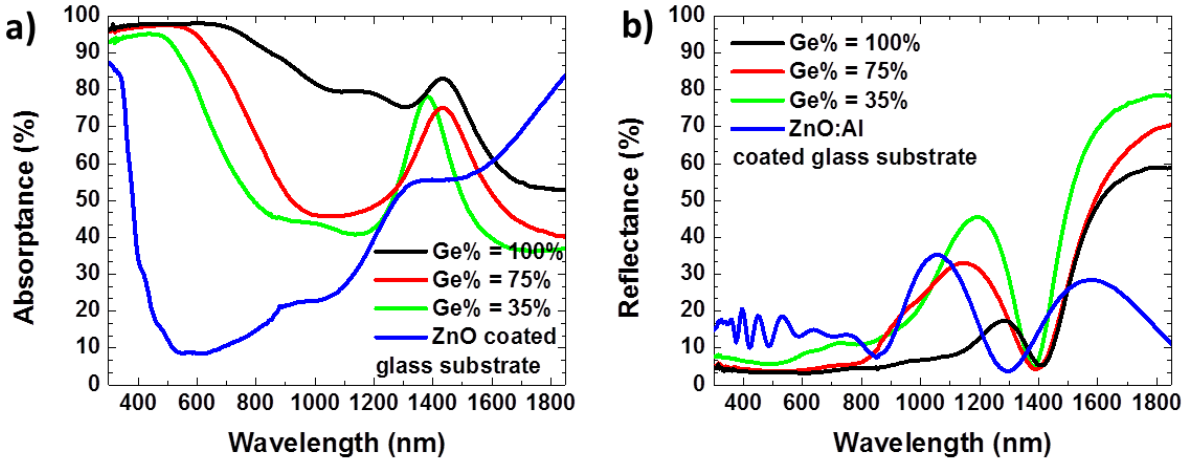


Figure 4.25. Absorptance and reflectance of SiGeNWs with different Ge concentration: a) absorptance; b) reflectance. The data of the ZnO:Al coated substrate shown by the blue curves are used as reference.

## 4.4 Summary

In this chapter, we have successfully grown SiGeNW with Sn, In, Au and Cu by plasma assisted VLS. We found at 400°C, Cu and In can catalyze SiGeNWs with larger $GeH_4/(SiH_4+GeH_4)$ ratio than Sn and Au. The morphology of the SiGeNWs catalyzed by these catalysts does not have significant difference. The length of the NW is mainly determined by the flux of the SiHx and GeHx, and also the catalyst droplets size. To our knowledge, this is the first report of SiGeNWs growth by plasma assisted VLS method.

By decreasing the substrate temperature, we have successfully grown high Ge concentration SiGeNWs. We found that there is no degradation of the SiGeNW morphology with the increase of Ge concentration and the decrease of substrate temperature. At 235°C, pure GeNW have also been grown with Sn, In and Cu.

By increasing the substrate temperature and $GeH_4$ partial pressure, we have found that straight GeNWs with constant diameter can be grown with Sn and In. We have divided the GeNW growth into two regimes. When the temperature is below 350°C and $GeH_4$ partial pressure is below 20 mTorr, the traditional plasma assisted VLS NW morphology (tapered NW morphology) is obtained. When the temperature is above 350°C and $GeH_4$ partial pressure is above 20 mTorr, non-tapered NWs can be obtained. We have shown that plasma and catalyst are essential for these non-tapered GeNW growth. By observing the growth process of these GeNWs, we found that three kinds of crystal growth occur simultaneously: small diameter GeNW growth, non-catalyzed Ge crystal growth, large

In droplets catalyzed crystal growth. To our knowledge, this is the first report which clearly shows NWs with constant diameter obtained by plasma-assisted VLS growth.

By Raman spectroscopy and EDX study, we show the relationship of Ge atomic concentration in the SiGeNWS and the $GeH_4/(GeH_4+SiH_4)$ gas flow rate ratio. The results deduced from Raman spectroscopy have a good agreement with the results deduced from EDX measurements.

We have studied the crystallinity of SiGe and Ge nanowires. We found that the NWs mainly have two types of crystallinities: monocrystalline and crystalline core-amorphous shell structure. The most common defects that we have found in these NWs are twins.

STEM-EDX has been carried to study cylindrical GeNWs. We found that the catalyst In is uniformly distributed in the GeNWs. This proves that In is involved during the cylindrical GeNW growth.

Photoluminescence measurements at 9 K show that the emission peak of the SiGeNWs is shifted to a longer wavelength value. This shows the decrease of the bandgap. The absorptance measurement of the SiGeNWs show that with the increase of Ge concentration, the absorption of the SiGeNWs in the infrared range increases significantly, which is highly desirable for solar cells applications.

## References


1 Fischetti, M. V. & Laux, S. E. Band structure, deformation potentals, and carrier mobility in strained Si, Ge, and SiGe alloys. *Journal of Applied Physics* **80**, 2234-2252, doi:10.1063/1.363052 (1996).

2 Abdul Hadi, S. *et al.* Thin-film Si1−xGex HIT solar cells. *Solar Energy* **103**, 154-159, doi:http://dx.doi.org/10.1016/j.solener.2014.01.039 (2014).

3 Bremner, S. P., Yi, C., Almansouri, I., Ho-Baillie, A. & Green, M. A. Optimum band gap combinations to make best use of new photovoltaic materials. *Solar Energy* **135**, 750-757, doi:http://dx.doi.org/10.1016/j.solener.2016.06.042 (2016).

4 Cariou, R., Tang, J., Ramay, N., Ruggeri, R. & Roca i Cabarrocas, P. Low temperature epitaxial growth of SiGe absorber for thin film heterojunction solar cells. *Solar Energy Materials and Solar Cells* **134**, 15-21, doi:http://dx.doi.org/10.1016/j.solmat.2014.11.018 (2015).

5 Brunner, K. Si/Ge nanostructures. *Reports on Progress in Physics* **65**, 27-72, doi:10.1088/0034-4885/65/1/202 (2002).

6 Wu, Y. Y., Fan, R. & Yang, P. D. Block-by-block growth of single-crystalline Si/SiGe superlattice nanowires. *Nano Letters* **2**, 83-86, doi:10.1021/nl0156888 (2002).

7 Lauhon, L. J., Gudiksen, M. S., Wang, C. L. & Lieber, C. M. Epitaxial core-shell and core-multishell nanowire heterostructures. *Nature* **420**, 57-61, doi:10.1038/nature01141 (2002).

8 Glas, F. & Daudin, B. Stress-driven island growth on top of nanowires. *Physical Review B* **86**, 174112 (2012).

9 Yu, L. *et al.* Bismuth-Catalyzed and Doped Silicon Nanowires for One-Pump-Down Fabrication of Radial Junction Solar Cells. *Nano Lett.* **12**, 4153-4158, doi:10.1021/nl3017187 (2012).

10 Misra, S., Yu, L., Foldyna, M. & Roca i Cabarrocas, P. High efficiency and stable hydrogenated amorphous silicon radial junction solar cells built on VLS-grown silicon nanowires. *Sol Energ Mat Sol C* **118**, 90-95, doi:http://dx.doi.org/10.1016/j.solmat.2013.07.036 (2013).

11 Amato, M., Palummo, M., Rurali, R. & Ossicini, S. Silicon-Germanium Nanowires: Chemistry and Physics in Play, from Basic Principles to Advanced Applications. *Chemical Reviews* **114**, 1371-1412, doi:10.1021/cr400261y (2014).

12 Wagner, R. S. & Ellis, W. C. Vapor-Liquid-Solid mechanism of single crystal growth. *Appl Phys Lett* **4**, doi:10.1063/1.1753975 (1964).

13 Duan, X. & Lieber, C. M. General Synthesis of Compound Semiconductor Nanowires. *Advanced Materials* **12**, 298-302, doi:10.1002/(SICI)1521-4095(200002)12:4<298::AID-ADMA298>3.0.CO;2-Y (2000).

14 Wolfsteller, A. *et al.* Comparison of the top-down and bottom-up approach to fabricate nanowire-based Silicon/Germanium heterostructures. *Thin Solid Films* **518**, 2555-2561, doi:10.1016/j.tsf.2009.08.021 (2010).

15 Givan, U. & Patolsky, F. Pressure-Modulated Alloy Composition in Si(1-x)Gex Nanowires. *Nano Letters* **9**, 1775-1779, doi:10.1021/nl803657z (2009).

16 Hanrath, T. & Korgel, B. A. Supercritical fluid-liquid-solid (SFLS) synthesis of Si and Ge nanowires seeded by colloidal metal nanocrystals. *Advanced Materials* **15**, 437-440, doi:10.1002/adma.200390101 (2003).

17 Morales, A. M. & Lieber, C. M. A laser ablation method for the synthesis of crystalline semiconductor nanowires. *Science* **279**, 208-211, doi:10.1126/science.279.5348.208 (1998).

18 Benkouider, A. *et al.* Selective growth and ordering of SiGe nanowires for band gap engineering. *Nanotechnology* **25**, 335303 (2014).

19 Sutter, E., Camino, F. & Sutter, P. One-step synthesis of Ge-SiO2 core-shell nanowires. *Applied Physics Letters* **94**, 3, doi:10.1063/1.3089235 (2009).

20 Lew, K. K., Pan, L., Dickey, E. C. & Redwing, J. M. Vapor-liquid-solid growth of silicon-germanium nanowires. *Advanced Materials* **15**, 2073, doi:10.1002/adma200306035 (2003).

21 Lockwood, D. J. *et al.* Bright photoluminescence from ordered arrays of SiGe nanowires grown on Si(111). *Beilstein Journal of Nanotechnology* **5**, 2498-2504, doi:10.3762/bjnano.5.259 (2014).

22 Chen, L., Fung, W. Y. & Lu, W. Vertical Nanowire Heterojunction Devices Based on a Clean Si/Ge Interface. *Nano Letters* **13**, 5521-5527, doi:10.1021/nl403112a (2013).

23 Mullane, E., Kennedy, T., Geaney, H., Dickinson, C. & Ryan, K. M. Synthesis of Tin Catalyzed Silicon and Germanium Nanowires in a Solvent–Vapor System and Optimization of the Seed/Nanowire Interface for Dual Lithium Cycling. *Chemistry of Materials* **25**, 1816-1822, doi:10.1021/cm400367v (2013).

24 Xiang, Y. *et al.* Single crystalline and core-shell indium-catalyzed germanium nanowires-a systematic thermal CVD growth study. *Nanotechnology* **20**, doi:10.1088/0957-4484/20/24/245608 (2009).

25 Schmidt, V., Wittemann, J. V., Senz, S. & Gosele, U. Silicon Nanowires: A Review on Aspects of their Growth and their Electrical Properties. *Advanced Materials* **21**, 2681-2702, doi:10.1002/adma.200803754 (2009).

26 Ratchford, J. B. *et al.* Gold Removal from Germanium Nanowires. *Langmuir* **25**, 9473-9479, doi:10.1021/la900725b (2009).

27 Wang, Y.-C. & Chen, I. C. Low-temperature plasma-assisted growth of germanium nanorods. *CrystEngComm* **16**, 2937-2943, doi:10.1039/C3CE42120A (2014).

28 Kang, K. *et al.* Low-Temperature Deterministic Growth of Ge Nanowires Using Cu Solid Catalysts. *Advanced Materials* **20**, 4684-4690, doi:10.1002/adma.200801764 (2008).

29 Vitos, L., Ruban, A. V., Skriver, H. L. & Kollar, J. The surface energy of metals. *Surf. Sci.* **411**, 186-202, doi:10.1016/s0039-6028(98)00363-x (1998).

30 Xia, Y. *et al.* One-Dimensional Nanostructures: Synthesis, Characterization, and Applications. *Advanced Materials* **15**, 353-389, doi:10.1002/adma.200390087 (2003).

31 Kodambaka, S., Tersoff, J., Reuter, M. C. & Ross, F. M. Germanium nanowire growth below the eutectic temperature. *Science* **316**, 729-732, doi:10.1126/science.1139105 (2007).

32 Vardi, A. *et al.* Room temperature demonstration of GaN/AlN quantum dot intraband infrared photodetector at fiber-optics communication wavelength. *Appl Phys Lett* **88**, 143101, doi:http://dx.doi.org/10.1063/1.2186108 (2006).

33 Meng, A. C. *et al.* Core/Shell Germanium/Germanium-Tin Nanowires Exhibiting Room Temperature Direct- and Indirect-Gap Photoluminescence. *Nano letters* (2016).

34 Meng, A. C. *et al.* Core-Shell Germanium/Germanium–Tin Nanowires Exhibiting Room-Temperature Direct- and Indirect-Gap Photoluminescence. *Nano Letters* **16**, 7521-7529, doi:10.1021/acs.nanolett.6b03316 (2016).

35 Periwal, P., Baron, T., Gentile, P., Salem, B. & Bassani, F. Growth strategies to control tapering in Ge nanowires. *Apl Materials* **2**, doi:10.1063/1.4870875 (2014).

36 Pei, L. Z. & Cai, Z. Y. A Review on Germanium Nanowires. *Recent Patents on Nanotechnology* **6**, 44-59 (2012).

37 Mohammad, S. N. VQS (vapor-quasiliquid-solid, vapor-quasisolid-solid) mechanism for the catalyst-free and catalyst-mediated non-eutectic syntheses of single-crystal nanowires. *Journal of Applied Physics* **120**, 16, doi:10.1063/1.4961092 (2016).

38 Kim, B. S. *et al.* Catalyst-free Growth of Single-Crystal Silicon and Germanium Nanowires. *Nano Letters* **9**, 864-869, doi:10.1021/nl803752w (2009).

39 Puzder, A., Williamson, A. J., Reboredo, F. A. & Galli, G. Structural Stability and Optical Properties of Nanomaterials with Reconstructed Surfaces. *Physical Review Letters* **91**, 157405 (2003).

40 Jin, C. B., Yang, J. E. & Jo, M. H. Shape-controlled growth of single-crystalline Ge nanostructures. *Applied Physics Letters* **88**, doi:10.1063/1.2201899 (2006).

41 Lauhon, L. J., Gudiksen, M. S. & Lieber, C. M. Semiconductor nanowire heterostructures. *Philosophical Transactions of the Royal Society of London Series a-Mathematical Physical and Engineering Sciences* **362**, 1247-1260, doi:10.1098/rsta.2004.1377 (2004).

42 Sierra-Sastre, Y., Dayeh, S. A., Picraux, S. T. & Batt, C. A. Epitaxy of Ge Nanowires Grown from Biotemplated Au Nanoparticle Catalysts. *ACS Nano* **4**, 1209-1217, doi:10.1021/nn901664r (2010).

43 Hanrath, T. & Korgel, B. A. Nucleation and growth of germanium nanowires seeded by organic monolayer-coated gold nanocrystals. *J. Am. Chem. Soc.* **124**, 1424-1429, doi:10.1021/ja016788i (2002).

44 Kamins, T. I., Li, X. & Williams, R. S. Growth and structure of chemically vapor deposited Ge nanowires on Si substrates. *Nano Letters* **4**, 503-506, doi:10.1021/nl035166n (2004).

45 Woodruff, J. H., Ratchford, J. B., Goldthorpe, I. A., McIntyre, P. C. & Chidsey, C. E. D. Vertically oriented germanium nanowires grown from gold colloids on silicon substrates and subsequent gold removal. *Nano Letters* **7**, 1637-1642, doi:10.1021/nl070595x (2007).

46 Day, R. W. *et al.* Plateau–Rayleigh crystal growth of periodic shells on one-dimensional substrates. *Nat Nano* **10**, 345-352, doi:10.1038/nnano.2015.23 (2015).

47 Day, R. W., Mankin, M. N. & Lieber, C. M. Plateau–Rayleigh Crystal Growth of Nanowire Heterostructures: Strain-Modified Surface Chemistry and Morphological Control in One, Two, and Three Dimensions. *Nano Letters* **16**, 2830-2836, doi:10.1021/acs.nanolett.6b00629 (2016).

48 Xue, Z. *et al.* Engineering island-chain silicon nanowires via a droplet mediated Plateau-Rayleigh transformation. *Nature Communications* **7**, 12836, doi:10.1038/ncomms12836 (2016).

49 Tsang, J. C., Mooney, P. M., Dacol, F. & Chu, J. O. Measurements of alloy composition and strain in thin GexSi1−x layers. *Journal of Applied Physics* **75**, 8098-8108, doi:http://dx.doi.org/10.1063/1.356554 (1994).

50 Kawashima, T. *et al.* Raman and electron microscopic studies of Si1−xGex alloy nanowires grown by chemical vapor deposition. *Journal of Applied Physics* **102**, 124307, doi:http://dx.doi.org/10.1063/1.2817619 (2007).

51 Lee, W.-J. *et al.* The modulation of Si1-xGexnanowires by correlation of inlet gas ratio with H2 gas content. *CrystEngComm* **13**, 5204-5211, doi:10.1039/C1CE05157A (2011).

52 Potié, A. *et al.* Growth and characterization of gold catalyzed SiGe nanowires and alternative metal-catalyzed Si nanowires. *Nanoscale Research Letters* **6**, 187, doi:10.1186/1556-276x-6-187 (2011).

53 Zhuang, X., Ning, C. Z. & Pan, A. Composition and Bandgap-Graded Semiconductor Alloy Nanowires. *Advanced Materials* **24**, 13-33, doi:10.1002/adma.201103191 (2012).

54 Lu, Q. *et al.* Raman Scattering from Si1-xGex Alloy Nanowires. *The Journal of Physical Chemistry C* **112**, 3209-3215, doi:10.1021/jp074764d (2008).

55 Cerva, H. HIGH-RESOLUTION ELECTRON-MICROSCOPY OF DIAMOND HEXAGONAL SILICON IN LOW-PRESSURE CHEMICAL VAPOR-DEPOSITED POLYCRYSTALLINE SILICON. *Journal of Materials Research* **6**, 2324-2336, doi:10.1557/jmr.1991.2324 (1991).

56 Meyerson, B. S. & Jasinski, J. M. Silane pyrolysis rates for the modeling of chemical vapor deposition. *Journal of Applied Physics* **61**, 785-787, doi:http://dx.doi.org/10.1063/1.338180 (1987).

57 Bootsma, G. A. & Gassen, H. J. A quantitative study on the growth of silicon whiskers from silane and germanium whiskers from germane. *Journal of Crystal Growth* **10**, 223-234, doi:http://dx.doi.org/10.1016/0022-0248(71)90188-6 (1971).

58 Chen, W. *et al.* Incorporation and redistribution of impurities into silicon nanowires during metal-particle-assisted growth. *Nature Communications* **5**, doi:10.1038/ncomms5134 (2014).

# Chapter 5 Towards low cost NW based radial junction solar cells

## Contents

## 5.1 Introduction

NWs have many fundamental advantages for solar cell applications, such as an excellent optical absorption[1], low consumption of the material, low requirements on the quality of the material, and a tunable bandgap[2]. Within the past two decades, the research on NWs and NW solar cells has witnessed fast developments and substantial achievements. Since 2002, NWs are used to fabricate photovoltaic devices[2]. In the first report, CdSe NWs (or nanorods) were used to fabricate hybrid solar cells with polymers. A power conversion efficiency of 1.7% was obtained. Since then, numerous studies have been done on NW solar cells, both with bottom up approach[3-6] and top down approach[7,8]. However, making high efficiency and low cost solar cells with NW arrays has great challenges. Firstly, the large surface to volume ratio of the nanowire structure might lead to large surface or interface recombination. Secondly, it is difficult to fabricate NW arrays with well controlled morphology and good uniformity on low cost substrates with low cost approach. Thirdly, with certain bottom up NW synthesis methods, the incorporation of the metal catalyst into the NWs might be a limitation for the solar cells performance. Lastly, it is challenging to deposit conformal, low defect density layers on the high aspect ratio NW arrays. As a matter of fact, the large majority of the NW solar cells reported in the literature have efficiency below 10%[9-13]. There are few group reports on NW solar cells with efficiencies bigger than 10%[14,15]. However, these solar cells have a high fabrication cost. Meanwhile, their efficiencies are still far lower than the record efficiency of the first generation Si solar cells, which has reached 26.3%.

Whether NW solar cells can exceed the efficiency of planar counterparts or not is still an open question. The significance of using NW geometry for solar cells applications is that they reduce the quantity and quality of material requirements. They provide the possibility to fabricate relatively high efficiency solar cells at a relatively low cost with respect to planar counterparts. To achieve low cost NW solar cells, it requires low cost fabrication processes on low cost substrates. At LPICM, we have worked on low cost SiNW based radial p-i-n junction solar cells since 2009. Progress has been made and reported annually: 2010, 0.25%[16]; 2011 4.9%[17]; 2012, 5.6%[18]; 2013, 8.7%[19]; 2015, 9.2%[20], and 2016 9.7%[21]. Since the efficiency is approaching the record of planar a-Si:H solar cells (10.2 ±0.3%[22]), it becomes more difficult to further improve the efficiency. A novel approach is needed to reach higher values. Multi junction solar cells are promising designs to this end. In a multi junction solar cell, there are materials with different bandgaps to absorb photons from different ranges of the solar spectrum. In our research, we use a low cost PECVD system to deposit the absorber material. With such a system, a high bandgap material pm-Si:H, middle bandgap material a-SiGe:H[23] or µc-Si, and low bandgap material crystalline SiGe (deposit with catalyst) can be deposited easily. During the past 5 years we have heavily invested the NW radial junction solar cells based on high bandgap materials (a-Si:H and pm-Si:H). However, the middle bandgap material and low bandgap materials have not been invested intensively, despite their successful application in solar cells leading to efficiencies up to 16.3[24-26]. Thus the potential for low cost NW radial junction solar cells has not been fully explored. Here, we will focus on the use of middle and low bandgap materials for single and tandem NW solar cells. These materials include a-SiGe:H, µc-Si:H and crystalline SiGe.

## 5.2 Fabrication and characterization of NW radial junction solar cells

A solar cell is a device which absorbs light and generates electricity. In order to realize these functions, the device needs to have the following main components: an absorber which absorbs the light and generates free carriers, a junction which separates the free carriers, and contacts which

collect the free carriers and conduct them to the outer circuit. Depending on the type of solar cells, there might be additional components such as a substrate for thin film solar cells.

The main components of our NW based radial junction solar cells are shown in figure 5.1. The absorber and the junction are in the wire form, and their structure can be seen in the enlarged picture on the right. In the center of the wire, there is a p-type doped NW core. The core is surrounded by a thick intrinsic absorber shell, and then a n-type doped second shell. Due to the different doping, an electric field is built across the intrinsic layer. The electric field direction starts from the n shell and points to the p core. The light will be absorbed mainly in the intrinsic absorber layer and electron-hole pairs will be generated there. Due to the built-in electric field, electrons will move to the n layer and get collected by the ITO, while holes will move to the p core and get collected by the ZnO:Al layer beneath. Because the solar cells have a wire form and the junction is along the radial direction, these solar cells are called NW radial junction solar cells. In order to have a better electrical contact between the solar cell and the outer circuit, Ag electrodes are deposited on both ITO and ZnO:Al layers. Since the thickness of our solar cell is only around 1 µm, which is around 50 times smaller than the thickness of the paper, we need a substrate to protect the solar cell mechanically. We use corning glass substrate.

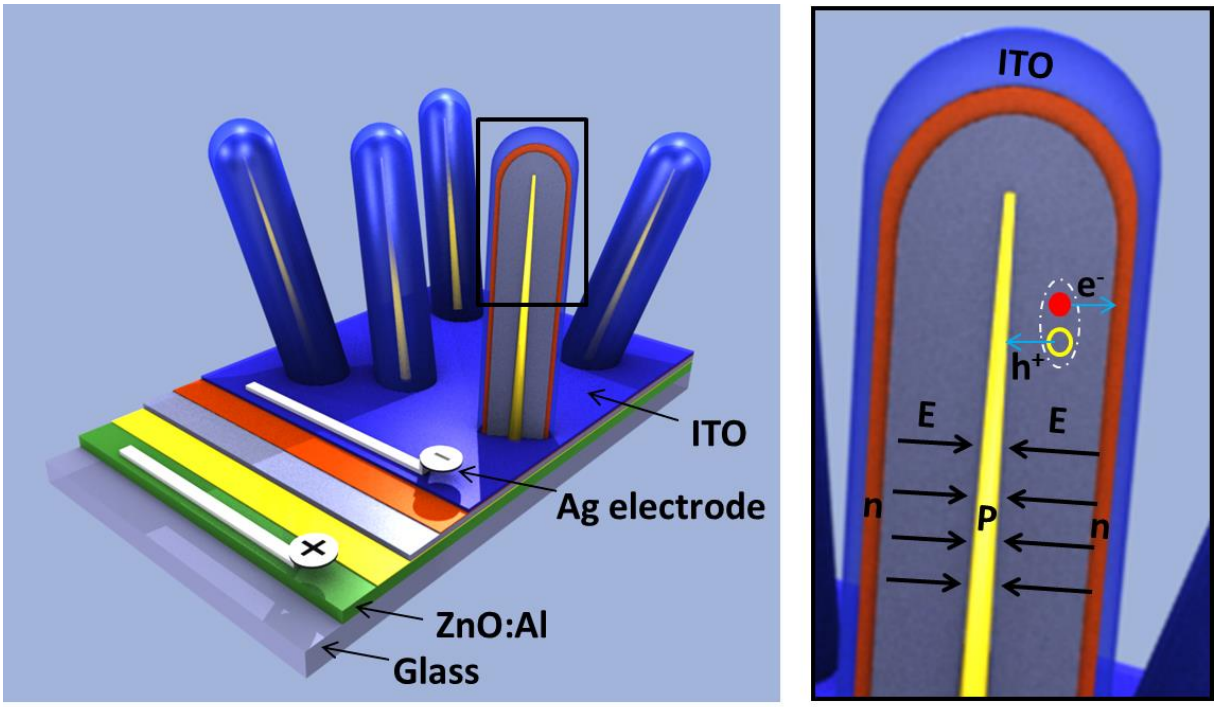


Figure 5.1. 3D illustration of the NW based solar cells. The materials of the planar multi-layers from bottom to top are: Corning glass, ZnO:Al, p-type material for junction formation, i-type (undoped) absorbing material, n-type material for junction formation, and ITO layer. The wires have a core shell structure. As for the planar part, the materials from core to outer shells are: p-type material for junction formation, i-type absorbing material, n-type material for junction formation, and ITO layer. The two strips on ZnO:Al layer and ITO layer are Ag electrodes.

The detailed fabrication processes of the solar cells are shown in figure 5.2. We start with a commercial Corning glass as substrate. On it, we deposit a transparent and conducting ZnO:Al layer for bottom contact. This layer is deposited by sputtering at 200°C. After that, Sn catalyst for NW

growth is deposited on ZnO:Al surface by thermal evaporation. The Sn forms droplets instead of a continuous layer. Then NWs are grown with plasma assisted VLS method. The detailed information on the NW growth can be found in chapters 3 and 4. The NWs are p-type doped. The doping gas is Trimethylboron (TMB). After the NW growth, the intrinsic absorber material is deposited on the NWs. On the absorber sidewall, a n-type material is deposited to form the p-i-n junction. We use $PH_3$ doped µc-SiOx:H for the n layer because this material has good optical transmittance.[20,27,28] The outer shell of the solar cell is another transparent and conducting ITO layer. This layer is deposited by sputtering at 200°C. Finally, silver contacts are deposited on the ZnO:Al layer and ITO layer manually.

As shown in figure 5.1, there is also a planar p-i-n junction deposited between the NWs array. However, because the fraction of the planar part is small and light cannot easily reach this part due to shadowing by the NWs, the planar part has a limited contribution to the solar cell efficiency. Since both the front and the back sides of the solar cell are transparent, our solar cells are bifacial. Compared with standard solar cells, bifacial ones provide the possibility for additional light to reach the absorber layers and can increase the energy output of the solar cells.[29]

These NW solar cells have many layers. However, the majority of the materials have wide bandgaps. For example the bandgap of ZnO:Al is around 3.3 eV, and that of ITO is around 4 eV[30]. The absorption in these layers is negligible. To tune the absorption of the solar cells, the NW material and the absorber material can be varied. These materials are deposited by PECVD, so their properties can be tuned by changing the deposition parameters and precursor gases. The NW material can be crystalline $Si_{1-x}Ge_x$ with x varying from 0 to 100%, and the absorber can be $Si_{1-x}Ge_x$ with crystallinity varying from microcrystalline to amorphous and x varying from 0 to 100%.

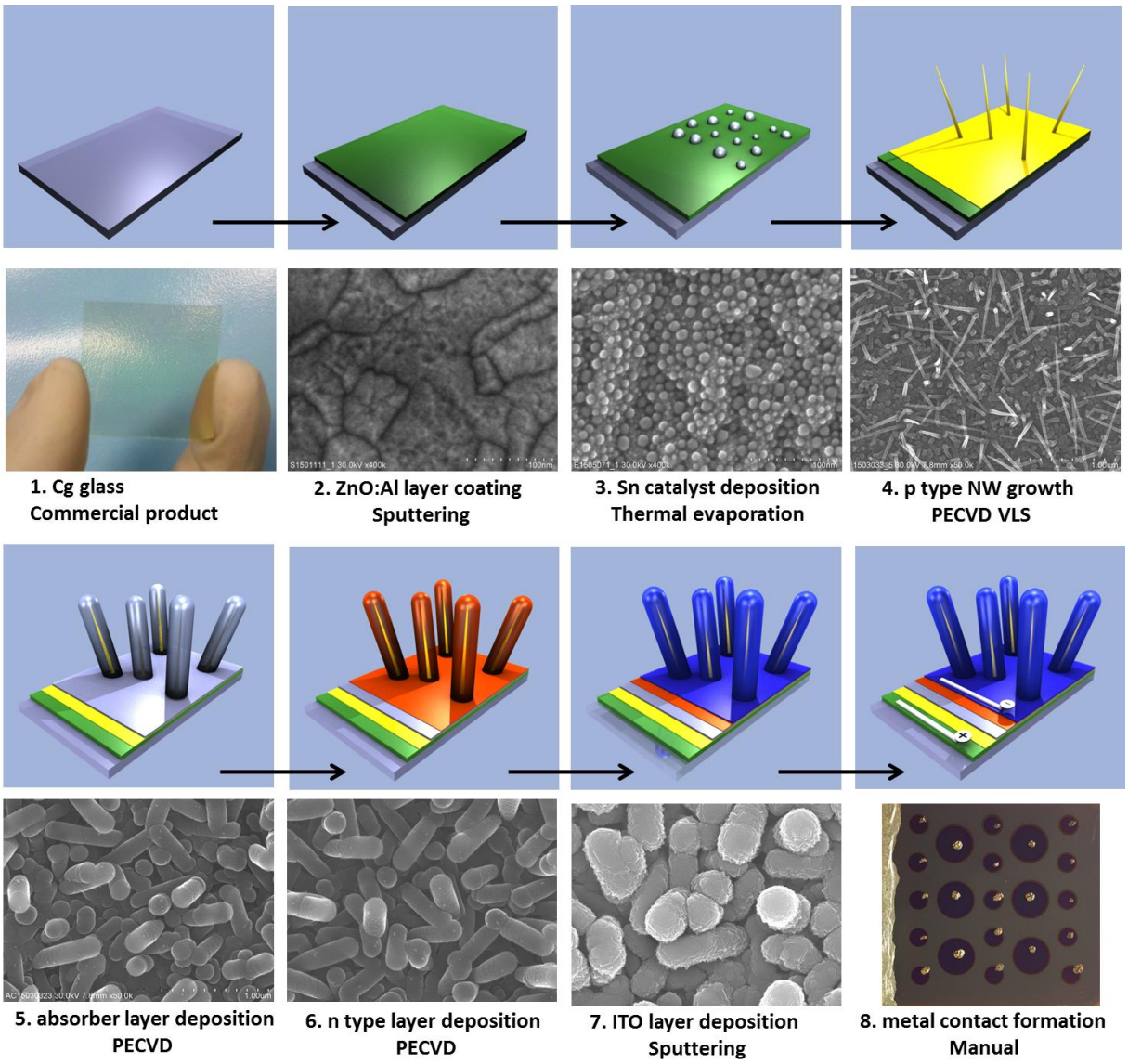


Figure 5.2. SiNW p-i-n radial junction solar cells fabrication processes.

The intrinsic layer and n-type doped layer are deposited in a PECVD reactor called ARCAM.[31] The picture of ARCAM is shown in figure 5.3 a). This is a multiplasma-monochamber system composed of 3 separated chambers located inside a isothermal vacuum vessel. The 3 chamber configuration provides the possibility of depositing different materials without breaking the vacuum. All the three chambers have a similar structure, as shown in figure 5.3 b). There is a radio frequency electrode at the bottom of the chamber to which a 13.56 MHz electromagnetic field is applied to trigger and maintain the plasma. The plasma is confined in the desired volume by a plasma box. The plasma box is closed by a rotating plate which contains the substrates. This reactor usually works in the temperature range between 100°C to 300°C. The absorber materials for NW solar cells are usually deposited at 150°C.

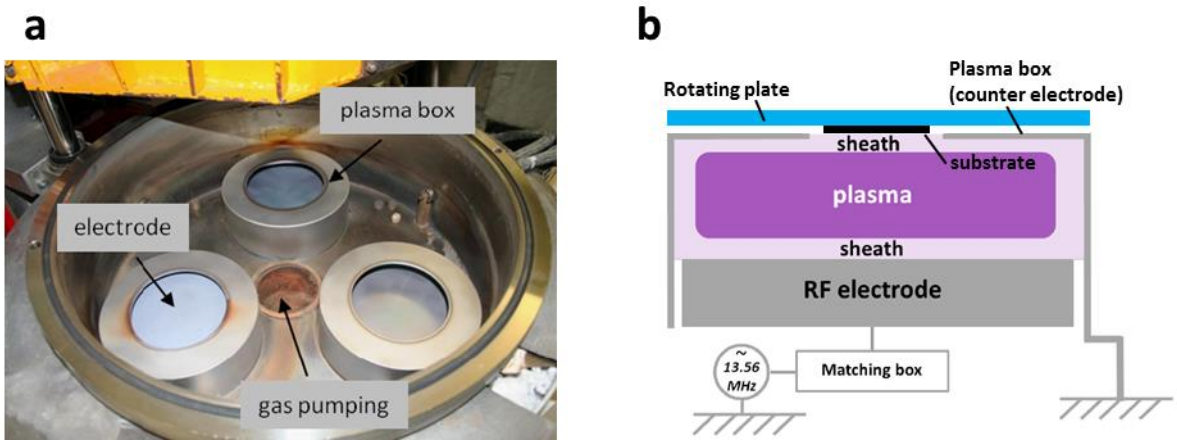


Figure 5.3. a) Picture of the ARCAM PECVD reactor. b) Schematic of the of the structure of the plasma box.

Once the solar cells fabrication processes are completed, the quality of the solar cells can be characterized. Generally, the energy conversion efficiency is the most interesting parameter of the solar cells. Current-voltage measurements are usually used to determine this efficiency. In this measurement, a lamp which emits similar light spectrum as the sun is used as the light source. A supply source is connected to the two electrodes of the solar cell. Then the light is shined on the solar cell and a voltage sweep is applied on the solar cell. The current generated from the solar cell at different applied voltages is measured. A set of data points which shows the output current as a function of applied voltage can be obtained from the measurement. The output power can be calculated as the product of the current and voltage. So we get the power output of the solar cell at different applied voltages. The maximum output power divided by the power of the incident light is the energy conversion efficiency of the solar cell. An example of the result of such measurement is shown in figure 5.4. In this figure, the vertical axis is the current density, which means the total current divided by the area of the solar cell. The horizontal axis is the applied voltage. When the applied voltage is 0, the solar cell is in short circuit condition. The current at this condition is called short circuit current (Jsc). When the applied voltage is increased to a certain value that the output current is 0, the solar cell is working at the open circuit condition. The voltage at this condition is called open circuit voltage (Voc). The fill factor (FF) is defined as the maximum output power divided by the product of Jsc and Voc.

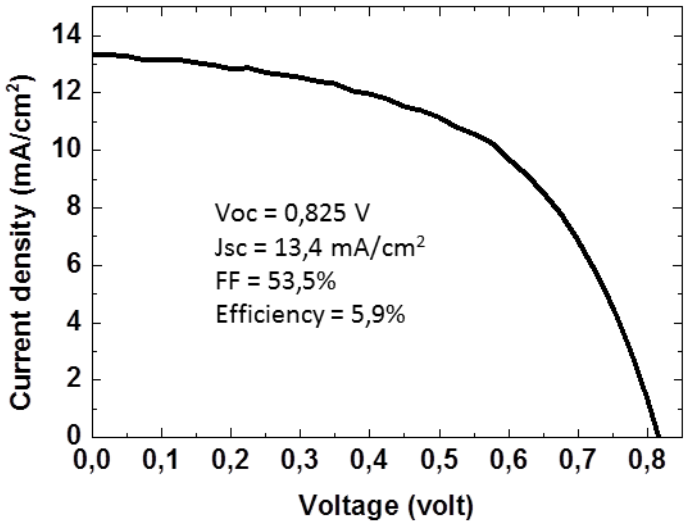


Figure 5.4. Current-Voltage characterization of a NW solar cell measured under AM 1.5

The sun light is composed of photons with different wavelengths. Because the solar cells have different absorption profile for these photons, so the energy conversion efficiency of the solar cell for different photons is different. The performance of the solar cell at each wavelength photon is a critical information to optimize the devices. This information can be obtained from external quantum efficiency measurements. External quantum efficiency (EQE) is defined as the collected electron number divided by the number of photons in the incident light. During the measurements, photons with a single wavelength are incident on the solar cell. Then the generated current is measured. The number of photons can be calculated through the wavelength of the photon and the incident light power, and the number of electrons can be calculated from the current density. An example of EQE measurement is shown in figure 5.5. In this figure, the horizontal axis shows the wavelength of the photons, and the vertical axis shows the EQE. The short circuit current can be calculated with EQE through integration:

$$J_{sc} = \int EQE(\lambda) \frac{W_{AM1.5}(\lambda)}{E_{(\lambda)}} d\lambda$$

Where $\lambda$ is wave length, $W_{AM1.5}(\lambda)$ is the solar energy spectrum, and $E_{(\lambda)}$ is the photon energy.

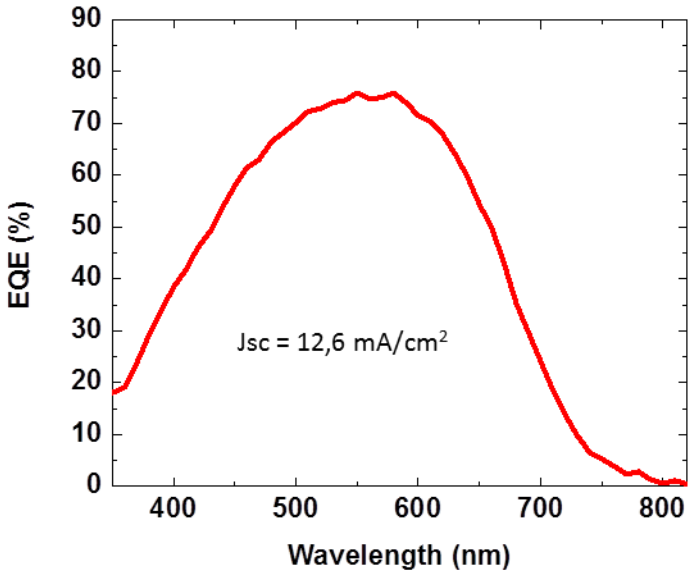


Figure 5.5. EQE measurement of a NW radial junction solar cell.

Due to the multiple reasons such as the dust on the surface, the uniformity of the substrate temperature of the substrate holder, the plasma, and manual operation, sometimes the solar cells do not have a good uniformity along the whole area of the substrate. So we defined 26 sub-cells on each 1" X 1" substrate by using a mask during ITO layer deposition. To find the best sub-cell on one substrate, firstly, all these sub-cells are measured with a voltmeter to estimate the open circuit voltage. Then the J(V) characterization of 3 to 10 sub-cells are measured. The performance of the best efficiency sub-cell is considered as the performance of the initial solar cell.

## 5.3 The performance of NW radial junction solar cells

### 5.3.1 SiNW based NW radial junction solar cells

During the past years, we have constantly investigated the NW radial junction solar cells. The best efficiency solar cells we have obtained have a hydrogenated polymorphous Si (pm-Si:H) as absorber material.[21] pm-Si:H is a heterogeneous material which is produced under plasma conditions close to powder formation. It is an excellent alternative to a-Si:H due to its better electron and hole transport properties.[32,33] However, this material has a relatively large optical bandgap (~ 1.7 eV) which makes pm-Si:H a poor absorber for λ> 700 nm. However, there are two straight forward ways to enhance the absorption of this material at red and infrared range. The first one to change the deposition conditions to achieve a-SiGe:H. During the PECVD deposition process, by adding $GeH_4$ to the $SiH_4$ and $H_2$ gas mixture, a-SiGe:H material can be obtained. a-SiGe:H is a material with a bandgap between 1.0 to 1.7 ev[34]. Its bandgap and absorption can be tuned easily by changing the Ge concentration.[23,35,36] The second one to change the deposition conditions to achieve µc-Si:H. Starting from the pm-Si:H deposition conditions, by decreasing the $SiH_4$ partial pressure and increasing the plasma power, µc-Si:H material can be obtained. µc-Si:H is a form of silicon which has small crystalline grains within the amorphous phase. Because µc-Si:H has a low absorption coefficient in the infrared range, thick layers are usually required to achieve a high absorption. However, as demonstrated in the second chapter, the NW array structure can strongly enhance the absorption of the µc-Si:H solar cells. This makes µc-

Si:H a desirable material for low cost NW radial junction solar cells. With a-SiGe:H and µc-Si:H, NW radial junction solar cells have been fabricated. Since solar cells with pm-Si:H have been well studied in our lab, we have also fabricated solar cells with pm-Si:H absorber as reference solar cells.

Figure 5.6 a) shows SEM images of the solar cells after p, i and n layer deposition, and figure 5.6 b) shows the solar cells after ITO coating. In figure 5.6 a), it can be seen that the wires have a relatively uniform dimeter along the axial direction. The diameters of these wires are in the range between 70 to 120 nm. After ITO coating, dense wires can be seen. The SEM images of the pm-Si:H reference cell are shown in figures 5.6 c) and d), c) shows the cell after p-i-n layer deposition and d) shows the cell after ITO coating, respectively.

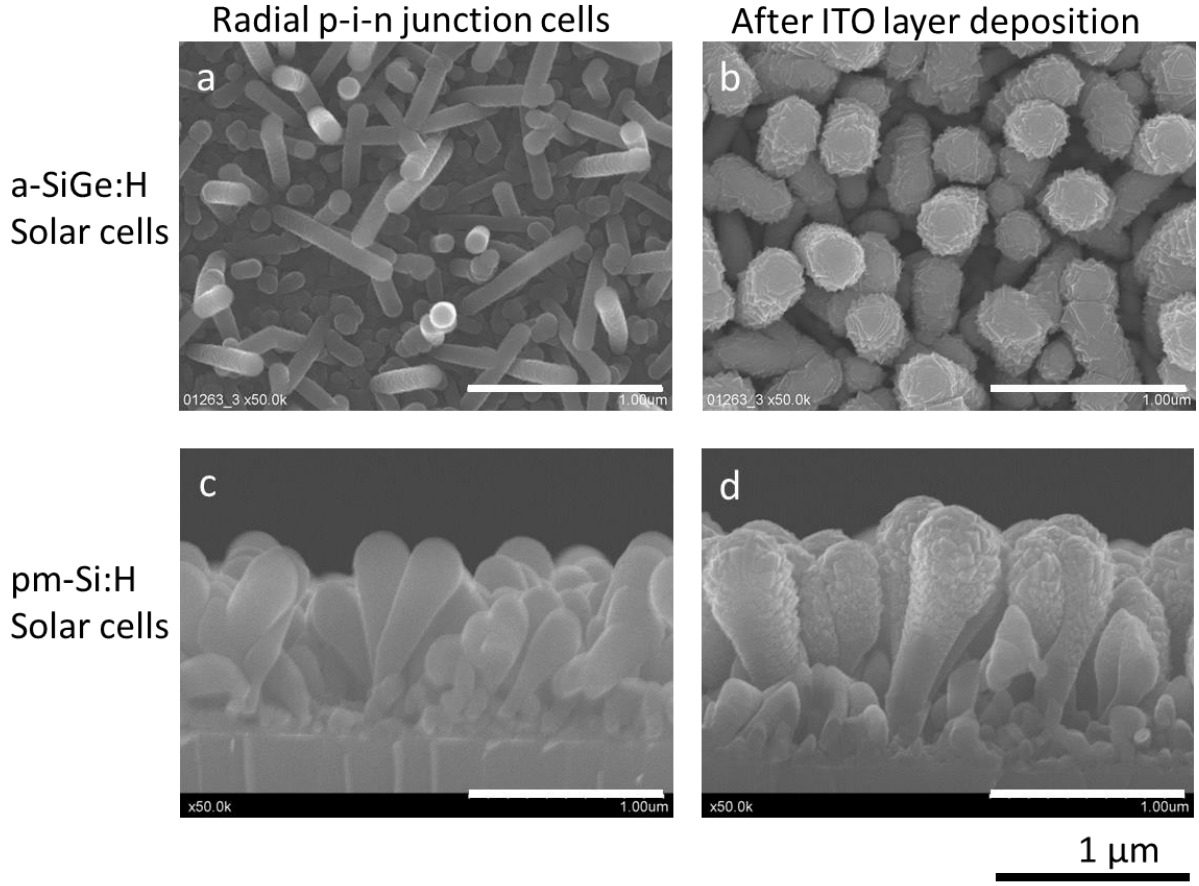


Figure 5.6. SEM images of NW radial junction solar cells. a) Top view of a solar cell with a-SiGe:H absorber. The cell has completed p-i-n junction. b) Same solar cells with ITO coating. c) Side view of pm-Si:H solar cells. The cell has completed p-i-n junction. d) Same as c) with ITO coating.

The EQE of both the a-SiGe:H solar cell and the pm-Si:H reference solar cell have been measured and plotted in figure 5.7 a). Compared with pm-Si:H solar cell, the EQE of the a-SiGe:H cell has a clear increase in the wavelength range from 610 to 800 nm. The increase of the absolute EQE percentage in this wavelength range is plotted in figure 5.7 b). Its value can be up to 10 percent at around 700 nm. In figure 5.6 a) and c), it can be seen that the diameter of the cell before the ITO coating is in the range between 70 nm to 120 nm for a-SiGe:H cells, and between 190 to 320 nm for pm-Si:H cells. The a-SiGe:H solar cells have stronger absorption with less material. This clearly shows that the enhancement in the red and infrared region is due to a lower Eg. According to the ellipsometry study

on the a-SiGe:H thin layers deposited under the similar conditions on planar substrate, the estimated Ge content in these films is between 20% to 30%. Further increasment of the absorption can be achieved by increasing the Ge content in the a-SiGe:H layers.

The absorption of the a-SiGe:H solar cells at wavelengths between 300 and 610 nm is smaller than that of the pm-Si:H solar cells. In this wavelength range both materials have strong light absorption. The carriers generated by absorbing the short wavelength photons are mainly located near the i-n layer interface. This indicates that the i-n interface of the a-SiGe:H solar cell has to be optimized.

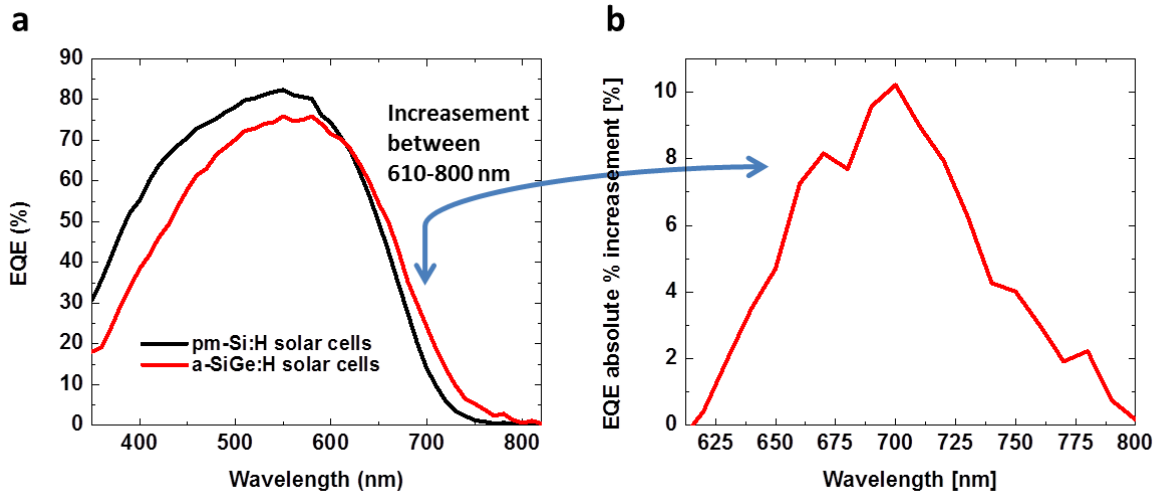


Figure 5.7. a) EQE of a-SiGe:H and pm-Si NW solar cell. b) The increase of EQE in the wavelength between 610 nm and 800 nm.

For the deposition of µc-Si:H absorber layer of the NW radial junction solar cells, the $H_2$ flow rate, $SiH_4$ flow rate, pressure, power density, and temperature are 200 sccm, 20 sccm, 2.6 Torr, 90 mW/cm$^2$ and 150°C, respecively. In a previous study, we have demonstrated the crystallinity of the µc-Si:H layer deposited on SiNWs by TEM characterization.[21] In this study, we used spectroscopic ellipsometry measurements to determine the material crystallinity. The same condition has been used to deposit µc-Si:H layer on Corning glass substrate as for the µc-Si:H solar cells. Then spectroscopic ellipsometry measurements are done on the µc-Si:H layers deposited on the planar glass substrates. The complex refractive index of the material is fitted from the measured data to determine the crystallinity of the material and shown in figure 2.10 of chapter 2. It can be seen that the material has a k value above 0.001 even the wavelength is 900 nm. It is a strong enhancement compared with a-Si:H.

The quality of the µc-Si:H films deposited by PECVD is closely linked with the plasma conditions, such as the effects of hydrogen dilution[37] and ion bombardment[38]. A main difference between the NW array substrate and the planar substrate is that there is shading in the NW arrays. This shading effect might influence the local plasma condition such as the ion bombardment energy. For the randomly orientated NW arrays, the NW length is an effective way to tune the space between wires. So the NW length should be an important parameter for the quality of the µc-Si:H deposited on the side wall of the NW. The quality of the µc-Si:H layer is also linked with the layer thickness, because the composition and the crystallinity changes with the layer thickness.[39] In this study we have fixed the

plasma conditions and changed the NW length and µc-Si:H thickness to study their influence on the µc-Si:H solar cells performance.

Figure 5.8 shows the performances of µc-Si:H solar cells with the same µc-Si:H layer deposition time but on different NW lengths. The NW lengths have been varied from 200 nm to 1000 nm, and the µc-Si:H layer thickness is around 200 nm (this is the nominal thickness on a planar substrate). It can be seen that with the increase of the NW length, the efficiency, open circuit voltage, short circuit current and fill factor decrease. This shows that the lower aspect ratio NWs gives better µc-Si:H solar cell performance.

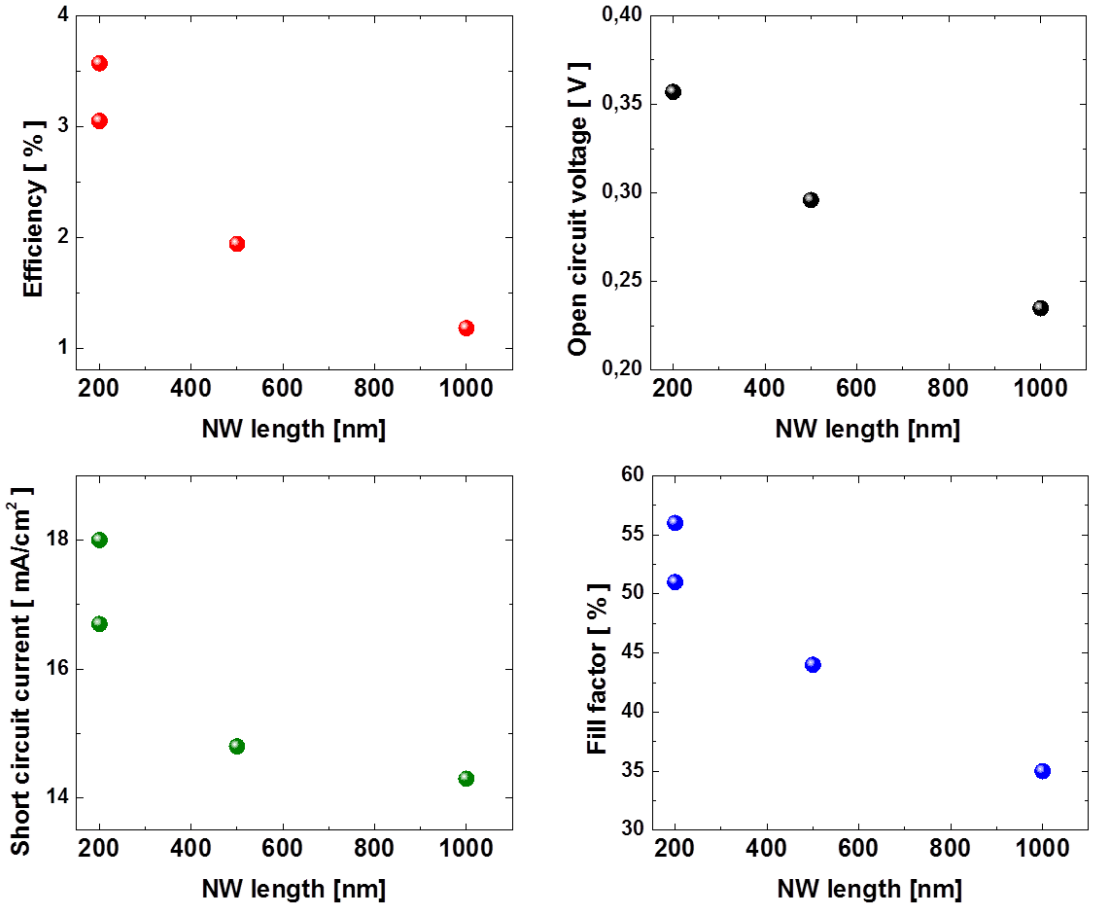


Figure 5.8. Effect of SiNW core length on the performances of µc-Si:H NW solar cells

We have also studied the effect of increasing the absorber layer thickness of the µc-Si:H NW solar cells. The variations of the performance are shown in figures 5.9. In these figures, the different symbols represent the solar cells with different NW core length. For 200 nm and 500 nm long SiNWs cores, the efficiency, short circuit current and fill factor increase with the increase of µc-Si:H layer thickness. This is due to the fact that the absorption increases with the increase of the volume of the absorber. However, it becomes more difficult to achieve conformal shell deposition when the µc-Si:H layer is too thick. The non-conformal shell deposition can increase the series resistance and decrease the open circuit voltage, as shown in the second figure. For 1000 nm long SINWs cores, there is no clear change of efficiency, short circuit current and fill factor when the µc-Si:H layer thickness is changed. This should be due to the fact that it is difficult to deposite good quality and conformal µc-Si:H layers on long SiNWs. Thus it leads to a poor solar cell performance.

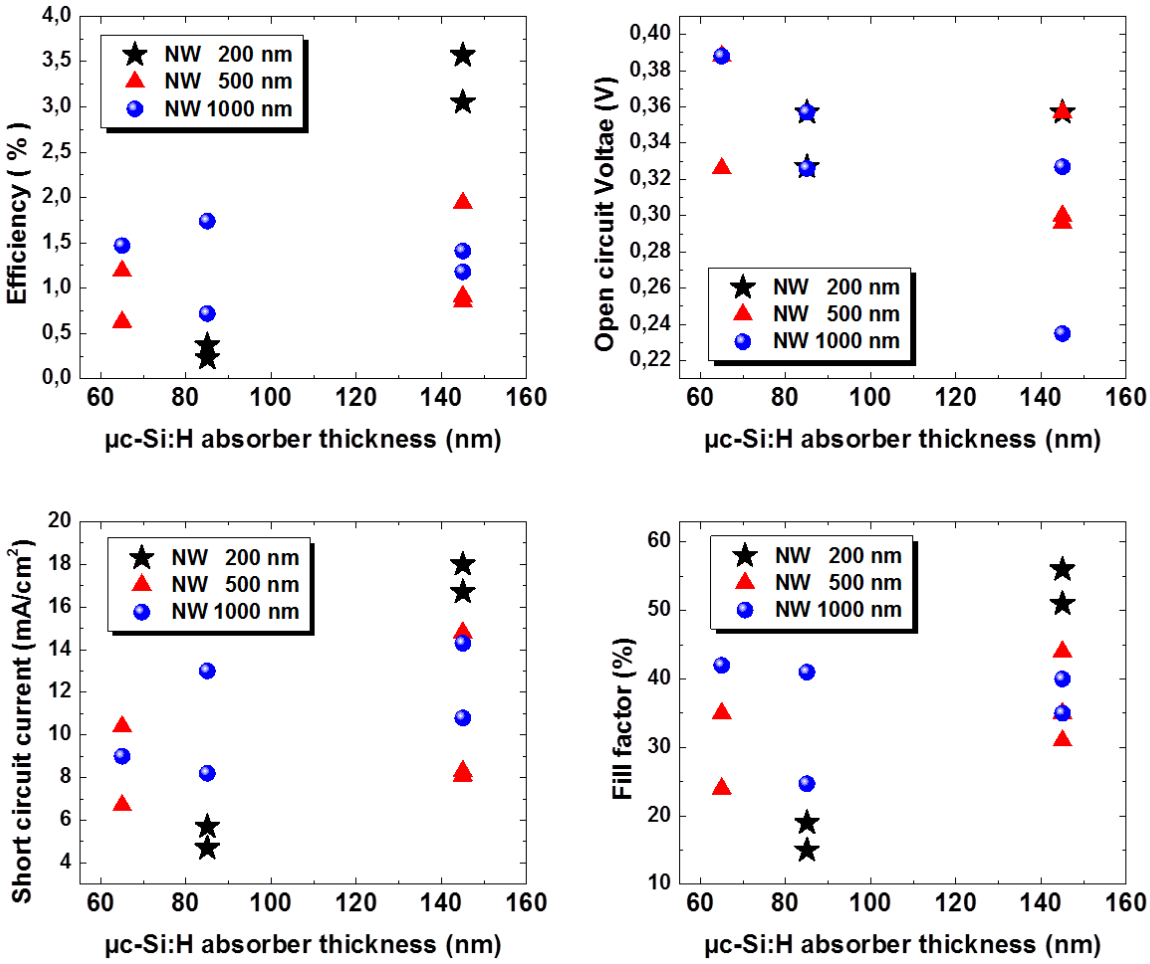


Figure 5.9. Effects of the thickness of the µc-Si:H layers on the performances of the solar cells.

For the purpose of comparison, we have plotted the performance of all the a-SiGe:H solar cells, µc-Si:H solar cells and pm-Si:H solar cells fabricated in this study in figure 5.10. In these figures, a) to c) show the Voc, Jsc and fill factor as a function of efficiency, respectively. It can be seen the efficiency has a large variation, which is mainly due to the difference of solar cell fabrication parameters and the reproducibility of the fabrication processes. The reproducibility is influenced by many parameters and can be clarified into two categories. The first one is human factors. For the solar cell fabrication, there are many operations which do not have standard procedures. Such as the waiting time, the sequence of the operations, the pressure applied to the sample by the hand tools. The second one is the equipment factor. The majority of the equipment for solar cells fabrication are shared with other users. This might bring the foreign elements contamination. There is also parameter shift due to the equipment upgrading and reparation.

From the comparison, it can be seen that the best performance pm-Si:H and a-SiGe:H solar cells have similar efficiencies. pm-Si:H cells have the highest Voc, while a-SiGe:H solar cells have highest Jsc. For µc-Si:H solar cells, a Jsc of 18 mA/cm$^2$ has been achieved with a absorber layer thickness of only 145 nm. With planar configuration, 2500 nm thick µc-Si:H is required to achieve such a Jsc (one light pass). This shows the strong enhancement of the absorption of the NW solar cells. The limiting factor for µc-Si:H solar cell is the low Voc. In the literature, the open circuit voltage for the best performance µc-Si:H solar cell is 0.548 V[40]. In our case, we have obtained 0.388 V. There is still 160 mV for

improvement. However, it already has a 128 mV improvement compared with the previous study in the group[21].

Figure 5.10 d) shows the J-V curves of the best performance a-SiGe:H, µc-Si:H and pm-Si:H NW RJ solar cells. The values of the efficiency, Voc, Jsc and fill factor are shown in table 5.1. It can be seen that the a-SiGe:H has a higher Jsc and smaller Voc compared with pm-Si:H solar cells. This is because a-SiGe:H has enhanced absorption in the red and infrared range but a smaller band gap. The µc-Si:H solar cell has a relatively low efficiency of 3.6 %. However, compared with the previous study in the group, there is 0.7% improvement of efficiency. This efficiency is also the highest efficiency for NW based µc-Si:H solar cells in the literature.[20,41,42]

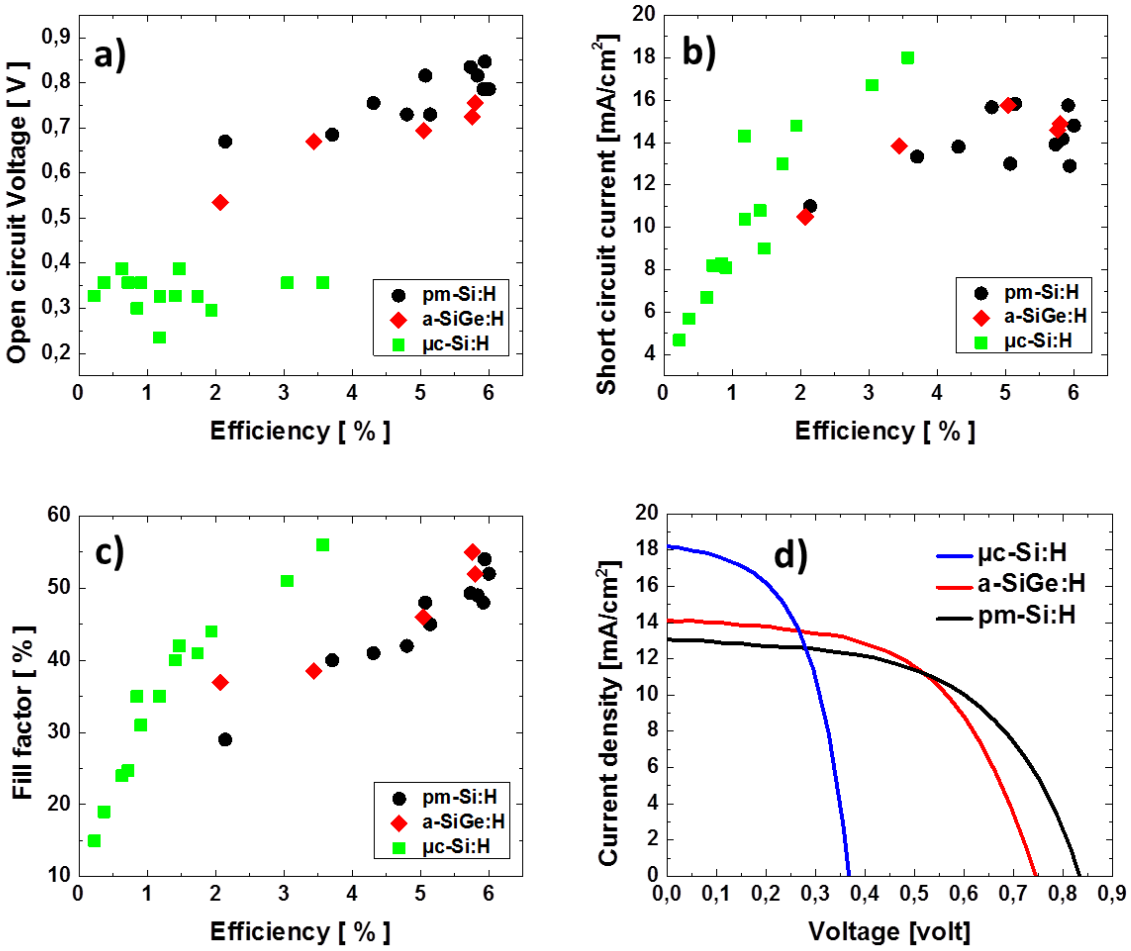


Figure 5.10. SiNW based solar cells performances. a) Open circuit voltage as a function of efficiency. b) Short circuit current as a function of efficiency. c) Fill factor as a function of efficiency. d) J-V curves of the best a-SiGe:H solar cell, pm-Si:H solar cell and µc-Si:H solar cells.

Table 5.1. Parameters of the best a-SiGe:H solar cell, pm-Si:H solar cell and µc-Si:H solar cells.

| Absorber | Voc [V] | Jsc [mA/cm$^2$] | FF [%] | η [%] |
|---|---|---|---|---|
| µc-Si:H | 0.36 | 18 | 56 | 3.6 |
| a-SiGe:H | 0.73 | 14.6 | 55 | 5.8 |
| pm-Si:H | 0.85 | 12.9 | 54 | 5.9 |

µ-Si:H and a-SiGe:H materials have also been used in the bottom cells of tandem radial junction tandem solar cells. The detailed structure of the solar cells is shown in figure 5.11. It can be seen that the solar cell has a multi-shell structure in the radial direction. For such a structure, it is very important to achieve conformal deposition. The NW length is the most important factor which influences the shading effects during the multilayer stack deposition. We have varied the NW length from 500 nm to 1500 nm to study the influence of NW length on the solar cell performance.

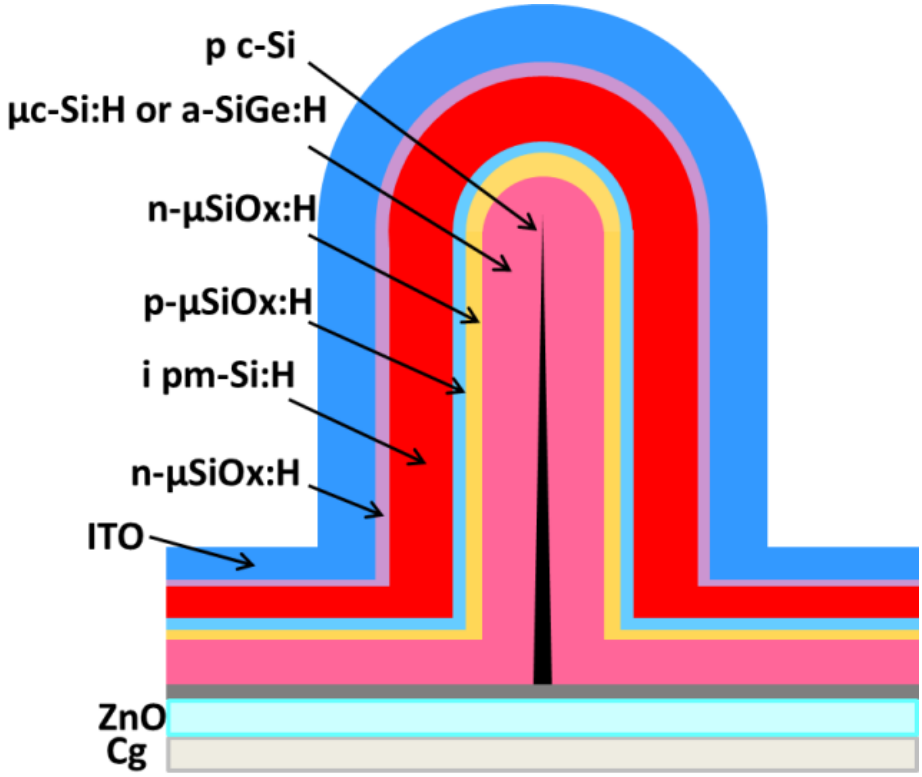


Figure 5.11. Schematic of the tandem solar cells multilayer structure

Figure 5.12 shows the solar cell parameters as functions of the NW length. The red circles represent the a-SiGe:H/pm-Si:H tandem solar cells, and the black triangles represent the µc-Si:H/pm-Si:H cells. For the a-SiGe:H solar cells, the efficiency, Jsc and FF almost keep constant when the NW length increased from 500 to 1000 nm. However, all the parameters decrease sharply when the NW length is increased to 1500 nm. The decrease could be due to the shading effect. For the µc-Si:H/pm-Si:H solar cells, the optimized NW length is around 1000 nm. This is because the optimized NW length for single junction pm-Si:H NW solar cells is around 1000 nm, and the pm-Si:H top cell has a dominant contribution to the tandem cell efficiency.

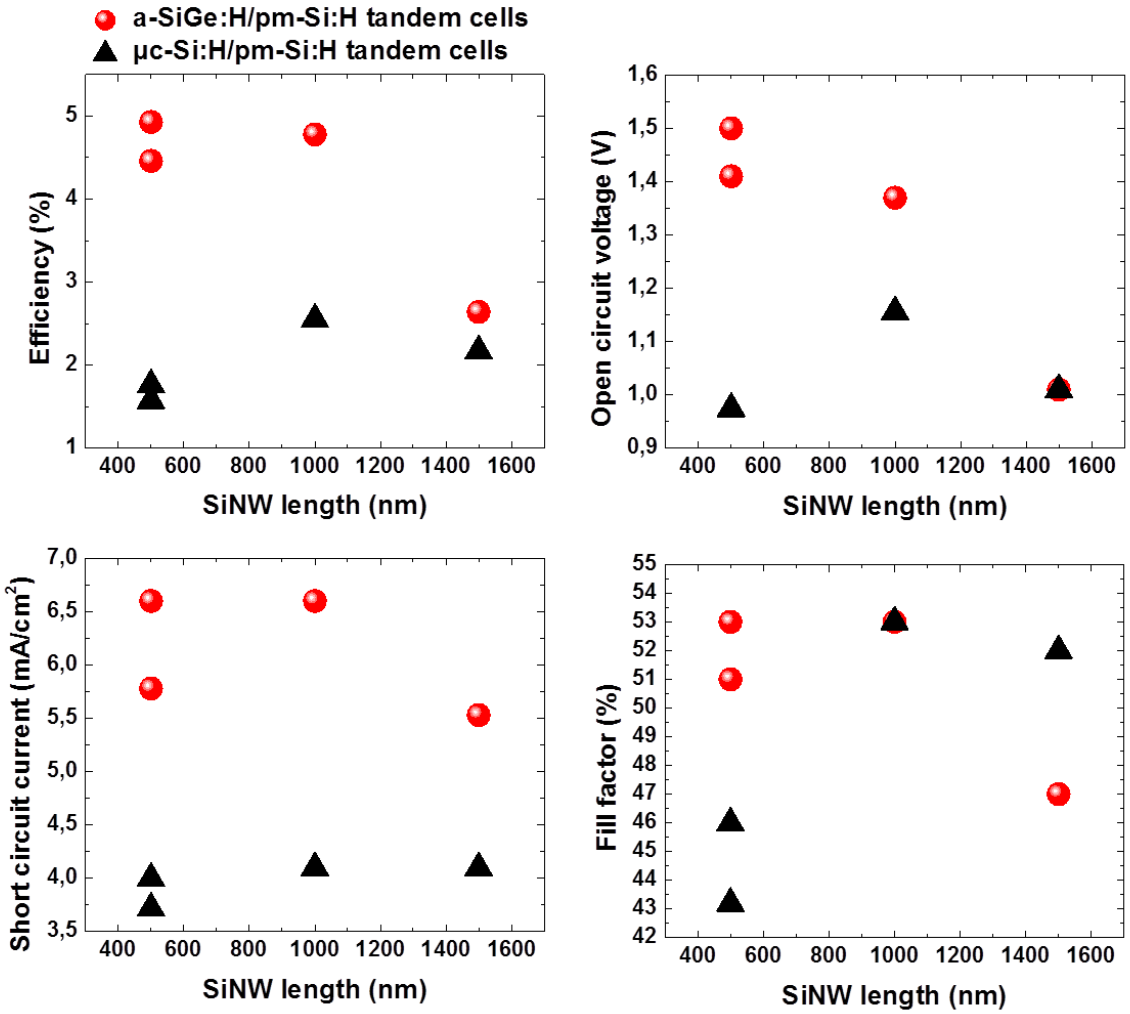


Figure 5.12. Efficiency, Voc, Jsc and FF of the tandem solar cells as a function of NW core length. The red circles represent the a-SiGe:H/pm-Si:H tandem solar cells and the black triangles represent the µc-Si:H/pm-Si:H cells.

The J-V curves of the best performance tandem solar cells are shown in figure 5.13. The efficiency, Voc, Jsc and fill factor are shown in table 5.2. The Voc of the best a-SiGe:H/pm-Si:H solar cell has a relative high value (1.41 V), but there is still room for improvement since it is only 89% of the summation of the Voc of best single junction a-SiGe:H and pm-Si:H solar cells shown in the previous part. The Jsc of this solar cell is smaller than the half of the average of the of best single junction a-SiGe:H and pm-Si:H solar cells. This is because the Ge content in the a-SiGe:H layer is around 30%. This makes the absorption spectrum of the a-SiGe:H bottom absorber has a large overlap with the top pm-Si:H absorber. The Ge content of the a-SiGe:H layer should be further increased to increase the bottom cell current. The Voc of the µc-Si:H/pm-Si:H solar cell is 1.16 V, this is 96% of the summation of the best Voc of the µc-Si:H solar cell and the pm-Si:H solar cell have been achieved previously. It also has a relative high FF of 53%. Thus the low efficiency should be limited by the poor current matching, which only gives a Jsc of 4.1 mA/cm$^2$.

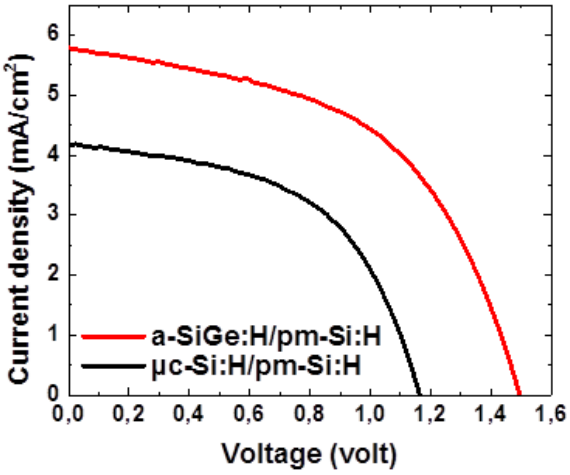


Figure 5.13. J-V curves of the best performance tandem solar cells. The red line represents the a-SiGe:H/pm-Si:H tandem solar cell and the black line represents the µc-Si:H/pm-Si:H solar cell.

Table 5.2. Parameters extracted for the J-V curves in figure 5.14.

| Absorber | Voc [V] | Jsc [mA/cm$^2$] | FF [%] | η [%] |
|---|---|---|---|---|
| a-SiGe:H/pm-Si:H | 1.41 | 6.6 | 55 | 4.93 |
| µc-Si:H/pm-Si:H | 1.16 | 4.1 | 53 | 2.55 |

### 5.3.2 SiGeNW based NW radial junction solar cells

Compared with c-Si, c-SiGe is a low bandgap material with enhanced carrier mobility and optical absorption. Due to the compatibility with Si and the possibility to improve the Si based device, this material has been heavily studied during the past 4 decades.[43,44] It is also a desirable material to be used as the bottom cell in the multi junction solar cells.[45,46] However, c-SiGe is usually obtained by epitaxial growth on Si wafer substrates.[47] This makes the c-SiGe high cost due to the c-Si wafer substrate. Metal catalyzed NW growth provides a new possibility to this end. It opens the door to fabricate low cost multi junction solar cells with c-SiGe.

Previously, µc-Si:H/pm-Si:H and a-SiGe:H/pm-Si:H tandem solar cells have been demonstrated. Since c-SiGe has a lower bandgap than µc-Si:H and a-SiGe, it can be used as a bottom absorber for triple junction solar cells. c-SiGe has high carrier mobility and absorption, so pn junction can be used instead of p-i-n junction. Thus this triple junction cell only requires two more layers than the tandem cell, a p doped layer (c-SiGeNW) and a thin n doped layer (µc-SiOx:H). Such a configuration will not increase the solar cell diameter significantly.

In the literature, SiGeNWs have not been used in the solar cells yet. In order to prove the possibility of using SiGeNWs for radial junction solar cells, we have replaced the SiNWs core in the standard p-i-n pm-Si:H solar cells with SiGeNWs core. In this experiment, the SiGeNWs are grown in ARCAM reactor. The SiGeNWs are in-situ doped with TMB gas. The Ge atomic concentration in these NWs is around 30%. Then an intrinsic pm-Si:H layer and a n-type µc-SiOx:H layer are deposited above the SiGeNW core. The SiGeNWs growth, intrinsic pm-Si:H layer deposition and µc-SiOx:H layer deposition

have been done without breaking the vacuum. Finally ITO and Ag contact layers are deposited. As a reference, SiNW based pm-Si:H solar cells have also been fabricated with same processes except for the NW growth step. The two solar cells have experienced the same fabrication processes except the NW growth.

The EQE of the SiGeNW and SiNW based pm-Si:H solar cell is shown in figure 5.14. It can be seen that there is no significant difference between the two solar cells. This demonstrates that the SiGeNWs based solar cells can function as SiNWs based solar cells. In the infrared range, the EQE of the SiGeNWs based solar cells is lower. The difference should mainly come from the difference of NW length and density of the NW core. Since the SiNWs and GeNWs are grown at different plasma composition and substrate temperature, it is not easy to obtain same NW density and length. The absorption for SiGeNWs based solar cell ends around 780 nm. The enhancement of absorption in the infrared range cannot be seen in the SiGeNW based solar cells. This is mainly because the SiGeNWs have small diameter and Ge concentration. The diameter at bottom of the SiGeNWs is around 40 nm and at top is around 10 nm. The volume of SiGeNW is too small compared with the volume of solar cells. The Ge concentration is around 30%. With such a concentration, the absorption is not significantly enhanced. The detailed explanations of absorption in the core can be found in chapter 2. This also suggests that in order to use SiGeNWs as absorber, the diameter and Ge concentration should be increased.

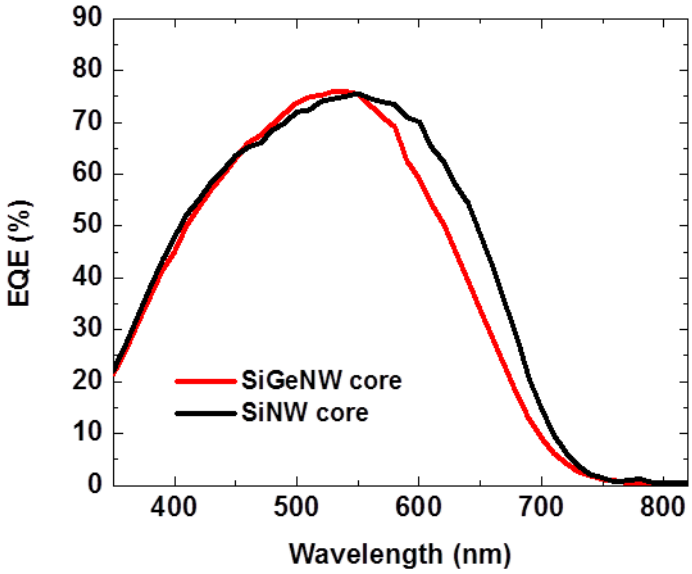


Figure 5.14. EQE of pm-Si:H NW radial junction solar cells. Red line is the solar cell based on $Si_{0.7}Ge_{0.3}$NW core, and black line is the cell based on SiNW core.

The J-V measurements results of the two solar cells are shown in figure 5.15. It can be seen that the two solar cells have very similar J-V curves. The Voc, Jsc, fill factor and efficiency are shown in table 5.3. The Voc and Jsc of SiGeNWs based solar cells are 10 mV and 0.5 mA/cm$^2$ smaller than the SiNWs based solar cells, respectively. However, SiGeNWs solar cells exhibit a higher FF and efficiency. As explained before, the p, i and n layer of the SiGeNWs based solar cells have been deposited without

breaking the vacuum. This can avoid the oxidation and contamination of the interface and give a higher FF.

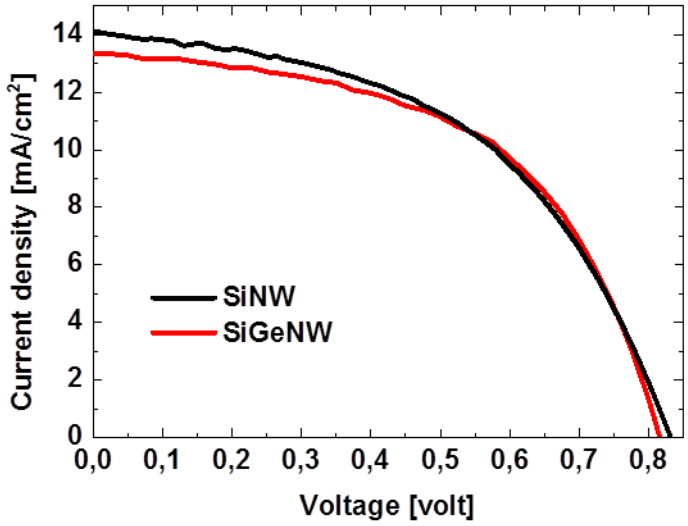


Figure 5.15. J-V curves of pm-Si:H NW radial junction solar cells. Red line is the solar cell based on $Si_{0.7}Ge_{0.3}$NW core, and black line is the cell based on SiNW core.

Table 5.3. Parameters of SiGeNWs and SiNWs based solar cells.

| NW core | Voc [V] | Jsc [mA/cm$^2$] | FF [%] | η [%] |
|---|---|---|---|---|
| SiGeNWs | 0.825 | 13.4 | 54 | 5.9 |
| SiNWs | 0.835 | 13.9 | 49 | 5.7 |

## 5.4 Summary

This chapter starts with the advantages and challenges of using NWs for solar cell applications. By briefly reviewing the NW solar cells in the literature, we show that the significance of using NW solar cells is to achieve a relatively high efficiency through low cost approach. Then we introduce the fabrication and characterization of our NW RJ solar cells. In this study, we have focused on developing low bandgap materials for single junction and multi junction solar cells. Single junction NW RJ solar cells based on a-SiGe:H and μc-Si:H absorbers have been fabricated. The light absorption enhancement of these solar cells in the red and infrared range has been demonstrated. By decreasing the NW core length and increasing the μc-Si:H layer thickness, we have improved the μc-Si:H solar cells performance significantly. After that, we have optimized the NW core length for a-Si:H/pm-Si:H and μc-Si:H/pm-Si:H tandem NW RJ solar cells. For the first of time, we have demonstrated that SiGeNWs can be used for NW radial junction solar cells application. A 6% energy conversion efficiency SiGeNW based radial junction solar cells has been achieved.

## References

1 Garnett, E. & Yang, P. Light Trapping in Silicon Nanowire Solar Cells. *Nano Letters* **10**, 1082-1087, doi:10.1021/nl100161z (2010).

2 Huynh, W. U., Dittmer, J. J. & Alivisatos, A. P. Hybrid Nanorod-Polymer Solar Cells. *Science* **295**, 2425-2427, doi:10.1126/science.1069156 (2002).

3 Law, M., Greene, L. E., Johnson, J. C., Saykally, R. & Yang, P. D. Nanowire dye-sensitized solar cells. *Nature Materials* **4**, 455-459, doi:10.1038/nmat1387 (2005).

4 Tsakalakos, L. *et al.* Silicon nanowire solar cells. *Applied Physics Letters* **91**, 233117, doi:http://dx.doi.org/10.1063/1.2821113 (2007).

5 Stelzner, T. *et al.* Silicon nanowire-based solar cells. *Nanotechnology* **19**, 4, doi:10.1088/0957-4484/19/29/295203 (2008).

6 Tian, B. *et al.* Coaxial silicon nanowires as solar cells and nanoelectronic power sources. *Nature* **449**, 885-U888, doi:10.1038/nature06181 (2007).

7 Wu, Y., Hu, J., Xu, Y., Peng, K. & Zhu, J. FABRICATION OF SILICON NANOWIRE （SiNW） ARRAYS AND APPLICATION IN SOLAR CELL. *Acta Energiae Solaris Sinica* **27**, 811-818 (2006).

8 Sivakov, V. *et al.* Silicon Nanowire-Based Solar Cells on Glass: Synthesis, Optical Properties, and Cell Parameters. *Nano Letters* **9**, 1549-1554, doi:10.1021/nl803641f (2009).

9 Garnett, E. C., Brongersma, M. L., Cui, Y. & McGehee, M. D. in *Annual Review of Materials Research, Vol 41* Vol. 41 *Annual Review of Materials Research* (eds D. R. Clarke & P. Fratzl) 269-295 (Annual Reviews, 2011).

10 Kuang, Y., Di Vece, M., Rath, J. K., van Dijk, L. & Schropp, R. E. I. Elongated nanostructures for radial junction solar cells. *Reports on Progress in Physics* **76**, doi:10.1088/0034-4885/76/10/106502 (2013).

11 Yu, M., Long, Y.-Z., Sun, B. & Fan, Z. Recent advances in solar cells based on one-dimensional nanostructure arrays. *Nanoscale* **4**, 2783-2796, doi:10.1039/c2nr30437f (2012).

12 Wang, Y. *et al.* Silicon Nanowires for Biosensing, Energy Storage, and Conversion. *Advanced Materials* **25**, 5177-5195, doi:10.1002/adma.201301943 (2013).

13 Misra, S., Yu, L., Chen, W., Foldyna, M. & Roca i Cabarrocas, P. A review on plasma-assisted VLS synthesis of silicon nanowires and radial junction solar cells. *Journal of Physics D-Applied Physics* **47**, doi:10.1088/0022-3727/47/39/393001 (2014).

14 Wallentin, J. *et al.* InP Nanowire Array Solar Cells Achieving 13.8% Efficiency by Exceeding the Ray Optics Limit. *Science* **339**, 1057-1060, doi:10.1126/science.1230969 (2013).

15 Åberg, I. *et al.* A GaAs Nanowire Array Solar Cell With 15.3% Efficiency at 1 Sun. *IEEE J. Photovolt.* **6**, 185-190, doi:10.1109/JPHOTOV.2015.2484967 (2016).

16 Yu, L., O'Donnell, B., Alet, P.-J. & Roca i Cabarrocas, P. All-in-situ fabrication and characterization of silicon nanowires on TCO/glass substrates for photovoltaic application. *Solar Energy Materials and Solar Cells* **94**, 1855-1859, doi:10.1016/j.solmat.2010.06.021 (2010).

17 Cho, J. *et al.* Sn-catalyzed silicon nanowire solar cells with 4.9% efficiency grown on glass. *Progress in Photovoltaics* **21**, 77-81, doi:10.1002/pip.1245 (2013).

18 O'Donnell, B., Yu, L. W., Foldyna, M. & Cabarrocas, P. R. I. Silicon nanowire solar cells grown by PECVD. *Journal of Non-Crystalline Solids* **358**, 2299-2302, doi:10.1016/j.jnoncrysol.2011.11.026 (2012).

19 Misra, S., Yu, L., Foldyna, M. & Roca i Cabarrocas, P. High efficiency and stable hydrogenated amorphous silicon radial junction solar cells built on VLS-grown silicon nanowires. *Sol Energ Mat Sol C* **118**, 90-95, doi:http://dx.doi.org/10.1016/j.solmat.2013.07.036 (2013).

20 Misra, S., Yu, L. W., Foldyna, M. & Cabarrocas, P. R. I. New Approaches to Improve the Performance of Thin-Film Radial Junction Solar Cells Built Over Silicon Nanowire Arrays. *IEEE J. Photovolt.* **5**, 40-45, doi:10.1109/jphotov.2014.2366688 (2015).

21 Misra, S. Thesis, Single and tandem radial junction silicon thin film solar cells based on PECVD grown crystalline silicon nanowire arrays. (2016).

22 Green, M. A., Emery, K., Hishikawa, Y., Warta, W. & Dunlop, E. D. Solar cell efficiency tables (version 48). *Progress in Photovoltaics: Research and Applications* **24**, 905-913, doi:10.1002/pip.2788 (2016).

23 Gueunier, M. E. *et al.* Properties of polymorphous silicon-germanium alloys deposited under high hydrogen dilution and at high pressure. *Journal of Applied Physics* **92**, 4959-4967, doi:10.1063/1.1508429 (2002).

24 Yan, B. *et al.* Innovative dual function nc-SiOx:H layer leading to a >16% efficient multi-junction thin-film silicon solar cell. *Applied Physics Letters* **99**, 113512, doi:http://dx.doi.org/10.1063/1.3638068 (2011).

25 Vetterl, O. *et al.* Intrinsic microcrystalline silicon: A new material for photovoltaics. *Solar Energy Materials and Solar Cells* **62**, 97-108, doi:http://dx.doi.org/10.1016/S0927-0248(99)00140-3 (2000).

26 Triple-junction thin-film silicon solar cell fabricated on periodically textured substrate with a stabilized efficiency of 13.6%. *Applied Physics Letters* **106**, 213902, doi:10.1063/1.4921794 (2015).

27 Pai, P. G., Chao, S. S., Takagi, Y. & Lucovsky, G. INFRARED SPECTROSCOPIC STUDY OF SIOX FILMS PRODUCED BY PLASMA ENHANCED CHEMICAL VAPOR-DEPOSITION. *J. Vac. Sci. Technol. A-Vac. Surf. Films* **4**, 689-694, doi:10.1116/1.573833 (1986).

28 Philipp, H. R. Optical properties of non-crystalline Si, SiO, SiOx and SiO2. *Journal of Physics and Chemistry of Solids* **32**, 1935-1945, doi:http://dx.doi.org/10.1016/S0022-3697(71)80159-2 (1971).

29 Zhao, L., Zhou, C. L., Li, H. L., Diao, H. W. & Wang, W. J. Design optimization of bifacial HIT solar cells on p-type silicon substrates by simulation. *Solar Energy Materials and Solar Cells* **92**, 673-681, doi:10.1016/j.solmat.2008.01.018 (2008).

30 Kim, H. *et al.* Electrical, optical, and structural properties of indium–tin–oxide thin films for organic light-emitting devices. *Journal of Applied Physics* **86**, 6451-6461, doi:http://dx.doi.org/10.1063/1.371708 (1999).

31 Roca i Cabarrocas, P. *et al.* A fully automated hot‐wall multiplasma‐monochamber reactor for thin film deposition. *Journal of Vacuum Science & Technology A* **9**, 2331-2341, doi:http://dx.doi.org/10.1116/1.577318 (1991).

32 Cabarrocas, P. R. I., Morral, A. F. I. & Poissant, Y. Growth and optoelectronic properties of polymorphous silicon thin films. *Thin Solid Films* **403**, 39-46 (2002).

33 Cabarrocas, P. R. I., Chaabane, N., Kharchenko, A. V. & Tchakarov, S. Polymorphous silicon thin films produced in dusty plasmas: application to solar cells. *Plasma Physics and Controlled Fusion* **46**, B235-B243, doi:10.1088/0741-3335/46/12b/020 (2004).

34 Gueunier, M. E., Kleider, J. P., Chatterjee, P., Roca i Cabarrocas, P. & Poissant, Y. Study of pm-SiGe:H thin films for p–i–n devices and tandem solar cells. *Thin Solid Films* **427**, 247-251, doi:http://dx.doi.org/10.1016/S0040-6090(02)01196-3 (2003).

35 Mackenzie, K. D. *et al.* Structural, electrical, and optical properties of a-$Si_{1-x}Ge_x$:H and an inferred electronic band structure. *Physical Review B* **31**, 2198-2212 (1985).

36 Ferlauto, A. S. *et al.* Analytical model for the optical functions of amorphous semiconductors from the near-infrared to ultraviolet: Applications in thin film photovoltaics. *Journal of Applied Physics* **92**, 2424-2436, doi:http://dx.doi.org/10.1063/1.1497462 (2002).

37 Hamma, S. & Roca i Cabarrocas, P. Long range effects of hydrogen during microcrystalline silicon growth. *Thin Solid Films* **296**, 11-14, doi:http://dx.doi.org/10.1016/S0040-6090(96)09386-8 (1997).

38 Kalache, B., Kosarev, A. I., Vanderhaghen, R. & Roca i Cabarrocas, P. Ion bombardment effects on the microcrystalline silicon growth mechanisms and structure. *Journal of Non-Crystalline Solids* **299–302, Part 1**, 63-67, doi:http://dx.doi.org/10.1016/S0022-3093(01)00995-4 (2002).

39 Cabarrocas, P. R. I. Plasma enhanced chemical vapor deposition of amorphous, polymorphous and microcrystalline silicon films. *Journal of Non-Crystalline Solids* **266**, 31-37 (2000).

40 Green, M. A. *et al.* Solar cell efficiency tables (version 49). *Progress in Photovoltaics: Research and Applications* **25**, 3-13, doi:10.1002/pip.2855 (2017).

41 Xie, X. *et al.* Radial n-i-p structure SiNW-based microcrystalline silicon thin-film solar cells on flexible stainless steel. *Nanoscale Research Letters* **7**, 621, doi:10.1186/1556-276x-7-621 (2012).

42 Adachi, M. M., Anantram, M. P. & Karim, K. S. Core-shell silicon nanowire solar cells. *Sci Rep* **3**, 6, doi:10.1038/srep01546 (2013).

43 Stroud, D. & Ehrenreich, H. Band structure of SiGe: Coherent-potential approximation. *Physical Review B-Solid State* **2**, 3197-3209, doi:10.1103/PhysRevB.2.3197 (1970).

44 Paul, D. J. Si/SiGe heterostructures: from material and physics to devices and circuits. *Semicond. Sci. Technol.* **19**, R75-R108, doi:10.1088/0268-1242/19/10/r02 (2004).

45 Cariou, R., Tang, J., Ramay, N., Ruggeri, R. & Roca i Cabarrocas, P. Low temperature epitaxial growth of SiGe absorber for thin film heterojunction solar cells. *Solar Energy Materials and Solar Cells* **134**, 15-21, doi:10.1016/j.solmat.2014.11.018 (2015).

46 Li, D. *et al.* Optical absorption of graded buffer layers and short circuit current improvement in SiGe solar cells grown on silicon substrates. *Solar Energy Materials and Solar Cells* **157**, 973-980, doi:10.1016/j.solmat.2016.08.019 (2016).

47 Schaffler, F., Tobben, D., Herzog, H. J., Abstreiter, G. & Hollander, B. HIGH-ELECTRON-MOBILITY SI/SIGE HETEROSTRUCTURES - INFLUENCE OF THE RELAXED SIGE BUFFER LAYER. *Semicond. Sci. Technol.* **7**, 260-266, doi:10.1088/0268-1242/7/2/014 (1992).

# Summary

This thesis is dedicated to develop new solar cell architectures based on nanowires. Both theoretical and experimental works have been carried out during this study.

## Optical modeling

The light absorption in the NW solar cells has been studied theoretically by optical modeling. The detailed field and absorption profile in the solar cells have been calculated. The enhanced light absorption of NW solar cells compared with the planar counterpart has been demonstrated. By varying the absorber layers thickness, 14.1 mA/cm$^2$ matched photon current has been achieved for a-Si:H/µc-Si:H tandem solar cells. This has been achieved with a ~290 nm of µc-Si:H layer and ~60 nm of a-Si:H layer. A preliminary electrical model for radial PN junction NW solar cells has been developed from first principle rules (see Annex 1). Simulation with this model shows that the NW radial junction solar cells have higher short circuit current and fill factor due to the small quasi-neutral region width. Detailed understanding of the carrier transport in the PN radial junctions has achieved.

## Silicon nanowire growth

Since our solar cells are deposited on a SiNW array, understanding the growth of SiNWs is fundamental for the solar cells performance. In this thesis, a deep understanding the SiNWs growth process has been achieved. We have studied SiNWs growth using Sn as a catalyst in a plasma-enhanced CVD system step by step. This allowed us to propose a detailed explanation to the strong evolution of NW density, morphology and crystallinity during the growth process.

By applying a $H_2$ plasma with high plasma power at 200°C, we show that the a-Si:H shell on the SiNWs can be removed. Thus crystalline SiNWs without any amorphous phase can be obtained by PECVD.

In the case of very small nanowires ( diameter < 10 nm), we have observed the rare hexagonal phase of Si. For the first of time, we provide the TEM characterizations from [11-20] direction to give a clear proof of the hexagonal Si phase in as grown SiNWs.

## Silicon-Germanium nanowire growth

To further increase the solar cells efficiency, low bandgap high quality material has to be developed for bottom cells. For the first of time, crystalline SiGeNWs and crystalline GeNWs growth has been achieved through plasma-assisted VLS growth. We have optimized the process pressure, plasma power and temperature range for the SiGeNWs and GeNWs growth. SiGeNWs with Ge content ranging from 0 to 100% has been achieved with In, Sn, and Cu catalysts. For Sn and In catalyzed NW growth, we have also found that above a critical temperature, micrometer long and straight Ge NWs with a constant diameter (10-20 nm) from bottom to top can be obtained. To our knowledge, this is the first report which shows NWs with constant diameter obtained by plasma-assisted VLS growth.

### Nanowire radial junction solar cells

Thanks to years of research on low cost SiNW based solar cells, a efficiency (9.7%) close to the record efficiency of the planar a-Si:H solar cells (10.2%) has been achieved. In order to further improve the efficiency, multi junction solar cells have to be developed. We have focused on the development of low bandgap materials for bottom solar cells. This include a-SiGe:H solar cell and µc-Si:H solar cells. The enhanced absorption in the red and infrared range of the solar spectrum have been demonstrated with a-SiGe:H solar cells. With µc-Si:H solar cells, an efficiency of 3.6% and an open circuit voltage of 0.36 V have been achieved. This is the highest efficiency for NW based µc-Si:H solar cells achieved in the literature.

SiGeNWs have been used in solar cells. With p-i-n configuration, ~6% energy conversion efficiency has been achieved. To our knowledge, this is the first demonstration of SiGeNW based photovoltaic device.

# Perspectives

## Optical and electrical modeling

In order to link the solar cell structure, material properties and solar cell performances, coupled optical and electrical model has to be built. COMSOL Multiphysics can be a platform for coupled optical and electrical modeling of NW solar cells.

The solar cells fabricated with our low cost approach have a random structure. In order to have a more realistic model, random NW array solar cell can be simulated with COMSOL Multiphysics.

## Silicon nanowire growth

For the NW synthesis methods presented in this thesis, the NW growth direction is mainly determined by the initial crystallization process. Substrate temperature is a key parameter to influence this process. However, due to the limitation of the PECVD reactor, NWs have not been grown at substrate temperatures above 450°C. At higher growth temperature, there might be a preferential growth direction. This might lead to ordered NWs growth on low cost substrates.

With high $H_2$ dilution (99%) and high substrate temperature (400°C), non-tapered GeNWs have been obtained. This might be also true for SiNWs. SiNWs growth experiments with increased $H_2$ dilution level, pressure, plasma power and temperature can be tried to grow non tapered SiNWs.

Hexagonal SiNWs have been grown during my thesis. However, the formation process of this metastable phase is not clear. Theoretical simulation and in situ TEM observation can be carried out to get more insight.

The behavior of low surface tension metals, such as Sn and In, during the SiNWs growth are a topic of discussion. From 2017, it will be possible to grow SiNWs in a new TEM microscope (NanoMax). The in-situ observation can give a direct evidence of the behavior of the metal during the growth.

## Silicon-Germanium nanowire growth

To use SiGeNWs as a solar cell absorber, they have to have a sufficiently large diameter. Controlling the catalyst droplet diameter is an efficient way to control the NWs diameter. Thus larger catalyst droplets can be prepared to grow thick SiGeNWs. Higher $GeH_4$ concentration gas line can be added to study the $H_2$ dilution on the GeNW morphology. Gas line with TMB diluted in $H_2$ can be added to study the doping of non-tapered GeNWs.

Quantum dots embed in NWs are promising building blocks for the developments of future spintronic and photonic devices. In this research, straight GeNWs with a diameter smaller than the Bohr exciton radius for Ge ( 24.3 nm) have been synthesized by plasma-assisted VLS method with Sn and In catalysts. We have also demonstrated that it is possible to achieve epitaxial radial growth for SiNWs. By starting with SiNW growth, then continue with a segment of GeNW growth, and finally end with SiNWs growth, it is possible to achieve Ge quantum dots embed in SiNWs structure.

## Nanowire radial junction solar cells

As demonstrated in the optical modeling part, the matched photo-current for μc-Si:H/a-Si:H tandem nanowire radial junction solar cells can be as large as 14.2 $mA/cm^2$ with 295 nm thick μc-Si:H layer and 55 nm a-Si:H layer. By assuming the Voc=1.4 V, FF=0.75, 15% energy conversion efficiency can be achieved. The dominant challenge for achieving such a efficiency is that it is difficult to achieve a good quality μc-Si:H with thickness close to 300 nm on the SiNWs substrate. Thus the main task shoud be optimize the μc-Si:H layer deposition on SiNW substrate.

SiGeNW and GeNW based tandem and triple junction solar cells are promising designs. For this design, SiGeNW or GeNW based pn junction can be used as bottom cell, μc-Si:H or a-SiGe:H based pin junction can be the middle cell, and a-Si:H or pm-Si:H based pin junction can be the top cell.

# Annex I: Electrical modeling of nanowire radial junction solar cells

## Contents

# 1 Introduction

Besides the strong absorption of the light, another advantage of using NW radial junction solar cells is the efficient carrier collection. For planar solar cells, in order to have enough absorption, a thick layer is needed in the light propagation direction. However, the thick layer requires the generated carriers to travel a long distance to get collected. On the contrary, for radial junction NW structure, the light absorption direction and the carrier separation direction can be decoupled. As shown in figure 1, the light is absorbed in the vertical direction while the generated free carriers are separated in the radial direction. Since the carriers only need to travel a short distance, a small diffusion length is sufficient to ensure the carriers to be collected. A short diffusion length means lower material quality requirements. Thus a less expensive material can be used to fabricate relatively high efficiency solar cells. This is an effective way to reduce the cost of solar cells.

Among the theoretical studies of radial junction solar cells, very few of them were carried out with analytical models[1-3]. An analytical model built from first principles helps us to achieve a good understanding of the detailed physics of the device. With this purpose, we have developed an electrical model to simulate the solar cells.

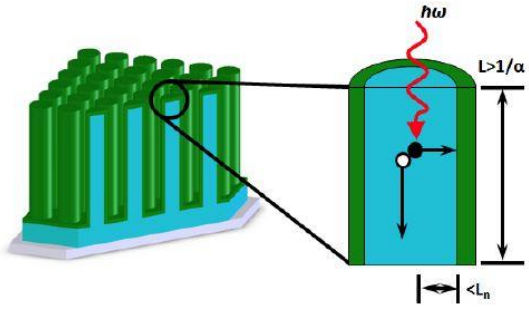


Figure 1. Schematic of the radial junction. (image credit: M. D. Kelzenberg)

# 2 Theoretical analysis of radial PN junction devices

## 2.1 PN junction at equilibrium

A PN junction is often the basis of solar cells and many other electrical devices. For the majority of the devices, the geometry of the PN junction is usually planar. Thus the planar PN junction has been well studied. From planar to radial structure, the mathematical expressions have to changed. In a planar structure the Cartesian coordinate system is used, while in the NW radial structure the cylindrical coordinate is used.

Since NW radial junction solar cells have rotational symmetry, the carrier transport along all the radial directions is the same. Thus only a cut plane along the axis is needed to model. In figure 2 a), a segment of radial PN junction is shown. The red core is P type doped Si, and the yellow shell is N type doped Si. Figure 2 b) shows the cut plane indicated in figure 2 a), and figure 2 c) is the top view of the radial junction. In order to simplify the carrier transport problem and to get an analytical expression, we consider that electrons flow along the radial direction, as indicated by the two black lines in figure 2 b) and 2 c). Thus, the electron flow in the cut plane shown in figure 2 b) is uniform along the vertical direction. Then we can simplify the problem to a the one dimensional line shown in figure 2 b)

and 2 c). In this line, 0 corresponds to the center of the wire, $R_1$ is the radius of p part, and $R_2$ is to the radius of the wire.

Figure 2 d) shows the charge distribution along the radial direction. Since there is a high density of holes in the p-doped region and a high density of electrons in the n-doped region, the electrons will diffuse to-p doped region and recombine with the holes there to achieve equilibrium state. As a result, there will be positively charged ions left in the n-doped region and negatively charged ions in the p-doped region. Generally, it is considered that the space charge region is localized concentrated in a region near the interface of the pn junction which is also called depletion region. In this region there are no free electrons and free holes. The rest parts of the NW are called quasi-neutral region. The charge distribution, together with electric field distribution and built-in potential at equilibrium state are shown in figure 2 d), e) and f), respectively.

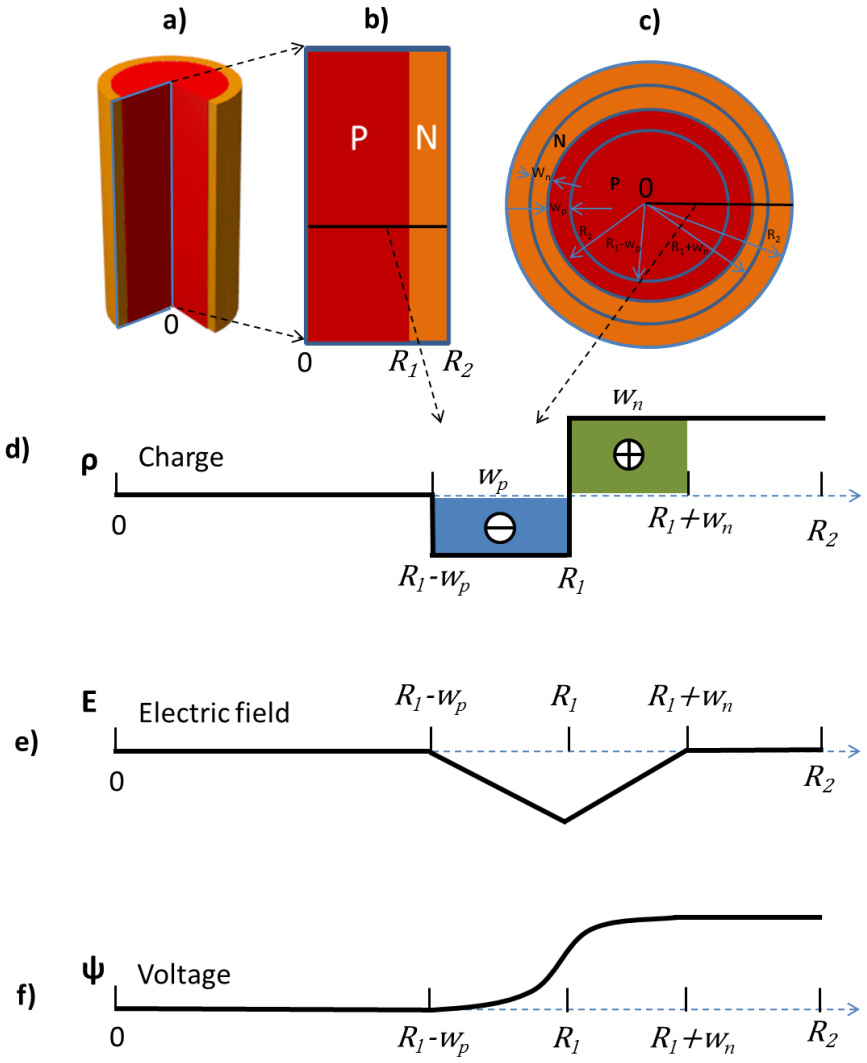


Figure 2. a) Geometry of the NW solar cell used for the electrical model, red color represents p type doped region, and yellow color represents n type doped region. b) Enlarged cut plane shown in a). c) Enlarged cut line shown in b), the depletion region at p part and n part are marked as $w_p$ and $w_n$, respectively. d)-f) Charge distribution, Electric field and built-in potential of PN junction at equilibrium: d) Charge distribution; e) Electric field; f) Built-in potential.

At equilibrium, the charge distribution ρ in the solar cell can be described below:

$$\rho = \begin{cases} 0, & 0 < x < R_1 - w_p \quad (1) \\ p, & R_1 - w_p < x < R_1 \quad (2) \\ n, & R_1 < x < R_1 + w_n \quad (3) \\ 0, & R_1 + w_n < x < R_2 \quad (4) \end{cases}$$

Where, $w_p$ and $w_n$ are the width of the depletion region at p part and n part, respectively. p is the concentration of holes in the p-doped region, and n is electron concentration in the n-doped region. We consider all the dopants are ionized and they have much larger concentration than the intrinsic free carrier concentration, so p and n also equal to the doping level.

From Gauss's law, the integration of the electric field along the volume equals the integration of the charges enclosed in the surface divided by the permittivity:

$$\oiint_{\partial\Omega} E \cdot dS = \frac{1}{\varepsilon} \iiint_{\Omega} \rho dV \quad (5)$$

Thus we can get the electrical field distribution from the charge distribution:

$$E = \begin{cases} 0, & 0 < x < R_1 - w_p \quad (6) \\ -\frac{p[x^2-(R_1-w_p)^2]}{2x\varepsilon}, & R_1 - w_p < x < R_1 \quad (7) \\ -\frac{p\left[{R_1}^2-(R_1-w_p)^2\right]-n(x^2-{R_1}^2)}{2x\varepsilon}, & R_1 < x < R_1 + w_n \quad (8) \\ 0, & R_1 + w_n < x < R_2 \quad (9) \end{cases}$$

By integrating the electric field, we can get the built-in potential distribution along the radial direction from the electrical field distribution:

$$\psi = \begin{cases} 0, & 0 < x < R_1 - w_p \quad (10) \\ \frac{p\left[x^2-(R_1-w_p)^2\right]}{4\varepsilon} - \frac{p(R_1-w_p)^2}{2\varepsilon} ln\frac{x}{R_1-w_p}, & R_1 - w_p < x < R_1 \quad (11) \\ \frac{p\left[{R_1}^2-(R_1-w_p)^2\right]}{4\varepsilon} - \frac{p(R_1-w_p)^2}{2\varepsilon} ln\frac{R_1}{R_1-w_p} + \frac{p\left[{R_1}^2-(R_1-w_p)^2\right]+n{R_1}^2}{2\varepsilon} ln\frac{x}{R_1} - \frac{x}{4\varepsilon}(x^2-{R_1}^2), & R_1 < x < R_1 + w_n \quad (12) \\ \frac{p\left[{R_1}^2-(R_1-w_p)^2\right]}{4\varepsilon} - \frac{p(R_1-w_p)^2}{2\varepsilon} ln\frac{R_1}{R_1-w_p} + \frac{p\left[{R_1}^2-(R_1-w_p)^2\right]+n{R_1}^2}{4\varepsilon} ln\frac{\frac{p}{n}\left[{R_1}^2-(R_1-w_p)^2\right]+{R_1}^2}{{R_1}^2} - \frac{n}{4\varepsilon}\left(\frac{p}{n}\left[{R_1}^2-(R_1-w_p)^2\right]\right), & R_1 + w_n < x < R_2 \quad (13) \end{cases}$$

In the equations described above, we have two unknowns: $w_n$ and $w_p$. From charge conservation, we know that the total extra electron number at p-side equals to the total extra holes number at n side. So we get:

$$n\left[(R_1+w_n)^2-{R_1}^2\right]=p\left[{R_1}^2-\left(R_1-w_p\right)^2\right] \quad (14)$$

Then $w_p$ can be described by $w_n$ :

$$w_p=R_1-\sqrt{R_1-\frac{n}{p}\left[(R_1+w_n)^2-{R_1}^2\right]} \quad (15)$$

The built-in potential reaches a maximum at the quasi neutral region of n side, as described by equation 13. It can also be calculated from the doping level and the neutral free carrier concentration by equation:

$$V_{bi}=k_BTln\left(\frac{np}{n_i^2}\right) \quad (16)$$

Combining equation 13 and equation 16, we can get the equation to calculate $w_p$:

$$k_BTln\left(\frac{np}{n_i^2}\right)=\frac{p\left[{R_1}^2-\left(R_1-w_p\right)^2\right]}{4\varepsilon}-\frac{p\left(R_1-w_p\right)^2}{2\varepsilon}ln\frac{R_1}{R_1-w_p}+\frac{p\left[{R_1}^2-\left(R_1-w_p\right)^2\right]+n{R_1}^2}{4\varepsilon}ln\frac{\frac{p}{n}\left[{R_1}^2-\left(R_1-w_p\right)^2\right]+{R_1}^2}{{R_1}^2}-\frac{n}{4\varepsilon}\left(\frac{p}{n}\left[{R_1}^2-\left(R_1-w_p\right)^2\right]\right) \quad (17)$$

However, if the theoretical depletion region width is larger than the real p or n regions size, then the built-in potential is not equal to the value calculated from the doping level.

When $R_1<w_p$, the electrical field can be calculated as:

$$E=\begin{cases}-\frac{px}{2\varepsilon}, & x<R_1 \quad (18)\\ -\frac{-nx^2+n{R_1}^2+p{R_1}^2}{2x\varepsilon}, & R_1<x<R_1+w_n \quad (19)\\ 0, & R_1+w_n<x<R_2 \quad (20)\end{cases}$$

And the built-in potential can be calculated as:

$$\psi=\begin{cases}\frac{px^2}{4\varepsilon}, & x<R_1 \quad (21)\\ \frac{p{R_1}^2+n{R_1}^2}{2\varepsilon}ln\frac{x}{R_1}+\frac{p{R_1}^2+n{R_1}^2-nx^2}{4\varepsilon}, & R_1<x<R_1+w_n \quad (22)\\ \frac{p{R_1}^2+n{R_1}^2}{2\varepsilon}ln\frac{R_1+w_n}{R_1}+\frac{p{R_1}^2+n{R_1}^2-n(R_1+w_n)^2}{4\varepsilon}, & R_1+w_n<x<R_2 \quad (23)\end{cases}$$

When the theoretical depletion at n side is bigger than the n region size, $R_2-R_1<w_n$, then the real depletion region is the same size as the n type region.

$$w_n=R_2-R_1 \quad (24)$$

Then $w_p$ and built-in potential can be calculated by equation 15 and 13, respectively.

### 2.2 Radial PN junction at steady state

In a semiconductor, there are two mechanisms which can contribute to the current flow: the drift and diffusion. This can be described by the following equation:

$$j = j_{diffusion} + j_{drift} \tag{25}$$

Where $j$ is the total current, $j_{diffusion}$ is the diffusion current, and $j_{drift}$ is the drift current.

In silicon PN junction solar cells, the photo-current can be calculated by summing the electron current at quasi-neutral region at p-side, the hole current at quasi-neutral region at p-side and all the current generated at depletion region. Since the electron flow and hole flow have similar mathematical expressions, we only show the expression for the electron flow. At p-side, the electron current can be described as:

$$J_n(x) = qD_n\nabla_n + q\mu_n nE, \tag{26}$$

Where $J_n(x)$ is the electron current density at position $x$, $q$ is electron charge, which is 1.602 x $10^{-19}$ coulombs, $D_n$ is electron diffusion coefficient in Si, $\nabla_n$ is electron density gradient at position $x$, $\mu_n$ is the electron mobility in Si, n is free electron density, E is electric field at position $x$.

However, outside the depletion region, the drift current can be neglected, thus the current density at the quasi-neutral region of p-side can be described as:

$$J_n(x) \approx qD_n\nabla_n \tag{27}$$

Inside solar cells, there are three phenomena which change the carrier density: change of current density, carrier generation and carrier recombination. From conservation of electron number, we can get :

$$\frac{\partial n}{\partial t} = -\frac{1}{q}\nabla J_n + G_n - U_n \tag{28}$$

Where $\nabla J_n$ is the change rate of the current density. Here we consider $J_n$ is the flow rate of electrons, it has a positive value. $G_n$ is the electron generation rate, and $U_n$ is the electron recombination rate.

The recombination rate can be described by the electron diffusion length:

$$U_n = \frac{n-n_0}{L_n^2} D_n \tag{29}$$

Where $L_n$ is the electron diffusion length, $n_0$ is the electron concentration at equilibrium, $D_n$ is the electron diffusion coefficient.

At steady state, electron density does not change with time, so we get:

$$\frac{\partial n}{\partial t} = 0 \tag{30}$$

Combine equation 27, 28, 29 and 30 we can get:

$$\frac{\partial^2 n}{\partial x^2} + \frac{1}{x}\frac{\partial n}{\partial x} - \frac{n-n_0}{L_n^2} + \frac{G}{D_n} = 0 \tag{31}$$

Note in cylindrical coordinate, the form of second order derivate is:

$$\nabla_n{}^2 = \frac{1}{x}\frac{\partial n}{\partial x}\left(x\frac{\partial n}{\partial x}\right) = \frac{1}{x}\frac{\partial n}{\partial x} + \frac{\partial^2 n}{\partial x^2} \tag{32}$$

Reform the equation 32, we can get:

$$x^2\frac{\partial^2 n}{\partial x^2} + x\frac{\partial n}{\partial x} - x^2\frac{1}{L_n^2}(n - n_0 - \frac{GL_n^2}{D_n}) = 0 \tag{33}$$

In order to get the form of modified Bessel function, we do the following substitution:

$$N = n - n_0 - \frac{GL_n^2}{D_n} \tag{34}$$

$$X = \frac{x}{L_n} \tag{35}$$

Thus:

$$n = N + n_0 + \frac{GL_n^2}{D_n} \tag{36}$$

$$x = L_n X \tag{37}$$

We get the following expressions from equation 36 and 37:

$$\frac{\partial n}{\partial x} = \frac{\partial N}{\partial x} = \frac{1}{L_n}\frac{\partial N}{\partial X} \tag{38}$$

$$\frac{\partial^2 n}{\partial x^2} = \frac{1}{L_n^2}\frac{\partial^2 N}{\partial X^2} \tag{39}$$

Combination equation 33, 36, 37, 38 and 39, we get:

$$X^2\frac{\partial^2 N}{\partial X^2} + X\frac{\partial N}{\partial X} - X^2 N = 0 \tag{40}$$

Compared with standard modified Bessel's equation :

$$z^2\frac{d^2 y}{dz^2} + z\frac{dy}{dz} - (z^2 - \nu^2)y = 0 \tag{41}$$

We can know that equation 40 is a modified zero order Bessel's equation, with $\nu = 0$.

Since $\nu = 0$ is a integer, we can use the modified Bessel functions of the first kind $I_\nu(z)$ and the modified Bessel functions of the second kind $K_\nu(z)$ to form a fundamental set of solutions of the modified Bessel's equation where

$$I_\nu(z) = \left(\frac{z}{2}\right)^\nu \sum_{(k=0)}^{\infty} \frac{\left(\frac{z^2}{4}\right)^k}{k!\Gamma(\nu+k+1)} \tag{42}$$

And:

$$K_\nu(z) = (\frac{\pi}{2})\frac{I_{-\nu}(z) - I_\nu(z)}{sin(\nu\pi)} \tag{43}$$

Where $\Gamma(v+k+1)$ is the gamma function. So the solution to equation 40 is:

$$N(X) = AI_0(X) + BK_0(X) \tag{44}$$

Where A and B are coefficients.

We can use the recurrence relation for $I_v(z)$ to calculate the derivative of $I_v(z)$:

$$I_{v-1}(x) + I_{v+1}(x) = 2I_v{}'(x) \tag{45}$$

From equation 43 and 45, we can get the derivative of $K_v(z)$ :

$$K_v{}'(z) = \left(\frac{\pi}{2}\right)\frac{I_{-v}{}'(z) - I_v(z)'}{\sin(v\pi)} = \frac{1}{2}\frac{\pi}{2}\frac{(I_{-v-1}(x)+I_{-v+1}(x)) - (I_{v-1}(x)+I_{v+1}(x))}{\sin(v\pi)} = \frac{1}{2}\frac{\pi}{2}\frac{I_{-(v-1)}(x) - I_{v-1}(x)}{\sin(v\pi)} + \frac{1}{2}\frac{\pi}{2}\frac{I_{-(v+1)}(x) - I_{v+1}(x)}{\sin(v\pi)} = \frac{1}{2}(K_{v-1}(x) + K_{v+1}(x)) \tag{46}$$

Then the derivative of $N(X)$ can be got:

$$N'(X) = AI_0{}'(X) + BK_0{}'(X) = \frac{A}{2}\big(I_{-1}(X) + I_1(X)\big) + \frac{B}{2}\big(K_{-1}(X) + K_1(X)\big) \tag{47}$$

The two coefficients A and B can be calculated by applying boundary conditions, which are surface recombination and the carrier density at the edge of depletion region. Figure 3 shows the electron density along the quasi-neutral region with and without the two boundary conditions. Without boundaries, the electron density is uniform along the quasi-neutral region, as shown in figure 3 a). In this case, the electron density only depends on the generation rate and the recombination rate. When there are boundary conditions, the electron density at the surface and interface will decrease because electrons recombine at the surface and get separated at the edge of depletion region.

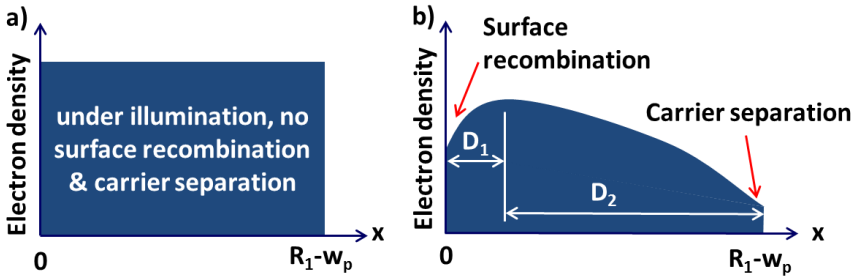


Figure 3. Boundary conditions for electron density distribution along the quasi-neutral region at p doped side. a) Electron density distribution when there is no surface recombination at the surface of the quasi-neutral region, no carrier separation at the interface of quasi-neutral region and depletion region. b) Electron density distribution when there is surface recombination at the surface of the quasi-neutral region and carrier separation at the interface of quasi-neutral region and depletion region.

The carrier separation at the interface of the quasi-neutral region and depletion region is determined by the voltage across the PN junction determined by the outer circuit. This boundary can be described as the relation between the applied voltage and the carrier density at $x = R_1 - w_p$:

$$n - n_0 = \frac{n_i^2}{N_a}\left(e^{\frac{qv}{k_B T}} - 1\right) \tag{48}$$

Where $N_a$ is doping level at p side, $n_i$ is free carrier concentration in the intrinsic Si, $k_B$ is Boltzmann constant, and T is temperature.

Unlike planar PN junction, the radial PN junction only has one surface which is the surface of the wire. In this case the quasi neutral region of the p side does not have surface along radial direction. Thus the surface recombination can be considered as 0. Then the boundary at $x = 0$ is:

$$D_n \frac{dn}{dx} = 0 \tag{49}$$

Combine equation 36, 37, 44, 47, 48 and 49, we can get

$$A = \left(\frac{n_i^2}{N_a}\left(e^{\frac{qv}{k_B T}} - 1\right) - \frac{GL_n^2}{D_n}\right) / I_0\left(\frac{R_1 - w_p}{L_n}\right), \tag{50}$$

And

$$B = 0 \tag{51}$$

Thus electron current density at quasi neutral region of p side is:

$$J_n(x) = qD_n \nabla_n = qD_n \frac{1}{L_n} N'(X) = qD_n \frac{1}{L_n}\left(\frac{A}{2}\left(I_{-1}\left(\frac{x}{L_n}\right) + I_1\left(\frac{x}{L_n}\right)\right)\right) \tag{52}$$

In the quasi neutral region of n side, the hole concentration has a similar expression as the electrons described in equation 33:

$$x^2 \frac{\partial^2 p}{\partial x^2} + x \frac{\partial p}{\partial x} - x^2 \frac{1}{L_p^2}\left(p - p_0 - \frac{GL_p^2}{D_p}\right) = 0 \tag{53}$$

Where $p$ is the hole concentration, $L_p$ is the hole diffusion length in Si, $D_p$ is hole diffusion coefficient. With the following substitution:

$$P = p - p_0 - \frac{GL_p^2}{D_p} \tag{54}$$

$$X = \frac{x}{L_p} \tag{55}$$

We can also get a modified Bessel's equation for holes

$$X^2 \frac{\partial^2 P}{\partial X^2} + X \frac{\partial P}{\partial X} - X^2 P = 0 \tag{56}$$

The solution to this equation has the same form with equation 44:

$$P(X) = AI_0(X) + BK_0(X) \tag{57}$$

Then the derivative of $P(X)$ has the similar form with equation 47:

$$P'(X) = AI_0{}'(X) + BK_0{}'(X) = \frac{A}{2}\left(I_{-1}(X) + I_1(X)\right) + \frac{B}{2}\left(K_{-1}(X) + K_1(X)\right) \tag{58}$$

The first boundary condition is the hole concentration at the interface of depletion region and the quasi neutral region, at $x = R_2 - w_n$. The value is a function of applied bias across the PN junction:

$$p - p_0 = \frac{n_i^2}{N_d}(e^{\frac{qv}{k_B T}} - 1) \quad (59)$$

Where $N_d$ is doping level at n side.

The second boundary condition is that the current at the surface is the surface recombination current. At $x = R_2$:

$$-D_p \frac{dp}{dx} = J = -S_p(p - p_0) \quad (60)$$

Where $S_p$ is the surface recombination velocity for holes.

Combine equation 54, 55, 57, 58 and 60, we can get

$$\left[\frac{D_p}{2L_p}\left(I_{-1}(X_1) + I_1(X_1)\right) - S_p I_0(X_1)\right]A + \left[\frac{D_p}{2L_p}\left(K_{-1}(X_1) + K_1(X_1)\right) - S_p K_0(X_1)\right]B = S_p \frac{GL_p^2}{D_p} \quad (61)$$

Where $X_1 = \frac{R_2}{L_p}$. And combine equation 54, 55, 57 and 59, we can get:

$$I_0(X_2)A + K_0(X_2)B = \frac{n_i^2}{N_a}\left(e^{\frac{qv}{k_B T}} - 1\right) - \frac{GL_p^2}{D_p} \quad (62)$$

Where $X_2 = \frac{R_2 - w_n}{L_p}$. With 61 and 62, the follow equation can be obtained:

$$\begin{vmatrix} \frac{D_p}{2L_p}\left(I_{-1}(X_1) + I_1(X_1)\right) - S_n I_0(X_1) & \frac{D_p}{2L_p}\left(K_{-1}(X_1) + K_1(X_1)\right) - S_n K_0(X_1) \\ I_0(X_2) & K_0(X_2) \end{vmatrix} \cdot \begin{vmatrix} A \\ B \end{vmatrix} = \begin{vmatrix} S_p \frac{GL_p^2}{D_p} \\ p_0\left(e^{\frac{qv}{k_B T}} - 1\right) - \frac{GL_p^2}{D_p} \end{vmatrix} \quad (63)$$

Substitute the elements of matrix in 63 with letters, we get:

$$\begin{vmatrix} a & b \\ c & d \end{vmatrix} \cdot \begin{vmatrix} A \\ B \end{vmatrix} = \begin{vmatrix} e \\ f \end{vmatrix} \quad (64)$$

Then A and B can be obtained easily:

$$\begin{vmatrix} A \\ B \end{vmatrix} = \begin{vmatrix} \frac{ed - bf}{ad - bc} \\ \frac{af - ec}{ad - bc} \end{vmatrix} \quad (65)$$

Finally, the hole current at quasi neutral region of n side is:

$$J_p(x) = qD_n \nabla_n = qD_n \frac{1}{L_n} N'(X) = qD_n \frac{1}{L_n}\left(\frac{A}{2}\left(I_{-1}\left(\frac{x}{L_n}\right) + I_1\left(\frac{x}{L_n}\right)\right) + \frac{B}{2}\left(K_{-1}\left(\frac{x}{L_n}\right) + K_1\left(\frac{x}{L_n}\right)\right)\right) \quad (66)$$

The total current generated by the solar cell is the sum of electron current at $x = R_1 - w_p$, hole current at $x = R_2 - w_n$, and the current generated in the depletion region.

$$J_{total} = J_n(R_1 - w_p) + J_p(R_2 - w_n) + J_{depletion\ region} \quad (67)$$

Since there is a strong electrical field in the depletion region, all the carrier generated in this region can be collected easily. So the $J_{depletion\ region}$ can be considered as all the photo-current generated in the depletion region.

The electrical modeling describes the carriers transport in the solar cells. So there need to have free carriers generation. We have used the light absorption data calculated in the optical modeling part 2.2.1 to calculate photo generation. To simplify the photo generation profile, we have considered that the carriers are generated uniformly in the solar cell.

## 3 Simulation results

Based on the theoretical analysis presented above, a Matlab code package has been developed to perform the simulation. This code package simulates a NW radial junction solar cell with a thick p-layer and a thin n-layer. It calculates the electron transport in p-type region to estimate the current in the whole solar cells.

The user interface of this code package is shown in figure 4. The main inputs are geometrical parameters such as NW diameter, pitch and length; and electrical parameters such as electron mobility and lift time. The main outputs are the width of depletion region and the performance of the solar cell. There is single NW Jsc and solar cell Jsc, The difference between the two is that the single NW Jsc is the generated current divided by the area of the top surface of the NW, while the solar cell current is the total generated current divided by the total area of the solar cell. Similarly, the single NW efficiency is the output power divided by the power incident on the top surface of the NW, while the solar cell efficiency is the output power divided by the power incident on the whole solar cell. The IV curve, band diagram, electric field along the radial direction of the NW, and the EQE are also plotted in the user interface.

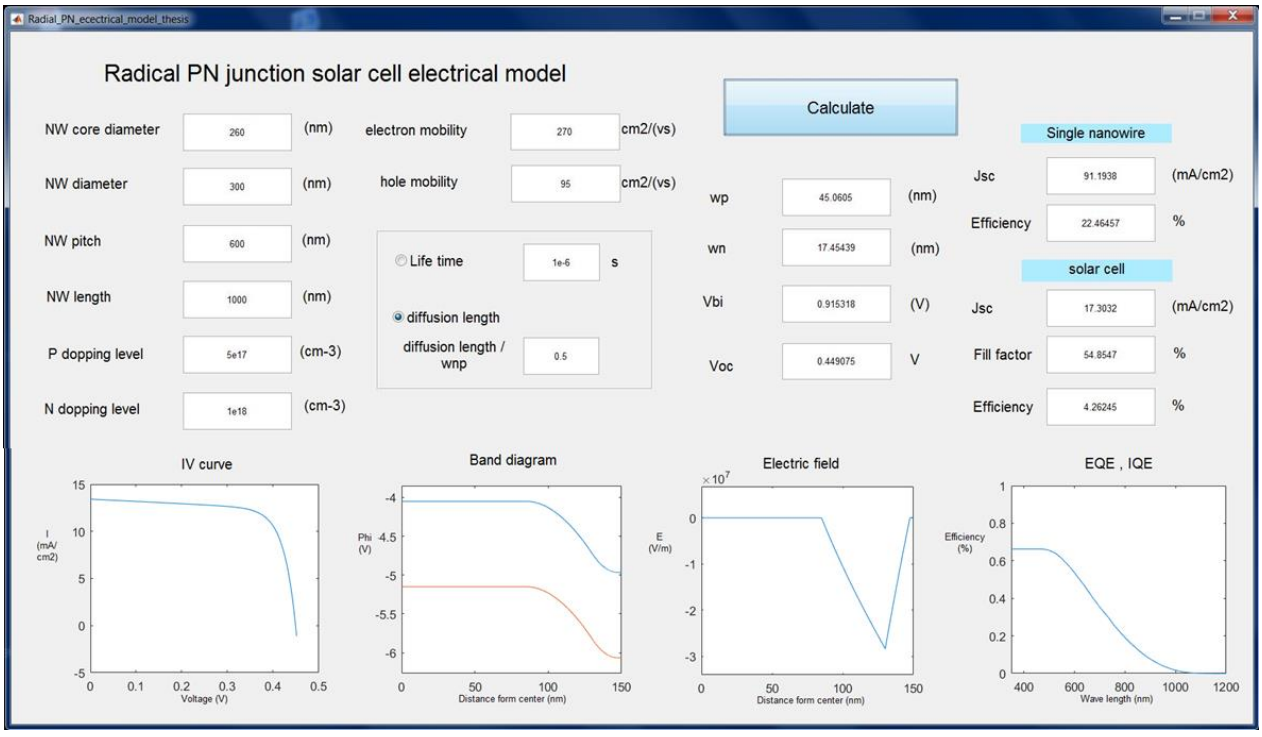


Figure 4. User interface of the code package for radial junction NW solar cell simulation.

One of the most important parameters for solar cell is the diffusion length of the carriers. We have calculated the IV curve by changing the diffusion length/quasi neutral region ratio, as shown in figure 5. The main parameters for this calculation are listed in table 2.

Table 2. Parameters have been used for NW radial PN junction solar cell electrical simulation.

| Parameter name | value | unit |
|---|---|---|
| NW core diameter | 260 | nm |
| NW diameter | 300 | nm |
| NW pitch | 600 | nm |
| NW length | 1000 | nm |
| P doping level | 5e17 | /cm$^3$ |
| N doping level | 1e18 | /cm$^3$ |
| Electron mobility | 270 | cm$^2$/(v*s) |
| Hole mobility | 95 | cm$^2$/(v*s) |
| Intrinsic carrier concentration at 300 K | 1.45e10 | /cm$^3$ |

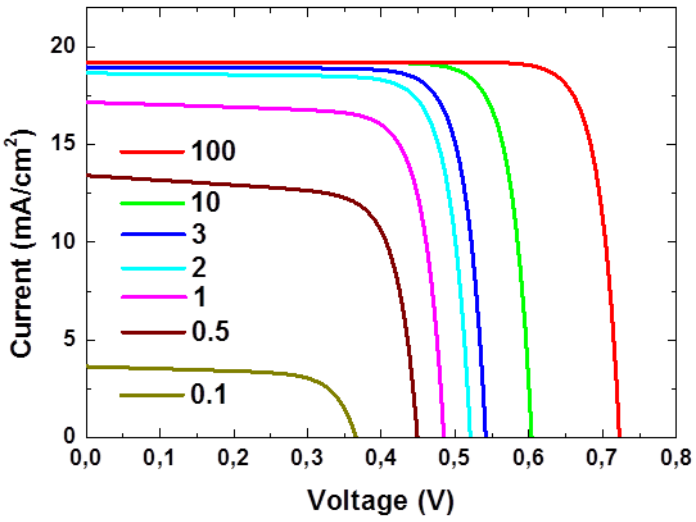


Figure 5. IV curves as a function of diffusion length/quasi-neutral region width ratio.

The Jsc, Voc, fill factor and efficiency have also extracted from the IV curves, as shown in figure 6. When the diffusion length is more than 3 times bigger than the width of the quasi neutral region, the Jsc approaches the saturation level. However, further increase of the ratio will increase the Voc. When the ratio is smaller than 3, both Jsc and Voc decrease with the ratio sharply. The Jsc, Voc, fill factor and efficiency have also extracted from the IV curves. As shown in figure 6, the fill factor has a similar trend with the Jsc. When the ratio is smaller than 3, Jsc and fill factor increase quickly with the increase of ratio. The efficiency has a similar trend with the Voc. From electrical point of view, the advantage of using NW radial junction is to reduce the length of the quasi-neutral region. This gives a high diffusion lenth/quasi-neutral region ratio, and consequently, a high solar cell performance.

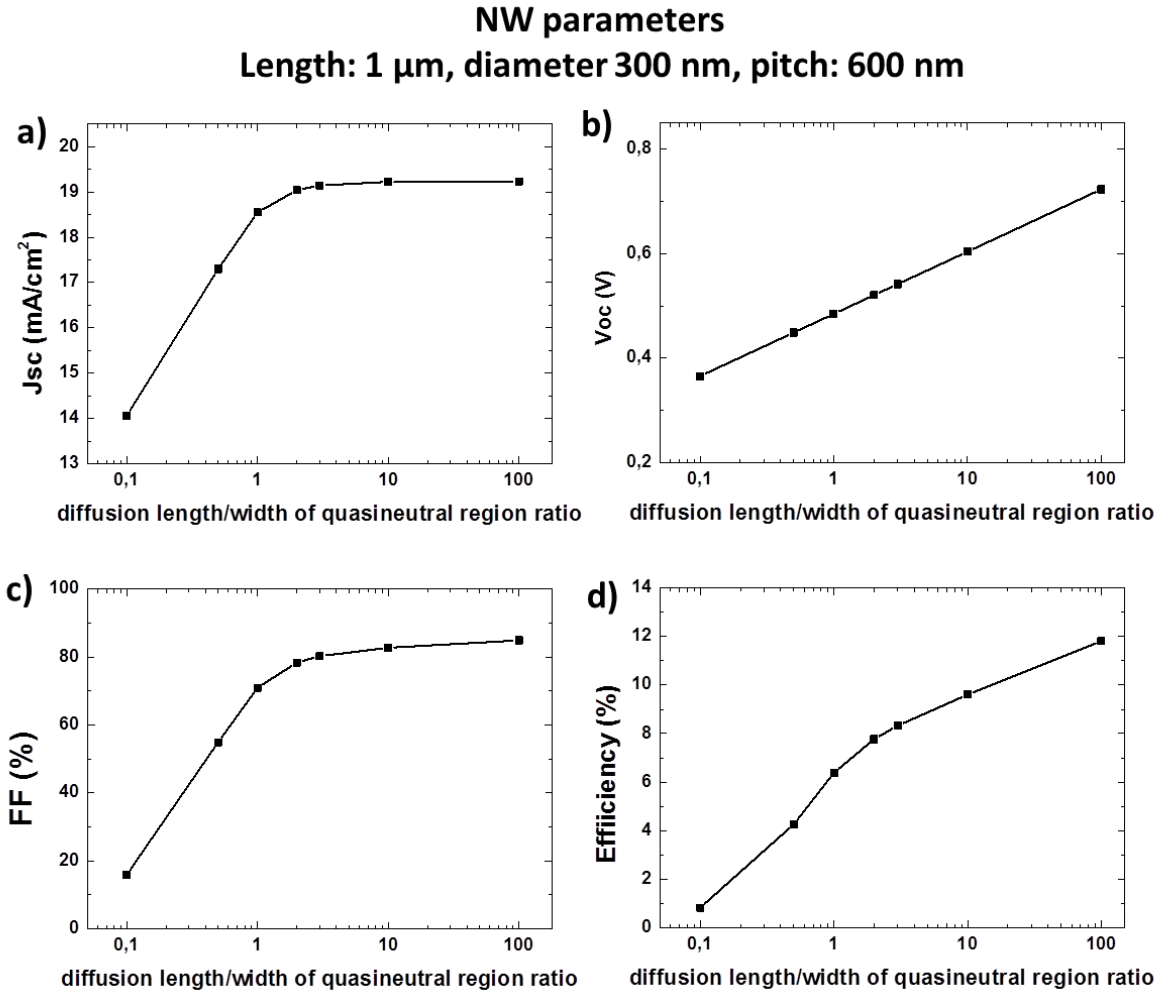


Figure 6. Jsc, Voc, fill factor and efficiency as a function of the diffusion length/quasi neutral region width ratio.

## 4 Summary of electrical modeling

In this part, the carrier transport in the radial junction solar cells has been analyzed from first principles. The theoretical analyses have been implemented into a matlab code package. With this code package, we have calculated the solar cell performance as a function of the carrier diffusion length/quasi-neutral region width ratio. We found that when the ratio is smaller than 3, the Jsc and fill factor increase rapidly with the ratio. When the ratio is bigger than 3, the Jsc and fill factor reach saturation level rapidly, but the Voc and efficiency keep on increasing till the limited value. This shows that by decreasing the quasi- neutral region length, the NW radial junction solar cell increase the carrier diffusion length/quasi-neutral region width ratio, and thus increase the solar cell efficiency.

## 5 Reference

1 Kandala, A., Betti, T. & Morral, A. F. I. General theoretical considerations on nanowire solar cell designs. *Phys Status Solidi A* **206**, 173-178, doi:10.1002/pssa.200723672 (2009).

2 Ali, N. M., Allam, N. K., Haleem, A. M. A. & Rafat, N. H. Analytical modeling of the radial pn junction nanowire solar cells. *J Appl Phys* **116**, 7, doi:10.1063/1.4886596 (2014).

3 Kayes, B. M., Atwater, H. A. & Lewis, N. S. Comparison of the device physics principles of planar and radial p-n junction nanorod solar cells. *J Appl Phys* **97**, 114302, doi:10.1063/1.1901835 (2005).

# List of publications

## Peer reviewed publications

- J. Tang, J. Wang, J.-L. Maurice, W. Chen, M. Foldyna, E. Johnson, L. Yu, and P. Roca i Cabarrocas. Cylindrical GeNWs grown by PECVD VLS method. (under preparation)
- J. Tang, J.-L. Maurice*, F. Fossard, I. Florea, W. Chen, E. V. Johnson, M. Foldyna, L. Yu and P. Roca i Cabarrocas. Natural occurrence of the diamond hexagonal structure in silicon nanowires grown by plasma assisted vapour-liquidsolid method. (Nanoscale, under review)
- J. Tang, J.-L. Maurice, W. Chen, S. Misra, M. Foldyna, E. V Johnson, and P. Roca i Cabarrocas*. Plasma-Assisted Growth of Silicon Nanowires by Sn Catalyst: Step-by-Step Observation. Nanoscale research letters, 11,1,455, 2016
- R. Cariou, J. Tang, N. Ramay, R. Ruggerid, and P. Roca i Cabarrocas. Low temperature epitaxial growth of SiGe absorber for thin film HIT solar cells, Solar Energy Materials and Solar cells 134, 15, 2015

## Conference proceedings

- J.-L. Maurice, J. Tang, I. Florea, F. Fossard, P. Roca i Cabarrocas, E. V. Johnson, and M. Foldyna. TEM characterisation of diamond-hexagonal silicon nanowires. European Microscopy Congress 2016
- R. Cariou, I. Massiot, R. Ruggeri, N. Ramay, J. Tang, A. Cattoni, S. Collin, J. Nassar, and P. Roca i Cabarrocas. Low temperature epitaxial growth of Si and SiGe and their transfer to foreign substrate. 28th EU PVSEC 2013, Paris, France, September 2013
- R. Cariou, I. Massiot, R. Ruggeri, N. Ramay, J. Tang, A. Cattoni, S. Collin, J. Nassar and P. Roca i Cabarrocas. Low-temperature SiGe PECVD epitaxy: from wafer equivalent to ultra-thin crystalline solar cells on inexpensive substrates. 39th IEEE Photovoltaic Specialist Conference proceeding, Tampa, USA, June 2013

# Résumé

La lumière du soleil, qui est abondante et propre, est une source d'énergie qui peut répondre aux besoins énergétiques croissants de la société. Avec les cellules solaires, l'énergie du soleil est transformée directement en électricité de manière propre. Pour une application à grande échelle des cellules solaires, réduire leur coût de production est un enjeu majeur. En raison de leur forte absorption de la lumière et leur collecte efficace des porteurs photogénérés, les cellules solaires à base de nanofils ont le potentiel de réduire le coût de l'énergie solaire photovoltaïque. Cette thèse a pour objectif de développer des nouvelles architectures de cellules solaires à base de nanofils. Des travaux expérimentaux appuyés par la modélisation ont été effectués.

Cette thèse commence par la modélisation de l'absorption de la lumière dans les cellules solaires à base de nanofils. Le champ électrique et le profil d'absorption dans les cellules solaires ont été calculés. L'amélioration de l'absorption de la lumière dans les cellules solaires à base de nanofils par rapport aux cellules ayant une architecture planaire a été démontrée. En faisant varier l'épaisseur des couches d'absorbeur, on a obtenu un photocourant de 14.1 mA/cm$^2$ pour des cellules solaires tandem a-Si:H/µc-Si:H. Ceci a été obtenu avec une couche de 60 nm de a-Si:H et 290 nm de µc-Si:H. Un modèle électrique préliminaire pour les cellules solaires à jonction PN a été développé sur matlab. La simulation avec ce modèle montre que les cellules solaires à jonction radiale à base de nanofils de silicum ont un courant de court-circuit et un facteur de forme plus élevé en raison de la petite largeur de la région quasi neutre. Une compréhension détaillée du transport des charges dans les jonctions PN radiales a été obtenu.

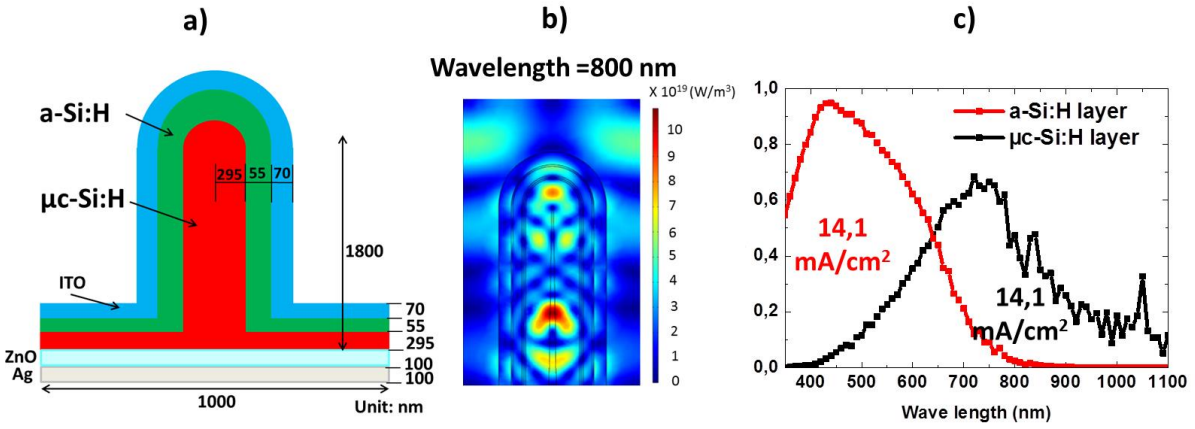


Figure 1. a) Schéma d'une cellule solaire tandem a-Si:H/µc-Si:H utilisé pour la modélisation optique. b) Exemple de distribution d'intensité du champ électrique dans la cellule exposée à une lumière monochromatique à 800 nm. c) Absorption dans les deux couches absorbantes de la cellule solaire tandem. On note que le même courant est photogénéré dans les deux cellules.

Pour la partie expérimentale, nous nous sommes d'abord concentrés sur l'étude des processus de croissance de nanofils par un procédé VLS assisté par plasma. Nous avons réalisé des expériences d'ingénierie des gouttelettes de Sn utilisées comme catalyseur pour la croissance des nanofils. Nous avons trouvé qu'avec un recuit, les gouttelettes présentent de petits changements dans leur taille et leur densité. Cependant, quand le recuit est effectué avec la présence d'une couche mince d'a-Si:H, il y des changements modérés de la taille et de la densité des gouttelettes; avec un traitement par

plasma de $H_2$, la taille et la densité des gouttelettes peuvent être considérablement modifiées. Une observation et une analyse détaillées du processus de croissance de nanofils silicium ont été réalisées étape par étape. La phase de croissance initiale détermine la densité, la direction de croissance et la taille des nanofils. Nous montrons qu'il y a une forte coalescence des gouttelettes de catalyseur en raison de la formation de nanofils pendant les dix premières secondes de croissance. En plus, nous fournissons une caractérisation systématique et une explication détaillée de la forte évolution de la densité de gouttes de catalyseur et de nanofils, la morphologie de nanofils et leur cristallinité pendant le processus de croissance, comme illustré schématiquement sur la figure ci-dessous.

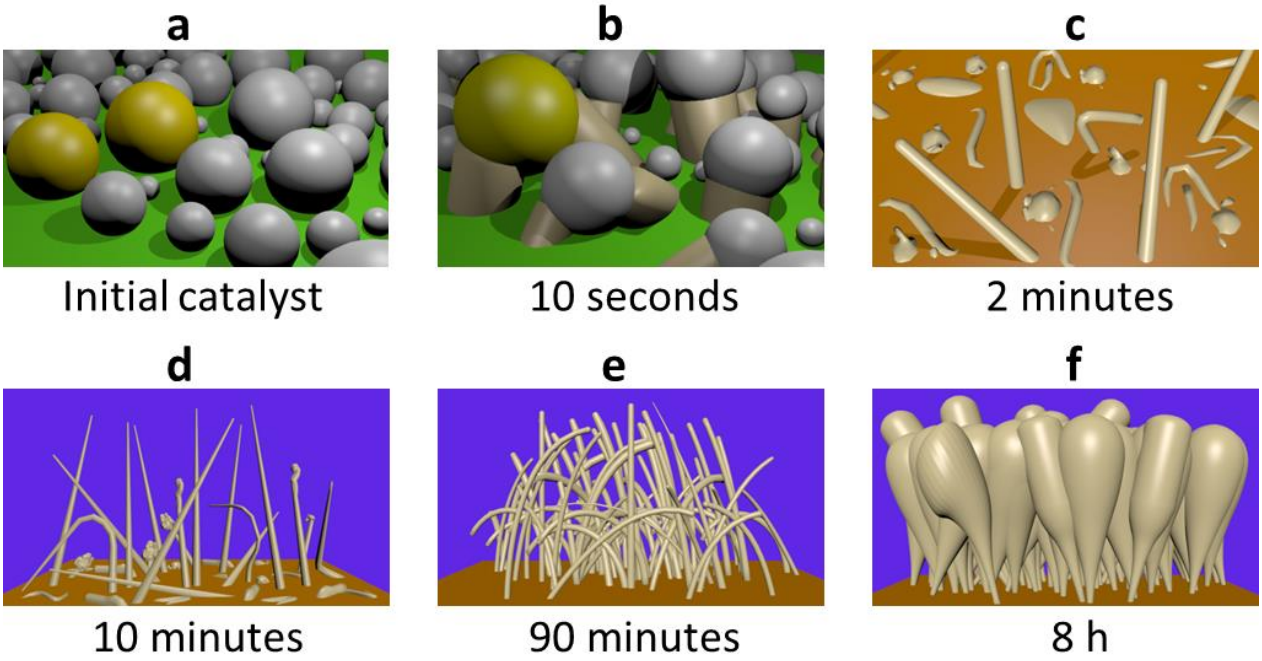


Figure 2. Illustration 3D de l'état de croissance de nanofils silicium avec des durées de croissances différentes.

Nous avons fait croitre de  nanofils silicium directement sur une grille de microscope en cuivre afin de faciliter leur observation au microscope électronique en transmission. Nous avons observé que ceux de petit diamètre (2 – 5 nm) ont une phase cristalline hexagonale. Les caractérisations par microscopie électronique en transmission dans l'axe de la zone [11-20] fournissent une preuve évidente d'un arrangement atomique hexagonal. La structure hexagonale est stable à température et pression ambiantes, et après un recuit à 230°C.

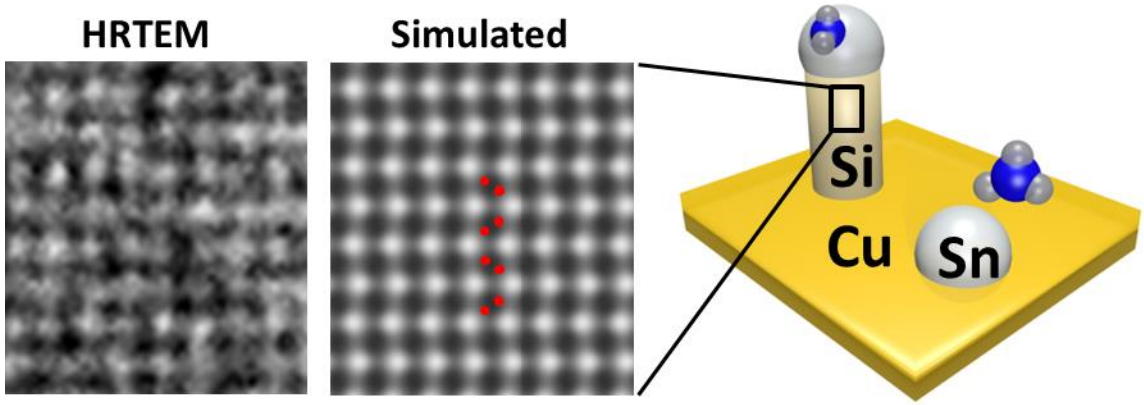


Figure 3. Phase cristalline hexagonale dans les nanofils silicium.

Une fois la croissance de nanofils de silicium optimisée, nous avons abordé la croissance de nanofils de Ge et d'alliages SiGe dans le but de réduire le gap et élargir le domaine spectral de nos cellules. Nous avons produit des nanofils de silicium-germanium avec des catalyseurs Sn, In, Au et Cu par un procédé VLS assisté par plasma. Nous avons observé qu'à 400°C, le Cu et l'In peuvent catalyser la croissance de nanofils de SiGe avec un ratio de $GeH_4$ / ($SiH_4$ + $GeH_4$) plus grand que pour Sn et Au. La morphologie des nanofils de silicium-germanium obtenus avec ces catalyseurs ne présente pas de différences significatives. La longueur des nanofils est principalement déterminée par le flux de radicaux SiHx et GeHx, ainsi que par la taille des gouttelettes de catalyseur. À notre connaissance, c'est le premier rapport sur la croissance de nanofils de silicium-germanium par un procédé VLS assisté par plasma. En diminuant la température du substrat, nous avons obtenu avec succès des nanofils de silicium-germanium avec une forte teneur en germanium. Nous avons trouvé qu'il n'y a pas de dégradation de la morphologie des nanofils de SiGe avec l'augmentation de la concentration de germanium et la diminution de la température du substrat. À 235°C, des nanofils de germanium ont été aussi obtenus avec Sn, In et Cu comme catalyseurs. En augmentant la température du substrat et la pression partielle de $GeH_4$, nous avons pu produire des nanofils germanium droits avec un diamètre constant (~20 nm) et cela pour les catalyseurs Sn et In. Nous avons divisé la croissance de GeNW en deux régimes. Lorsque la température est inférieure à 350°C et que la pression partielle de $GeH_4$ est inférieure à 20 mTorr, on obtient la morphologie traditionnelle par un procédé VLS assisté par plasma (morphologie conique). Lorsque la température est supérieure à 350°C et que la pression partielle de $GeH_4$ est supérieure à 20 mTorr, on peut obtenir des nanofils cylindriques. À notre connaissance, c'est le premier rapport qui montre clairement des nanofils avec un diamètre constant obtenu par un procédé VLS assisté par plasma.

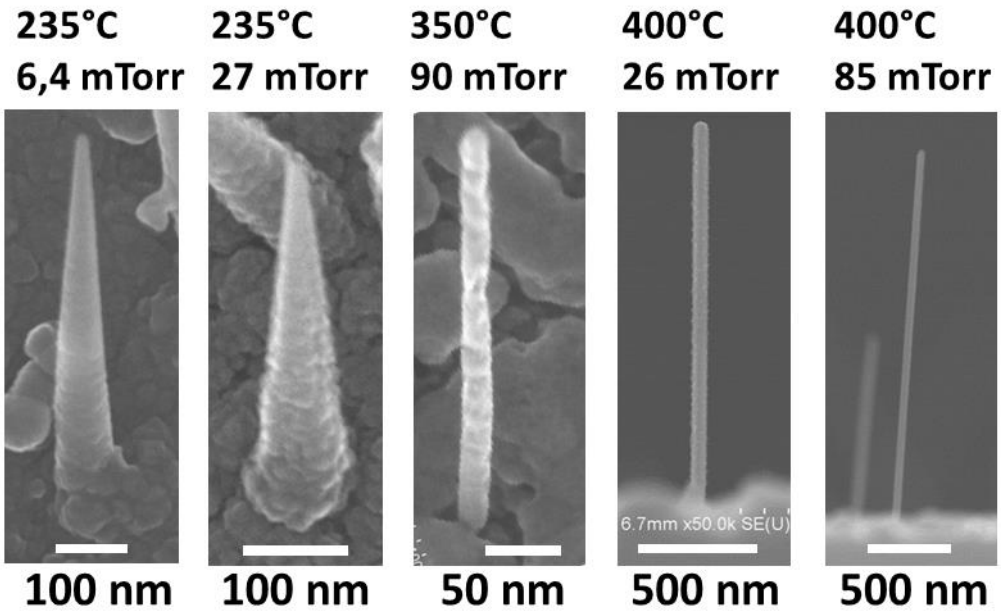


Figure 4. Nanofils de germanium produits par un procédé VLS assisté par plasma, pour des températures et pressions partielles de $GeH_4$ différents. Le catalyseur est In.

Enfin, nous nous sommes intéressés au le développement de cellules solaires à jonction radiale à base de nanofils. Des cellules solaires avec l'absorbeur a-SiGe:H ou µc-Si:H ont été fabriquées. L'amélioration de l'absorption de lumière dans la gamme spectrale rouge et infrarouge a été démontrée. En diminuant la longueur des nanofils et en augmentant l'épaisseur de la couche de µc-Si:H, nous avons amélioré significativement la performance des cellules solaires à base de µc-Si:H. Après cela, nous avons optimisé la longueur des nanofils pour les cellules solaires tandem a-Si:H / pm-Si:H et µc-Si:H / pm-Si:H. Pour la première fois, nous avons démontré que les nanofils de silicium-germanium peuvent être utilisés dans des cellules solaires à jonction radiale. Un rendement de conversion énergétique de 6% a été obtenu avec des cellules solaires à jonction radiale à base de nanofils de silicium-germanium.

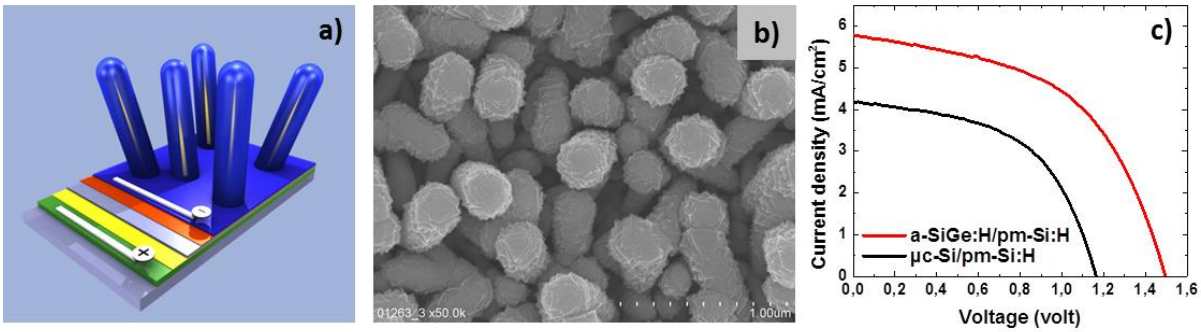


Figure 5. a) Schéma de cellules solaires à jonction radiale à base de nanofils. b). Image au microscope électronique à balayage de cellules solaires à jonction radiale à base de nanofils. c) Courbes de densité de courant-tension des cellules solaires tandem a-Si:H/µc-Si:H et de µc-Si:H/pm-Si:H.

# List of acronyms

| Acronym | Unit | Definition |
|---|---|---|
| **AC** | | Alternating Current |
| **a-Si:H** | | Hydrogenated amorphous silicon |
| **a-SiGe:H** | | Hydrogenated amorphous silicon germanium alloy |
| **c-Si** | | Crystalline Silicon |
| **Cg** | | Corning Glass |
| **c-Ge** | | Crystalline Germanium |
| **CVD** | | Chemical vapor Deposition |
| **DC** | | Direct Current |
| **EDX** | | Energy dispersive X-ray spectroscopy |
| **EQE** | % | External quantum efficiency |
| **$E_g$** | eV | Optical bandgap |
| **EELS** | | Electron energy loss spectroscopy |
| **FF** | % | Fill factor |
| **FFT** | | Fast Fourier Transform |
| **GeNW** | | Germanium nanowires |
| **HRTEM** | | High Resolution Transmission Electron Microscopy |
| **ITO** | | Indium Tin Oxide |
| **$J_{sc}$** | $mA.cm^{-2}$ | Short-circuit current |
| **J-V** | | Current density-Voltage |
| **LPCVD** | | Low-temperature chemical vapor deposition |
| **MBE** | | Molecular beam epitaxy |
| **NW** | | nanowire |
| **PECVD** | | Plasma Enhanced Chemical Vapor Deposition |
| **PL** | | Photoluminescence |
| **pm-Si:H** | | Hydrogenated polymorphous silicon |
| **RJ** | | Radial junction |
| **SEM** | | Scanning electron microscopy |
| **sccm** | $cm^3min^{-1}$ | Standard cubic centimeter per minute |
| **SFLS** | | Supercritical fluid-liquid-solid |
| **SiNW** | | Silicon nanowire |
| **SiGe** | | Silicon Germanium alloy |
| **STEM** | | Scanning transmission electron microscopy |
| **TEM** | | Transmission Electron Microscopy |
| **µc-Si:H** | | Hydrogenated microcrystalline silicon |
| **µc-SiOx:H** | | Hydrogenated microcrystalline silicon oxide |
| **UHV** | | Untra-High-Voltage |
| **$V_{oc}$** | V | Open-circuit voltage |
| **VLS** | | Vapor Liquid Solid |
| **VSS** | | Vapor Solid Solid |
| **ZnO:Al** | | Aluminum doped Zinc oxide |

université PARIS-SACLAY

ÉCOLE DOCTORALE
INTERFACES
Approches Interdisciplinaires : Fondements, Applications et Innovation

**Titre :** Processus de croissance de nanofils de Si et Ge: application a des cellules solaires

**Mots clés :** Energie solaire, nano fils, VLS assisté par plasma, Silicium-germanium, modélisation

**Résumé :** Cette thèse a pour objectif de développer des nouvelles architectures de cellules solaires à base de nanofils produites par un procédé VLS assisté par plasma. La modélisation optique est utilisée pour déterminer le champ et le profil d'absorption dans les cellules solaires. Un courant de 14 mA/cm$^2$ a été obtenu pour des cellules tandem a-Si:H/µc-Si:H. Un modèle électrique a aussi été développé, permettant une compréhension approfondie du transport dans ces dispositifs. En étudiant la croissance de SiNWs étape par étape, une bonne compréhension du processus de croissance a été obtenue, permettant d'expliquer la forte évolution de la densité de nanofils, de leur morphologie et de leur cristallinité. La phase hexagonale de Si a été observée dans les nanofils de silicium de petit diamètre (< 10 nm). Nous avons fait des caractérisations TEM dans la direction [11-20] qui apportent une preuve claire de la phase hexagonale de Si dans les SiNWs. Une fois la croissance de nanofils de silicium optimisée, nous avons abordé la croissance de nanofils de Ge et d'alliages SiGe dans le but de réduire le gap et élargir le domaine spectral de nos cellules. Le contenu en Ge a été varié entre 0 et 100% avec des catalyseurs Sn, In et Cu. Nous avons constaté qu'au-dessus d'une température critique (~350 °C), on peut obtenir des nanofils de Ge cylindriques, longs de plusieurs microns. Des cellules solaires PIN à jonction radiale avec une couche intrinsèque à base d'a-Si:H, de µc-Si:H ou d'-SiGe:H ont été fabriquées. A notre connaissance, c'est la première démonstration d'un tel dispositif à base de nano fils SiGe.

**Title :** From Silicon to Germanium Nanowires: growth processes and solar cell structures

**Keywords :** Solar energy, nanowires, plasma-assisted VLS, Silicon-Germanium, modeling

**Abstract :** This thesis is dedicated to develop new solar cell architectures based on nanowires produced by a plasma-assisted Vapor Liquid Solid process. By optical modeling, detailed field and absorption profiles in the NW solar cells have been obtained and a 14 mA/cm$^2$ matched photocurrent has been achieved for a-Si:H/µc-Si:H tandem solar cells. An electrical model for radial PN junction NW solar cells has also been developed from first principle rules, allowing a good understanding of the carrier transport. By analyzing step by step the SiNWs growth in a PECVD system we could propose a detailed explanation for the strong evolution of the NW density, morphology and crystallinity during growth. The rare hexagonal phase of Si has been observed in the as grown SiNWs with diameters smaller than 10 nm. For the first of time, we have provided TEM characterizations from [11-20] direction to give a clear proof of the hexagonal Si phase in as grown SiNWs. To develop low band bap, high mobility material for multi junction NW solar cells, we added germane to silane during the plasma-assisted VLS growth process. Ge contents from 0 to 100% have been achieved with Sn, In and Cu catalysts. We have found that above a critical temperature (~ 350 °C), micrometer long cylindrical Ge NWs can be obtained. NW based PIN radial junction solar cells having a-Si:H, a-SiGe:H and µc-Si:H as intrinsic absorber layers have been fabricated. For the SiGeNWs based solar cells, a 6% energy conversion efficiency has been achieved with p-i-n configuration. To our knowledge, this is the first demonstration of SiGeNWs based photovoltaic device.